

**FINAL REPORT**  
**INVESTIGATION OF LIGHT HYDROCARBON FUELS**  
**WITH**  
**FLUORINE-OXYGEN MIXTURES**  
**AS**  
**LIQUID ROCKET PROPELLANTS**

**15 SEPTEMBER 1967**

**Prepared for**  
**NATIONAL AERONAUTICS AND SPACE ADMINISTRATION**  
**CONTRACT NAS3-6296**

FACILITY FORM 602

**N67-35368**

(ACCESSION NUMBER)

(THRU)

(PAGES)

(CODE)

**827**

(CATEGORY)

(NASA CR OR TMX OR AD NUMBER)

**Pratt & Whitney Aircraft**  
**FLORIDA RESEARCH AND DEVELOPMENT CENTER**

DIVISION OF UNITED AIRCRAFT CORPORATION

**U**  
**A®**

## NOTICE

This report was prepared as an account of Government sponsored work. Neither the United States, nor the National Aeronautics and Space Administration (NASA), nor any person acting on behalf of NASA:

- A.) Makes any warranty or representation, expressed or implied, with respect to the accuracy, completeness, or usefulness of the information contained in this report, or that the use of any information, apparatus, method, or process disclosed in this report may not infringe privately owned rights; or
- B.) Assumes any liabilities with respect to the use of, or for damages resulting from the use of any information, apparatus, method or process disclosed in this report.

As used above, "person acting on behalf of NASA" includes any employee or contractor of NASA, or employee of such contractor, to the extent that such employee or contractor of NASA, or employee of such contractor prepares, disseminates, or provides access to, any information pursuant to his employment or contract with NASA, or his employment with such contractor.

Requests for copies of this report should be referred to

National Aeronautics and Space Administration  
Office of Scientific and Technical Information  
Attention: AFSS-A  
Washington, D.C. 20546



**FINAL REPORT**  
**INVESTIGATION OF LIGHT HYDROCARBON FUELS**  
**WITH**  
**FLUORINE-OXYGEN MIXTURES**  
**AS**  
**LIQUID ROCKET PROPELLANTS**

22 JUN 1965 13 JUN 1967

**Prepared for**  
**NATIONAL AERONAUTICS AND SPACE ADMINISTRATION**  
**CONTRACT NAS3-6296**

**PRATT & WHITNEY AIRCRAFT**  
**PROGRAM MANAGER**  
**A. I. MASTERS**

**TECHNICAL MANAGEMENT**  
**JOHN W. GREGORY**  
**LIQUID ROCKET TECHNOLOGY BRANCH**  
**NASA LEWIS RESEARCH CENTER**  
**CLEVELAND, OHIO**

**Pratt & Whitney Aircraft**  
**FLORIDA RESEARCH AND DEVELOPMENT CENTER**

**U**  
**A**<sup>®</sup>  
**DIVISION OF UNITED AIRCRAFT CORPORATION**

## FOREWORD

This report was prepared by the Pratt & Whitney Aircraft Division of United Aircraft Corporation under Contract NAS3-6296. The contract was administered by the Lewis Research Center of the National Aeronautics and Space Administration, Cleveland, Ohio. This report is the final report on the subject contract and summarizes the technical work conducted during the period 22 June 1965 to 15 June 1967. The NASA Project Manager for the contract was Mr. John W. Gregory.

The following Applied Research personnel at Pratt & Whitney Aircraft's Florida Research and Development Center contributed to the technical effort and preparation of this report: J. C. Matheson, T. E. Bailey, A. I. Masters (Program Manager), and J. E. Colbert (Deputy Program Manager) — program direction; R. A. Simmons and A. C. Schnell — theoretical performance analysis and data reduction; J. E. Jackson and J. Stettler — heat transfer analysis and testing; R. D. Steger — hardware design and test; and L. L. Kirkby — transpiration cooling analysis and nonequilibrium performance calculations. In addition, numerous groups and individuals outside the Applied Research project group made major contributions to the program, most notably: M. H. Staggs and G. D. Devane — test facility operations; and R. C. Frink — flox analysis.

### **ABSTRACT**

Performance and cooling analyses were made to determine the highest performing light hydrocarbon fuels for use with flox in regeneratively cooled and transpiration cooled pressure-fed thrust chambers. Sea level and simulated-altitude rocket firings were made at nominal 100-psia chamber pressure and 5000-lb vacuum thrust in uncooled, transpiration cooled, and regeneratively cooled chambers using flox with methane, propane, and butene-1. Based on the data obtained in these tests, predicted performance was calculated for these propellants over a range of thrust levels.

## CONTENTS (continued)

SECTION	PAGE
VII    TRANSPIRATION-COOLED ALTITUDE TESTS —	
TASK IV .....	81
A. Test Description .....	81
B. Performance .....	84
C. Cooling Requirements .....	88
D. Nozzle Heat Transfer .....	92
VIII    REGENERATIVELY COOLED ALTITUDE TESTS —	
TASK V .....	93
A. Test Description .....	93
B. Performance .....	98
C. Cooling Results .....	98
IX     PREDICTED PERFORMANCE OF FLOX/LIGHT HYDROCARBON PROPELLANTS .....	101
A. Theoretical Performance .....	101
B. Performance Losses .....	101
C. Predicted Engine Performance .....	107
D. Range of Applicability .....	113
X     REFERENCES .....	115
APPENDIX A — Data Reduction and Performance Calculations .....	A-1
APPENDIX B — Transpiration Cooling Flow Analysis .....	B-1
APPENDIX C — Distribution List .....	C-1

## CONTENTS

SECTION	PAGE
ABSTRACT .....	iii
ILLUSTRATIONS .....	vii
TABLES .....	xi
NOMENCLATURE .....	xiii
I INTRODUCTION .....	1
II SUMMARY .....	3
III TEST COMPONENT ANALYSIS AND DESIGN —	
TASK I .....	7
A. Design Requirements .....	7
B. Injectors .....	7
C. Uncooled Thrust Chambers and Exhaust Nozzles .....	17
D. Acoustic Absorbing Liner .....	19
E. Transpiration-Cooled Chamber .....	21
F. Regeneratively Cooled Thrust Chamber .....	24
IV TEST FACILITIES AND EQUIPMENT .....	29
A. Liquid Propellant Research Facility .....	29
B. Propellant Supply System .....	31
C. Control System .....	36
D. Instrumentation and Data Acquisition .....	37
V UNCOOLED SEA LEVEL PERFORMANCE TESTS —	
TASK II .....	41
A. Test Description .....	41
B. Test Performance .....	46
C. Ignition .....	52
D. Combustion Stability .....	53
E. Heat Transfer .....	54
VI UNCOOLED ALTITUDE TESTS — TASK III .....	61
A. Test Description .....	61
B. Performance .....	63
C. Altitude Ignition .....	72
D. Acoustic Liner Operation .....	73
E. Nozzle Heat Transfer .....	74

## ILLUSTRATIONS (continued)

FIGURE		PAGE
V-1	Engine Installation for Uncooled Sea Level Tests .....	41
V-2	Flox/Methane Characteristic Exhaust Velocity, 82.6% Fluorine in Flox .....	49
V-3	Flox/Propane Characteristic Exhaust Velocity, 76% Fluorine in Flox .....	50
V-4	Flox/Butene-1 Characteristic Exhaust Velocity, 70.4% Fluorine in Flox .....	51
V-5	Characteristic Exhaust Velocity Efficiency vs Momentum Ratio .....	52
V-6	Typical Frequency – Amplitude Relationship From Unstable Flox/Butene-1 Test (Test No. 78) .....	53
V-7	Comparison of Heat Transfer Coefficients for Flox/Propane With Injector S(1) .....	55
V-8	Comparison of Heat Transfer Coefficients for Flox/Methane With Injector S(1) .....	55
V-9	Comparison of Heat Transfer Coefficients for Flox/Butene-1 With Injector R(1-C) .....	55
V-10	Comparison of Heat Transfer Coefficients for Flox/Butene-1 With Injector S(2) .....	55
V-11	Ratio of Measured to Predicted Heat Transfer Rates to Copper Chamber .....	57
V-12	Effect of Fuel Hydrogen-to-Carbon Ratio on Chamber Heat Transfer .....	57
V-13	Circumferential Temperature Rise Profile, Flox/Methane, Test No. 11UA .....	58
V-14	Circumferential Temperature Rise Profile, Flox/Propane, Test No. 4 .....	58
V-15	Circumferential Temperature Rise Profile, Flox/Butene-1, Test No. 65 .....	59
VI-1	Uncooled Chamber and Nozzle Mounted in Test Facility .....	61
VI-2	Flox/Methane Characteristic Exhaust Velocity With Injector R(1-C): 82.6% F <sub>2</sub> in Flox .....	65
VI-3	Flox/Methane Vacuum Specific Impulse With Injector R(1-C): 82.6% F <sub>2</sub> in Flox .....	66

## ILLUSTRATIONS

FIGURE		PAGE
III-1	Performance Loss Due to Incomplete Mixing .....	9
III-2	Solid Face Quadruplet Injector .....	11
III-3	Rigimesh Face Triplet Injector .....	12
III-4	Rigimesh Face Triplet Injector Faceplate Installation .....	13
III-5	Solid Face Pentad Injector .....	14
III-6	Injector Water Flow Patterns .....	15
III-7	Typical Swirler Installation .....	15
III-8	Flox/Butene-1 Mixture Ratio Distribution for Pentad Injector: Overall Mixture Ratio = 3.85 .....	16
III-9	Uncooled Copper 15-Degree Nozzle Thrust Chamber .....	17
III-10	Uncooled Truncated Bell Nozzle Extension .....	18
III-11	Uncooled Chamber and Nozzle Assembly for Altitude Tests ....	19
III-12	Absorption Coefficient for Quarter-Length Acoustic Liner ....	20
III-13	Quarter-Length Acoustic Liner ....	20
III-14	Transpiration-Cooled Chamber Assembly .....	21
III-15	Transpiration-Cooled Chamber .....	22
III-16	Transpiration-Cooled Chamber Segment .....	22
III-17	Transpiration-Radiation Cooled Nozzle Assembly .....	24
III-18	RL10 Thrust Chamber Modified for Butene-1 Testing .....	25
III-19	RL10 Chamber Coolant Flow Path .....	26
III-20	Modification Included in Second Chamber Modification .....	27
IV-1	Liquid Propellant Research Facility .....	29
IV-2	Liquid Propellant Research Facility Schematic .....	30
IV-3	Flox-LPG Test Stand Flow Schematic .....	32
IV-4	Mercury Absorption Apparatus .....	34
IV-5	Schematic Diagram of Mercury Absorption Apparatus .....	34
IV-6	Gas Chromatograph System .....	35
IV-7	Schematic Diagram of Multicolumn Gas Chromatograph System for Analysis of Fluorine-Oxygen Mixtures .....	35
IV-8	LPRF Control Room .....	36
IV-9	LPRF Data Recording Equipment .....	38

## ILLUSTRATIONS (continued)

FIGURE		PAGE
VI-4	Flox/Methane Vacuum Thrust Coefficient With Injector R(1-C): 82.6% $F_2$ in Flox .....	67
VI-5	Flox/Butene-1 Characteristic Exhaust Velocity With Injector S(2-A): 70.4% $F_2$ in Flox .....	68
VI-6	Flox/Butene-1 Vacuum Specific Impulse With Injector S(2-A): 70.4% $F_2$ in Flox .....	69
VI-7	Flox/Butene-1 Vacuum Thrust Coefficient With Injector S(2-A): 70.4% $F_2$ in Flox .....	70
VI-8	Chamber Pressure Stability With Flox/Butene-1: r 4.1 .....	73
VI-9	Chamber Pressure Stability With Flox/Butene-1; r 3.65 ....	74
VI-10	Comparison of Flox/Methane Heat Transfer Coefficients: Test No. 6UA .....	74
VI-11	Comparison of Flox/Methane Heat Transfer Coefficients: Test No. 9UA .....	75
VI-12	Comparison of Flox/Methane Heat Transfer Coefficients: Test No. 10UA .....	75
VI-13	Comparison of Flox/Methane Heat Transfer Coefficients: Test No. 11UA .....	76
VI-14	Circumferential Throat Temperature Rise Profile: Methane Test No. 6UA (Superimposed on Copper Chamber Photograph Taken After the Test) .....	77
VI-15	Circumferential Throat Temperature Rise Profile: Methane Test No. 11UA (Superimposed on Copper Chamber Photograph Taken After the Test) .....	77
VI-16	Nozzle Deposits After Test No. 6UA (Flox/Methane) .....	78
VI-17	Comparison of Flox/Butene-1 Heat Transfer Coefficients: Test No. 12UA .....	78
VI-18	Comparison of Flox/Butene-1 Heat Transfer Coefficients: Test No. 14UA .....	79
VI-19	Chamber Deposits After Test No. 16UA (Flox/Butene-1) .....	79
VI-20	Nozzle Deposits After Test No. 16UA (Flox/Butene-1) .....	80
VII-1	Transpiration-Cooled Chamber Mounted in Test Facility .....	81
VII-2	Correlation of Uncooled Chamber Heat Flux Pattern With Transpiration-Cooled Chamber Damage .....	83



## ILLUSTRATIONS (continued)

FIGURE	PAGE
VII-3 Flox/Methane Transpiration-Cooled Test Results — Vacuum Specific Impulse .....	86
VII-4 Flox/Methane Transpiration-Cooled Test Results — Characteristic Exhaust Velocity Efficiency .....	87
VII-5 Flox/Methane Transpiration-Cooled Test Efficiencies .....	87
VII-6 Comparison of Measured and No-Mixing Predicted Vacuum Specific Impulse for Transpiration-Cooled Tests .....	89
VII-7 Ratio of Transpiration-Cooled Chamber Film Coefficients to Film Coefficients From Uncooled Chamber .....	91
VII-8 Ratio of Transpiration-Cooled Chamber Film Coefficients to Bartz Short Form Predicted Film Coefficients .....	91
VII-9 Comparison of Flox/Methane Average Nozzle Heat Transfer Film Coefficients .....	92
VIII-1 Damage to Tubular Chamber After Test 1R .....	93
VIII-2 Time History Showing Coolant Pressure Surge During Test No. 2R .....	96
VIII-3 Comparison of Methane and Butene-1 Temperature Profiles with Injector R(1C) .....	97
IX-1 Theoretical Vacuum Specific Impulse of Flox/Light Hydrocarbon Propellants .....	102
IX-2 Effect of Area Ratio on Vacuum Specific Impulse .....	102
IX-3 Measured and Predicted Full Thrust Characteristic .....	104
IX-4 Kinetic Expansion Efficiency .....	105
IX-5 Variation of Kinetic Expansion Efficiency for Throttling Operation .....	106
IX-6 Flox/Butene-1 Performance .....	108
IX-7 Predicted Flox/Butene-1 Performance With Throttling .....	109
IX-8 Flox/Methane Performance With Transpiration-Cooling .....	111
IX-9 Predicted Flox/Methane Performance With Throttling .....	112
IX-10 Flox/Methane Transpiration-Cooling Flow Requirements .....	112
IX-11 Predicted Flox/Propane Performance .....	113

## TABLES

TABLE	PAGE
III-1 Comparison of Butene-1 Regenerative Cooling Configurations .....	26
IV-1 Estimated Performance Data Accuracy .....	40
V-1 Summary of Uncooled Sea Level Tests .....	42
V-2 Summary of Injector Modifications .....	43
V-3 Calculated Performance Data — Uncooled Sea Level Tests .....	47
V-4 Injector Performance Comparison — Uncooled Sea Level Tests .....	48
V-5 Comparison of Measured and Predicted Chamber Heat Transfer Rates .....	56
VI-1 Summary of Uncooled Altitude Tests .....	62
VI-2 Calculated Performance Data — Uncooled Altitude Tests .....	64
VI-3 Reduction in Vacuum Specific Impulse Due to Reaction Rate Limited Expansion .....	71
VI-4 Elementary Reactions and Reaction Rate Constants Employed in Flox/Methane Reaction Mechanism .....	72
VI-5 Average Ignition Delays for Sea Level and Altitude Tests .....	72
VI-6 Measured and Predicted Heat Transfer Rates for Altitude Tests .....	80
VII-1 Test Conditions —Transpiration-Cooled Tests .....	82
VII-2 Calculated Performance Data — Transpiration-Cooled Tests .....	85
VII-3 Coolant Flow and Rigimesh Temperature Data .....	90
VIII-1 Measured Performance Data — Regenerative-Cooling Tests .....	99
VIII-2 Calculated Performance Data — Regenerative-Cooling Tests .....	99
VIII-3 Experimental and Theoretical Heat Transfer Rates for Regenerative Tests .....	100

## NOMENCLATURE

SYMBOL	DESCRIPTION	UNITS
$AC_D$	Effective injector flow area	$\text{in}^2$
$C$	Constant	
$C_F$	Thrust Coefficient	
$C'_s$	Theoretical stream thrust coefficient, (predicted aerodynamic efficiency accounting for friction and divergence losses)	
$c^*$	Characteristic velocity	ft/sec
$\eta_c^*$	Characteristic velocity efficiency	
$D$	Diameter	in.
$D_{30}$	Volume — mean-drop diameter	in.
$\epsilon_e$	Nozzle exit to throat area ratio, $A_e/A_t$	
$F_{sl}$	Thrust at sea level	$\text{lb}_f$
$F_{vac}$	Thrust at $P_a = 0$	$\text{lb}_f$
$I_{sl}$	Specific impulse at sea level	$\frac{\text{lb}_f - \text{sec}}{\text{lb}_m}$
$I_{vac}$	Specific impulse at $P_a = 0$	$\frac{\text{lb}_f - \text{sec}}{\text{lb}_m}$
$L^*$	Characteristic chamber length	in.
$P_c$	Chamber pressure	psia
$P_d$	Diffuser pressure	psia
$\Delta P$	Injector pressure drop	psid
$r$	Mixture ratio (oxidizer-to-fuel) by weight	
$T$	Injector inlet temperature	$^{\circ}\text{R}$
$V$	Velocity through injector	ft/sec
$w$	Flow rate	$\text{lb}/\text{sec}$
Subscripts		
$c$	Coolant	
$ch$	Chamber	
$cor$	Data corrected for momentum and heat losses	
$f$	Fuel	
$g$	Gas	
$j$	Jet	
$n$	Nozzle	

# **NOMENCLATURE (continued)**

<b>SYMBOL</b>	<b>DESCRIPTION</b>	<b>UNITS</b>
Subscripts (continued)		
$_{\text{o}}$	Oxidizer	
$_{\text{p}}$	Propellant	
$_{\text{vac}}$	Indicates parameter at $P_{\text{a}} = 0$	
Superscripts		
	Theoretical value	

## SECTION I

### INTRODUCTION

Continuing interest in the flox/light hydrocarbon propellant combinations can be attributed to their ability to satisfy a variety of engine and vehicle requirements for upper-stage rocket applications. The flox/light hydrocarbon combinations provide (1) high delivered performance, (2) high density, (3) space storability, (4) availability, (5) hypergolic ignition, and (6) the capability of cooling the thrust chamber with the fuel.

An initial program conducted under Contract NAS3-4195 (Reference 1) had two major objectives relative to the use of flox/light hydrocarbon propellants. The first objective was to select the most promising fuels for low chamber pressure (nominal 100-psia) upper-stage rocket engines. The second was to conduct an experimental evaluation of the selected fuels. Because the prime advantage of light hydrocarbons over other high-energy space-storable fuels is their cooling characteristics, the experimental work was primarily an evaluation of chamber cooling in regenerative and transpiration cooled thrust chambers. To facilitate the cooling study, modified RL10 concentric element injectors designed for gaseous fuel and liquid oxidizer were used rather than attempting to design and test a new injector.

Concurrently with the contracted work, Pratt & Whitney Aircraft also conducted several separate programs covering (1) determination of the physical properties of hydrocarbon blends, (2) experimental investigation of hypergolic ignition characteristics, and (3) heated-tube tests to determine the coolant film coefficients in the nucleate, film, and bulk boiling regions. These programs were also reported in Reference 1.

Some of the more significant conclusions drawn from these programs can be summarized as follows:

1. Methane provides the highest theoretical specific impulse with flox of all the light hydrocarbon fuels, and is superior to all other hydrocarbons as a transpiration coolant.
2. Propane provides the best combination of high theoretical performance with flox, good transpiration cooling characteristics, and good regenerative cooling characteristics for use in a composite cooling scheme; i.e., regenerative cooling of the exhaust nozzle and transpiration cooling of the thrust chamber and throat. Propane also has a much wider liquid range than methane, making its storage in space easier.

3. Measured thrust chamber heat fluxes are well below conventional analytical predictions for the flox/hydrocarbon combinations because of carbon deposition on the walls and/or free carbon in the boundary layer. This reduction in heat flux increases markedly with decreasing hydrogen-to-carbon atomic ratio.
4. The reduced heat fluxes encountered make full regenerative cooling with butene-1 or a eutectic blend of pentane and isopentane feasible over a wider range of thrust and chamber pressure than predicted theoretically.
5. All the flox/light hydrocarbon combinations are hypergolic under conditions of an ambient sea level start.

The work detailed in this report was a logical extension of the previous investigation; the primary objective was to develop injectors suitable for liquid oxidizer/liquid fuel injection and to determine the altitude performance of cooled thrust chambers using flox with methane, propane and either butene-1 or the pentane blend. The choice between the latter two fuels was to be determined by their regenerative cooling capabilities based on the experimental data previously obtained. The program was divided into five tasks. Task I – Analysis and Design, included prediction of engine-delivered performance, determination of the cooling capabilities of the three selected combinations, and design of hardware for the Task II, III, IV, and V testing. Task II – Uncooled Sea Level Performance Tests, consisted of short-duration firings with flox/methane, flox/propane, and flox/butene-1 for determination of injection requirements for high performance. Task III – Uncooled Altitude Tests, consisted of short-duration firings with flox/methane and flox/butene-1 to obtain altitude performance and nozzle heat transfer data. Task IV – Transpiration Cooled Altitude Tests, was an experimental evaluation of a methane transpiration cooled thrust chamber under simulated altitude conditions. Task V – Regeneratively Cooled Altitude Tests, was an experimental evaluation of butene-1 in a convectively cooled tubular thrust chamber.

## SECTION II

### SUMMARY

Sea level and simulated altitude tests were conducted to determine the chamber cooling capability and vacuum performance of fluorine-oxygen mixtures (flox) with light hydrocarbon fuels. The investigation was an extension of analyses and sea level testing that were completed under Contract NAS3-4195 (Reference 1) using gaseous hydrocarbon fuels and liquid flox. From the success of that program it was evident that further investigation of the flox/light hydrocarbon combinations was warranted. As a logical continuation of the previous work, liquid-liquid injectors were designed and tested in uncooled and cooled thrust chambers at sea level and simulated altitude conditions. The fuels considered were the four fuels tested under Contract NAS3-4195: methane, propane, butene-1, and a eutectic blend of pentane and isopentane. Of the four, methane, propane, and butene-1 were selected for test under this program. Test conditions, nominal 5000-lb vacuum thrust and 100-psia chamber pressure, were selected to provide data applicable to pressure-fed upper-stage engines. The fluorine concentration in the oxidizer was optimized for maximum theoretical performance with each fuel tested.

Because of its high theoretical specific impulse and superior transpiration-cooling properties, methane was tested in a transpiration-cooled chamber with a radiation-cooled skirt. Based on its high specific impulse and regenerative-cooling capabilities, but somewhat limited liquid heat capacity, propane was selected for use in a composite chamber using a regeneratively-cooled nozzle and transpiration-cooled chamber. Complete regenerative cooling with propane would have resulted in bulk-boiling and two-phase injection. Butene-1 was shown to have a wider range of applicability than the pentane blend and was selected for testing in a completely regeneratively cooled thrust chamber. Detailed analytical studies, which took into account performance losses associated with transpiration-cooling were conducted in the initial phase of this program. These studies indicated that at all thrust levels below 20,000 pounds the performance of methane and butene-1 was superior to propane; hence, propane testing was suspended after early uncooled sea level tests. The analysis and design of the test hardware are discussed in Section III.

Eighty-four uncooled sea level tests were conducted, with 13 modifications of four basic injector designs, to determine injector performance and chamber heat transfer rates. These tests are discussed in Section V. It was found that relatively high performance could be obtained using unlike impinging multielement injectors only at mixture ratios below optimum. It was also determined that because the flox/light hydrocarbon propellants have theoretical optimum mixture ratios that correspond to the stoichio-

metric mixture ratio, complete mixing was a critical requirement for obtaining high efficiencies. With the unlike-impinging injectors, high momentum ratios were a prerequisite in obtaining good mixing and high performance. At equal momentum ratios no appreciable efficiency difference was shown for the three fuels or for the various injector element configurations tested. Severe high frequency combustion instability encountered with butene-1 was eliminated by the use of a quarter-length acoustic liner.

Sixteen uncooled simulated altitude tests, which are discussed in Section VI, provided vacuum specific impulse and nozzle heat flux data with a nozzle having an expansion ratio of 40. The peak in the measured vacuum specific impulse curve for flox/methane was 368 seconds (91% of the theoretical vacuum specific impulse) at a mixture ratio of 4.0. Flox/butene-1 had a maximum delivered vacuum specific impulse of 362 seconds (90% of the theoretical vacuum specific impulse) at a mixture ratio of approximately 3.85. Nozzle expansion losses due to kinetically limited recombination were estimated to be 2 to 4%, or only 20 to 40% of the theoretically predicted amounts. In all sea level and simulated altitude tests the flox/light hydrocarbon propellants were reliably hypergolic and produced smooth repeatable chamber pressure buildups.

Heat transfer rates were generally below the analytically predicted values and showed the same trend measured in previous work, that of decreasing heat transfer with decreasing fuel hydrogen-to-carbon ratio. For flox/methane the total heat transfer rates were approximately 83% of analytical predictions as compared to 31% for flox/butene-1. As would be expected, chamber heat transfer was significantly affected by the injector pattern, and for one injector using flox/butene-1 the heat flux was above the theoretically predicted value. It was also found that injector design affected heat transfer rates throughout the nozzle. The heat transfer data are discussed in Sections V, VI, and VIII.

The feasibility of transpiration cooling, established under Contract NAS3-4195, was further proved in ten flox/methane tests with durations up to 30 seconds. Coolant flow rates were varied from a conservative 8% of the total propellant flow down to the predicted minimum of 4%. Maximum vacuum specific impulse was 374 seconds (96% of the theoretical vacuum specific impulse) at an engine mixture ratio of approximately 3.2. This reduction in the optimum mixture ratio below that measured in the uncooled tests corresponded to that predicted from no-mixing calculations. Coolant carryover significantly reduced the uncooled nozzle heat transfer rates for approximately 20 inches downstream of the last transpiration-cooled section. The transpiration-cooling data are discussed in Section VII.



Two convectively cooled tests were conducted using flox/butene-1 in modified RL10 thrust chambers. The butene-1 was supplied separately to the injector and the tubular coolant jacket. In both tests moderate thrust chamber damage was incurred. Damage consisted of several small holes in the tubes near the injector face and a few split tubes in the convergent portion of the chamber. The damage occurred primarily during the start transient. Both tests ran the planned 10.0 seconds, and no damage occurred to the nozzle throat or the divergent portion of the nozzle. The primary problem areas discovered from the testing were as follows: (1) normal circumferential heat flux variations are significantly increased with flox/butene-1 and other flox/hydrocarbon combinations because of the interrelationship between circumferential heat flux variations and the thickness of carbon deposits on the chamber wall, and (2) a coolant pressure surge, caused by sudden expansion of the coolant, occurs during the thrust chamber start transient. It is believed that both problems could be adequately minimized with moderate development, and that regenerative cooling with butene-1 at nominal 100 psia chamber pressure and thrust levels of 5000-lb or higher is entirely feasible.

In Section IX, analytically predicted engine performance values based on 100-psia chamber pressure and an expansion area ratio of 40 are shown for each of the three fuels with flox. A range of values is presented covering engines with full thrust ratings from 3,000 to 20,000 pounds with 10-to-1 throttling capability. At 5000-lb full thrust the following deliverable performance is predicted: 386 seconds for a transpiration-radiation cooled flox/methane engine, 373 seconds for a regeneratively cooled flox/butene-1 engine, and 368 seconds for a transpiration-regeneratively cooled flox/propane engine. These predictions are based on the conservative assumption that a 1.5% performance increase could be realized with further injector development at low mixture ratios, and an increase of 2.5% could be obtained at the theoretical optimum mixture ratios where increased mixing is a critical factor.

The measured vacuum specific impulse with both flox/methane and flox/butene-1 was higher than has been demonstrated with any other space-storable propellants in fuel-cooled thrust chambers. Substantial improvements in flox/light hydrocarbon performance can be obtained with moderate injector development aimed at improving combustion product mixing. The superior cooling ability of these fuels coupled with their demonstrated high performance indicate that additional flox/light hydrocarbon research and development are warranted.

## SECTION III

### TEST COMPONENT ANALYSIS AND DESIGN — TASK I

#### A. DESIGN REQUIREMENTS

The nominal design conditions for all test hardware were 100-psia chamber pressure and 5000-lb vacuum thrust based on a nozzle expansion ratio of 40. Injector designs were based on an oxidizer inlet temperature of approximately 160°R and a fuel inlet temperature of 180 to 500°R. Uncooled copper thrust chambers were designed to provide test durations of 4.0 to 6.0 seconds for evaluation of sea level performance and heat transfer. Uncooled stainless steel nozzle extensions were designed for attachment to existing copper thrust chambers to provide an area ratio of 40 bell nozzle for simulated altitude performance tests. Design modifications were made to transpiration-cooled thrust chambers fabricated under Contract NAS3-4195 and RL10 tubular regeneratively cooled thrust chambers for use in cooled firings at simulated altitude conditions.

#### B. INJECTORS

##### 1. DESIGN CONSIDERATIONS

The processes for combustion of liquid rocket propellants are generally categorized as atomization, vaporization, mixing, and reaction. From the standpoint of the time required for efficient combustion, atomization and vaporization are directly related and may be considered together as the vaporization rate. The vaporization rate is a function of the degree of atomization or propellant droplet size, the combustion chamber geometry, and the physical and thermodynamic properties of the propellants and their combustion products. Mixing is promoted primarily by turbulent mixing of the propellants and their combustion products near the injector face, and secondarily by turbulence and diffusion of the hot gases as they flow through the combustion chamber. Chemical reaction rates are very high for most common rocket propellant combinations, hence their effects are generally neglected.

The effect of atomization on vaporization rate and ultimately on combustion efficiency has been studied analytically and experimentally (References 2 and 3). It has been shown that in many cases the predominant rate controlling factor is the propellant droplet size. Droplet diameter has been correlated empirically for like-on-like impinging jets to the ratio of Weber number to Reynolds number (References 4, 5, and 6), and, more conveniently, as a function of jet diameter, jet velocity, and gas velocity as shown (Reference 7):

$$D_{30} = C_1 \sqrt{D_j / V_j} + C_2 D_j \Delta V \quad \left( \text{where: } \Delta V = V_g - V_j \right)$$

Similar correlations have not been developed for unlike impinging jets; however, such correlations would be expected to relate droplet size primarily with the same parameters as the like impinging jets.

In the operating regime where combustion is limited by propellant vaporization it would be expected that, although performance efficiency would drop off as orifice diameter is increased, there would exist a certain minimum orifice diameter below which efficiency may no longer be improved by further reduction in orifice size. Experience with various propellant combinations, including several using fluorine-base oxidizers (References 8 and 9), has indicated this to be so. For oxidizer injection velocities on the order of 75 to 100 ft/sec, performance was shown to drop off rapidly as the orifice diameter was increased above 0.090 inch, whereas reductions in the diameter below 0.030 inch showed little performance improvement.

For a given propellant flow rate and chamber geometry, a reduction in orifice diameter can only be accomplished by increasing either the propellant velocity or the number of orifices. To determine the effect of orifice diameter at constant velocity and flow rate; chamber pressure, chamber geometry, or injector element density must be varied. Such changes in pressure, geometry, or element density will affect turbulent mixing near the injector as well as propellant vaporization. Thus, it is difficult to separate the effects of atomization and the effects of mixing on gradual increases in performance with decreasing orifice diameter. While it is not now possible to separate the effects of atomization and mixing on the slope of a curve of orifice diameter versus efficiency, a sharp break in the curve, as found in Reference 9, is undoubtedly caused by a sudden change in the extent of vaporization in the chamber.

Vaporization occurs continually down the length of the combustion chamber to the point of complete vaporization; therefore, low efficiency caused by incomplete vaporization can be at least partially offset by increased chamber length. On the other hand, radial mixing of gases downstream of the primary combustion zone near the injector face occurs at a relatively slow rate. Thus, for high efficiency within a permissible chamber volume it is necessary that the propellants be well mixed near the injector face either by liquid phase mixing or by turbulent gas phase mixing generated by the combustion process. As the propellants are injected, mixture ratio variations across the face of the injector may occur either from variations of flow through the various elements or from incomplete mixing of the propellants flowing through an individual element. Element-to-element mixture ratio variations can be virtually eliminated by careful design and manufacture of orifices and propellant manifolds. The only significant mixture ratio variations for a well-constructed injector are those intentional variations that are designed into the injector for control of chamber wall heat flux.

Minimization of mixture ratio variations within individual elements is more difficult to accomplish. The most widely accepted mixing correlations for impinging stream injectors were developed by the Jet Propulsion Laboratory (References 10 and 11). The JPL equations are based on correlation of nonreactive flow-bench test data using two immiscible fluids. Application of the JPL correlations to flox/light hydrocarbon propellants is of questionable validity because: (1) mixture ratios for maximum theoretical specific impulse with flox/light hydrocarbon propellants are considerably higher than the experimental flow data, and (2) for hypergolic propellants with short ignition delay times such as the flox/light hydrocarbon combinations, the mixing process is disturbed by gas evolution at the impingement point (Reference 11).

A high degree of mixing is extremely critical with the flox/light hydrocarbon combinations because the oxidizer-to-fuel ratio for maximum theoretical specific impulse occurs at a high mixture ratio and at the stoichiometric mixture ratio rather than at some value below the stoichiometric ratio as with most other propellant combinations. As a result, a given amount of incomplete mixing results in a substantially higher performance loss than a similar degree of incomplete mixing with other propellants.

The criticality of propellant mixing is compared in figure III-1 for flox/ $\text{CH}_4$  and  $\text{N}_2\text{O}_4/50\% \text{N}_2\text{H}_4 + 50\% \text{UDMH}$ . For comparison, it is assumed that the combustion products of the propellant combinations of interest may be divided into two stream tubes of equal mass flow rate. The fuel concentration in one stream tube is assumed to be less by some arbitrary amount than the fuel concentration based on the average overall mixture ratio. The percentage of fuel in the second stream tube required to provide the average mixture ratio is then determined. The two stream tubes are

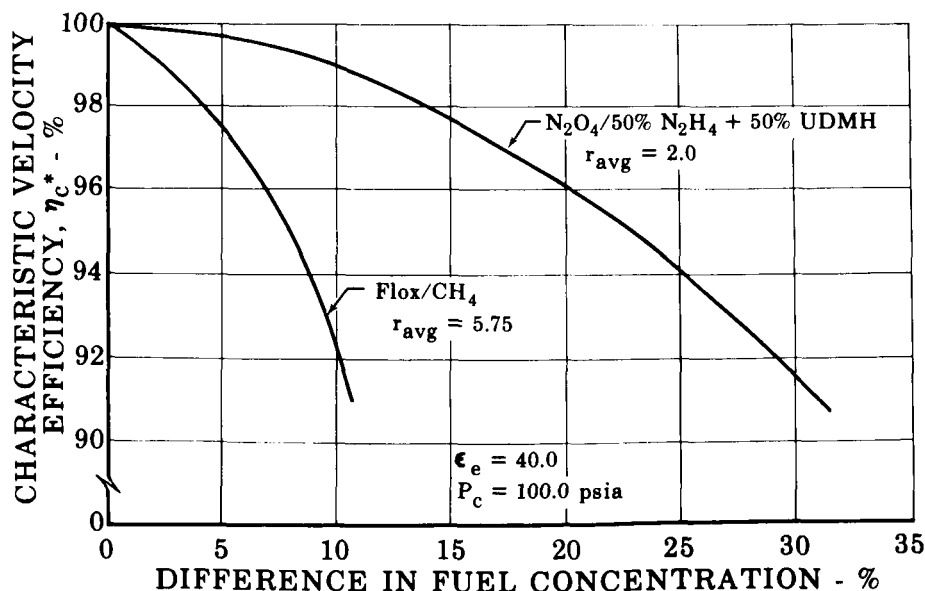


Figure III-1. Performance Loss Due to Incomplete Mixing

FD 19737

expanded isentropically and the averaged characteristic velocity compared to the value based on complete mixing. A comparison of the criticality of mixing of two propellant combinations may then be obtained by comparing the performance degradation for an equal differential fuel concentration between the two stream tubes. As shown in figure III-1, a differential of 10% in fuel concentration between the high and low mixture ratio stream tubes results in less than a 1.0%  $c^*$  loss for the  $N_2O_4/50\% N_2H_4 + 50\%$  UDMH combination, while the same difference in fuel concentration results in more than a 7.5%  $c^*$  loss with flox/methane. The model used does not, of course, describe the mixture ratio distribution that occurs with incomplete mixing. It does, however, provide comparison of the relative criticality of mixing for the two propellant combinations.

One restraint imposed on the injector design for this particular program was that the injector diameter be 10 inches to match the RL10 tubular thrust chamber and the transpiration-cooled thrust chamber fabricated under Contract NAS3-4195. The 10-inch diameter injector in conjunction with the existing chambers produced a contraction ratio of 2.8. Estimation of face heating of the 10-inch diameter injector operating at 100-psia chamber pressure indicated that adequate regenerative cooling of the injector was possible with either propane or butene-1. Conversely, the higher heat fluxes predicted for flox/methane combined with the narrow liquid range of methane indicated that supplementary face cooling was required. This was accomplished by using transpiration cooling for the injector face.

## 2. INJECTOR DESCRIPTION

Four basic element patterns were designed and tested. Unlike impinging quadruplet and triplet configurations were selected for the initial testing based on their inherently good mixing characteristics; later, like-on-like doublet and unlike impinging pentad configurations were chosen. Two modifications of the basic patterns were also designed and tested: (1) a combination triplet-quadruplet injector having approximately 50% of each type element, and (2) a quadruplet injector with swirlers in the oxidizer orifices. In addition to the six different configurations tested, several different orifice sizes were used with the triplet, quadruplet, and pentad injectors to provide variation in the fuel-to-oxidizer injection momentum ratio. Thirteen different modifications were tested using four separate injector bodies. A table summarizing the injector flow characteristics is presented in Section V in conjunction with the experimental sea level performance.

*a. Quadruplet*

The quadruplet injector (figure III-2) had 232 elements each consisting of two oxidizer orifices and two fuel orifices whose streams impinged at a common point. The first configuration of the quadruplet injector, S(1), had oxidizer and fuel orifice diameters of 0.028 and 0.0145 inch, respectively, to provide a high degree of atomization. Later modifications, designated S(1-A) and S(1-C), had increased oxidizer orifice diameters of 0.031 and 0.038 inch to provide increased fuel-to-oxidizer momentum ratios. Injector S(1-B) had swirlers in the oxidizer orifices in an attempt to improve propellant distribution as discussed in paragraph 3. These injectors also had 40 0.0135-inch diameter fuel orifices drilled in the circumference of the injector to provide a small amount of film cooling.

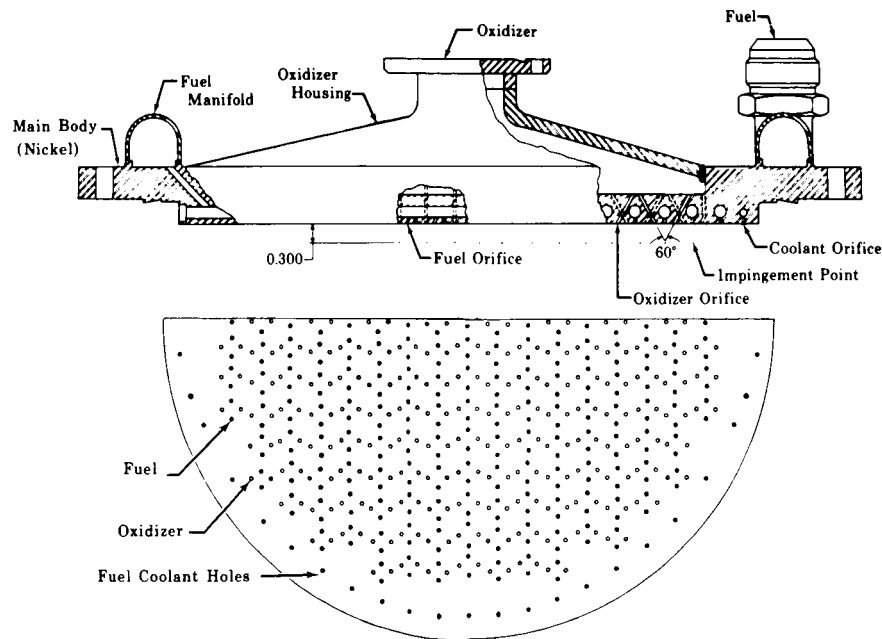


Figure III-2. Solid Face Quadruplet Injector

FD 19738

The injector was fabricated from nickel to provide a high metal kindling temperature with fluorine and good high temperature strength. Complete separation of fuel and oxidizer was assured by fabricating the body from a single nickel forging so that mechanical seals and welds were not required for separation of propellants. Blind passages were avoided in all areas exposed to liquid floc to assure adequate cleaning and passivation. Good distribution across the face of the injector was maintained by providing adequate interior manifolding. The fuel orifices were fed by 21 0.215-inch diameter holes across the face of the injector, and the oxidizer holes were fed from the large cavity in the back of the injector.

b. *Triplet*

The triplet injectors (figure III-3) consisted of 241 elements each having two oxidizer orifices and one fuel orifice. Injector R(1) had 0.028-inch diameter oxidizer orifices and 0.020-inch diameter fuel orifices. The injector face was transpiration cooled. The porous faceplate material was Rigimesh<sub>TM</sub>, a sintered wire material made by Aircraft Porous Media, Inc. Injector R(1) used 3-ply stainless steel Rigimesh rated at 120 scfm for a 2-psi pressure differential. A second injector R(2) was designed and fabricated using 30-scfm Rigimesh to reduce face coolant flow, thereby improving propellant distribution. The faceplate of injector R(1) was later replaced to provide an intermediate coolant flow with 60-scfm Rigimesh. This modification was designated R(1-C). Other modifications included: (1) increasing the oxidizer orifice diameters to 0.038 inch to increase the fuel-to-oxidizer momentum ratio: designation R(1-C), (2) making 50% of the elements into a quadruplet configuration: designations R(1-A) and R(1-B), and (3) replacing the Rigimesh face with a solid nickel face: designation R(2-B).

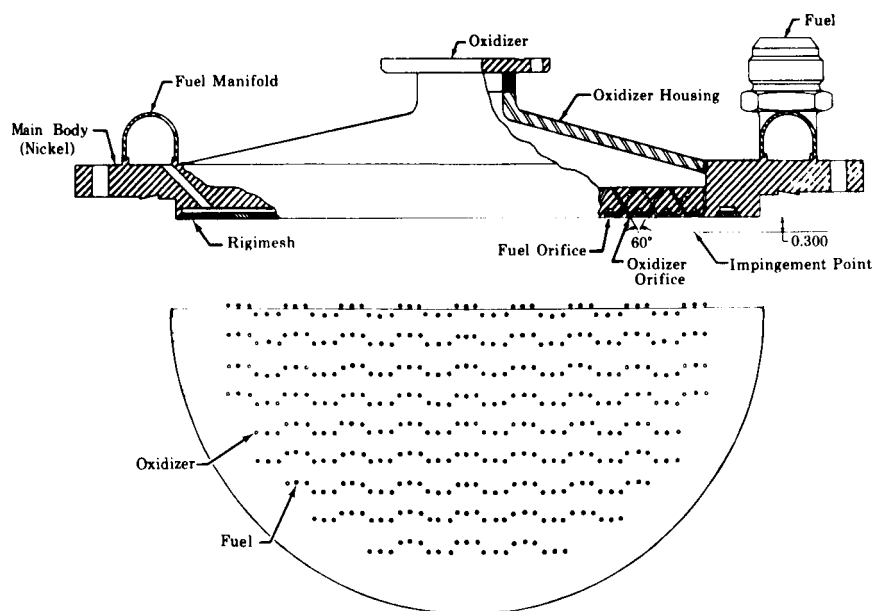


Figure III-3. Rigimesh Face Triplet Injector

FD 19739

The injector body was constructed of solid nickel. The face of the injector was machined leaving oxidizer spuds through which the oxidizer orifices were drilled. The Rigimesh face fitted around the spuds covering milled fuel passages that distributed the fuel. Fuel was injected through orifices drilled through the Rigimesh and through the porous Rigimesh face itself. Faceplates were attached with screws in the first designs. In later modifications the faceplate was welded to the injector body, as shown in figure III-4, to eliminate fuel leakage around the oxidizer spuds. Oxidizer manifolding was identical to the quadruplet design.

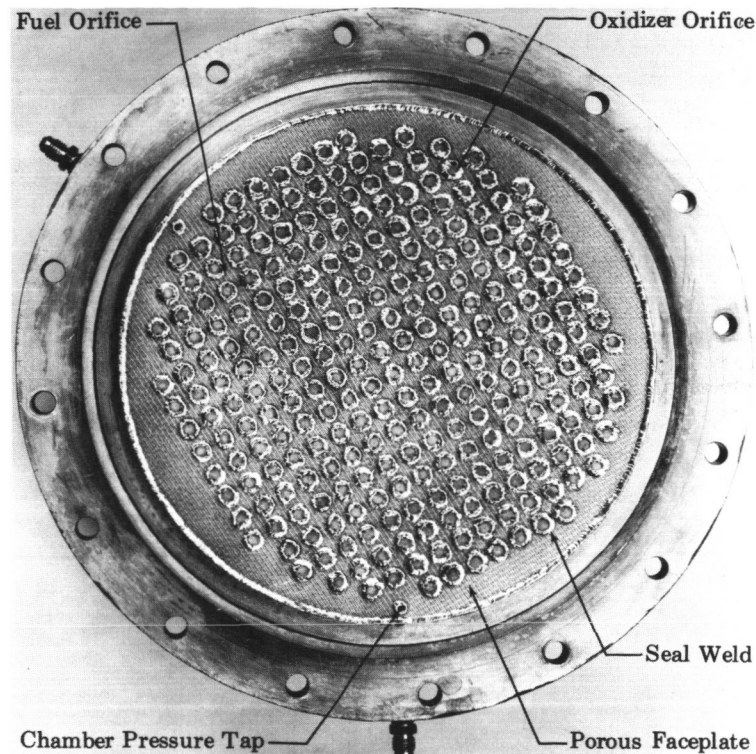


Figure III-4. Rigimesh Face Triplet Injector Faceplate Installation

FD 19740

*c. Doublet*

A triplet injector was converted to a like-on-like doublet configuration by replacing the Rigimesh faceplate. The resulting injector designated R(2-A) had 241 pairs of 0.028-inch diameter oxidizer orifices and 124 pairs of 0.021-inch diameter fuel orifices.

*d. Pentad*

A pentad injector, designated S(2), is shown in figure III-5. The design had 205 elements each consisting of four 0.028-inch oxidizer orifices and one 0.022-inch fuel orifice. A subsequent modification, S(2-A), had 0.025-inch diameter fuel orifices and 0.033-inch diameter oxidizer orifices. Construction and manifolding were similar to the quadruplet injector.



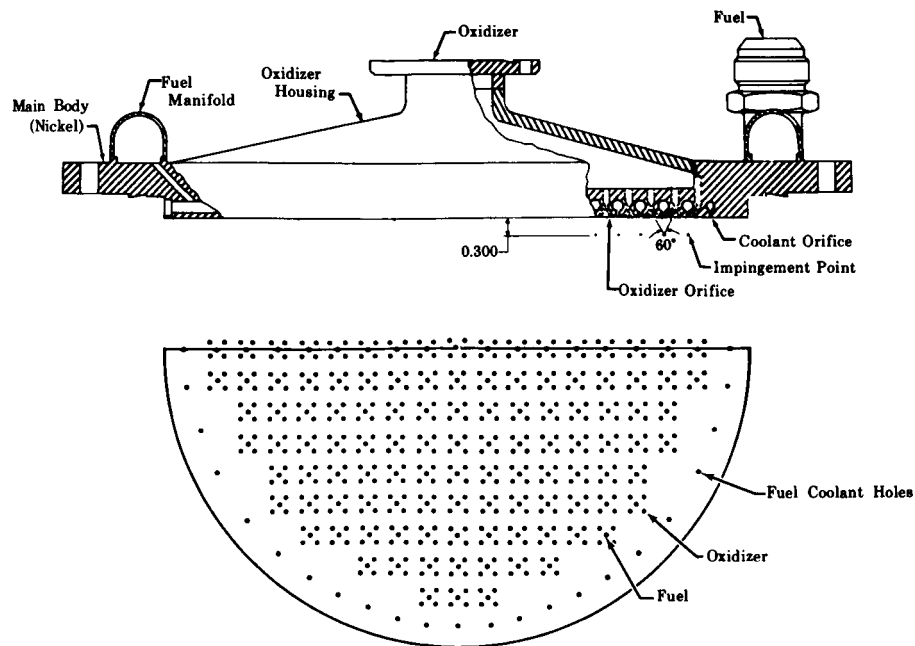


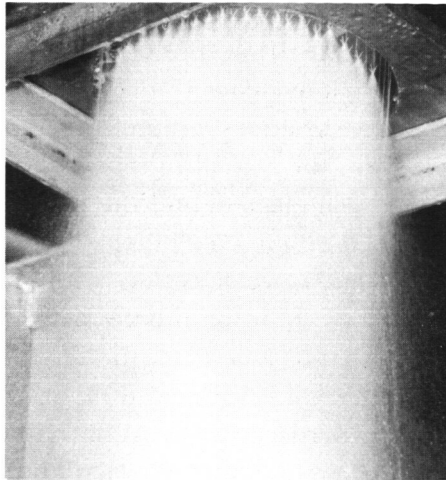
Figure III-5. Solid Face Pentad Injector

FD 19741

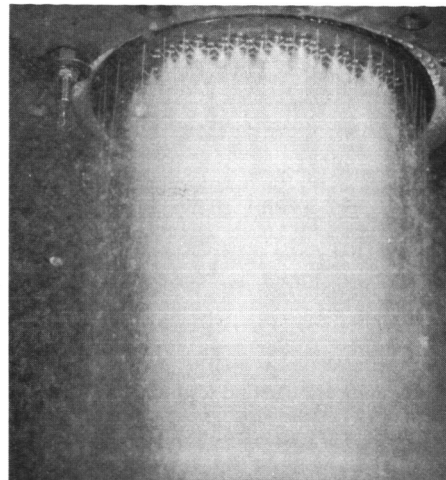
### 3. WATER FLOW BENCH TESTS

Flow areas for the various injector modifications were determined by water flow calibrations. Figure III-6 shows the flow pattern obtained with several of the element configurations tested. Note that good atomization is obtained with all injectors. The porous face injectors show some droplet flow through the face; however, this does not occur during a hot firing, particularly with methane, because the fuel vaporizes within the faceplate restricting the amount of flow.

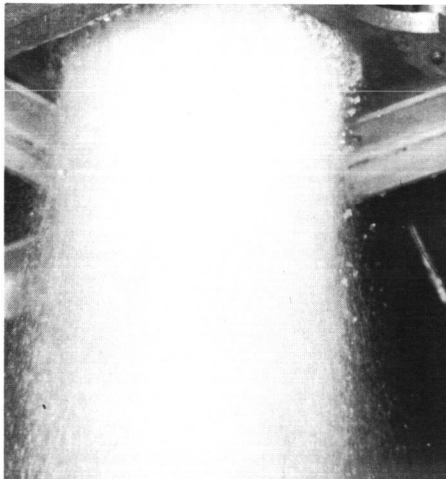
Water flow examination of sample like-on-like impinging jets showed that jet breakup produced by the swirlers allowed the streams to penetrate each other and produce a spray fan in a plane passing through the center-lines of the two orifices. This is in contrast to the perpendicular fan produced by two impinging streams without swirlers. A water flow of a sample quadruplet element with swirlers in the oxidizer orifices was then made. As expected, the water flow indicated that an even mixture ratio was obtained across the coincident fans. On this basis the quadruplet injector was modified to include swirlers in the oxidizer orifices as previously discussed in paragraph 2a. The swirler and orifice dimensions are shown in figure III-7.



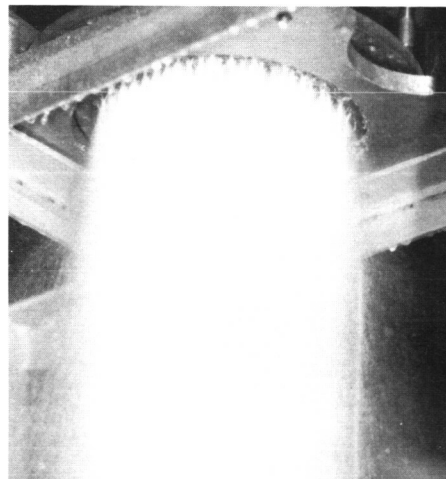
Solid Face Quadruplet - S(1)



Solid Face Pentad - S(2-A)



Porous Face Triplet - R(1-C)  
60 scfm Rigimesh



Porous Face Triplet-Quadruplet  
R(1-A) - 30 scfm Rigimesh

Figure III-6. Injector Water Flow Patterns

FD 19742

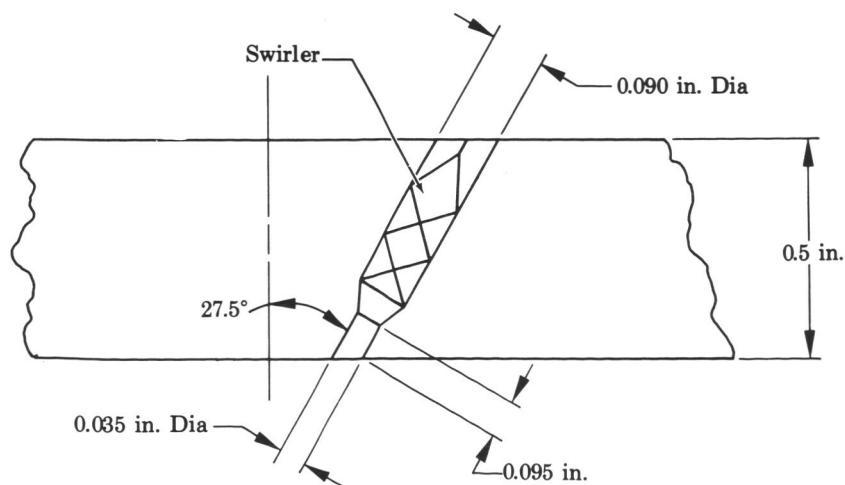


Figure III-7. Typical Swirler Installation

FD 19743

Because the effect of incomplete mixing was known to be severe with the flox/light hydrocarbon combinations, a water flow investigation was conducted to determine the extent of element-to-element mixture ratio variations and the potential effect of these variations on performance. Figure III-8 shows the measured distribution for the pentad injector, S(2-A). Both the water-calibrated mixture ratios for each element and the percentage flow through each element are shown based on flox/butene-1 at an average mixture ratio of 3.85. The characteristic velocity loss with this distribution would be less than 4% even if there were no mixing between elements. The major source of this calculated loss came from the mixture ratio shift produced by the 10.5% of the fuel that was injected through the fuel coolant orifices at the circumference of the injector face. With all the other injectors tested, the fuel flow through the circumferential coolant holes was less than 5%, hence the calculated loss from no element-to-element mixing would be only about half of the calculated loss for injector S(2-A), or less than 2%.

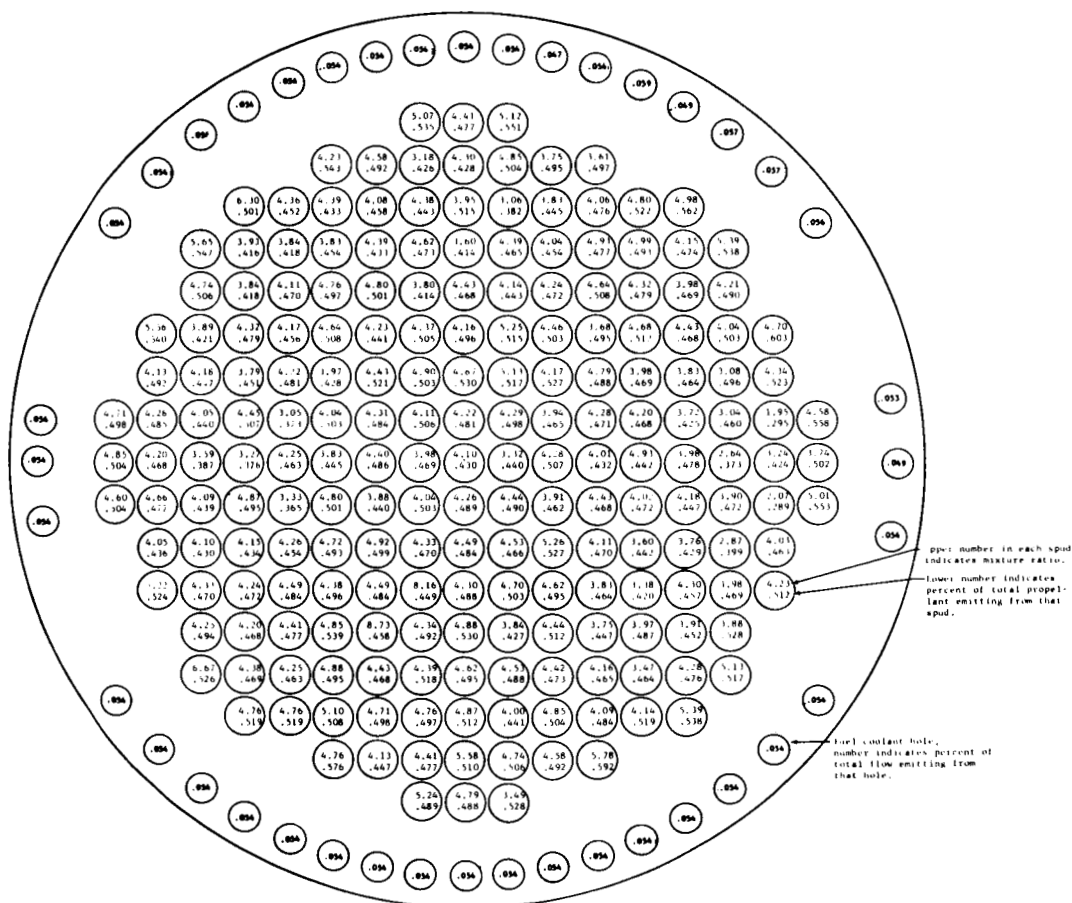


Figure III-8. Flox/Butene-1 Mixture Ratio Distribution for Pentad Injector: Overall Mixture Ratio=3.85

FD 18983A

### C. UNCOOLED THRUST CHAMBERS AND EXHAUST NOZZLES

The uncooled chambers were fabricated from high purity oxygen-free copper. Copper was selected because of its high thermal conductivity, high specific heat, and satisfactory yield strength at elevated temperatures. The 15-degree thrust chamber used for sea level tests was machined from a single copper billet. Dimensions of this chamber, shown in figure III-9, are identical to those in chambers tested under Contract NAS3-4195 (Reference 1) except for the nozzle divergence angle and area ratio. The exhaust nozzle of this chamber had a 15-degree half-angle and an area ratio of 1.98, which permitted operation at sea level conditions without flow separation for chamber pressures well below the 100-psia design point. The chamber length was 12.00 inches from the injector to the throat and the contraction ratio was 2.8 to provide a characteristic length,  $L^*$ , of 27 inches. A 10-inch cylindrical chamber extension was also designed to provide a total  $L^*$  of 55 inches. The wall thickness for the chambers and extension was a constant 0.50 inch in a plane perpendicular to the chamber centerline. This thickness was chosen to keep predicted maximum wall temperatures at an acceptable level for test durations of 4 to 6 seconds and still provide good transient temperature measurements on the outside surface. The uncooled chamber used with stainless steel skirts in the simulated altitude tests was a modified chamber previously used under Contract NAS3-4195. Modifications consisted of welding a nozzle attachment flange to the exit and changing the chamber injector seal surface. Chamber dimensions (upstream of the throat) were identical to those of the sea level chambers. The nozzle had a 30-degree half-angle and an expansion ratio of 3.54.

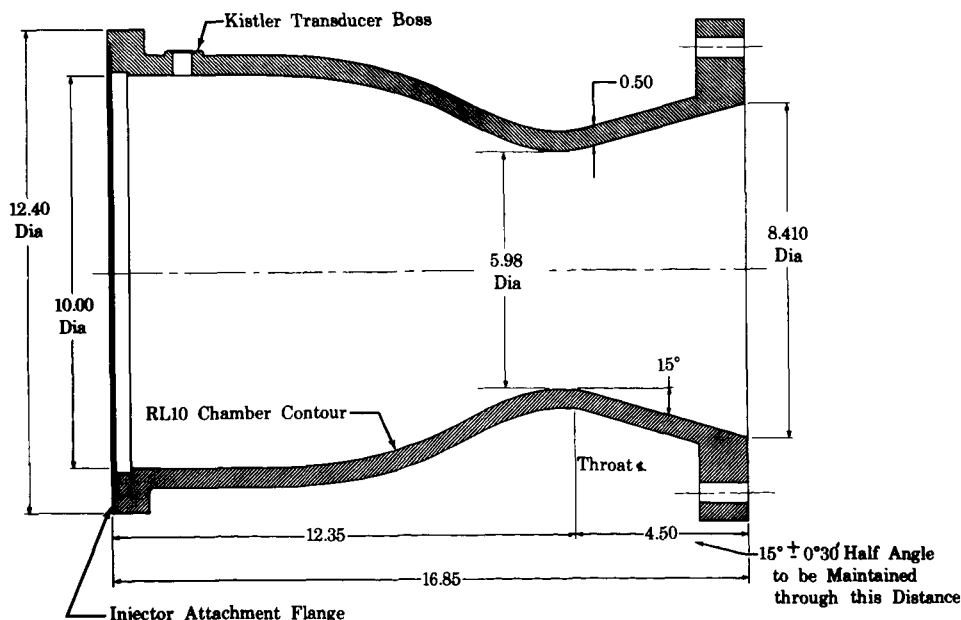


Figure III-9. Uncooled Copper 15-Degree Nozzle Thrust Chamber

FD 13420A

Instrumentation for both chambers consisted of 35 chromel-alumel thermocouples located axially along the chamber and 24 located circumferentially in two locations: 12 at the throat and 12 at points 5 inches from the injector face. In addition, the sea level chamber had 16 thermocouples spaced at 0.25-inch intervals over a 90-degree quadrant located 1.5 inches from the injector face. All thermocouples were imbedded in the outer surface of the chambers and the junctions were flame-sprayed with copper to provide high conductivity and strength. The chambers were then wrapped with insulation and given a protective glass-fiber coating. The insulation provided the necessary adiabatic boundary condition for heat transfer data reduction. Kistler high-frequency transducers were installed 90 degrees apart and approximately 1.5 inches from the injector face.

An uncooled truncated bell nozzle extension was fabricated for the simulated altitude tests. The nozzle provided an area ratio of 40 when attached to the uncooled or the transpiration-cooled chambers. The contoured nozzle had a perfect nozzle contour of 78, truncated to 40. The attachment area ratio was 3.54. The nozzle, shown in figure III-10, was constructed of 0.100-inch thick stainless steel. The thickness was selected as an optimum for obtaining accurate heat transfer data from 4- to 6-second uncooled tests. Strength and rigidity were provided by circumferential bands at four locations along the nozzle. One band also served as a sliding seal surface for the diffuser during altitude tests.

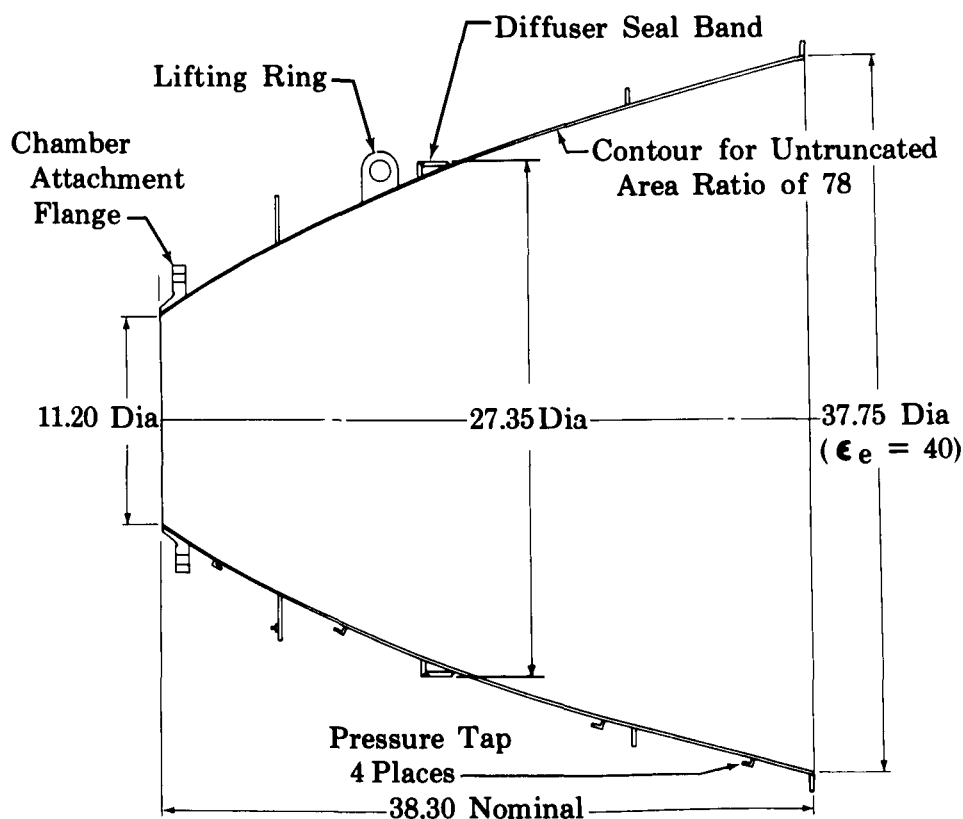


Figure III-10. Uncooled Truncated Bell Nozzle Extension

FD 13423A

Exhaust nozzle extension instrumentation consisted of 12 axial and 8 circumferential chromel-alumel thermocouples. The circumferential thermocouples were located every 45 degrees in a plane approximately 9 inches from the throat ( $\epsilon_e = 8$ ). Chromel-alumel thermocouples were tack-welded to the outer surface and covered with an insulating blanket and fiberglass in a manner similar to that of the copper chambers. Combustion gas static pressures were measured at four places along the nozzle. The uncooled chamber and nozzle assembly shown in figure III-11 includes an acoustic combustion liner that was used in tests with butene-1.

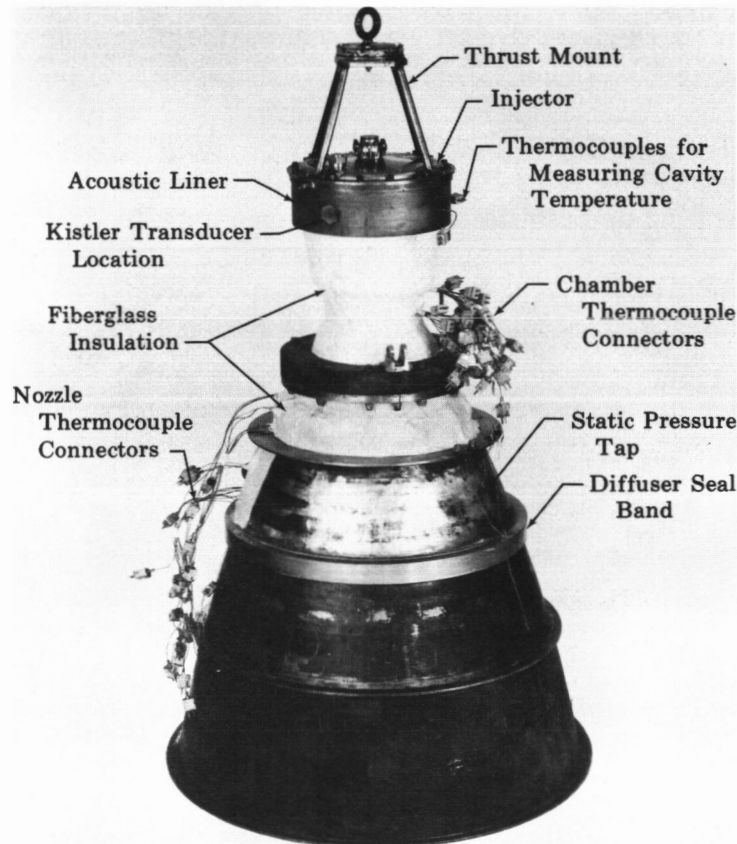


Figure III-11. Uncooled Chamber and Nozzle Assembly for Altitude Tests FD 19744

#### D. ACOUSTIC ABSORBING LINER

An acoustic absorbing liner was designed for use with the uncooled altitude firings if high frequency combustion instability was encountered during early tests. The liner is basically a series of energy-attenuating perforations in the chamber wall. The liner design was based on methods presented in Reference 12. It was configured to attenuate pressure oscillations caused by combustion instability of the first tangential mode at a predicted frequency of approximately 3100 cps for the flox/light hydrocarbon propellants in the 10-inch diameter chamber. The design covered one-quarter of the chamber wall in the area nearest to the injector. It has been shown that this location is the most effective for suppressing combustion oscillations and that a quarter-length liner is adequate.

The design analysis included the variation of aperture diameter, backing distance, and open area ratio using the copper chamber which provided a constant liner thickness of 0.5 inch. The results of the analysis, shown in figure III-12, indicate that it is possible to obtain an absorption coefficient of 99% for an aperture diameter of 0.10 inch and an open area of 8.5%; this design would require approximately 1000 holes. To reduce fabrication costs, a liner with fewer holes — each having an aperture diameter of approximately 0.21 inch (9.7% open area) — was selected. This produced an absorption coefficient above 95% over a frequency range of 2900 to 3250 cps. A schematic diagram of the acoustic liner is shown in figure III-13 and the exterior pressure vessel can be seen in the assembled chamber previously shown in figure III-11.

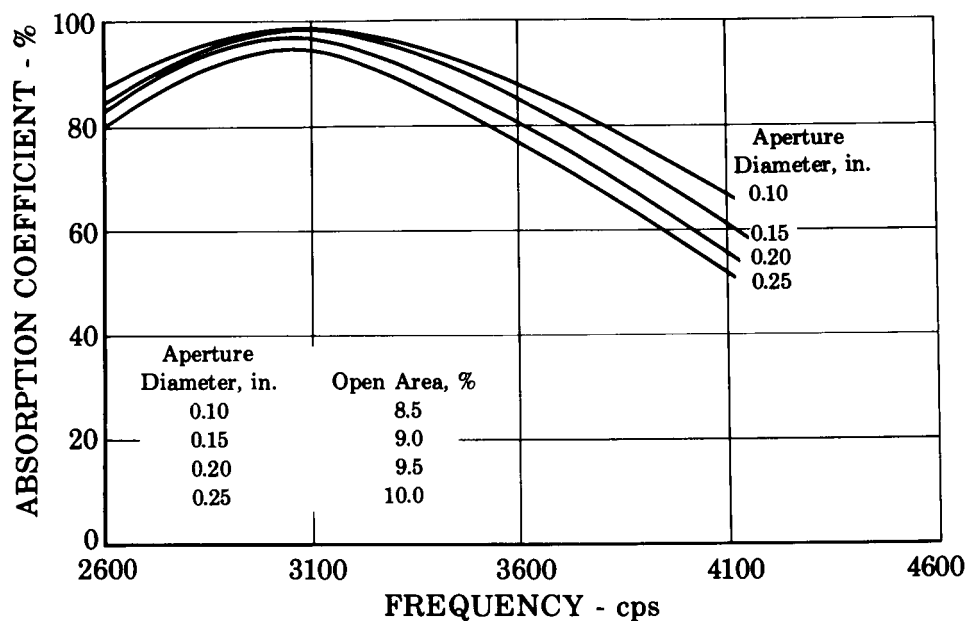


Figure III-12. Absorption Coefficient for Quarter-Length Acoustic Liner FD 19745

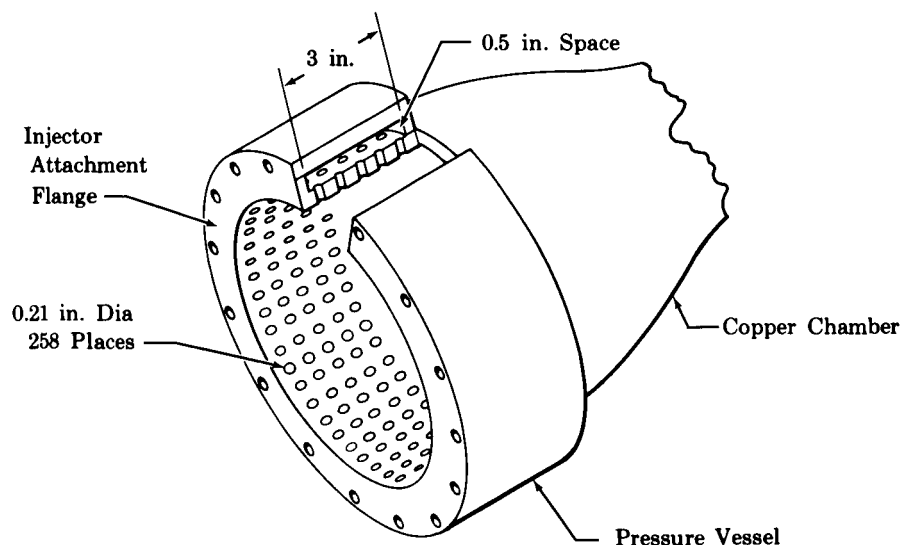


Figure III-13. Quarter-Length Acoustic Liner

FD 19300.4

## E. TRANSPIRATION-COOLED CHAMBER

The transpiration-cooled chamber used in previous tests under Contract NAS3-4195 was modified for simulated altitude testing. The chamber is divided into eight separate segments enclosed in a cylindrical shell, shown in figure III-14. Internal dimensions are similar to the uncooled chambers except that the contoured convergent section is replaced by a conical section to reduce fabrication costs. Chamber walls are constructed of Rigimesh. Coolant flow orifices within each segment provide for distribution of coolant among the eight segments to match coolant flow to the axial variation of heat flux.

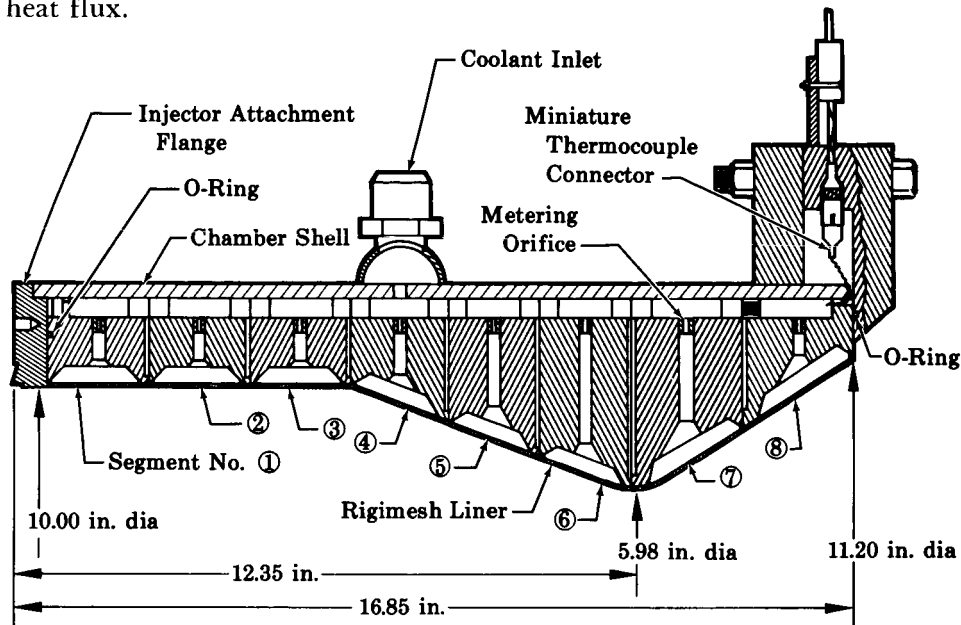


Figure III-14. Transpiration-Cooled Chamber Assembly

FD 19746

The assembled chamber is shown in figure III-15. The eight segments are stacked in a stainless steel cylinder that serves as a common coolant manifold. Alignment pins running through the segment stack maintain segment alignment and provide seal compression between the segments. The exit end of the cylinder is connected to a flange containing sealed instrumentation connections for joining internal and external portions of the instrumentation circuits. Modifications to the chamber for use in this program included: (1) changing the injector seal surface for acceptance of the liquid-liquid type injectors (RL10 injectors were used in the previous program) and (2) modification of the nozzle exit flange for acceptance of an exhaust nozzle extension. The segments are constructed to have the same inside diameter as the adjacent segments at the segment junctions. This is done to form smooth chamber walls and prevent localized hot spots. A typical segment is shown in figure III-16. Each segment is machined from a solid piece of stainless steel with internal passages to permit axial and radial coolant flow within the segment. The Rigimesh chamber wall liners, formed to the proper inside diameter, are mated to the segments by butt-welding. The two ends of each liner are cut diagonally with respect to the chamber axis so that coolant carries over the full penetration butt welds.



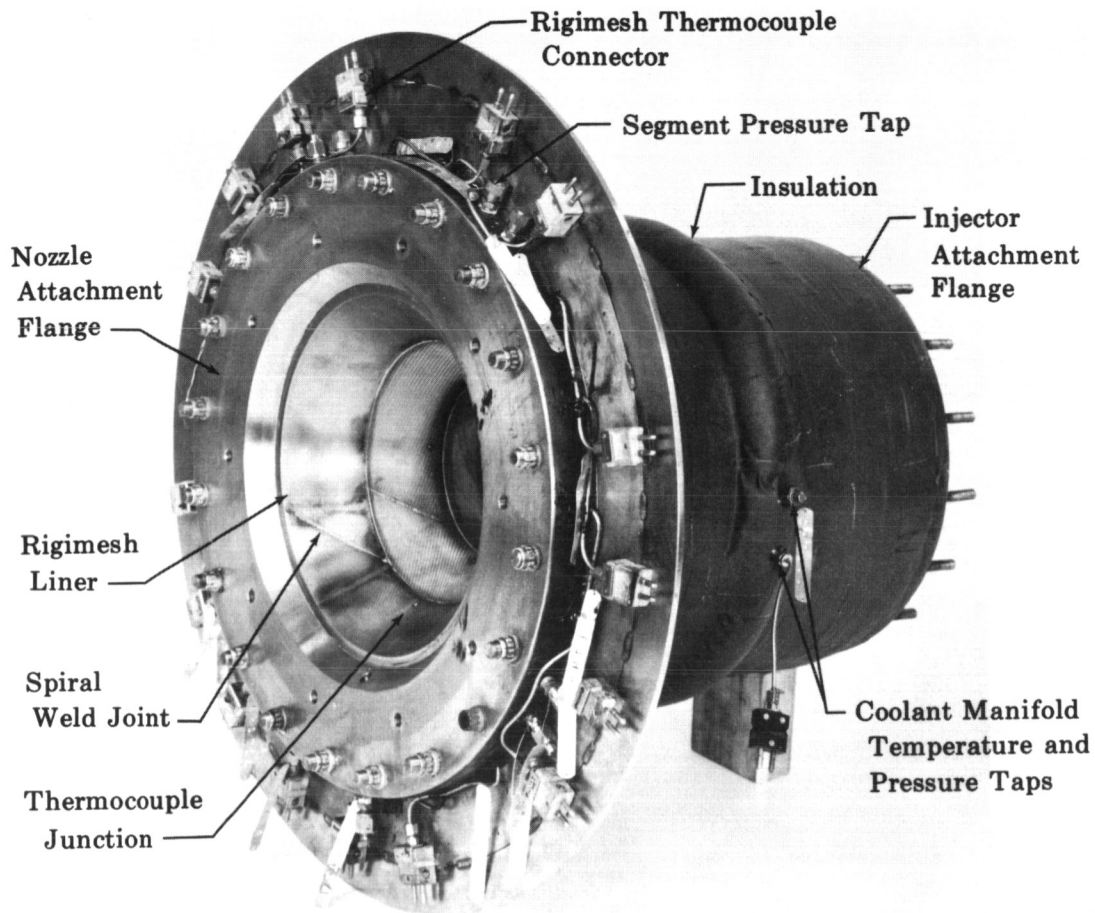


Figure III-15. Transpiration-Cooled Chamber

FD 19747

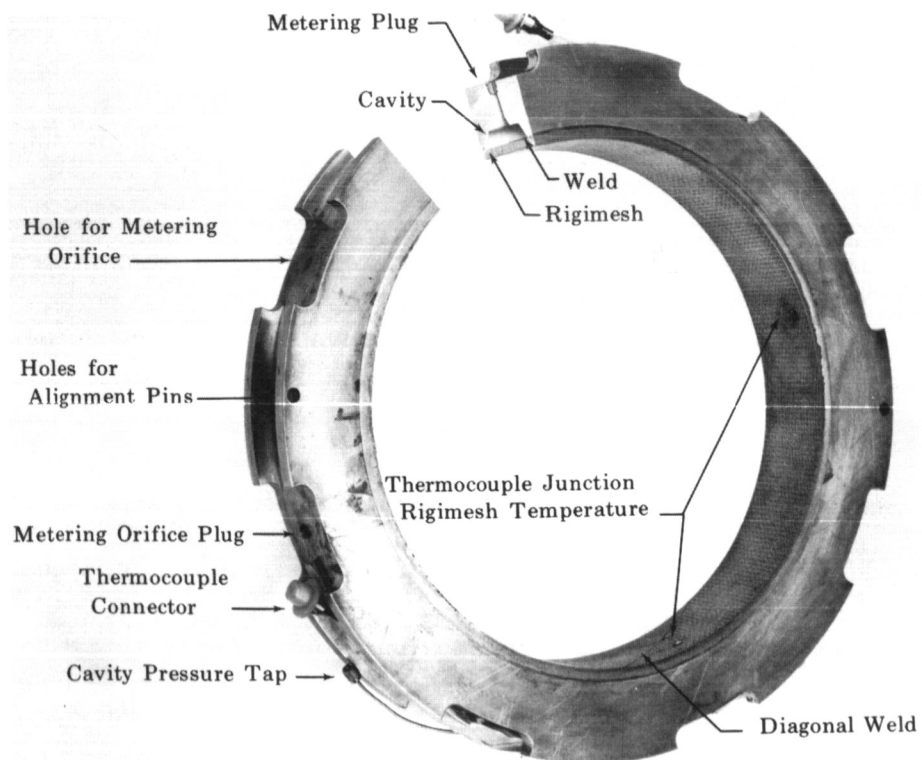


Figure III-16. Transpiration-Cooled Chamber Segment

FD 19748

Coolant flow to the Rigimesh is controlled by four metering orifices located around the outer diameter of each segment. The orifices can be drilled to any diameter up to 0.150 inch to obtain any desired coolant distribution to the segments. Because of variations and uncertainties in coolant pressure drop across the Rigimesh, the orifices are designed to take 60 to 95% of the total coolant pressure drop, thus maintaining the desired distribution. The predicted Rigimesh drops and the prediction method are presented in Appendix B. Rigimesh liner material capable of satisfying the flow requirements is available in many combinations of thickness and number of mesh layers. Eight-layer 12 x 64 mesh material with the required porosities was selected to provide a workhorse-type chamber.

The chamber was instrumented with 16 chromel-alumel thermocouples (0.032-inch diameter metal-sheathed) imbedded within the Rigimesh chamber walls and 8 pressure taps located internally within each segment. Fourteen of these thermocouples provided chamber combustion-side (Rigimesh hot-side) temperatures and two provided liner outer diameter (Rigimesh cold-side) temperatures. Circumferential hot-side temperature variations were measured in the 2nd and 7th segments with four thermocouples in each segment oriented 90 degrees apart. A single hot-side thermocouple was located at the top of each of the six remaining segments and single cold-side thermocouples were located at the top of the 3rd and 6th segments. Coolant cavity pressure was measured in each segment by means of hypodermic tubing connecting the segments to fittings located in the instrumentation flange.

A design of a transpiration-radiation cooled nozzle extension, scheduled for use in Task IV testing, was completed using experimental film coefficients which included the effect of coolant carryover determined from the transpiration-cooled tests with an uncooled nozzle. It was found that attachment of a radiation-cooled skirt at an area ratio of 9 would result in a maximum wall temperature of 2460°R. This wall temperature would be acceptable with a Hastelloy X, TD Nickel or TZM skirt, coated to resist oxidation. Operation at wall temperatures of 2160°R would allow the use of a stainless steel skirt, but would require transpiration cooling to a significantly higher area ratio for steady-state operation.

Figure III-17 shows an assembly drawing of the nozzle. The transpiration-cooled section is manufactured from a single sheet of constant porosity Rigimesh. The coolant manifold is divided into two separate sections to provide control over coolant distribution. Any desired flow split could be obtained by changing the removable metering orifices located in the coolant inlet fittings.

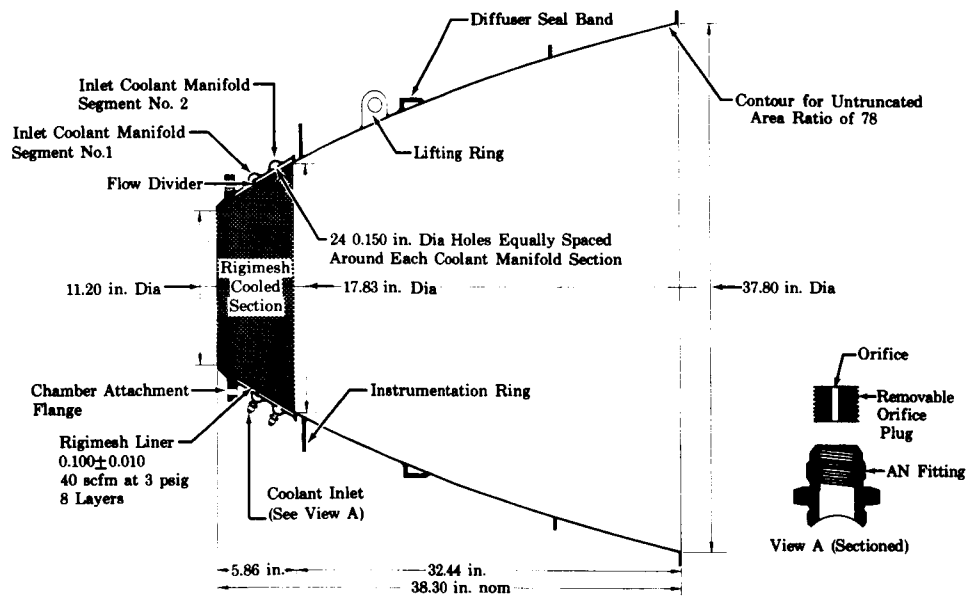


Figure III-17. Transpiration-Radiation Cooled Nozzle Assembly

FD 18131A

Heat transfer results from the transpiration-cooled tests with the uncooled nozzle indicated that the uncooled stainless steel nozzle, which attached at an area ratio of 3.54, would be acceptable for test durations of 35 to 40 seconds. This exceeded the maximum 30-second test duration specified in the Transpiration Cooled Test Plan. It was decided that the transpiration-cooled program objectives could be achieved with the uncooled nozzle because: (1) engine performance would not be significantly affected by the small amount of coolant injected between the area ratios of 3.5 and 9, and (2) the feasibility of transpiration cooling had been proved in the hard-to-cool throat and chamber regions. Therefore, the transpiration-radiation cooled nozzle was not fabricated and the program was completed using the uncooled stainless steel nozzle.

#### F. REGENERATIVELY COOLED THRUST CHAMBER

Two RL10 thrust chambers were modified for use in regeneratively cooled simulated altitude tests with flox/butene-1. The RL10 thrust chamber, shown in figure III-18, is a pass-and-a-half tubular chamber constructed with 180 full-length tubes interspaced with 180 shorter tubes in the nozzle. Combustion chamber dimensions are identical to the uncooled chambers. The nozzle contour is based on the method of characteristics perfect contour for an untruncated area ratio of 78, truncated to an area ratio of 40 to achieve minimum surface area per unit thrust. This contour is the same as that of the uncooled nozzles. Fabrication and tube dimensional details are given in Reference 13.

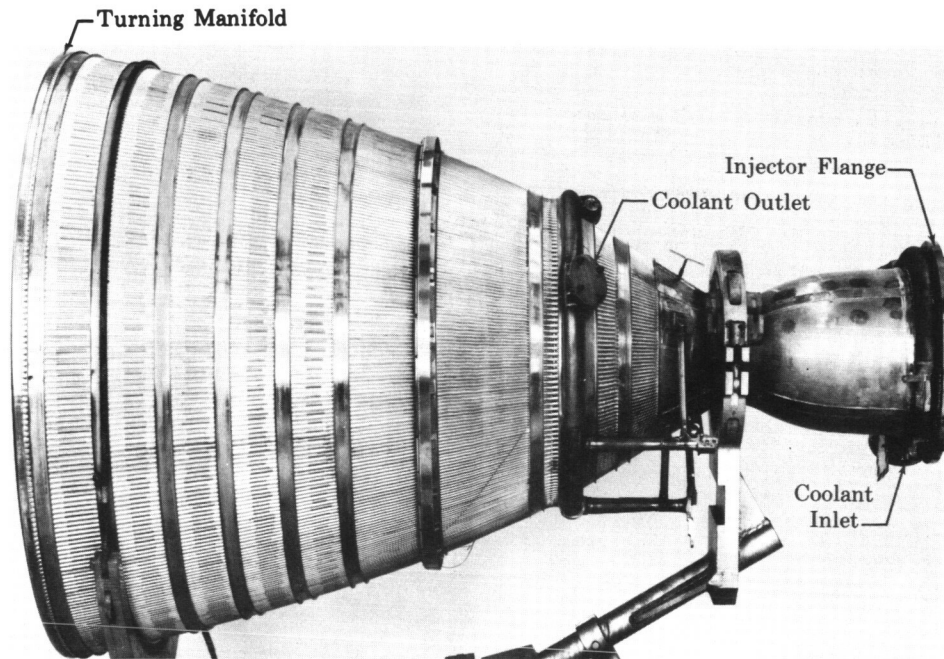


Figure III-18. RL10 Thrust Chamber Modified for Butene-1 Testing

FD 18469

For a preliminary cooling feasibility study, combustion-side film coefficients equal to 25% of those predicted by the Bartz short form (Reference 14) were used in the chamber and at nozzle area ratios below 4. This reduction was based on experimental sea level data obtained in Contract NAS3-4195 and in early uncooled sea level testing under this contract. Experimental film coefficients at area ratios above 4 were not available for the study; however, extrapolation of sea level data appeared to indicate that the reduction below the theoretical film coefficient would be slightly less than that observed in the chamber. Therefore, film coefficients in the nozzle were reduced to 35% of the Bartz short form values. Coolant-side nucleate and film boiling data used were based on the experimental heated tube data presented in Reference 1.

Table III-1 compares the various cooling conditions and configurations investigated. Note that a parallel-flow coolant path provided the lowest wall temperatures. Parallel flow was thus selected for the planned test program. The flow path is shown schematically in figure III-19. This flow path is the reverse of the normal coolant direction of the RL10 when used with hydrogen. Convective cooling in the nucleate boiling regime throughout the cooling jacket resulted in a maximum tube wall temperature of approximately 700°R. Because of the uncertainty in the nozzle heat transfer level, Configurations D and E were investigated using higher percentages of the Bartz coefficients at area ratios above 4.0. For nozzle heat transfer rates below approximately 70% of the Bartz predictions, the coolant would remain in the liquid phase throughout the jacket.

TABLE III-1. COMPARISON OF BUTENE-1 REGENERATIVE COOLING CONFIGURATIONS<sup>(1)</sup>

Configuration	Chamber Coolant Flow Direction	Inlet Temperature, °R	Maximum Wall Temperature, °R	Coolant Subcooling at Exit, °R <sup>(2)</sup>	Type of Boiling Encountered	Film Coefficient
A	Counter Flow	200	1800 (in chamber)	123	Nucleate to 1 in. before throat; film boiling remainder	25% of Bartz in chamber to $\epsilon_e = 4$ , 35% to $\epsilon_e = 40$
B	Parallel Flow	200	700	107	Nucleate	25% of Bartz in chamber to $\epsilon_e = 4$ , 35% to $\epsilon_e = 40$
C	Parallel Flow	175	700	128	Nucleate	25% of Bartz in chamber to $\epsilon_e = 4$ , 35% to $\epsilon_e = 40$
D	Parallel Flow	175	700	74	Nucleate	25% of Bartz in chamber to $\epsilon_e = 4$ , 50% to $\epsilon_e = 40$
E	Parallel Flow	175	700	-14	Nucleate to just before exit	25% of Bartz in chamber to $\epsilon_e = 4$ , 75% to $\epsilon_e = 40$

(1) Based on an RL10 tubular pass-and-a-half chamber with an  $\epsilon_c = 40$ ,  $P_c = 100$  psia,  $r = 3.85$ . Coolant inlet pressure = 200 psia.

(2) Coolant saturation temperature minus coolant exit temperature.

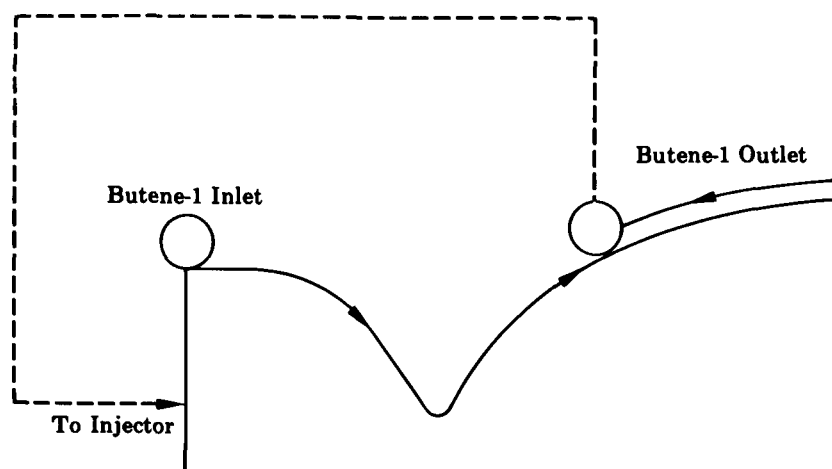


Figure III-19. Chamber Coolant Flow Path

FD 19749

Based on these calculations the use of an unmodified RL10 chamber was satisfactory, therefore, the first chamber modification was limited to a change in the injector attachment flange. Tube failures encountered in testing that chamber (see Section VIII) indicated that additional modifications were necessary to provide increased cooling margin in the chamber area immediately downstream of the injector. The second chamber was modified using spiral tube fillers extending from the inlet manifold to a

point 8 inches downstream of the injector face. These fillers, shown schematically in figure III-20, allowed higher heat fluxes to be absorbed while remaining in the nucleate boiling regime. Based on heat flux data obtained in uncooled tests, the heat fluxes near the injector were approximately 22% below the upper limit value without the fillers and 35% below with the fillers. These fillers had previously been used successfully in chamber tests under Contract NAS3-4195. Additional protection against high local heat flux was provided by filling the areas between the tube crowns with silver braze for a distance of 2.5 inches from the injector, figure III-20. The high conductivity silver provided additional conduction paths in the areas of nonuniform heat flux.

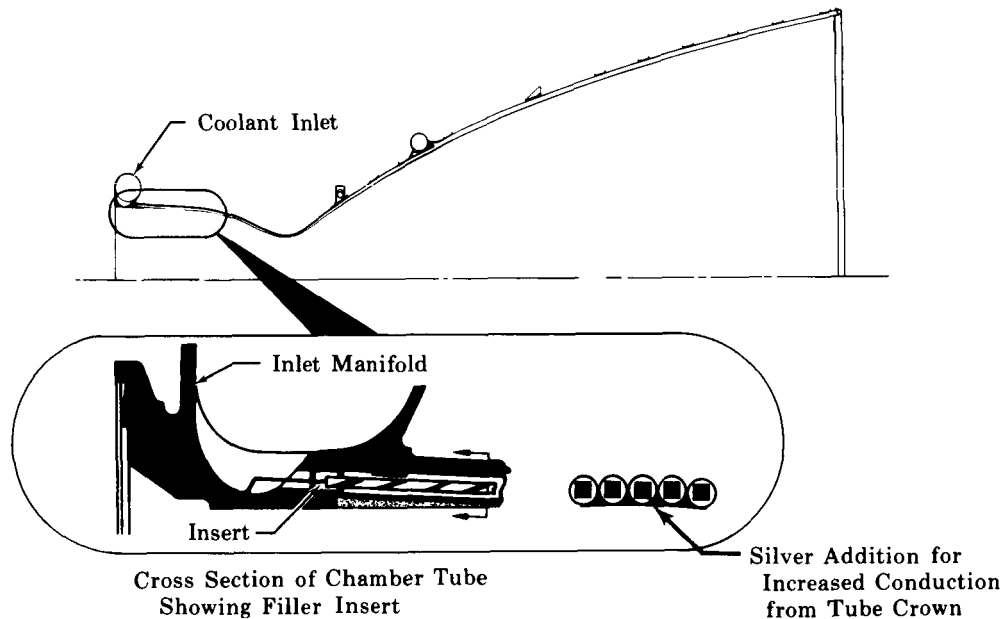


Figure III-20. Modifications Included in Second Chamber Modification FD 1281C

Because the butene-1 regenerative cooling tests were primarily a feasibility demonstration, cooling jacket instrumentation consisted only of coolant inlet and outlet temperatures and pressures. This permitted a verification of total heat flux with calculations based on the uncooled test gas film coefficients.

## SECTION IV

### TEST FACILITIES AND EQUIPMENT

#### A. LIQUID PROPELLANT RESEARCH FACILITY

All testing was conducted at Pratt & Whitney Aircraft's Liquid Propellant Research Facility (figure IV-1). This test complex has the capability of flowing storable and cryogenic propellants at feed pressures up to 5500 psi. The facility is divided into four firing bays for 1000-, 5000-, 15,000-, and 50,000-lb thrust levels (figure IV-2). The 5000- and 15,000-lb thrust bays are connected to a continuous acting steam-driven ejector system for altitude simulation. This system uses two exhaust diffusers discharging into a common crossover duct. After leaving the crossover duct, the exhaust products are cooled in a tube-in-shell water-cooled heat exchanger and pumped through a two-stage steam ejector. Before venting, the combustion products are cooled further and the steam is condensed in a scrubber-condenser that removes all but trace concentrations of hydrogen fluoride. Before being reused, discharge water from the scrubber is neutralized with lime and passed into a settling pond. For the 5000-lb thrust chambers used in this program, the ejection system was capable of maintaining a pressure of approximately 0.2 psia (simulated altitude of approximately 100,000 ft).

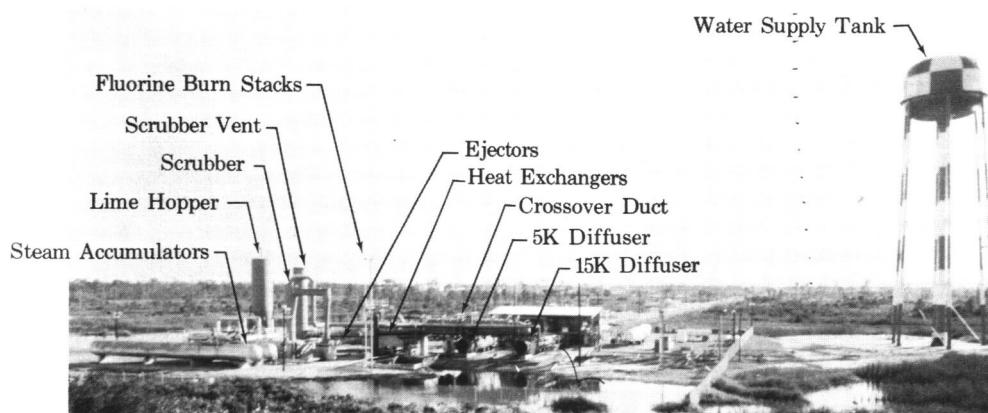
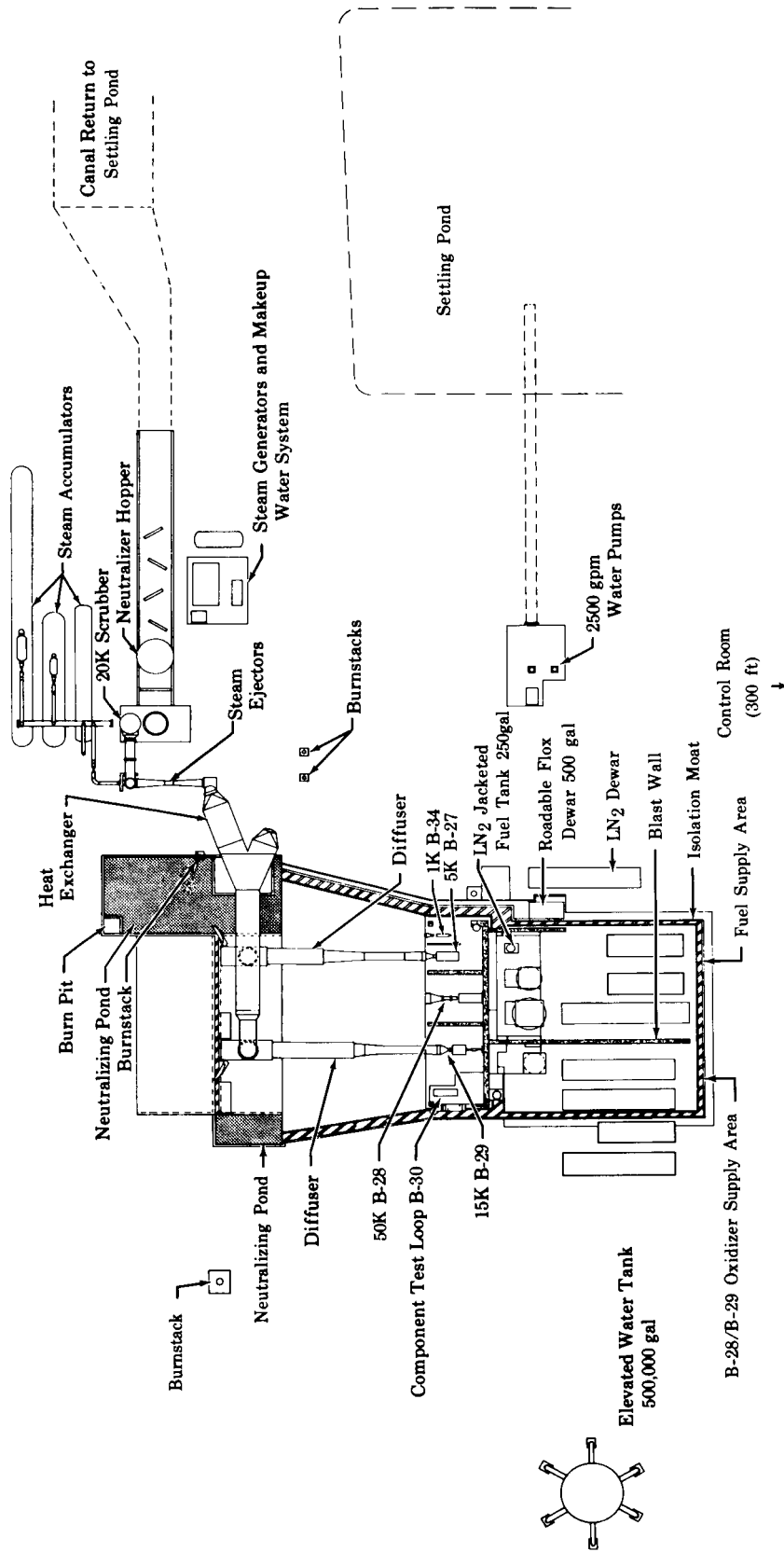


Figure IV-1. Liquid Propellant Research Facility

FD 19750

The Liquid Propellant Research Facility (LPRF) is used for all liquid fluorine and floc operations at the Florida Research and Development Center. Liquid fluorine handling is accomplished remotely from the facility control room, which is located about 300 feet east of the test stands. All operations are carried out using remote-operated valves except for transfer from the delivery vehicles, which are equipped with manual valves. Liquid fluorine is stored in roadable Dewars similar to the delivery vessels, but equipped with remote-operated valves. The facility itself is west of all other test facilities and takes advantage of the prevailing easterly winds to carry fluorine vapors or reaction products away from inhabited areas.



FD 12808B

Figure IV-2. Liquid Propellant Research Facility Schematic

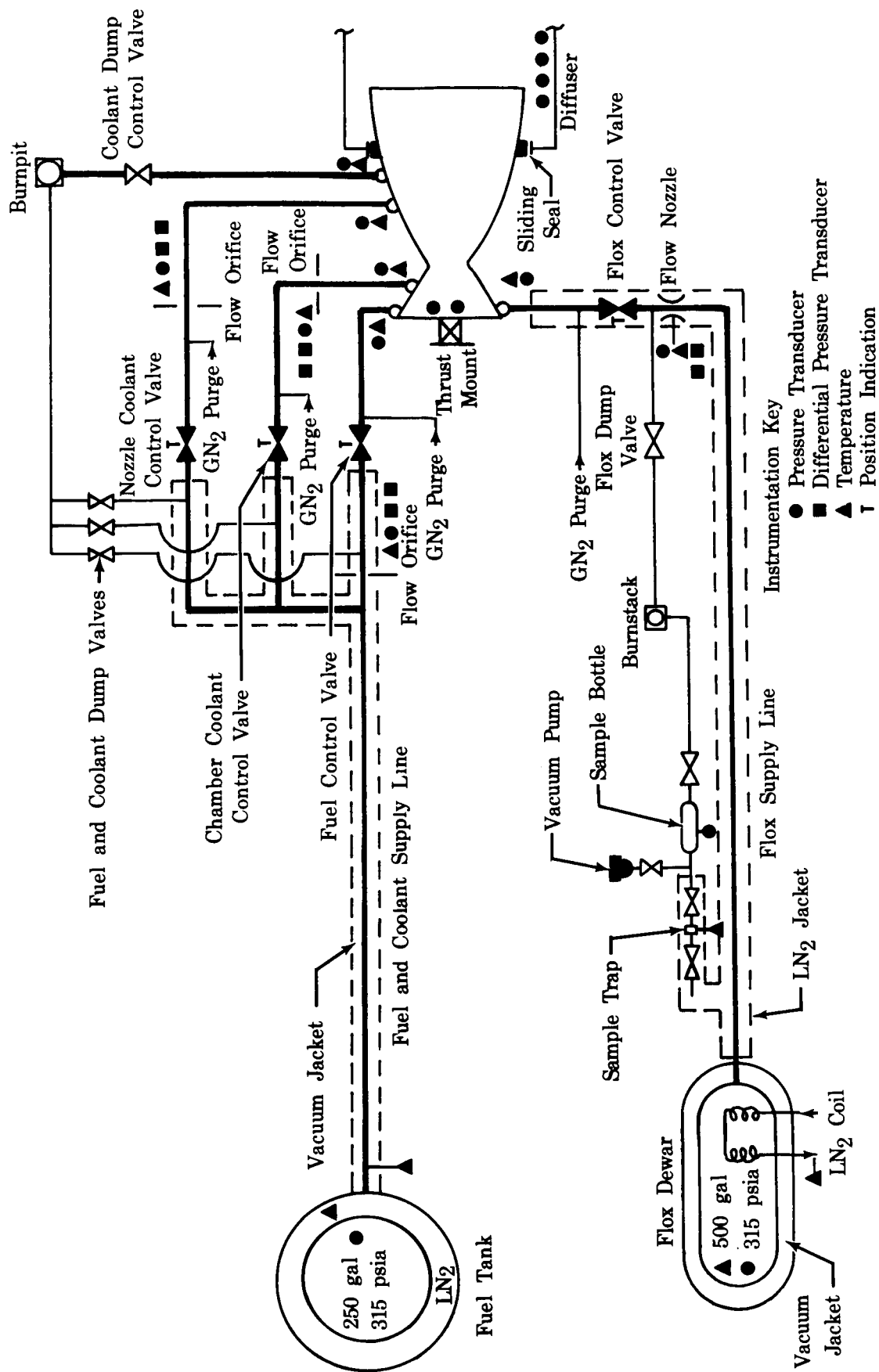


The closest inhabited area west of the stand is approximately ten miles distant. Fluorine operations are suspended when the wind directions or velocities are such that toxic vapors can be carried toward adjoining test facilities or industrial neighbors.

Rigorous standards of materials selection, fabrication, cleaning, passivation, and leak detection are followed for fluorine test facility design and operations. Metals of proved compatibility and durability (such as nickel, aluminum, copper and series 300 stainless steels) are used. During system design, mechanical joints were eliminated and full penetration welds used wherever possible. Facility valves are of the top-entry solid body type, having copper braid rings and Teflon chevron stem packings. Test stand fluorine systems are cleaned upon initial installation and after modifications involving cutting and welding. Cleaning is accomplished by flushing the system with an acidic solvent followed by flushing with demineralized water and vacuum drying. After cleaning, the system is passivated using gaseous fluorine at a pressure of approximately 200 psig. Bolted subsystems, such as instrumentation transducers, are individually passivated before installation. Prior to the first test of each series, the facility is passivated for 1 hour using gaseous fluorine at 15 psig. During this passivation a complete sniff check is made on all fluorine joints and valve stems. A detailed description of the fluorine procedures used by Pratt & Whitney Aircraft is presented in Reference 15. More than 210,000 pounds of liquid fluorine have been consumed at the LPRF in over 400 thrust chamber firings and in numerous valve and pump seal tests. While there have been several incidents involving fluorine leakage or reactions, no serious personnel injuries and only minimal facility damage have been encountered.

## **B. PROPELLANT SUPPLY SYSTEM**

All rocket chamber test firings under Contract NAS3-6296 were conducted in the 5000-lb thrust B-27 stand firing bay; the propellant flow path is shown in figure IV-3. The liquefied hydrocarbon fuels were supplied from a 250-gallon liquid-nitrogen-jacketed tank. Fuel temperature settings between 140 and 180°R were obtained by controlling the nitrogen jacket pressure from 0 to 100 psig. Gaseous methane, purchased in high-pressure cylinders was liquefied by allowing the gas to enter the cooled tank where it was condensed. Propane and butene-1 were purchased as pressurized liquids and were tanked by pressurized transfer from the shipping cylinders. Both these fuels could be maintained either at ambient temperature or precooled with liquid nitrogen. The fuel supply lines were all vacuum-jacketed up to the test chamber inlets. Four electrohydraulic servo-operated control valves were available for separate control of (1) the injector fuel flow, (2) chamber transpiration or regenerative coolant flow, (3) transpiration-cooled nozzle flow, and (4) coolant jacket exit pressure in the supplementary cooled tests. The liquid flow was supplied during tests from a



FD 19751

Figure IV-3. Flox-LPG Test Stand Flow Schematic

500-gallon vacuum-jacketed roadable Dewar. Liquid nitrogen cooling coils within the Dewar minimize boiloff losses to a negligible amount. Flox was supplied to the test chamber through a liquid-nitrogen jacketed line and controlled by a single servo-operated control valve.

Flox was mixed within the roadable Dewar by adding liquid oxygen and liquid fluorine while the Dewar weight was monitored within the control room. Flox concentration, calculated from the oxidizer weights, was verified by laboratory analyses of samples taken after mixing and after each test series. Accurate samples were obtained by trapping liquid flox in an evacuated space between two remotely operated valves.

The two valves and the sample chamber were liquid nitrogen jacketed to ensure that liquid was trapped. This prevented changes in flox concentration caused by fractional distillation. After the liquid flox was trapped, the sample system was isolated and the nitrogen flow was secured to allow complete evaporation of the liquid flox into an evacuated sample bottle. The system was allowed to remain intact for a period sufficient to ensure that a homogeneous gas was contained throughout.

The sample bottle was then removed to the chemistry laboratory for mercury absorption analysis. This analysis is one of the oldest direct methods for the determination of fluorine concentration and utilizes the rapid absorption of fluorine gas by elemental mercury to reduce the pressure of a gaseous sample. The quantity of fluorine absorbed is determined by measurement of the pressure and volume of the sample before and after absorption. A highly successful system developed at the Florida Research and Development Center (figures IV-4 and IV-5) uses a fluorine pressure transducer to automatically record the pressure of the sample within a constant volume system. In operation, a portion of the vaporized flox sample was transferred into a small evacuated chamber and the initial pressure set at 100%. A measured quantity of mercury was then allowed to flow into the reaction chamber. The pressure immediately decayed as the fluorine was absorbed by the mercury. Because an inert interface of mercury fluoride forms over the mercury surface, complete absorption was obtained by stirring the mercury with a magnetic stirrer. When complete absorption was indicated, by a leveling of the pressure decay rate, the reaction flask was opened to an evacuated expansion coil having a volume equal to the volume of the mercury added; thus the system was returned to its original volume. The pressure recorder then indicated directly the percentage of sample that was not absorbed. Duplicate analyses of samples in the range of 63-93% fluorine have shown a repeatability of 0.23% with this system.

Consideration was given to using the flox storage Dewar equilibrium pressure and temperature to determine mole concentrations using the law of partial pressures. This method was abandoned because of the inherent inaccuracies that arise due to temperature variations throughout the Dewar and the unknown partial pressure of residual helium pressurant gas.

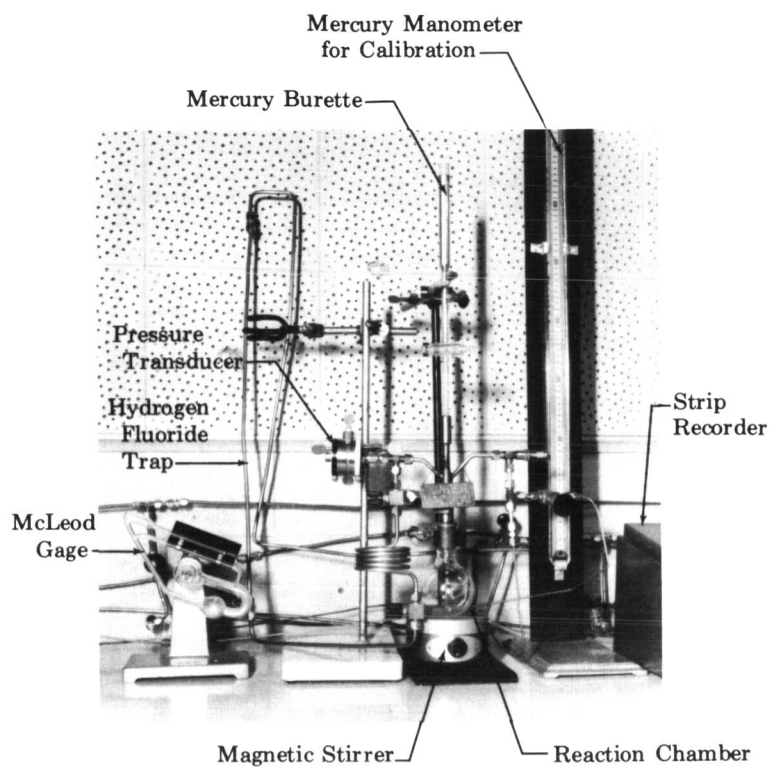


Figure IV-4. Mercury Absorption Apparatus

FD 19752

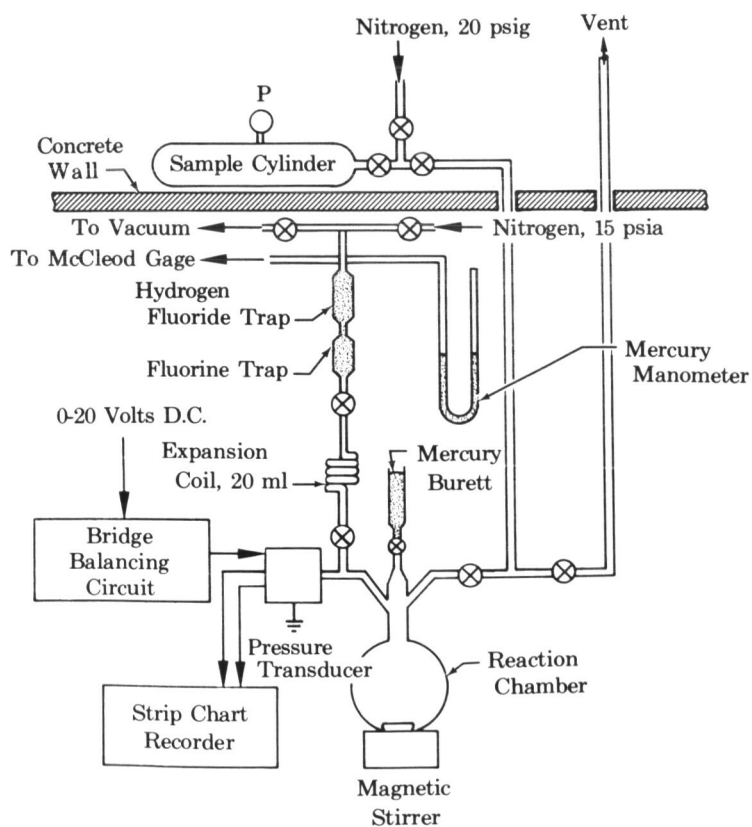


Figure IV-5. Schematic Diagram of Mercury Absorption Apparatus

FD 19753

A third method of determining flox concentrations is now being developed using a gas chromatograph. This system offers the potential advantage of allowing continuous sampling on the test stand and providing analysis for constituents other than fluorine. Figure IV-6 shows the Micro-Tek GC 2500R-II chromatograph now being used to develop this procedure. To date, no molecular sieve columns have been found that are sufficiently inert to fluorine. This system therefore uses two columns: one to separate fluorine from the sample and another to separate oxygen from the residuals.

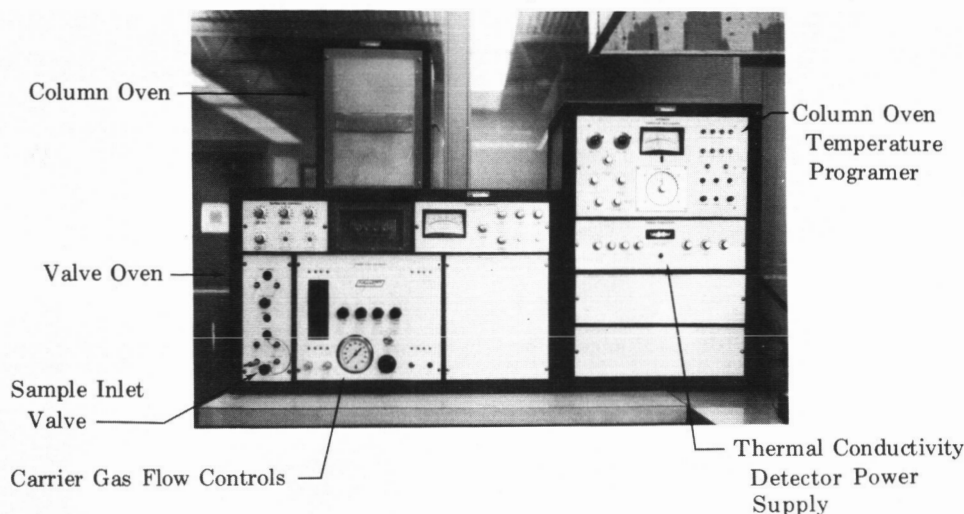


Figure IV-6. Gas Chromatograph System

FD 19754

Communication between the two columns is accomplished by means of a column-switching valve. A sodium chloride precolumn has been developed for the quantitative conversion of fluorine to chlorine. Partition columns that use a silicone or halogenated oil as a stationary liquid phase effectively separate the converted sample into an "air" peak (composed of oxygen, nitrogen, and helium) and a chlorine peak that can be quantitated as fluorine. A column-switching system (figure IV-7) has been used successfully to pass the air peak into a molecular sieve column for further separation and then divert the chlorine peak around the molecular sieve column into the nickel thermal conductivity detector. Calibration is accomplished by filling the sample inlet system with various pressures of pure chlorine, fluorine, oxygen,

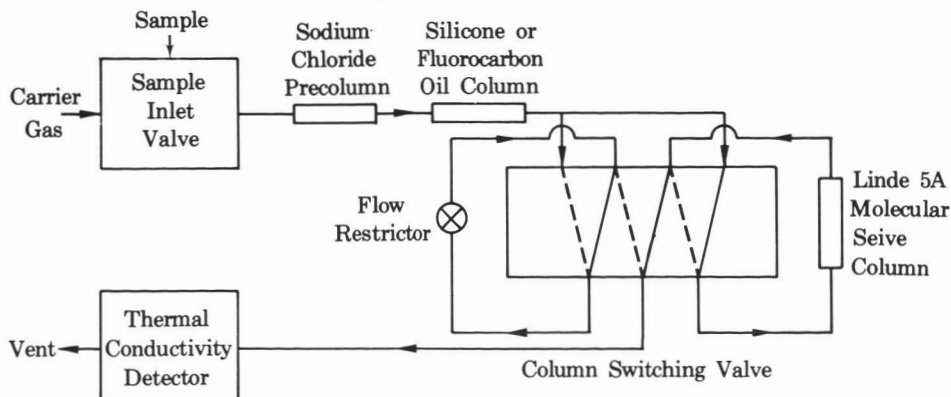


Figure IV-7. Schematic Diagram of Multicolumn Gas Chromatograph System for Analysis of Fluorine-Oxygen Mixtures

FD 19755

nitrogen, or helium, and plotting the instrument responses to the various gases versus their partial pressures.

### C. CONTROL SYSTEM

Test firing events are controlled by a digital-sequencer, analog-computer, electrohydraulic valve combination. The digital sequencer can be programed to operate 40 relay channels in 1-millisecond increments over a total duration of 2000 seconds. These relays can be operated in series, parallel, cascade, and time-delayed sequences. In conjunction with the analog computer, the sequencer can be programed to interrogate certain parameters at specific time intervals to provide a go/no-go indication for the test to proceed or advance automatically to a controlled shutdown.

Figure IV-8 is a partial view of the LPRF control room and shows the 64-amplifier analog computer that is used for automatic closed-loop control of the servo-operated control valves. The computer can control 8 to 10 functions depending on the nature of the controlling reference. Among the reference parameters that may be selected are: (1) line pressure, (2) flow rate, (3) chamber pressure, (4) mixture ratio, and (5) valve position. Combinations of the above modes can be biased to obtain control of several parameters simultaneously, e.g., varying propellant flow rates to obtain specific chamber pressure while maintaining a preset mixture ratio.

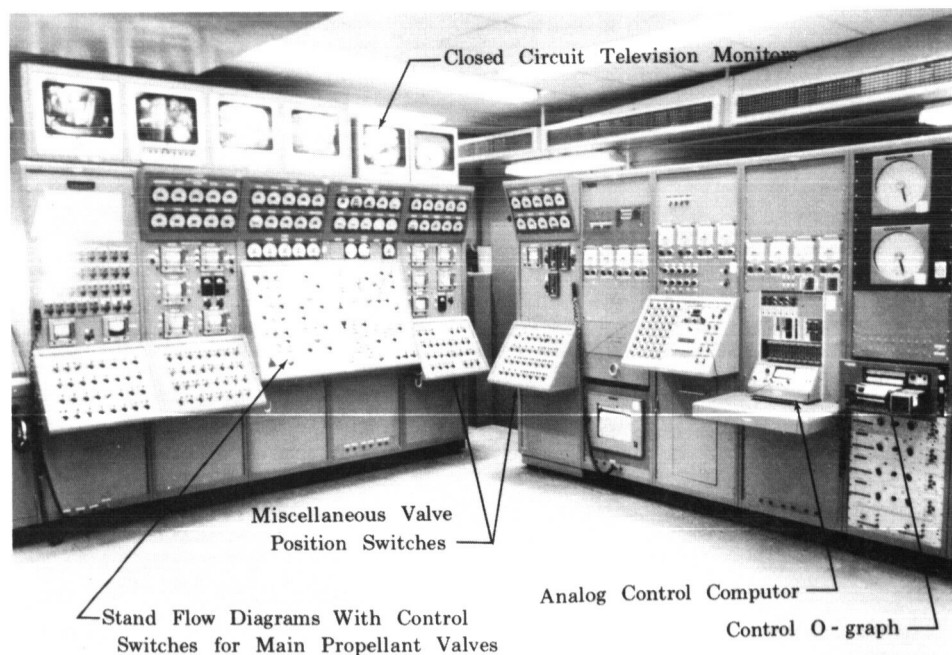


Figure IV-8. LPRF Control Room

FD 19756

For the flox/light hydrocarbon tests both the fuel and oxidizer valves were opened in position control using controlled ramp durations with a 25- to 50-millisec fuel lead. The valves remained in the specified position until liquid propellant flow was attained at the injector, and chamber pressure was near the nominal value. Use of the position reference eliminated valve upsets during the transitory period when gaseous or two-phase flow was present. At approximately 1.0 sec the fuel and oxidizer control references were sequenced to control propellant flow rate with approximately a 0.10-sec lead of the fuel switch to minimize transient mixture ratio spikes. Two sequenced go/no-go checks were made to ensure that ignition was obtained before a large quantity of propellants had been injected. A weighted wire in front of the exhaust was electrically sampled to determine that it had burned through and released the weight before 1.2 seconds had elapsed. A continuous sample of chamber pressure was made to determine that chamber pressure did not drop below 50 psia after 1.0 sec. Shutdown was conducted using 0.5-sec flow rampdowns having a slight fuel lag. Exact timing and initial valve positions were determined in liquid nitrogen cold flows. Valve sequencing for the altitude tests was identical to the sea level tests with the addition of a sequenced go/no-go check of maximum diffuser pressure immediately before initiation of the start sequence.

In the supplementary cooled tests, the coolant control valve was opened with a position ramp approximately 6 seconds before the oxidizer valve started to open. After the jacket was filled and flow stabilized, the reference was switched to flow rate control (approximately 3 seconds after opening). The coolant dump valve was set at a preset position before the coolant valve opened. After the coolant flow rate was stabilized the dump valve control was switched to maintain a preset cooling jacket exit pressure. Coolant shutdown was initiated (after the chamber pressure had decreased to the diffuser pressure) with a flow rampdown of the inlet valve and a return to the initial position of the dump valve.

Control of the transpiration coolant was accomplished in approximately the same manner; the coolant valve opened in position control with a sufficient lead time to fill the coolant cavity and stabilize flow before the injector sequence was initiated. Shutdown was made with a flow ramp having a slight lag on the injector shutdown sequence.

#### **D. INSTRUMENTATION AND DATA ACQUISITION**

The LRPf data system has capacity for approximately 135 measurement channels. The system provides capability for measurement of pressure, temperature, thrust and flow rate. Excellent recording accuracy and response are available through a 96-channel low-level-input analog-to-digital converter that feeds a magnetic tape system. The data recording equipment is shown in figure IV-9. Also provided are 36 oscillograph channels

and 10 direct-inking strip chart channels. Isolation amplifiers are available to permit redundant analog recording of 18 channels of digital tape. A separate system, consisting of a high-speed 14-track tape recorder, amplifiers, and transducers, provides high-frequency data capability to 20,000 cps. Six closed-circuit television channels provide continuous test observation.

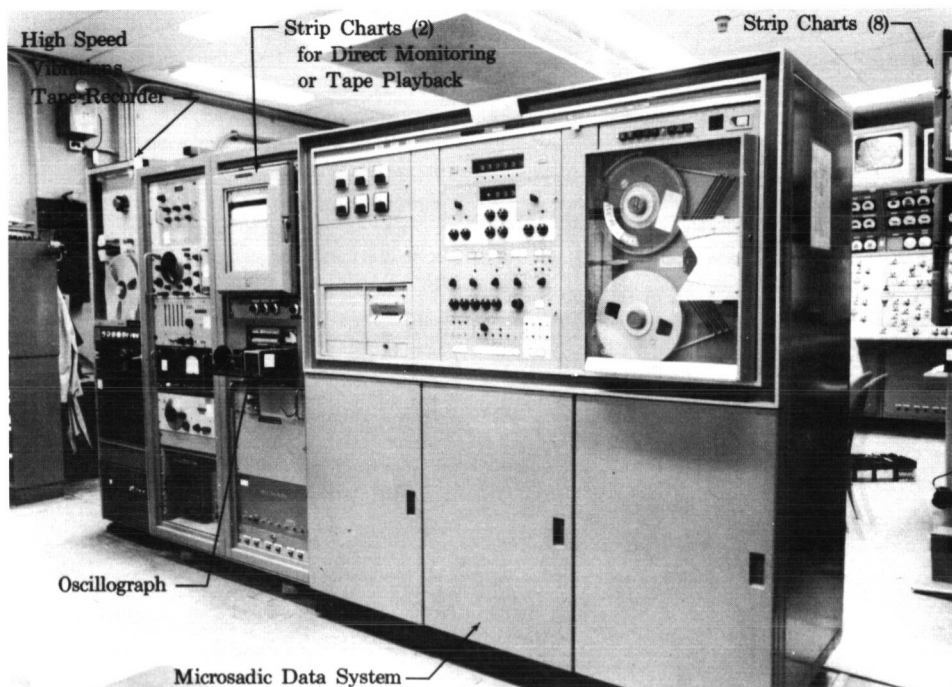


Figure IV-9. LPRF Data Recording Equipment

FD 19757

To assure the validity of test data, redundant instrumentation and accurate calibration procedures traceable to the National Bureau of Standards (NBS) are used. It is normal to achieve total data measurement accuracies (three standard deviations) of  $\pm 0.5\%$  for pressures,  $\pm 0.5\%$  for thrust, and  $\pm 0.1\%$  for turbine mass flow measurements with the digital recording system.

The Instrumentation Engineering Section maintains a complete computerized record of evaluations, calibrations and maintenance history relating to all sensing and/or recording instrumentation. When instrument calibrations are performed, the information is transferred to a magnetic tape for computer processing. The computer then scans the new information, combines it with past history and provides a tabulated statistical analysis for each of the instruments. Studies are continually being made to determine instrument calibration intervals, trends, deterioration, and maintenance adequacy.

Statistical analyses have established current primary calibration intervals of 4 months for pressure transducers and bridge completion networks,



6 months for temperature probes and turbine-type flowmeters, and 12 months for thrust load cells. In addition, instrumentation secondary calibrations are performed before and after the testing of each engine.

Pressures are sensed with standard 4-arm bridge strain gage pressure transducers. These transducers are calibrated by comparing them to working standards maintained in the Instrumentation Laboratory. These working standards are in turn compared with a primary standard that has been calibrated by the NBS.

Temperature measurements are made with standard resistance thermometers and chromel-alumel or copper-constantan thermocouples. In use, the resistance thermometers form the active arm of a bridge completion network (BCN). The resistance thermometers are acceptance-calibrated at known temperatures, and the BCN's are checked for system resistance by comparing them with resistances directly traceable to the NBS. Thermocouple temperature measurement accuracy is maintained by acceptance testing of the thermocouple materials and accurate calibration of voltmeters and reference ovens used. The thermocouple material is acceptance tested by testing samples of the wire at known temperatures derived in the same manner as those temperatures used for the resistance thermometer acceptance test.

Liquid propellant flow rates were measured by orifices and nozzles. These flow-measuring devices are calibrated on special calibration stands by flowing the devices with cryogenic liquids at accurately known temperatures and flow rates. All flow devices are recalibrated at periodic intervals.

Thrust measurements are made with 4-arm bridge strain gage load cells that are calibrated in the same manner as pressure transducers. Thrust mount systems, including load transducers, are calibrated weekly or after any changes made in the test rig or stand plumbing. Primary calibration is accomplished with dead weights, the accuracy of which is directly traceable to the NBS through a system of secondary and primary standards.

The instrumentation locations used in this test program are shown in the schematic flow diagram (figure IV-3). As shown on this diagram, redundant measurements were made for all critical performance parameters (e.g., flow rates, chamber pressure, diffuser pressure, and thrust). All instrumentation was recorded by the digital system. Redundant oscillograph recordings of the critical performance parameters were made to guarantee that data would be available in the event of a digital system failure. Additional readout of the critical starting temperatures and pressures was available on the control room strip charts. Table IV-1 presents the maximum estimated performance data errors for a typical uncooled simulated altitude test. Appendix A contains a complete statistical accuracy estimate for all recorded and calculated performance parameters during simulated altitude tests.

TABLE IV-1. ESTIMATED PERFORMANCE DATA ACCURACY\*

Parameter	Estimated Error, %	
	1 $\sigma$ (68% Confidence)	2 $\sigma$ (95% Confidence)
Characteristic Velocity	$\pm 0.443$	$\pm 0.887$
Vacuum Specific Impulse	$\pm 0.643$	$\pm 1.287$
Vacuum Thrust Coefficient	$\pm 0.523$	$\pm 1.047$

\*Maximum statistical error estimates for a simulated altitude test using an uncooled chamber with flox-methane at a mixture ratio of 5.7.

## SECTION V

### UNCOOLED SEA LEVEL PERFORMANCE TESTS — TASK II

#### A. TEST DESCRIPTION

A total of 84 uncooled sea level tests were conducted: 39 with methane and 82.6% flox, 19 with propane and 76.0% flox, and 26 with butene-1 and 70.4% flox. Test objectives were to determine the effects of injector design on combustion efficiency and to provide heat transfer data for analysis of chamber cooling requirements. The performance objective for these tests was achievement of characteristic velocity efficiency of 95% of theoretical shifting at the optimum mixture ratio for each fuel. The tests were conducted using liquid-liquid impingement-type injectors and uncooled copper thrust chambers. Construction details for the chambers and injectors are given in Section III. Figure V-1 shows a typical installation of the engine in the test stand. A discussion of test operating procedures and control modes is given in Section IV. Nominal test conditions were 100-psia chamber pressure and 5000-lb vacuum thrust based on an expansion area ratio of 40. With the nozzle expansion ratio of 1.98, the chamber produced approximately 3000-lb thrust at sea level. The flox was injected as a liquid at approximately 160°R. The fuels were normally injected as subcooled liquids at 180 to 300°R, but several tests were made with liquid butene-1 at higher temperatures (440-540°R) to determine the effect of fuel volatility on combustion stability and to simulate injector performance with regenerative cooling. Table V-1 presents a summary of the Task II — Uncooled Sea Level Tests. Thirteen modifications of four injectors were tested using varying combinations of propellant injection momentum ratio, faceplate porosity, and element configuration. Table V-2 is a summary of the injector configurations tested.

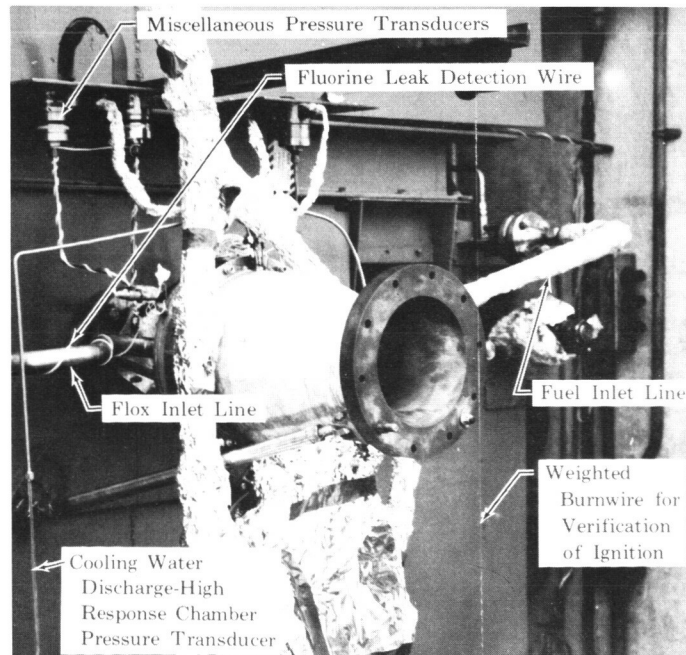


Figure V-1. Engine Installation for Uncooled Sea Level Tests

FD 19758

TABLE V-1. SUMMARY OF UNCOOLED SEA LEVEL TESTS

Series No.	Test No.	Fuel	Percent F <sub>2</sub> in Flow	Test Duration, sec	P <sub>c</sub> , psia	F <sub>1</sub> , lb	Q <sub>0</sub> , lb/sec	W <sub>f</sub> , lb/sec	T <sub>01</sub> , °R	T <sub>1</sub> , °R	ΔP <sub>01</sub> , psi	ΔP <sub>1</sub> , psi	Injector	Ignition Delay, millise	Comments <sup>(1)</sup>
1	1	Propane	76.0	2.0	100.0	3027	10.9	3.09	167	267	78	137	S(1)	85	Ignition check.
	2	Propane	76.0	4.0	100.0	3056	10.6	3.12	165	260	80	134	S(1)	70	
	3	Propane	76.0	4.0	97.3	2945	11.0	2.83	164	300	84	112	S(1)	50	
	4	Propane	76.0	4.0	94.5	2833	11.0	2.68	163	280	78	103	S(1)	45	
	5	Propane	76.0	6.0	91.4	2706	11.4	2.32	155	274	81	78	S(1)	70	
2	6	Methane	82.6	2.0	94.4	2802	11.2	1.80	167	203	93	197	S(1)	110	Ignition check.
	7	Methane	82.6	4.0	95.3	2875	11.3	1.92	160	203	94	198	S(1)	115	
	8	Methane	82.6	4.0	95.5	2883	11.3	1.99	165	187	93	192	S(1)	100	
3	9	Methane	82.6	2.0	99.0	2978	11.3	2.68	168	184	66	131	R(1)	65	Ignition check.
	10(2)	Methane	82.6	1.5	59.8	1485	11.4	0.84	170	195	109	212	R(1)	95	Aborted - low fuel flow.
	11	Methane	82.6	4.0	91.3	2686	11.2	1.88	164	200	61	174	R(1)	110	
	12	Methane	82.6	4.0	73.4	1963	10.9	1.44	165	201	71	215	R(1)	90	
	13(2)	Methane	82.6	4.0	84.4	2755		1.69	172	208	209	98	R(1)	120	Ran out of flow. Flow measurements were bad due to helium gas in line.
4	14	Propane	76.0	4.0	96.0	2865	11.1	2.56	166	233	52	104	S(1-A)	90	
	15(2)	Propane	76.0	1.5	48.8	1110	10.7	1.88	165	359	57	236	S(1-A)	100	Low chamber pressure abort due to low fuel flow.
	16	Propane	76.0	4.0	100.5	3082	10.9	3.08	168	265	50	162	S(1-A)	110	
	17	Propane	76.0	4.0	96.6	2918	10.8	2.75	168	283	54	123	S(1-A)	65	
	18	Propane	76.0	4.0	93.4	2764	11.2	2.31	167	293	67	87	S(1-A)	100	
5	19	Methane	82.6	4.0	97.2	2957	11.1	2.46	165	215	61	109	R(2)	85	
	20	Methane	82.6	4.0	91.0	2728	11.1	2.16	169	222	62	74	R(2)	50	
	21	Methane	82.6	4.0	83.8	2457	11.2	1.86	172	258	70	114	R(2)	50	
6	22	Methane	82.6	4.0	75.5	2146	11.0	1.20	170	235	61	218	S(1-B)	90	
	23	Methane	82.6	4.0	79.9	2315	11.0	1.23	167	225	52	210	S(1-B)	80	
	24	Methane	82.6	4.0	72.7	2058	11.1	1.04	164	241	58	222	S(1-B)	65	
7	25	Propane	76.0	4.0	93.5	2866	10.6	2.84	175	229	51	154	S(1-B)	100	
	26	Propane	76.0	4.0	92.8	2788	10.5	2.43	177	242	58	213	S(1-B)	120	
	27	Propane	76.0	4.0	87.9	2584	10.7	2.25	177	246	58	96	S(1-B)	75	
8	28	Propane	76.0	4.0	95.5	2908	9.94	3.78	171	208	53	93	R(2)	80	
	29	Propane	76.0	4.0	96.6	2934	11.0	3.08	165	222	58	65	R(2)	65	
	30(2)	Propane	76.0	1.5	21.9	295	10.9		167	299	124		R(2)	75	Ruptured fuel line burst disk diverting fuel flow from rig.
	31	Propane	76.0	4.0	91.9	2721	10.9	2.54	173	238	81	28	R(2)	75	Mild instability, approximately 10 psi amplitude.
	32	Propane	76.0	4.0	90.4	2661	10.6	3.62	178	250	68	37	R(2)	70	
9	33	Propane	76.0	4.0	90.1	2676	9.69	3.05	179	269	88	26	R(2)	65	Mild instability, approximately 10 psi amplitude.
	34	Butene-1	70.4	2.0	91.7	2767	10.1	3.62	170	255	25	158	S(1-C)	90	Ignition check. High frequency instability.
	35	Butene-1	70.4	4.0	90.1	2689	10.5	3.24	164	220	25	128	S(1-C)	115	Stability similar to test No. 34.
	36	Butene-1	70.4	4.0	97.5	3138	12.1	2.87	173	248	72	165	S(1-C)	120	3000 cps oscillations with 300-400 cps modulation, amplitude 130 psi.
	37	Butene-1	70.4	4.0	101.4	3260	13.0	2.83	181	265	89	159	S(1-C)	70	3100 cps oscillations with 250-400 cps modulation, amplitude 120 psi.
10	38	Methane	82.6	4.0	73.8	2054	10.8	1.33	167	199	18	216	R(1-A)	100	
	39	Methane	82.6	4.0	94.8	2828	11.9	1.86	162	198	20	167	R(1-A)	65	
	40	Methane	82.6	4.0	96.0	2874	11.4	2.00	167	189	20	111	R(1-A)	115	
	41	Methane	82.6	4.0	99.2	3019	11.1	2.22	172	197	19	133	R(1-A)	55	
	42(2)	Methane	82.6	1.5	50.4	1150	10.4	1.53	165	202	23	213	R(1-A)	50	Ran out of fuel, shutdown due to low chamber pressure.
11	43	Methane	82.6	4.0	94.5	2830	11.6	1.87	167	190	21	127	R(1-A)	110	L* = 55 inches.
	44	Methane	82.6	4.0	98.7	3025	11.3	1.98	167	196	22	137	R(1-A)	55	L* = 55 inches.
	45	Methane	82.6	4.0	95.9	2919	11.2	2.19	171	199	20	165	R(1-A)	55	L* = 55 inches.
	46	Methane	82.6	4.0	95.0	2880	10.6	2.18	170	202	17	176	R(1-A)	70	L* = 55 inches.
12	47	Methane	82.6	4.0	70.3	1891	11.8	1.09	162	224	18	242	R(1-B)	50	High fuel side injector differential pressure.
	48	Methane	82.6	4.0	85.1	2432	11.7	1.77	159	186	23	208	R(1-B)	105	High fuel side injector differential pressure.
	49	Methane	82.6	4.0	84.0	2393	12.8	1.47	160	193	23	223	R(1-B)	50	High fuel side injector differential pressure.
13	50	Methane	82.6	4.0	79.6	2202	11.2	1.81	170	201	76	59	R(2-A)	140	
	51	Methane	82.6	4.0	79.9	2160	11.0	1.94	172	197	83	51	R(2-A)	140	
	52	Methane	82.6	4.0	84.7	2197	10.8	2.15	171	195	71	52	R(2-A)	60	
	53	Methane	82.6	4.0	90.0	2615	10.6	2.54	173	198	72	64	R(2-A)	60	
	54	Methane	82.6	4.0	91.6	2688	10.5	2.69	173	198	72	68	R(2-A)	55	
14	55	Methane	82.6	4.0	91.6	2675	10.3	2.89	175	197	65	84	R(2-A)	55	
	56	Methane	82.6	4.0	94.2	2833	11.8	1.84	168	206	13	127	R(1-C)	100	
	57	Methane	82.6	4.0	95.5	2907	11.8	1.96	162	205	22	128	R(1-C)	50	
	58	Methane	82.6	4.0	100.5	3088	11.7	2.14	163	212	19	108	R(1-C)	45	
	59	Methane	82.6	4.0	101.1	3108	11.4	2.34	165	212	22	134	R(1-C)	50	
15	60	Methane	82.6	4.0	101.2	3140	11.2	2.55	166	197	15	105	R(1-C)	50	
	61	Methane	82.6	4.0	104.5	3264	11.1	2.90	165	193	23	120	R(1-C)	50	
	62	Methane	82.6	4.0	101.3	3146	11.7	2.37	164	193	25	72	R(1-C)	60	
	63	Butene-1	70.4	2.0	81.1	2282	10.9	2.13	169	436	17	61	R(1-C)	75	
	64	Butene-1	70.4	4.0	77.2	2136	10.8	2.15	161	449	17	55	R(1-C)	40	
16	65	Butene-1	70.4	4.0	92.3	2714	10.6	2.83	165	490	16	52	R(1-C)	50	
	66	Butene-1	70.4	4.0	96.9	2900	10.6	3.32	167	493	20	66	R(1-C)	45	
	67	Butene-1	70.4	4.0	91.1	2677	10.6	2.91	169	538	19	60	R(1-C)	40	
	68	Butene-1	70.4	3.7	93.5	2765	10.4	3.13	178	535	21	65	R(1-C)	50	Aborted - shorted fluorine leak detection wire.
	69	Butene-1	70.4	4.0	98.0	2931	10.5	3.66	163	534	14	81	R(1-C)	45	
	70	Butene-1	70.4	4.0	99.6	2976	10.2	4.04	170	533	15	100	R(1-C)	65	Possible fuel dilution with liquid nitrogen.
	71	Butene-1	70.4	2.0	72.7	1972	11.1	2.95	166	320	18	84	R(1-C)	55	Aborted - low fuel flow.
	72	Butene-1	70.4	4.0	94.4	2829	10.2	3.39	162	267	18	124	R(1-C)	65	Aborted - low fuel flow.
	73(2)	Butene-1	70.4	2.0	54.8	1295	10.5	3.03	172	295	21	185	R(1-C)	65	Aborted - low fuel flow.
	74(2)	Butene-1	70.4	2.0	53.0	1252	10.5	3.08	174	329	24	195	R(1-C)	45	
17	75(2)	Butene-1	70.4	2.0	99.5	2975	----(3)	2.68	281	280	34	150	S(2)	75	Aborted - oxidizer flow transducer failure.
	76(2)	Butene-1	70.4	2.0	30.3	527	11.0	1.54	266	374	53	207	S(2)	325	Aborted - fuel diluted with GN <sub>2</sub> .
	77	Butene-1	70.4	4.0	94.4	2850	11.0	2.42	167	249	42	78	S(2)	270	
	78	Butene-1	70.4	4.0	92.5	3054	10.9	3.18	163	269	68	147	S(2)	75	Instability, 3100 cps oscillations, amplitude 45 psi.
	79	Butene-1	70.4	4.0	86.6	2779	11.1	2.56	172	521	75	163	S(2)	65	Instability, 3000 cps oscillations, amplitude 60 psi.
18	80	Butene-1	70.4	4.0	91.1	2920	10.9	2.69	162	218	52	71	S(2-A)	120	Instability, 3200 cps oscillations, amplitude 56 psi.
	81	Butene-1	70.4	4.0	89.4	2848	10.6	2.96	178	510	56	131	S(2-A)	90	Instability, 3100 cps oscillations, amplitude 23 psi.
	82	Butene-1	70.4	4.0	93.5	3073	10.4	3.43	163	209	45	106	S(2-A)	135	Instability, 3200 cps oscillations, amplitude 45 psi.
18	83	Butene-1	70.4	4.0	82.4	2618	11.3	2.70	158	273	48	88	R(2-B)	170	High frequency instability.
	84	Butene-1	70.4	4.0	91.8	2962	10.9	3.43	157	208	37	20	R(2-B)	125	High frequency instability.

(1) L\* = 27 inches unless noted.

(2) Data not reduced. Values shown are transient at the steadiest section of the test.

(3) Differential pressure transducers failed.

TABLE V.2. SUMMARY OF INJECTOR MODIFICATIONS

Injector	Number of Elements	Type of Elements	Fuel Orifice Diameter, in.	ACd <sub>f</sub> <sup>(1)</sup> , in.	Oxidizer Orifice Diameter, in.	ACd <sub>o</sub> <sup>(1)</sup> , in.	Number of Fuel Coolant Holes	Coolant Hole Diameter, in.	Faceplate
S(1)	232	Quadruplet	0.0145	0.056	0.028	0.199	40	0.0135	Solid nickel
S(1-A)	232	Quadruplet	0.0145	0.056	0.031	0.246	40	0.0135	Solid nickel
S(1-B)	229	Quadruplet with swirlers in 367 oxidizer orifices	0.0145	0.056	0.031 (91 orifices) 0.035 (367 orifices)	0.300	40	0.0135	Solid nickel
S(1-C)	225	Quadruplet	0.0145	0.050 <sup>(2)</sup>	0.038	0.457	40	0.0135	Solid nickel
S(2)	205	Pentad	0.022	0.066	0.028	0.317	40	0.0135	Solid nickel
S(2-A)	205	Pentad	0.025	0.084	0.033	0.410	40	0.020	Solid nickel
R(1)	241	Triplet	0.020	0.200	0.028	0.199	0	120 scfm - Rigimesh	
R(1-A)	241	120 Quadruplet and 121 Triplet	0.0135 (240 orifices) 0.018 (121 orifices)	0.079	0.038	0.450	0	30 scfm - Rigimesh	
R(1-B)	241	120 Quadruplet and 121 Triplet	0.018 (240 orifices) 0.025 (121 orifices)	0.092	0.038	0.430	0	30 scfm - Rigimesh	
R(1-C)	241	Triplet	0.018	0.120	0.038	0.430	0	60 scfm - Rigimesh	
R(2)	241	Triplet	0.018	0.069	0.028	0.213	0	30 scfm - Rigimesh	
R(2-A)	241 124	Oxidizer doublets Fuel doublets	0.021	0.105	0.028	0.213	0	60 scfm - Rigimesh	
R(2-B)	241	Triplet	0.024	0.083	0.038	0.506	38	0.016	Solid nickel

(1) Based on water flow calibrations.

(2) No modifications have been made to the fuel side of injector S(1). The decrease in ACd<sub>f</sub> was noted in water flow calibrations of modification S(1-C). Fuel pressure drops in tests with previous modifications of injector S(1) agreed with the initial value of ACd<sub>f</sub>.

Test series 1 and 2 were conducted using the solid face quadruplet injector, S(1), with propane and methane. Performance in both of these series was lower than expected. Attempts to correlate combustion efficiency with the JPL mixing parameters (Reference 10) were unsatisfactory; however, correlation of propellant injection conditions indicated that efficiency improved with increased fuel-to-oxidizer velocity and momentum ratios. High methane injection differential pressures were encountered. These were attributed to methane boiling within the fuel manifold, as had been predicted from the design studies (Section III). When high methane differential pressures were experienced in series 3 with injector R(1), which had a high-porosity Rigimesh faceplate, it was determined that frozen  $\text{CO}_2$  impurities in the methane were causing blocking. All methane used in later tests was scrubbed to reduce the  $\text{CO}_2$  content to less than 0.1%. This eliminated the excessive differential pressure in tests with Rigimesh face injectors; however, test series 6 with injector S(1-B) confirmed that methane boiling did occur in the solid face injectors.

After these initial tests, injectors S(1) and R(1) were modified by enlarging the oxidizer orifices to decrease the oxidizer injection velocity and thereby increase fuel-to-oxidizer momentum ratio. To improve fuel distribution and produce higher fuel velocities, the 120-scfm Rigimesh faceplate of injector R(1) was replaced with a 30-scfm plate. Later tests, series 10 through 12, showed that as testing progressed the porosity of the 30-scfm Rigimesh faceplate decreased due to high temperature effects. A comparison of water calibrations performed before series 10 and after series 11 showed that the Rigimesh flow area had decreased 85% during these tests. This reduction resulted in methane boiling within the injector during series 12. The use of 60-scfm Rigimesh faceplates in later injectors provided satisfactory cooling and negligible performance loss due to poor methane distribution. In test series 13 a self-impinging doublet injector was fabricated by installing a new faceplate on injector R(2). The doublet injector R(2-A) was tested to determine if improved performance could be obtained by vaporizing the propellants before mixing. At equal momentum ratios, performance with this injector was not improved over the unlike-impinging designs. Because element spacing is critical in self-impinging injectors, performance improvements might have been attained by additional experimentation.

Other than freezing the  $\text{CO}_2$  and determining the correct Rigimesh porosity, the only other problem experienced in the methane tests was obtaining satisfactory supply line temperatures. To obtain line temperatures below  $200^\circ\text{R}$  while staying above methane's  $163^\circ\text{R}$  freezing point, it was necessary to precool the vacuum-jacketed supply line with liquid nitrogen ( $140^\circ\text{R}$ ) and then warm the line with a gaseous nitrogen purge. Several tests were aborted when gaseous nitrogen trapped in the line reduced the fuel flow and, therefore, chamber pressure. This problem was eliminated by revising the pretest line filling procedures.

Test series 4 indicated that the higher momentum ratios of injector S(1-A) provided increased performance with propane, but combustion efficiency was still below 95% at the theoretical optimum mixture ratio. Single element water flow investigations had indicated that when swirlers were used in opposing orifices the resulting spray fan was in a plane passing through the centers of the two holes. This is in comparison to the perpendicular fan usually produced. When swirlers were used in the oxidizer orifices of a quadruplet element, the resulting fuel and oxidizer fans were parallel. It was believed that parallel fans would produce a better mixture ratio distribution, and swirlers were added to the oxidizer orifices of this injector (see Section III). The quadruplet injector with swirlers, S(1-B), was tested with propane in series 7. The swirlers did not produce any performance improvement when compared at equal momentum ratios and they were removed for subsequent tests.

Propane tests with the triplet element Rigimesh injector R(2), series 8, substantiated the correlation of combustion efficiency and momentum ratio previously obtained; however, mild high frequency instability was encountered. Because data obtained in other test programs indicated that quadruplet elements were inherently more stable than triplet elements (Reference 16), the next Rigimesh injector modification was designed with a combination of triplet and quadruplet elements. Injector R(1-A) included 121 triplet and 120 quadruplet elements. This was the largest number of quadruplet elements that could be included due to the design of the injector body. Because of a change in emphasis from propane to butene-1, the triplet-quadruplet injector was never tested with propane. No stability problems were encountered with methane in any tests, hence the effect of this element change on stability could not be evaluated.

The first series of butene-1 tests, series 9, was made with injector S(1-C) and experienced severe high-frequency instability. All tests in series 15, using butene-1 in the Rigimesh face injector, R(1-C), were stable, but performance was low due to excessive flow of butene-1 through the faceplate. The high flow through the Rigimesh occurred because butene-1 transpires as a liquid or dense gas as compared to more volatile methane, which vaporizes within the Rigimesh and thus reduces the flow rate. A second solid face injector, S(2), was fabricated for butene-1 testing. This injector used a pentad element configuration to provide high momentum ratios while maintaining approximately equal fuel and oxidizer orifice diameters. In five butene-1 tests with this injector, high-frequency instability was encountered in all but one test. Examination of these data and data from other butene-1 tests produced one similarity. All tests with fuel velocities less than 125 ft/sec were stable, whereas all tests with fuel velocities above 140 ft/sec were unstable. The fuel and oxidizer orifices of pentad injector S(2) were enlarged to reduce fuel velocity to below 125 ft/sec while maintaining momentum ratios approximately equal to the initial configuration.

All firings during test series 17 with the modified pentad injector were highly unstable. Performance from both series of tests provided the same correlation with momentum ratio, indicating that the 0.025-inch diameter fuel holes used in the modified pentad injector were still below the value where fuel vaporization controls the reaction. A third injector was fabricated for use with liquid butene-1 by replacing the Rigimesh faceplate of injector R(2-A) with a solid nickel plate. This injector, R(2-B), had fuel velocities similar to injector S(2-A) and was drilled in a triplet pattern. Both tests made with this injector (series 18) experienced high-frequency instability, which resulted in some faceplate erosion.

## B. TEST PERFORMANCE

Table V-3 presents calculated performance data and table V-4 contains data relative to correlation of injector performance for the uncooled sea level tests. Performance calculations were made using methods described in Appendix A. In some tests, combustion instability was present and a deviation in characteristic velocity efficiency based on chamber pressure,  $\eta_{c^*_{Pc(cor)}}$ , and characteristic velocity efficiency based on thrust,  $\eta_{c^*_{F(cor)}}$ , of 5 to 7% was calculated. In stable tests, the difference in  $\eta_{c^*_{Pc(cor)}}$  and  $\eta_{c^*_{F(cor)}}$  was usually less than 2%. Because of the relatively slow response of the transducers and load cells used for steady-state data measurements, all data obtained in unstable tests are of questionable validity; but in these cases performance data based on thrust measurements are usually more indicative than those based on chamber pressure.

Figures V-2, V-3, and V-4 show theoretical characteristic exhaust velocities, corrected characteristic exhaust velocities, and characteristic exhaust velocity efficiencies for methane, propane, and butane-1 with their respective optimum flox mixtures. For the stable tests, these data are based on chamber pressure measurements corrected for momentum and heat losses,  $c^*_{Pc(cor)}$ . For the unstable tests, the data are based on thrust measurements corrected for the same losses,  $c^*_{F(cor)}$ . With methane and butene-1, characteristic velocities up to 95% of the maximum theoretical value were measured. For both of these fuels the peak experimental values occurred at mixture ratios below the theoretical optimum. The peak values could probably be moved closer to the theoretical optimum mixture ratio with additional injector development aimed at improving mixing within and between elements. Tests at two different  $L^*$ 's with flox/methane in injector R(1-A) indicated no appreciable increase in  $\eta_{c^*}$  from doubling  $L^*$  above the initial value of 27. This is taken to be an indication that the performance is limited by reaction product mixing rather than propellant vaporization. Performance attained with propane is not as high as that of the other fuels because testing with propane was discontinued before the high-momentum-ratio injectors were fabricated.



TABLE V-3. CALCULATED PERFORMANCE DATA — UNCOOLED  
SEA LEVEL TESTS

Series No.	Test No.	Fuel	r	$\dot{V}_p$ , lb/sec	$c^*$ , ft/sec	$I_{sl}$ , sec	$C_F$	$c^*_{P_c}$ , ft/sec	$c^*_{P_F}$ , ft/sec	Q, Btu/sec	$\eta_{c^*P_c}$	$\eta_{c^*P_F}$	$\eta_{c^*P_{c(cor)}}$	$\eta_{c^*P_{F(cor)}}$	$I_{sl}$ , sec	$\eta_{I_s}$	$\eta_{I_{s(cor)}}$	$C_F$	$\eta_{C_F}$	$\eta_{C_{F(cor)}}$	$\Delta t$ Used, <sup>(1)</sup> sec
1	1	Propane	3.53	14.0	6673	244	1.181	6669	6177	550	0.969	0.926	0.950	0.935	217	0.887	0.928	1.078	0.922	0.984	0.7
	2	Propane	3.39	13.7	6653	243	1.168	6597	6372	479	0.992	0.958	0.973	0.968	223	0.962	1.009	0.932	0.996	2.1	
	3	Propane	3.88	13.8	6747	245	1.162	6367	6124	437	0.944	0.908	0.927	0.917	213	0.872	0.912	1.078	0.928	0.988	0.6
	4	Propane	4.09	13.7	6784	244	1.153	6244	5999	447	0.921	0.884	0.903	0.894	207	0.851	0.891	1.069	0.927	0.989	0.7
	5	Propane	4.92	13.7	6764	239	1.142	6002	5749	464	0.887	0.850	0.877	0.859	197	0.822	0.862	1.055	0.924	0.980	1.9
2	6	Methane	6.26	13.0	6906	248	1.153	6545	6229	826	0.948	0.902	0.922	0.912	215	0.869	0.911	1.058	0.918	0.989	0.5
	7	Methane	5.87	13.2	6956	250	1.155	6515	6287	772	0.935	0.903	0.914	0.912	218	0.870	0.912	1.075	0.931	0.998	1.4
	8	Methane	5.67	13.3	6985	251	1.157	6503	6270	750	0.931	0.898	0.909	0.907	217	0.866	0.907	1.076	0.930	0.998	2.3
3	9	Methane	4.22	14.0	6818	249	1.170	6413	6089	750	0.941	0.893	0.917	0.903	214	0.858	0.901	1.072	0.916	0.985	0.5
	11	Methane	5.98	13.1	6946	247	1.141	6281	5986	765	0.904	0.862	0.882	0.871	205	0.831	0.871	1.049	0.919	0.988	1.7
	12	Methane	7.57	12.3	6737	223	1.062	5359	5000	750	0.795	0.742	0.775	0.753	159	0.710	0.747	0.953	0.897	0.971	6.2
4	14	Propane	4.34	13.7	6823	246	1.159	6350	6048	550	0.931	0.886	0.913	0.900	210	0.855	0.895	1.065	0.919	0.981	1.9
	16	Propane	3.55	14.0	6675	245	1.169	6486	6283	550	0.972	0.941	0.956	0.951	221	0.901	0.943	1.094	0.935	0.995	2.0
	17	Propane	3.95	13.6	6762	245	1.160	6420	6180	400	0.949	0.914	0.936	0.923	215	0.879	0.919	1.077	0.929	0.986	3.0
	18	Propane	4.87	13.5	6779	241	1.149	6224	5931	400	0.918	0.875	0.904	0.884	204	0.846	0.886	1.056	0.919	0.977	1.5
5	19	Methane	4.50	13.6	6854	250	1.163	6484	6264	800	0.946	0.914	0.931	0.925	219	0.876	0.918	1.085	0.932	0.993	1.5
	20	Methane	5.16	13.3	6943	247	1.141	6186	6006	800	0.891	0.865	0.877	0.875	205	0.832	0.873	1.069	0.936	0.999	0.9
	21	Methane	6.01	13.1	6945	240	1.113	5795	5648	800	0.834	0.813	0.822	0.824	188	0.783	0.823	1.045	0.939	1.002	0.4
6	22	Methane	9.20	12.2	6146	206	1.078	5610	5412	1000	0.913	0.880	0.904	0.910	177	0.859	0.910	1.014	0.961	1.007	1.9
	23	Methane	8.98	12.2	6203	212	1.099	5894	5756	1000	0.950	0.928	0.939	0.946	189	0.894	0.946	1.032	0.975	1.026	2.9
	24	Methane	10.7	12.1	5744	190	1.063	5400	5339	1000	0.941	0.929	0.939	0.951	169	0.894	0.951	1.010	0.950	1.013	0.9
7	25	Propane	3.74	13.4	6704	241	1.149	6254	6125	500	0.933	0.914	0.918	0.923	211	0.874	0.916	1.086	0.945	1.005	0.9
	26	Propane	4.33	12.9	6828	244	1.148	6455	6246	500	0.945	0.915	0.935	0.924	215	0.882	0.923	1.072	0.933	0.988	0.4
	27	Propane	4.75	13.0	6796	238	1.130	6121	5895	500	0.901	0.867	0.890	0.877	200	0.838	0.879	1.049	0.928	0.985	0.5
8	28	Propane	2.63	13.7	6661	232	1.155	6287	6121	350	0.973	0.948	0.953	0.957	212	0.914	0.957	1.085	0.940	1.004	1.9
	29	Propane	3.56	13.1	6671	242	1.158	6206	6011	350	0.930	0.901	0.915	0.910	209	0.863	0.902	1.083	0.935	0.991	0.9
	31	Propane	4.28	13.4	6816	243	1.145	6181	5901	1100	0.907	0.866	0.895	0.866	203	0.834	0.876	1.055	0.921	0.981	1.0
	32	Propane	2.93	14.2	6567	232	1.137	5738	5490	1100	0.874	0.836	0.864	0.848	187	0.808	0.850	1.049	0.923	0.982	0.9
	33	Propane	3.18	12.7	6624	234	1.136	6384	6177	1100	0.964	0.932	0.954	0.946	210	0.898	0.945	1.059	0.932	0.992	0.7
9	34	Butene-1	2.80	13.7	6463	233	1.146	6008	5861	1000	0.930	0.907	0.914	0.921	201	0.865	0.909	1.078	0.941	1.007	0.5
	35	Butene-1	3.25	13.7	6603	235	1.140	5897	5724	1000	0.893	0.867	0.880	0.879	196	0.833	0.875	1.067	0.936	0.998	1.1
	36	Butene-1	4.20	15.0	6686	242	1.162	5882	6034	1400	0.880	0.902	0.868	0.917	210	0.868	0.913	1.151	0.990	1.056	2.6
	37	Butene-1	4.61	15.8	6574	241	1.173	5758	5839	1400	0.876	0.888	0.867	0.902	206	0.852	0.900	1.149	0.979	1.040	2.0
10	38	Methane	8.13	12.1	6424	213	1.064	5495	5334	700	0.855	0.830	0.842	0.843	170	0.797	0.835	0.993	0.934	1.001	1.3
	39	Methane	6.39	13.7	6874	246	1.153	6230	5963	700	0.906	0.867	0.893	0.877	206	0.837	0.877	1.065	0.923	0.983	0.9
	40	Methane	5.69	13.4	6985	252	1.158	6482	6194	700	0.928	0.887	0.911	0.896	215	0.855	0.896	1.068	0.922	0.984	1.3
	41	Methane	4.99	13.3	6950	252	1.167	6719	6478	700	0.967	0.932	0.953	0.942	227	0.900	0.942	1.086	0.930	0.989	2.2
11	43	Methane	6.18	13.4	6914	248	1.152	6350	6102	750	0.918	0.883	0.903	0.893	211	0.851	0.893	1.068	0.927	0.989	0.8
	44	Methane	5.70	13.3	6990	254	1.166	6695	6501	750	0.958	0.930	0.947	0.940	227	0.897	0.940	1.093	0.937	0.992	0.4
	45	Methane	5.10	13.3	6956	250	1.158	6486	6303	750	0.932	0.906	0.925	0.917	219	0.874	0.916	1.086	0.938	0.991	0.7
	46	Methane	4.89	12.8	6935	249	1.155	6687	6495	750	0.964	0.937	0.955	0.947	225	0.904	0.948	1.082	0.937	0.992	1.6
12	47	Methane	10.9	12.9	5790	188	1.047	4914	4685	650	0.849	0.809	0.838	0.824	147	0.778	0.824	0.960	0.916	0.983	0.8
	48	Methane	6.64	13.5	6814	237	1.117	5687	5380	600	0.835	0.789	0.820	0.799	180	0.760	0.799	1.019	0.912	0.975	1.2
	49	Methane	8.72	14.3	6275	217	1.116	5315	5019	600	0.847	0.800	0.835	0.810	168	0.772	0.813	1.015	0.910	0.970	2.2
13	50	Methane	6.20	13.0	6905	235	1.096	5514	5160	575	0.799	0.747	0.784	0.757	169	0.719	0.757	0.986	0.901	0.966	1.6
	51	Methane	5.70	13.0	6971	238	1.097	5570	5083	575	0.799	0.729	0.783	0.738	167	0.702	0.738	0.964	0.880	0.944	2.0
	52	Methane	5.03	12.9	6945	241	1.118	5913	5536	575	0.851	0.797	0.837	0.806	185	0.768	0.806	1.008	0.902	0.963	0.9
	53	Methane	4.17	13.1	6933	242	1.141	6200	5835	575	0.907	0.854	0.893	0.862	200	0.825	0.867	1.036	0.908	0.966	1.4
	54	Methane	3.89	13.2	6785	242	1.148	6282	5935	575	0.926	0.875	0.913	0.883	204	0.844	0.886	1.046	0.911	0.967	0.6
	55	Methane	3.56	13.2	6735	240	1.146	6286	5916	575	0.933	0.878	0.919	0.886	203	0.847	0.887	1.040	0.908	0.964	2.7
14	56	Methane	6.40	13.6	6873	246	1.151	6246	6027	700	0.909	0.877	0.896	0.887	208	0.846	0.887	1.072	0.931	0.993	0.6
	57	Methane	6.01	13.8	6942	249	1.155	6265	6100	700	0.902	0.879	0.886	0.888	211	0.848	0.888	1.085	0.939	1.003	2.4
	58	Methane	5.45	13.8	6982	254	1.172	6563	6353	700	0.940	0.910	0.927	0.920	223	0.878	0.919	1.095	0.935	0.993	0.8
	59	Methane	4.52	15.0	6895	252	1.175	6527	6306	700	0.947	0.915	0.933	0.923	222	0.884	0.926	1.096	0.933	0.990	0.9
	60	Methane	4.37	13.7	6873	251	1.176	6661	6486	700	0.969	0.944									

other data due to excessive fuel flow through the porous faceplate. Other methods of correlating efficiency, such as velocity ratio or mixing parameters, did not produce satisfactory results. The importance of high momentum ratio is attributed to the criticality of mixing on performance with the flox/light hydrocarbon combinations. At equal momentum ratios, no difference in performance was noted for the three unlike impinging elements tested.

TABLE V-4. INJECTOR PERFORMANCE COMPARISON —  
UNCOOLED SEA LEVEL TESTS

Series No.	Test No.	Fuel	Injector	$\dot{w}_f$ , lb/sec	$\dot{w}_o$ , lb/sec	$ACd_f$ , in <sup>2</sup>	$ACd_o$ , in <sup>2</sup>	$V_f$ , <sup>(1)</sup> ft/sec	$V_o$ , <sup>(1)</sup> ft/sec	$\dot{w}_f V_f$ , <sup>(1)</sup> lb-ft/sec <sup>2</sup>	$\dot{w}_o V_o$ , <sup>(1)</sup> lb-ft/sec <sup>2</sup>	$V_f/V_o$ , <sup>(1)</sup>	$\dot{w}_f V_f / \dot{w}_o V_o$ , <sup>(1)</sup>	$\eta_c \cdot P_{c(cor)}$	$r$
1	1	Propane	S(1)	3.09	10.9	0.056	0.199	190	92.8	588	978	2.05	0.602	0.950	3.53
	2	Propane	S(1)	3.12	10.6	0.056	0.199	190	89.8	595	952	2.11	0.625	0.973	3.39
	3	Propane	S(1)	2.83	11.0	0.056	0.199	179	92.9	507	1022	1.93	0.495	0.927	3.88
	4	Propane	S(1)	2.68	11.0	0.056	0.199	166	92.5	445	1018	1.80	0.437	0.903	4.09
	5	Propane	S(1)	2.32	11.4	0.056	0.199	143	94.0	332	1072	1.52	0.310	0.877	4.92
2	6	Methane	S(1)	1.80	11.2	0.056	0.199	177	93.0	318	1042	1.90	0.305	0.922	6.26
	7	Methane	S(1)	1.92	11.3	0.056	0.199	188	92.3	362	1062	2.04	0.347	0.914	5.87
	8	Methane	S(1)	1.99	11.3	0.056	0.199	189	93.3	376	1055	2.02	0.355	0.909	5.67
3	9	Methane	R(1)	2.68	11.3	0.200	0.199	70.9	94.0	190	1062	0.76	0.179	0.917	4.22
	11	Methane	R(1)	1.88	11.2	0.200	0.199	51.0	92.4	96	1035	0.55	0.093	0.882	5.98
	12	Methane	R(1)	1.44	10.9	0.200	0.199	38.2	90.3	56.5	983	0.42	0.058	0.775	7.57
4	14	Propane	S(1-A)	2.56	11.1	0.056	0.246	153	76.1	392	844	2.01	0.463	0.913	4.34
	16	Propane	S(1-A)	3.08	10.9	0.056	0.246	189	75.2	582	820	2.52	0.710	0.956	3.55
	17	Propane	S(1-A)	2.75	10.8	0.056	0.246	171	74.9	470	809	2.29	0.581	0.936	3.95
	18	Propane	S(1-A)	2.31	11.2	0.056	0.246	145	77.2	335	864	1.87	0.388	0.904	4.87
5	19	Methane	R(2)	2.46	11.1	0.069	0.213	193	82.4	475	912	2.34	0.521	0.931	4.50
	20	Methane	R(2)	2.16	11.1	0.069	0.213	170	83.9	367	933	2.03	0.393	0.877	5.16
	21	Methane	R(2)	1.86	11.2	0.069	0.213	152	84.9	284	950	1.79	0.298	0.822	6.01
6	22	Methane	S(1-B)	1.20	11.0	0.056	0.300	116	59.1	140	653	1.98	0.219	0.904	9.20
	23	Methane	S(1-B)	1.23	11.0	0.056	0.300	119	58.6	148	648	2.04	0.231	0.939	8.98
	24	Methane	S(1-B)	1.04	11.1	0.056	0.300	103	59.0	108	645	1.75	0.164	0.939	10.7
7	25	Propane	S(1-B)	2.84	10.6	0.056	0.300	176	61.5	501	654	2.87	0.765	0.918	3.74
	26	Propane	S(1-B)	2.43	10.5	0.056	0.300	147	61.4	358	647	2.40	0.554	0.935	4.33
	27	Propane	S(1-B)	2.25	10.7	0.056	0.300	142	62.3	321	666	2.29	0.481	0.890	4.75
8	28	Propane	R(2)	3.78	9.94	0.069	0.213	181	80.3	683	799	2.25	0.859	0.953	2.63
	29	Propane	R(2)	3.08	11.0	0.069	0.213	149	87.3	460	958	1.71	0.481	0.915	3.56
	31	Propane	R(2)	2.56	10.9	0.069	0.213	125	88.4	317	962	1.41	0.329	0.895	4.28
	32	Propane	R(2)	3.62	10.6	0.069	0.213	180	87.2	650	924	2.06	0.704	0.864	2.93
	33	Propane	R(2)	3.05	9.69	0.069	0.213	154	80.0	468	775	1.92	0.604	0.954	3.18
9	34	Butene-1	S(1-C)	3.62	10.1	0.050	0.457	217	38.5	785	390	5.64	2.013	0.914	2.80
	35	Butene-1	S(1-C)	3.24	10.5	0.050	0.457	189	39.4	612	414	4.80	1.481	0.880	3.25
	36	Butene-1	S(1-C)	2.87	12.1	0.050	0.457	171	46.4	493	560	3.70	0.882	0.868	4.20
	37	Butene-1	S(1-C)	2.83	13.0	0.050	0.457	171	51.4	483	669	3.32	0.722	0.867	4.61
10	38	Methane	R(1-A)	1.33	10.8	0.079	0.450	91	40.0	121	433	2.28	0.281	0.842	8.13
	39	Methane	R(1-A)	1.86	11.9	0.079	0.450	127	43.4	236	514	2.93	0.459	0.893	6.39
	40	Methane	R(1-A)	2.00	11.4	0.079	0.450	134	42.3	268	481	3.18	0.559	0.911	5.69
	41	Methane	R(1-A)	2.22	11.1	0.079	0.450	151	41.7	336	463	3.63	0.728	0.953	4.99
11	43	Methane	R(1-A)	1.87	11.6	0.079	0.450	126	42.9	236	496	2.94	0.476	0.903	6.18
	44	Methane	R(1-A)	1.98	11.3	0.079	0.450	135	42.1	268	476	3.21	0.563	0.947	5.70
	45	Methane	R(1-A)	2.19	11.2	0.079	0.450	150	41.8	327	466	3.5 <sup>a</sup>	0.702	0.925	5.10
	46	Methane	R(1-A)	2.18	10.6	0.079	0.450	150	39.8	327	424	3.77	0.774	0.955	4.89
12	47	Methane	R(1-B)	1.09	11.8	0.092	0.430	67.1	45.5	73.2	539	1.48	0.137	0.838	10.9
	48	Methane	R(1-B)	1.77	11.7	0.092	0.430	102	44.9	180	528	2.27	0.344	0.820	6.64
	49	Methane	R(1-B)	1.47	12.8	0.092	0.430	85.3	49.4	125	633	1.73	0.199	0.835	8.72
13	50	Methane	R(2-A)	1.81	11.2	0.105	0.213	94.0	89.1	170	1000	1.06	0.171	0.784	6.20
	51	Methane	R(2-A)	1.94	11.0	0.105	0.213	100	88.4	194	977	1.13	0.162	0.783	5.70
	52	Methane	R(2-A)	2.15	10.8	0.105	0.213	110	86.0	236	928	1.28	0.199	0.837	5.03
	53	Methane	R(2-A)	2.54	10.6	0.105	0.213	131	84.8	332	897	1.55	0.371	0.893	4.17
	54	Methane	R(2-A)	2.69	10.5	0.105	0.213	139	84.1	374	883	1.65	0.425	0.913	3.89
	55	Methane	R(2-A)	2.89	10.3	0.105	0.213	150	82.8	431	851	1.81	0.507	0.919	3.56
	56	Methane	R(1-C)	1.84	11.8	0.120	0.430	84.1	45.9	155	541	1.83	0.286	0.894	6.40
14	57	Methane	R(1-C)	1.96	11.8	0.120	0.430	90.3	45.7	177	538	1.98	0.330	0.886	6.01
	58	Methane	R(1-C)	2.14	11.7	0.120	0.430	99.2	45.0	213	525	2.21	0.405	0.927	5.45
	59	Methane	R(1-C)	2.54	11.4	0.120	0.430	117	44.2	299	506	2.65	0.590	0.933	4.52
	60	Methane	R(1-C)	2.55	11.2	0.120	0.430	115	43.2	293	483	2.65	0.608	0.955	4.37
	61	Methane	R(1-C)	2.90	11.1	0.120	0.430	130	43.0	377	478	3.02	0.794	0.979	3.82
	62	Methane	R(1-C)	2.37	11.7	0.120	0.430	106	45.3	251	532	2.33	0.471	0.921	4.95
	63	Butene-1	R(1-C)	2.13	10.9	0.120	0.430	62.7	44.6	134	486	1.41	0.277	0.852	5.15
	64	Butene-1	R(1-C)	2.15	10.8	0.120	0.430	64.6	44.5	140	479	1.46	0.292	0.817	5.02
	65	Butene-1	R(1-C)	2.83	10.6	0.120	0.430	88.0	42.9	254	456	2.05	0.556	0.912	3.85
	66	Butene-1	R(1-C)	3.32	10.6	0.120	0.430	104	43.2	347	459	2.41	0.759	0.929	3.21
15	67	Butene-1	R(1-C)	2.91	10.6	0.120	0.430	94.9	42.8	276	454	2.22	0.607	0.885	3.65
	68	Butene-1	R(1-C)	3.13	10.4	0.120	0.430	94.8	42.8	297	446	2.22	0.665	0.918	3.33
	69	Butene-1	R(1-C)	3.66	10.5	0.120	0.430	119	42.6	437	449	2.80	0.976	0.934	2.88
	70	Butene-1	R(1-C)	4.04	10.2	0.120	0.430	131	41.2	530	420	3.18	1.261	0.954	2.53
	71	Butene-1	R(1-C)	2.95	11.1	0.120	0.430	79.5	44.3	238	490	1.79	0.485	0.687	3.80
	72	Butene-1	R(1-C)	3.39	10.2	0.120	0.430	86.3	40.5	293	414	2.13	0.709	0.941	3.01
	73	Butene-1	S(2)	2.72	11.0	0.066	0.317	125	60.0	341	657	2.08	0.519	0.922	4.03
	74	Butene-1	S(2)	3.18	10.9	0.066	0.317	149	59.7	473	650	2.49	0.728	0.888	3.43
	75	Butene-1	S(2)	2.56	11.1	0.066	0.317	151	61.3	388	682	2.47	0.569	0.852	4.34
	76	Butene-1	S(2-A)	2.69	10.9	0.084	0.410	93.9	46.0	253	506	2.03	0.499	0.892	4.07
16	77	Butene-1	S(2-A)	2.96	10.6	0.084	0.410	134	47.0	402	499	2.86	0.806	0.880	3.61
	78	Butene-1	S(2-A)	3.43	10.4	0.084	0.410	119	44.9	408	469	2.65	0.870	0.919	3.05
	79	Butene-1	S(2-A)	2.70	11.3	0.083	0.506	96.3	38.5	261	435	2.50	0.600	0.787	4.20
17	80	Butene-1	R(2-B)	3.43	10.9	0.083	0.506	122	36.8	418	400	1.07	1.046	0.869	3.17
	81	Butene-1	R(2-B)	3.43	10.9	0.083	0.506	122	36.8	418	400	1.07	1.046	0.869	3.17

(1) Velocities are based on injector water flow.

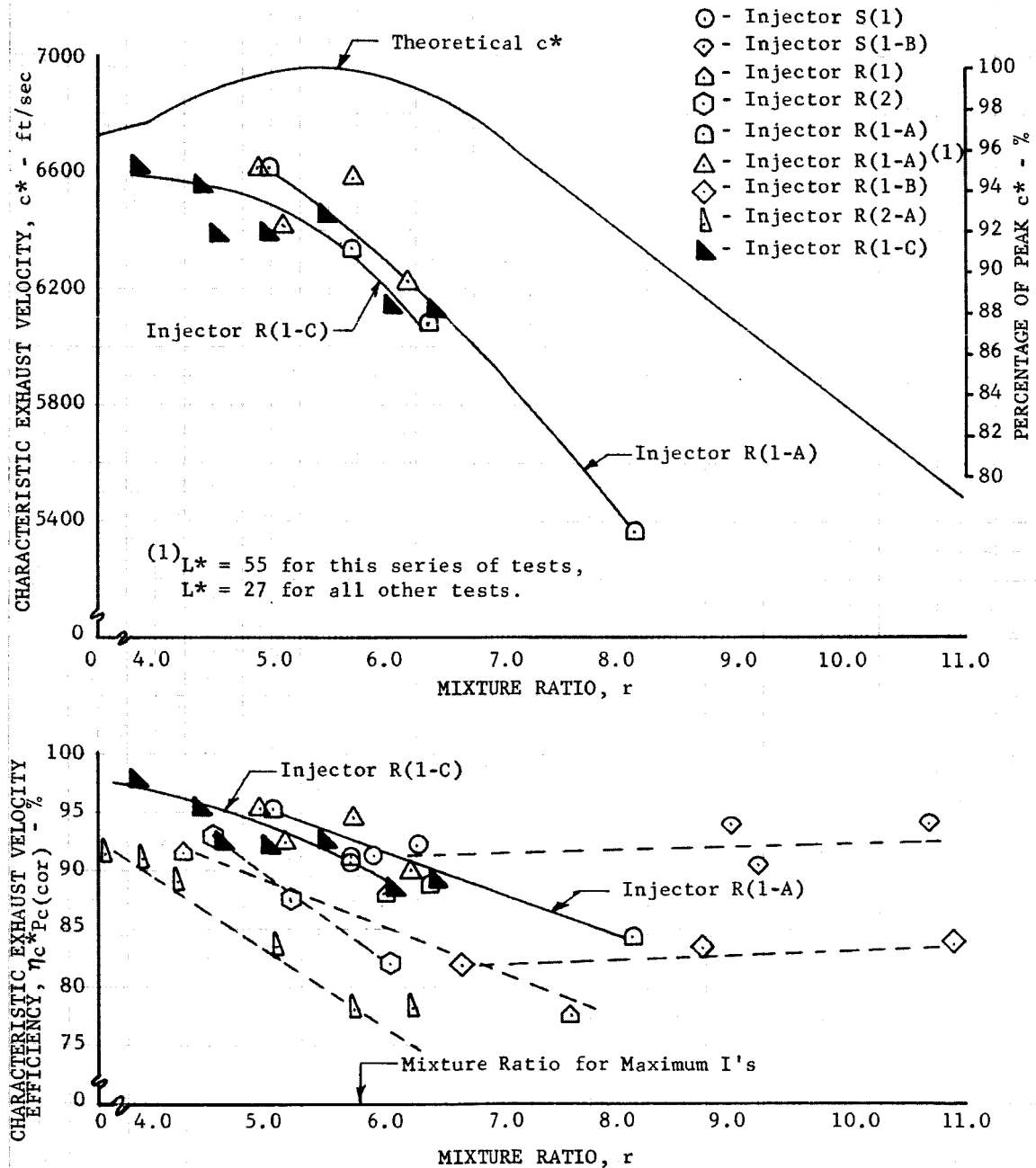


Figure V-2. Flox/Methane Characteristic Exhaust Velocity,  
82.6% Fluorine in Flox

DF 49022

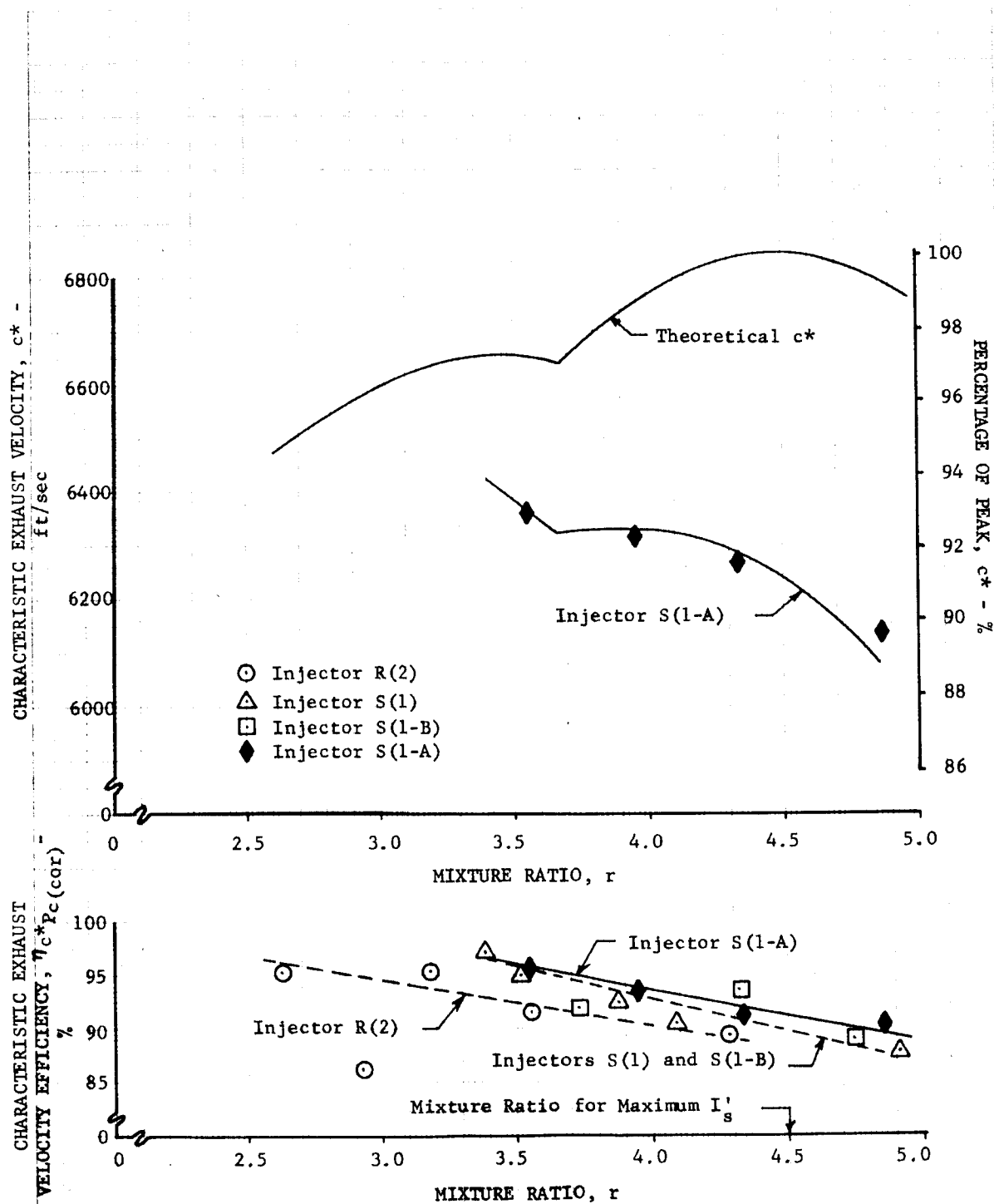


Figure V-3. Flox/Propane Characteristic Exhaust Velocity,  
76% Fluorine in Flox

DF 45936B

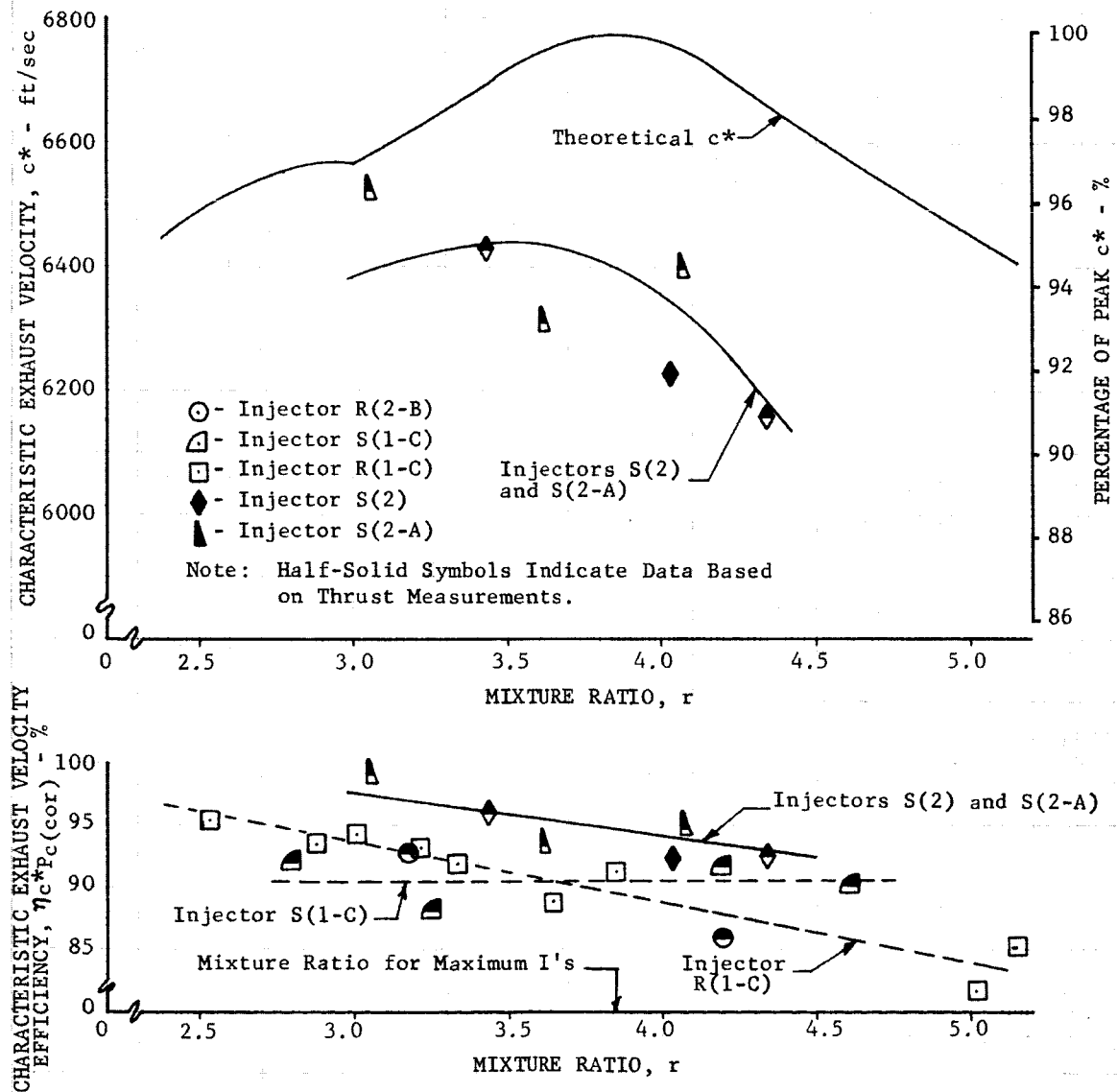


Figure V-4. Flox/Butene-1 Characteristic Exhaust Velocity,  
70.4% Fluorine in Flox

DF 53506A

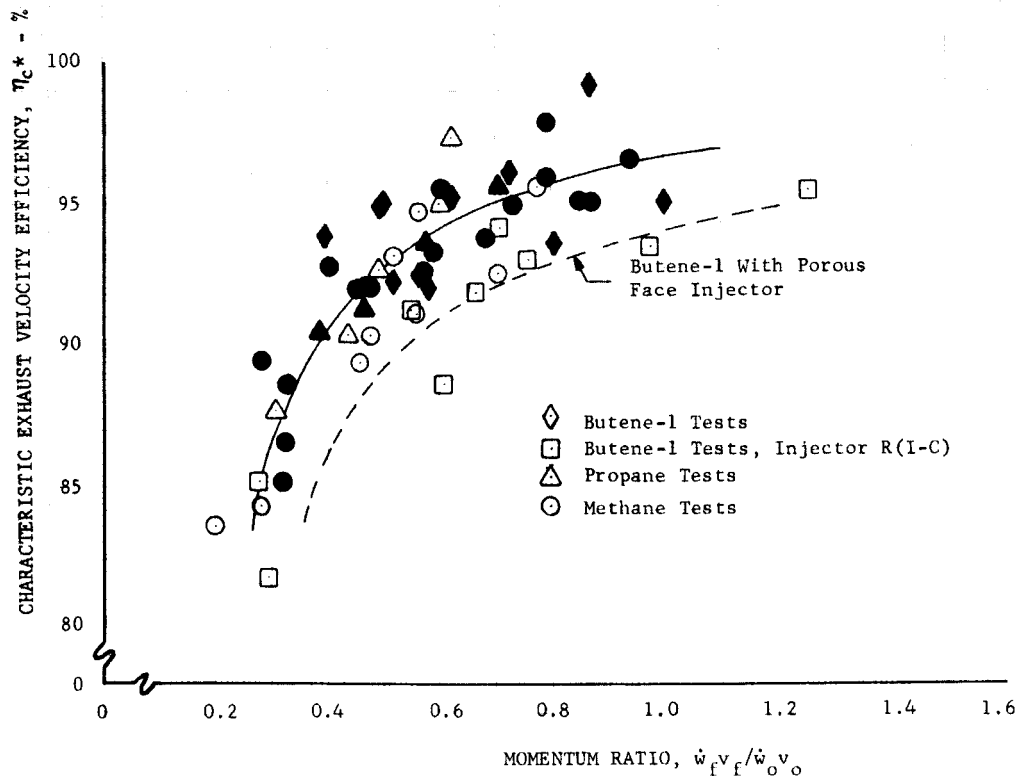


Figure V-5. Characteristic Exhaust Velocity Efficiency vs Momentum Ratio DF 53505

### C. IGNITION

Reliable hypergolic ignition was obtained in all tests. Ignition was followed by a smooth rise in chamber pressure; no pressure spikes occurred during ignition on any tests. Ignition delays were given in table V-1 for the sea level tests. The delay times were measured from the time that the oxidizer (lagging propellant) valve began to open until ignition. Delay time, therefore, includes injector fill time (20 milliseconds or more depending upon nitrogen purge rates). Ignition delays ranged from 45 to 325 milliseconds. Only three tests showed delays over 140 milliseconds, and these are attributed to gaseous nitrogen being left in the run line from the pretest purge. Previous hypergolicity studies on flox/light hydrocarbon propellants (Reference 17) using single element subscale injectors, showed a definite correlation of delay time and mixture ratio. No relationship was found for these full-scale tests. This was expected because mixture ratios during the start transient can vary considerably from the programed steady-state mixture ratio. In addition, with multielement injectors there is a variation in mixture ratio across the injector face during the start transient due to manifold filling and temperature variations. While these variations preclude the correlation of ignition data, they increase the reliability of obtaining hypergolic conditions in a multielement injector.

#### D. COMBUSTION STABILITY

Combustion was stable in 69 of the 84 sea level tests. Of the 15 unstable tests, 2 were with propane and the remainder were with butene-1. Combustion was stable during all flox/methane tests.

Several tests with propane experienced mild instability during the start transient. This instability attenuated and combustion was stabilized as chamber pressure approached the steady-state value (less than 1.0 sec). The propane tests in which instability occurred during steady-state operation were characterized by low fuel differential pressures. The low injector drops were caused by fuel leaks around the faceplate retaining screws that were used in early porous face injectors. It was concluded that the screws were loosened by oscillations during the start transient. The continued instability after the start transient may have been caused by the low fuel differential pressure and poor distribution.

Thirteen of the 26 flox/butene-1 tests were highly unstable. High response chamber pressure measurements indicated primary instability of 2900 to 3200 cps (first tangential mode) with peak-to-peak amplitudes up to 130 psi. Lower amplitude harmonics of this mode were also recorded. Figure V-6 shows a typical frequency-amplitude plot from one of the butene-1 tests. Because the most volatile fuel (methane) was surprisingly stable and the next most volatile fuel (propane) was slightly less stable, several tests were made with ambient temperature butene-1. By increasing the butene-1 inlet temperature from the normal operating temperature of 180°R to a temperature of 530°R, the amount of liquid subcooling was reduced from 415°R to 65°R (compared to 75°R for methane and 335°R for propane). No stability improvement was found. Because of the limited amount of data, other methods of correlating the occurrence of instability were unsatisfactory. The fact that all butene-1 tests with the porous face injectors were stable is probably connected with the breakup in energy pattern caused by the somewhat random flow through the injector face.

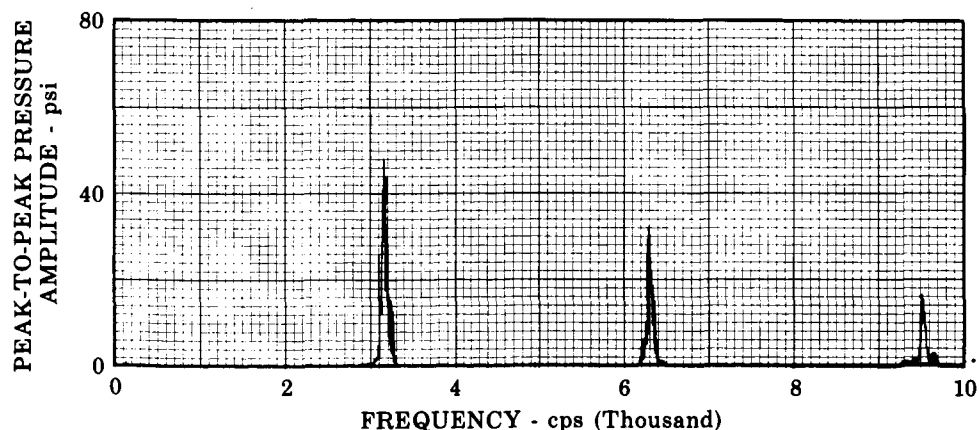


Figure V-6. Typical Frequency-Amplitude Relationship From Unstable Flox/Butene-1 Test (Test No. 78)

FD 19760

## E. HEAT TRANSFER

Figures V-7 through V-10 compare measured heat transfer coefficients with those predicted using the Bartz short form equation, Reference 14. Film coefficients were not calculated for all sea level tests; however, a representative range of data was covered. Additional data for methane and butene-1 are presented in the discussion of the uncooled altitude tests, Section VI. The results of these data are similar to those obtained with the gaseous hydrocarbon fuels under Contract NAS3-4195, Reference 1. In most cases, the film coefficient reaches a maximum upstream of the throat and has a maximum value well below the predicted maximum. Heat transfer rates with butene-1 using the solid face pentad injector were significantly higher than the Bartz predictions throughout the chamber, figure V-10. This is probably due to the greater impingement angle used in this injector (90 degrees compared with approximately 55 degrees in other injectors) and the pentad element design that surrounds the fuel streams with oxidizer. Tests with this injector had significantly less carbon deposition on the walls than other butene-1 tests.

Table V-5 compares measured and predicted heat transfer rates for the same sea level tests shown in figures V-7 through V-10 and for all uncooled simulated altitude tests. These rates are for heat transferred to the copper chambers and include the copper expansion section downstream of the throat. Figure V-11 shows the ratios of experimental-to-predicted heat transfer rates plotted as functions of mixture ratio for methane, propane, and butene-1. The "X" on each curve shows the interpolated value of the measured-to-predicted total heat transfer rate at each fuel's respective mixture ratio for maximum theoretical specific impulse. Figure V-12 shows the "X" values plotted as functions of fuel hydrogen-to-carbon ratio. Also shown on figure V-12 are similar data from Contract NAS3-4195. While there are differences in magnitude among the three curves, all show significant similarities in correlating reduced heat transfer rates with increasing percentages of carbon in the fuel. The reduction in heat transfer rate is primarily due to increased carbon deposition on the wall resulting from increased free carbon in the boundary layer. The differences in magnitude among the three sets of data may be due somewhat to circumferential variations in heat flux, but are caused primarily by differences in the injectors used in the two programs. Figures V-13 through V-15 show the circumferential temperature profiles for methane, propane, and butene-1 near the theoretical optimum mixture ratio for each. Note that, while there was considerable circumferential variation, the axial heat transfer data were taken at approximately an average heat flux location.



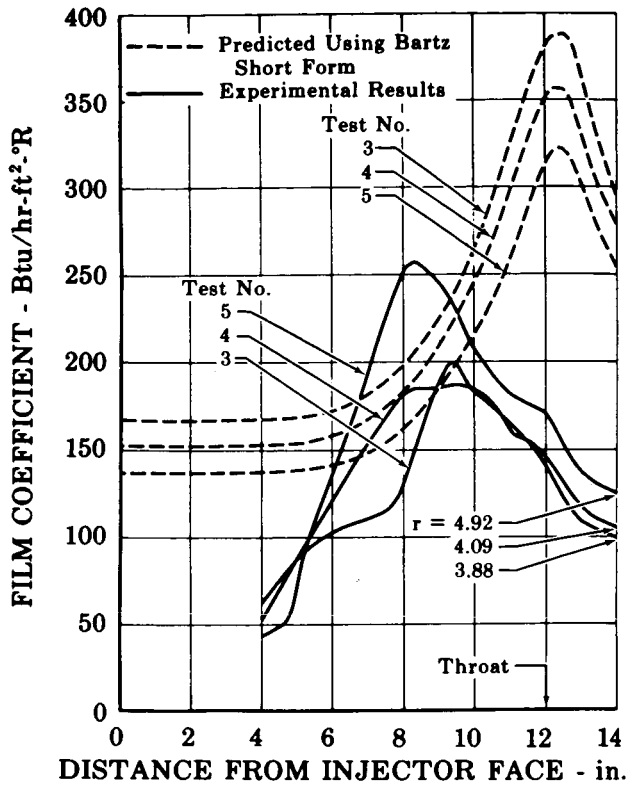


Figure V-7. Comparison of Heat Transfer Coefficients for Flox/Propane With Injector S(1)

FD 19761

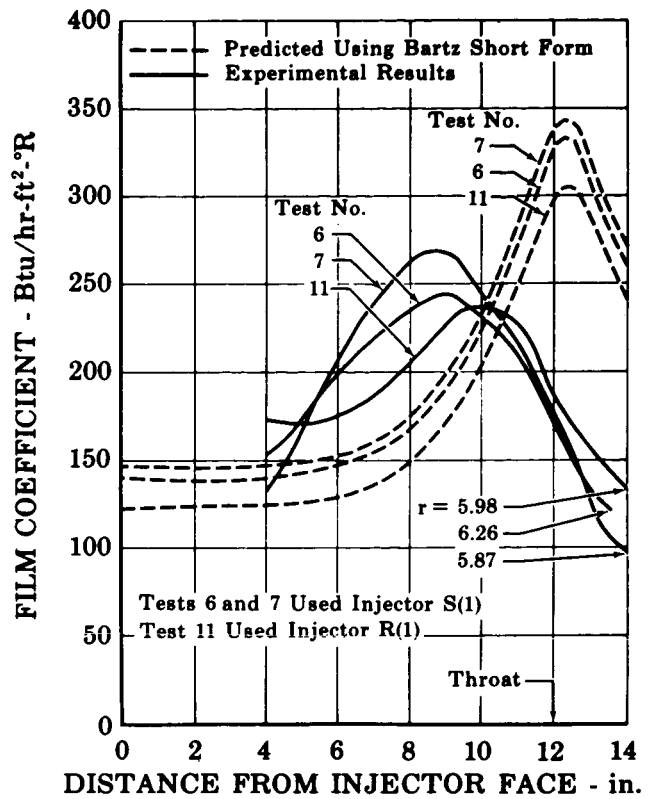


Figure V-8. Comparison of Heat Transfer Coefficients for Flox/Methane With Injector S(1)

FD 19762

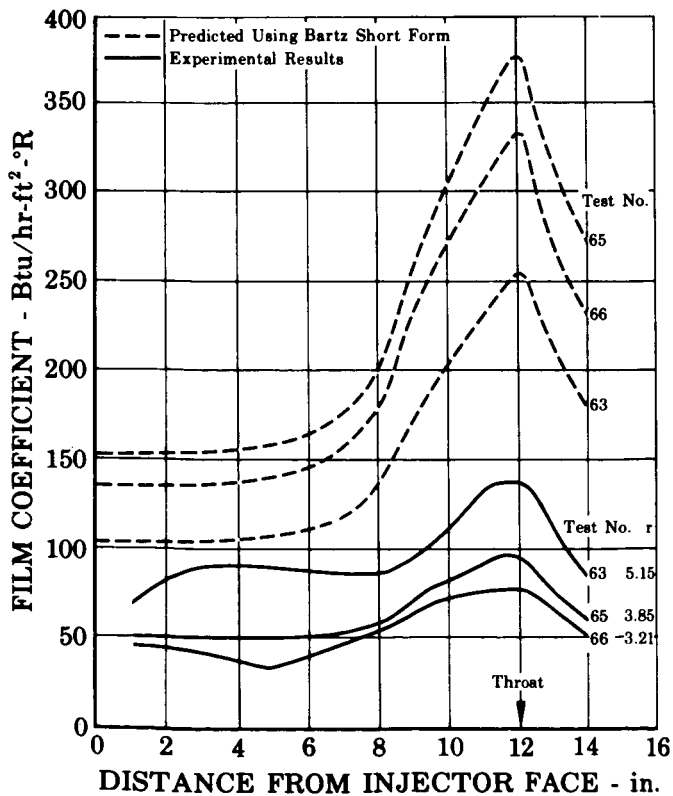


Figure V-9. Comparison of Heat Transfer Coefficients for Flox/Butene-1 With Injector R(1-C)

FD 19763

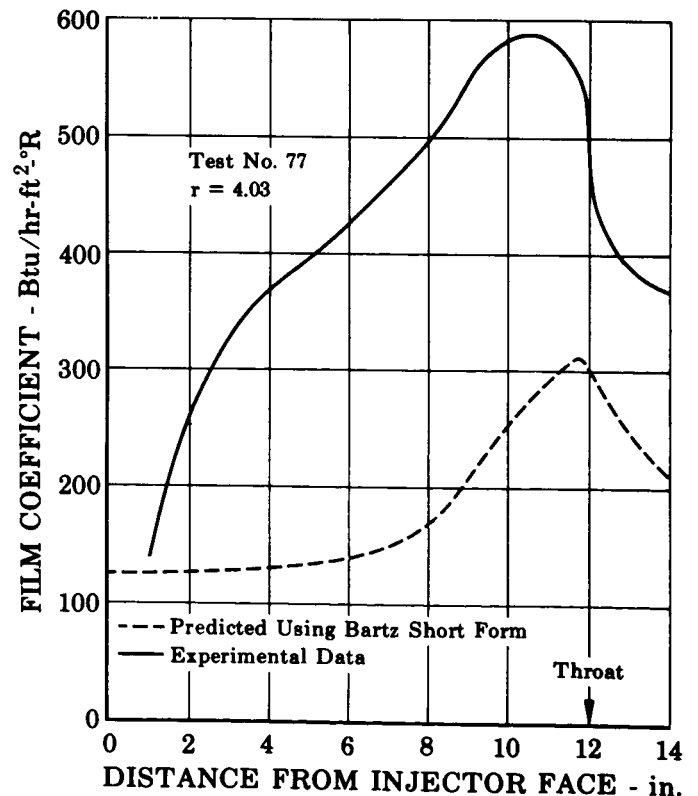


Figure V-10. Comparison of Heat Transfer Coefficients for Flox/Butene-1 With Injector S(2)

FD 19764

TABLE V-5. COMPARISON OF MEASURED AND PREDICTED CHAMBER  
HEAT TRANSFER RATES<sup>(1)</sup>

Test No.	Fuel	Mixture Ratio	Injector	Measured Heat Loss Rate, Btu/sec	Predicted Heat Loss Rate, Btu/sec	Experimental-to-Theoretical, %
6	Methane	6.26	S(1)	826	878	94.1
7	Methane	5.87	S(1)	772	892	86.6
11	Methane	5.98	R(1)	765	727	105.0
2UA	Methane	4.54	R(1-C)	712	796	89.5
3UA	Methane	5.16	R(1-C)	672	739	91.0
4UA	Methane	4.17	R(1-C)	665	785	84.7
5UA	Methane	3.81	R(1-C)	574	814	70.7
6UA	Methane	3.57	R(1-C)	538	845	63.7
7UA	Methane	3.85	R(1-C)	554	732	75.8
8UA	Methane	3.67	R(1-C)	544	747	72.8
9UA	Methane	4.00	R(1-C)	584	815	71.6
10UA	Methane	4.96	R(1-C)	545	767	71.2
11UA	Methane	5.99	R(1-C)	539	638	84.5
2	Propane	3.39	S(1)	479	1092	43.8
3	Propane	3.88	S(1)	437	975	44.8
4	Propane	4.09	S(1)	447	866	51.6
5	Propane	4.92	S(1)	464	710	65.4
63	Butene-1	5.15	R(1-C)	338	526	64.4
65	Butene-1	3.85	R(1-C)	275	936	29.4
66	Butene-1	3.21	R(1-C)	219	829	26.4
69	Butene-1	2.88	R(1-C)	218	850	25.6
77	Butene-1	4.03	S(2)	1617	719	225.0
12UA	Butene-1	4.10	S(2-A)	1222	621	197.0
13UA	Butene-1	2.77	S(2-A)	1240	636	195.0
14UA	Butene-1	3.76	S(2-A)	1365	676	202.0
15UA	Butene-1	3.68	S(2-A)	1438	742	194.0
16UA	Butene-1	4.66	S(2-A)	1395	662	211.0

(1) Total heat transferred to the uncooled copper chamber. Predicted rates are based on Bartz short form film coefficients.

As would be expected, injector design had a significant effect on the total heat transfer rates and on the distribution of heat transfer. This is evidenced by comparison of the axial profiles shown in figures V-7 through V-10 and also by the extremely high heat transfer rates obtained with butene-1 using the pentad injector. Two factors contributing to the lower heat transfer rates in the gaseous fuel tests were (1) the use of coaxial injector elements in which each oxidizer stream was completely surrounded by fuel, and (2) the 15-degree angle on the conical injector face, which directed propellants away from the chamber wall. These data indicate that, with all flox/light hydrocarbon combinations, injector design techniques can be used to reduce heat transfer rates significantly while maintaining high combustion efficiencies. Also, because of the effect of decreased hydrogen-to-carbon ratio on reducing heat transfer rates (predicted rates are roughly the same for all flox/light hydrocarbon combinations) it would be expected that the lowest rates can be attained with the high carbon content fuels.

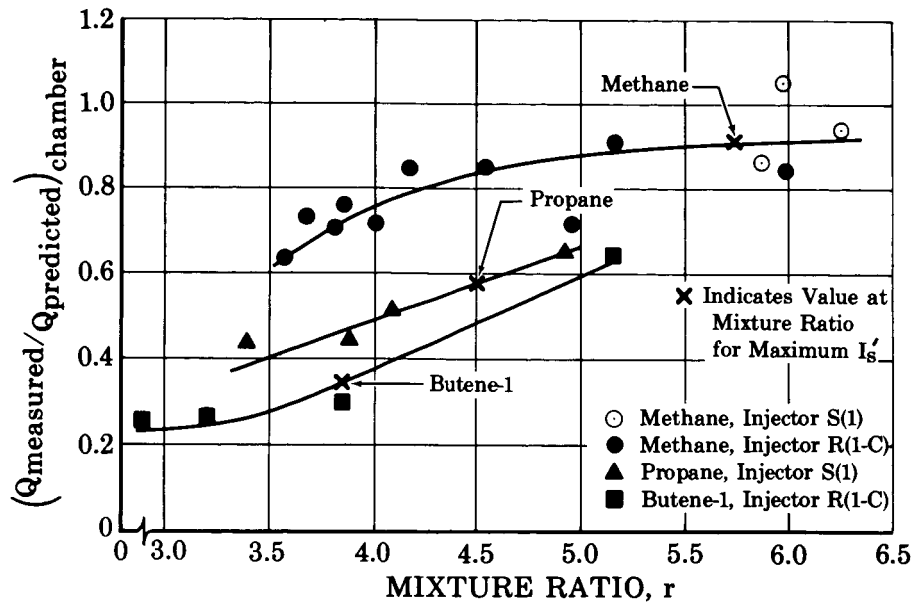


Figure V-11. Ratio of Measured to Predicted Heat Transfer Rates to Copper Chamber

FD 19765

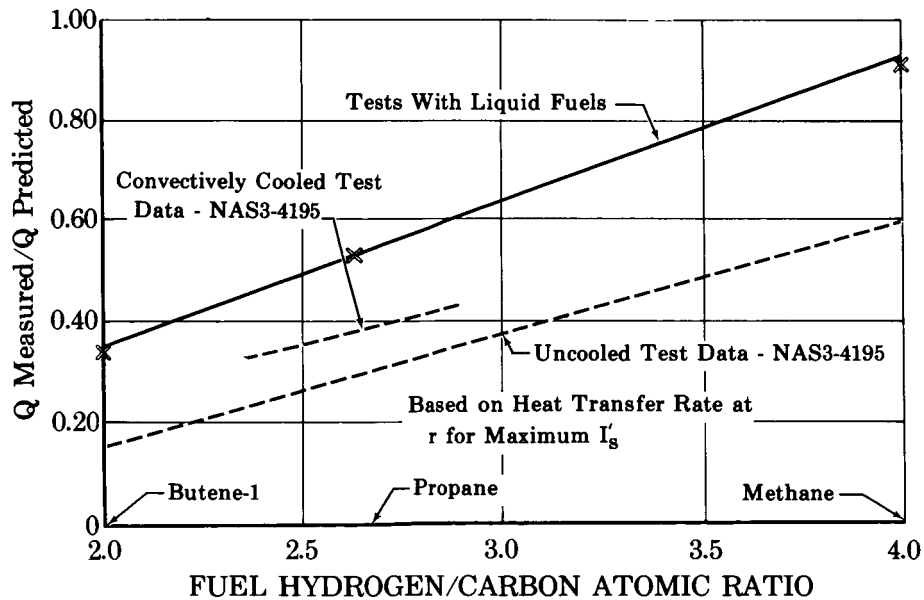


Figure V-12. Effect of Fuel Hydrogen-to-Carbon Ratio on Chamber Heat Transfer

FD 18473A

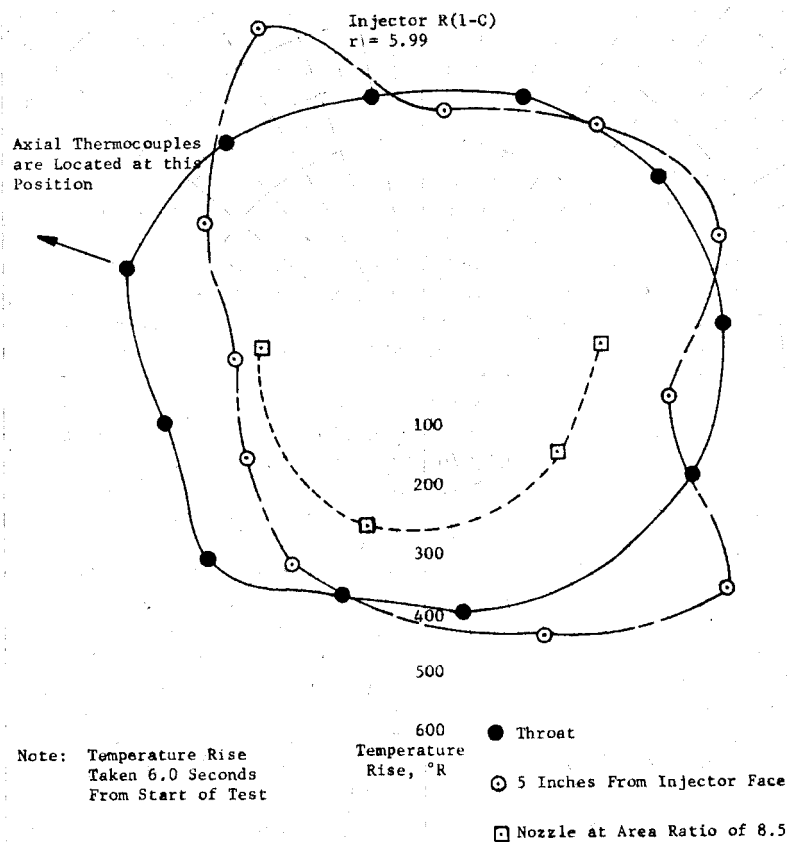


Figure V-13. Circumferential Temperature Rise Profile,  
Flox/Methane, Test No. 11UA

DF 50874A

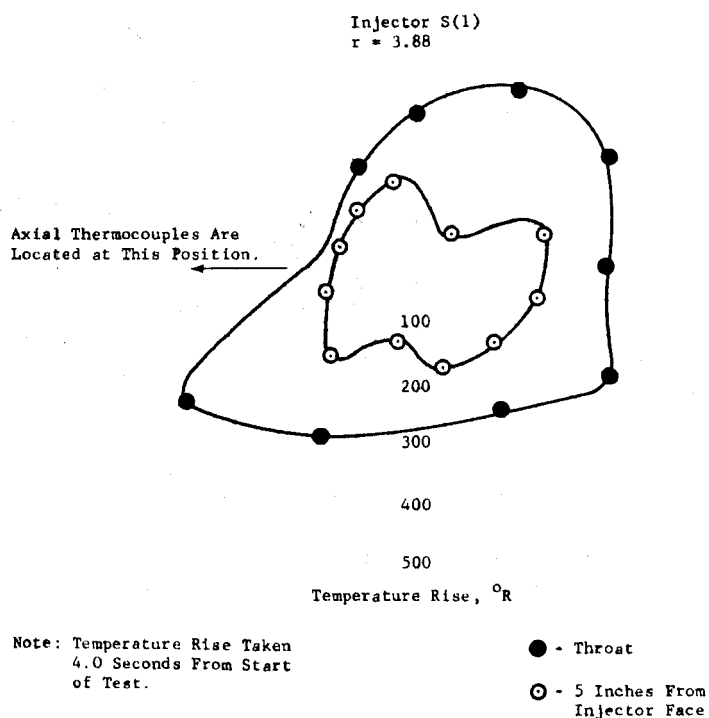


Figure V-14. Circumferential Temperature Rise Profile,  
Flox/Propane, Test No. 4

DF 54469

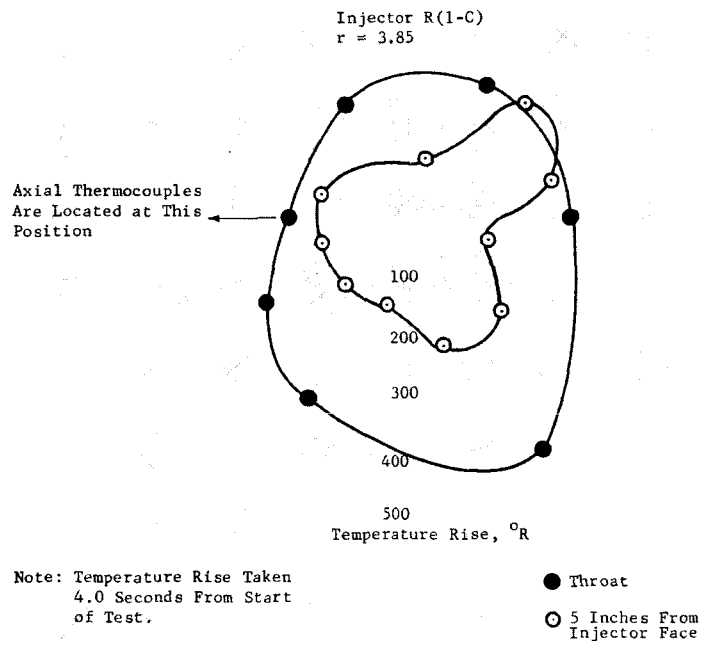


Figure V-15. Circumferential Temperature Rise Profile,  
Flox/Butene-1, Test No. 65

DF 54470

## SECTION VI

### UNCOOLED ALTITUDE TESTS — TASK III

#### A. TEST DESCRIPTION

The uncooled simulated altitude test objectives were: (1) to determine delivered vacuum specific impulse, (2) to evaluate kinetic equilibrium expansion losses, (3) to provide chamber and nozzle heat transfer coefficients, and (4) to verify hypergolicity under vacuum start conditions. The uncooled copper thrust chambers and uncooled stainless steel nozzles described in Section III were used for these tests. Injectors were selected based on their performance in the sea level tests. Nominal test conditions were 100-psia chamber pressure and 5000-lb vacuum thrust at a nozzle area ratio of 40. Propellant inlet conditions were liquid flox at approximately 160°R and subcooled liquid fuels at 200-270°R. Altitude conditions were simulated by a continuous-acting steam-driven diffuser that was capable of maintaining pressures of approximately 0.2 psia. Figure VI-1 shows the chamber mounted in the test facility. Table VI-1 presents a summary of the sixteen uncooled simulated altitude tests.

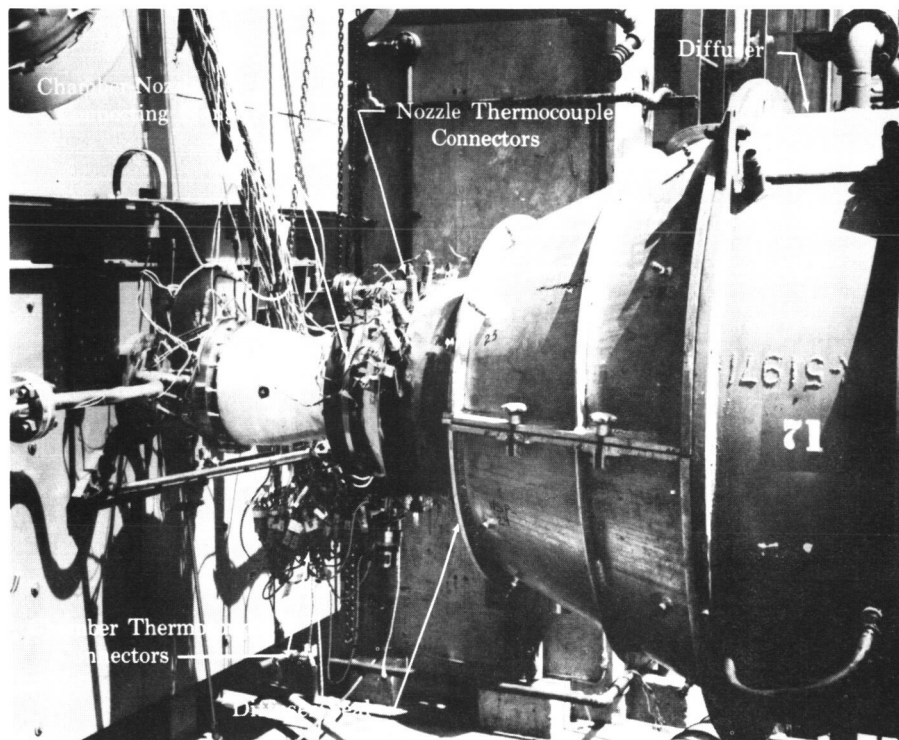


Figure VI-1. Uncooled Chamber and Nozzle Mounted in Test Facility

FD 16098

TABLE VI-1. SUMMARY OF UNCOOLED ALTITUDE TESTS

Test No.	Fuel	Percent $F_2$ in Flow	Test Duration, sec	$P_c$ , psia	$F$ , lb	$\dot{w}_o$ , lb/sec	$\dot{w}_f$ , lb/sec	$T_o$ , °R	$T_f$ , °R	$\Delta P_o$ , psi	$\Delta P_f$ , psi	Injector	Injector Delay, millisec	Diffuser Pressure, psia	Comments
1UA	Methane	82.6	2.0	88.6	4322	11.3	1.94	168	214	17	166	R(1-C)	150	0.22	
2UA	Methane	82.6	4.0	96.1	4681	11.0	2.42	163	204	23	154	R(1-C)	125	0.18	
3UA	Methane	82.6	6.0	96.6	4758	11.3	2.18	154	204	21	125	R(1-C)	40	0.17	
4UA	Methane	82.6	6.0	100.4	5101	11.2	2.69	166	205	16	157	R(1-C)	110	1.19	Diffuser pressure too high - possible nozzle separation.
5UA	Methane	82.6	6.0	99.8	4983	11.0	2.88	154	215	18	151	R(1-C)	125	0.23	
6UA	Methane	82.6	6.0	101.1	4996	10.8	3.01	162	210	14	159	R(1-C)	115	0.23	
7UA	Methane	82.6	6.0	95.4	5025	10.5	2.72	156	204	14	167	R(1-C)	100	0.31	Probable incorrect thrust tare values.
8UA	Methane	82.6	6.0	101.7	5263	11.1	3.05	158	203	17	151	R(1-C)	40	0.31	Probable incorrect thrust tare values.
9UA	Methane	82.6	6.0	100.9	5105	11.2	2.80	158	209	18	154	R(1-C)	110	0.28	
10UA	Methane	82.6	6.0	97.1	4865	11.4	2.29	157	211	19	103	R(1-C)	50	0.28	
11UA	Methane	82.6	6.0	91.2	4536	11.6	1.94	158	209	18	67	R(1-C)	55	0.27	
12UA	Butene-1	70.4	4.0	97.9	4905	11.1	2.70	165	236	24	54	S(2-A)	155	0.21	Possible fuel dilution with gaseous nitrogen.
13UA	Butene-1	70.4	4.0	97.6	4949	10.4	3.77	179	212	27	117	S(2-A)	190	0.24	
14UA	Butene-1	70.4	4.0	94.2	4746	10.7	2.86	178	250	33	56	S(2-A)	160	0.53	
15UA	Butene-1	70.4	4.0	103.3	5185	11.4	3.10	158	217	25	68	S(2-A)	160	0.22	
16UA	Butene-1	70.4	4.0	100.0	4945	12.1	2.58	165	270	29	52	S(2-A)	150	0.19	

The 11 methane tests were all made with 82.6% flox using injector R (1-C). The two initial tests, of 2.0 and 4.0 seconds duration, verified the ability of the uncooled nozzle to withstand test durations up to 6.0 seconds with flox/methane. Because some improvement in injector performance had been noted toward the end of the 4.0-second sea level tests, it was decided to conduct the altitude tests for a longer duration to determine the effects of injector cooldown on performance. The remaining flox/methane tests were, therefore, of 6.0-seconds duration. Prior to the last five methane tests, 38 0.009-inch diameter fuel holes were drilled near the outer circumference of the injector to produce a more uniform circumferential heat flux profile. These holes were located to intersect the oxidizer fans nearest to the chamber wall, and to prevent oxidizer impingement on the chamber wall in the event that the outer oxidizer streams did not completely impinge on each other.

The five butene-1 tests were made with 70.4% flox and the modified pentad injector, S (1-A). Because the sea level tests with this injector were unstable, a quarter-length acoustic liner was incorporated in the chamber. The design of this liner was discussed in Section III.

## B. PERFORMANCE

Calculated performance data for the simulated altitude tests are presented in table VI-2. Performance data were calculated using the methods detailed in Appendix A. Characteristic velocity for the flox/methane simulated altitude tests are presented in figure VI-2. Figures VI-3 and VI-4 show vacuum specific impulse and vacuum thrust coefficient as functions of mixture ratio for the flox/methane tests. Open symbols on these figures indicate data obtained in short-duration tests or tests in which the thrust measurements were questionable, due to either nonrepeatable tare values or high diffuser pressure that might have caused nozzle separation. Good agreement between data obtained in the two series of methane altitude tests indicated that the fuel cooling holes added to the injector between test No. 6UA and 7UA had no significant effect on performance. A maximum vacuum specific impulse of 368 seconds was indicated at a mixture ratio of approximately 4.0. The shift of the peak mixture ratio below the theoretical optimum of 5.75 is due to the decrease in combustion efficiency and thrust coefficient efficiency at high mixture ratios. The most significant of these is the steep decrease in combustion efficiency obtained with injector R (1-C), i.e., 7% decrease between mixture ratios of 4.0 and 5.75. Characteristic velocity, vacuum specific impulse and vacuum thrust coefficient as functions of mixture ratio are shown for flox/butene-1 in figures VI-5, VI-6, and VI-7. A maximum specific impulse of 362 seconds is indicated at a mixture ratio of 3.85. Figures VI-2 and VI-5 show a small difference in characteristic velocity measured in the sea level and altitude tests. While this difference is generally within the experimental accuracy of the data (see Appendix A), some data scatter from both the sea level and altitude tests can be attributed to the effect of variations in propellant inlet temperatures on injection momentum ratio.



**TABLE VI-2. CALCULATED PERFORMANCE DATA - UNCOOLED ALTITUDE TESTS**

Test No.	Fuel	$\tau$	$\dot{V}_{in}$ lb/sec	$c_s^*$ , ft/sec	$I_{vac}^*$ sec	$C_F^*$ vac	$c_F^*$ $P_c$ ft/sec	$c_F^*$ $P_c$ ft/sec	$Q_{in}^*$ Btu/sec	$Q_c^*$ Btu/sec	$\eta_{c^*P_c}^*$	$\eta_{c^*F}^*$	$\eta_{c^*P_c}^*$ (cor)	$\eta_{c^*F}^*$ (cor)	$I_{vac}^*$ sec	$I_{vac}^*$ (cor)	$\eta_{I_{vac}}^*$	$\eta_{I_{vac}}^*$ (cor)	$C_F^*$ vac	$C_F^*$ vac (cor)	$\eta_{C_F^*vac}^*$	$\eta_{C_F^*vac}^*$ (cor)	$\Delta t$ , Used, sec (1)
1UA	Methane	5.85	13.3	6953	416	1.918	6047	5630	700	500	0.870	0.810	0.851	0.813	327	330	0.787	0.793	1.737	1.737	0.906	0.929	0.9
2UA	Methane	4.54	6893	409	1.911	6479	6042	712	432	432	0.940	0.877	0.926	0.879	349	353	0.855	0.863	1.734	1.734	0.907	0.925	0.5
3UA	Methane	5.16	13.4	6955	414	1.917	6505	6112	672	427	0.935	0.879	0.919	0.882	354	357	0.856	0.863	1.753	1.753	0.914	0.929	2.0
4UA	Methane	4.17	13.9	6837	405	1.908	6533	6364	665	444	0.956	0.931	0.938	0.933	367	371	0.907	0.915	1.808	1.808	0.948	0.964	1.1
5UA	Methane	3.81	13.9	6767	400	1.900	6512	6285	574	307	0.962	0.926	0.951	0.927	360	364	0.899	0.909	1.778	1.778	0.936	0.951	0.5
6UA	Methane	3.57	13.8	6733	397	1.892	6641	6344	538	399	0.986	0.942	0.966	0.944	363	367	0.914	0.924	1.759	1.759	0.930	0.948	1.7
7UA	Methane	3.65	13.2	6773	401	1.901	6531	6634	554	554	0.964	0.979	0.959	0.981	381	386	0.952	0.962	1.879	1.879	0.988	0.995	1.2
8UA	Methane	3.63	14.1	6738	398	1.894	6491	6501	544	515	0.963	0.965	0.950	0.965	372	376	0.936	0.945	1.846	1.846	0.974	0.989	1.6
9UA	Methane	4.00	14.0	6802	403	1.905	6506	6331	584	481	0.957	0.931	0.949	0.933	365	368	0.906	0.914	1.804	1.804	0.947	0.957	1.3
10UA	Methane	4.96	13.7	6944	413	1.913	6420	6160	545	412	0.924	0.887	0.920	0.891	356	360	0.863	0.870	1.787	1.787	0.934	0.942	1.3
11UA	Methane	5.99	13.6	6943	416	1.916	6065	5772	539	335	0.874	0.831	0.865	0.834	334	338	0.808	0.816	1.774	1.774	0.926	0.939	1.4
12UA	Butene-1	4.10	13.8	6711	398	1.912	6430	6162	1222	1099	0.958	0.918	0.950	0.926	356	360	0.895	0.902	1.783	1.783	0.933	0.949	1.4
13UA	Butene-1	2.77	14.2	6505	386	1.907	6212	6045	1298	1298	0.955	0.929	0.950	0.938	349	354	0.902	0.911	1.805	1.805	0.947	0.961	0.3
14UA	Butene-1	3.76	13.6	6751	403	1.921	6267	6010	1365	858	0.928	0.890	0.920	0.897	349	353	0.867	0.874	1.792	1.792	0.933	0.948	2.4
15UA	Butene-1	3.68	14.5	6750	401	1.920	6435	6154	1438	1116	0.953	0.912	0.951	0.919	357	361	0.890	0.896	1.787	1.787	0.931	0.940	0.5
16UA	Butene-1	4.66	14.6	6552	385	1.904	6174	5867	1395	932	0.942	0.895	0.938	0.904	338	343	0.877	0.884	1.760	1.760	0.925	0.938	1.9

(1)  $\Delta t$  used is the amount of time over which the performance figures are averaged.

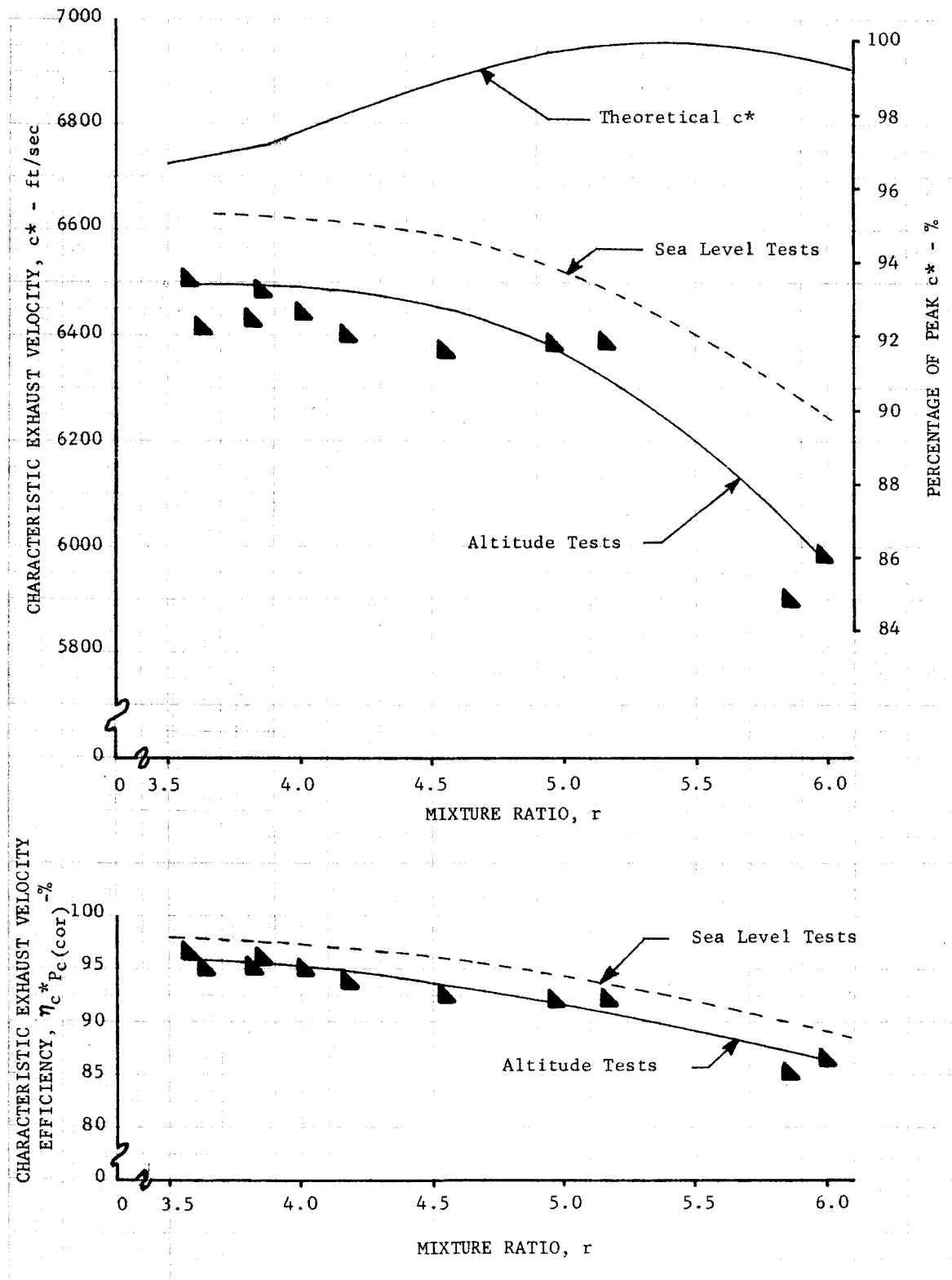


Figure VI-2. Flox/Methane Characteristic Exhaust Velocity With  
Injector R(1-C): 82.6%  $F_2$  in Flox

DF 54462

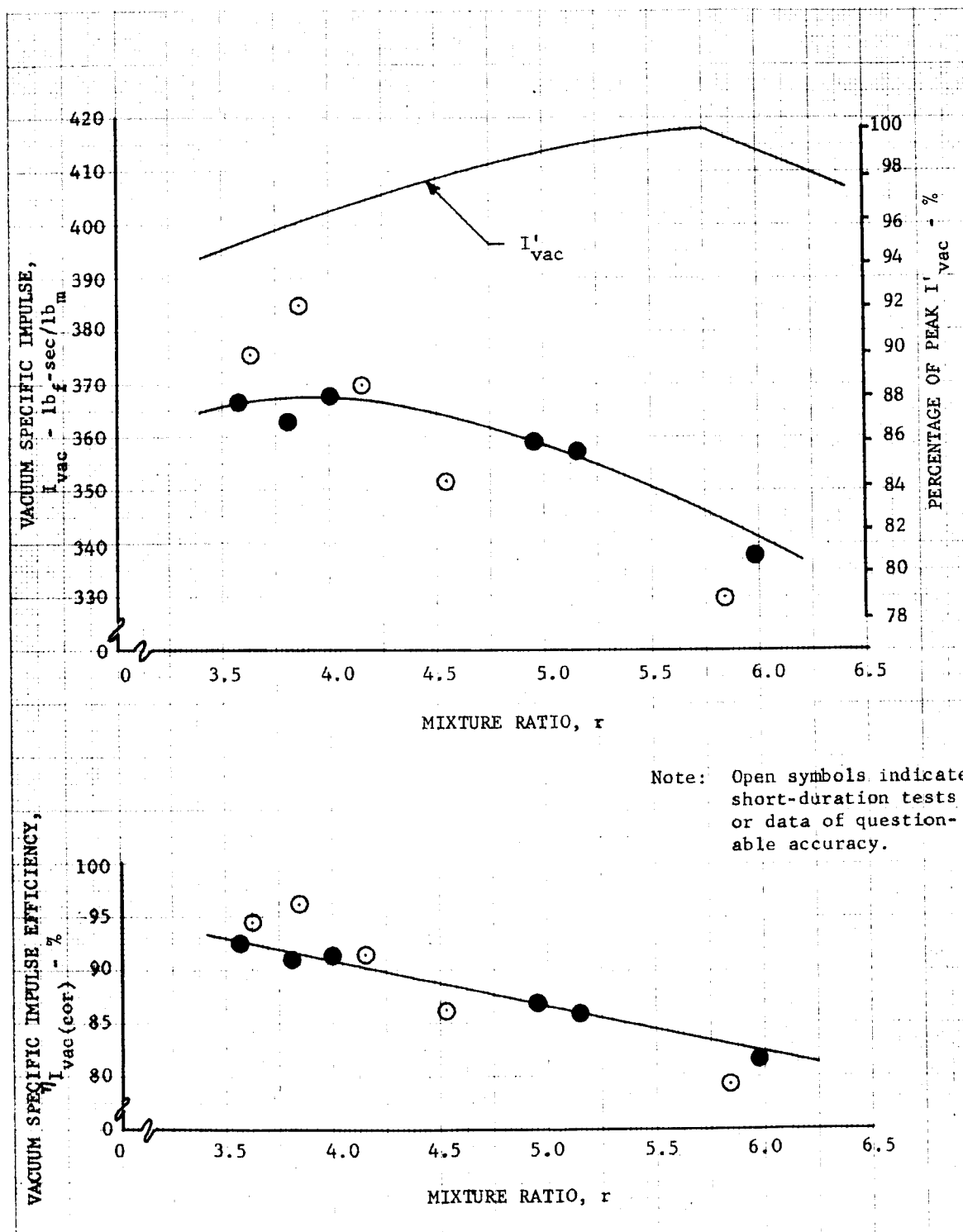


Figure VI-3. Flox/Methane Vacuum Specific Impulse With  
Injector R(1-C): 82.6%  $F_2$  in Flox

DF 50109

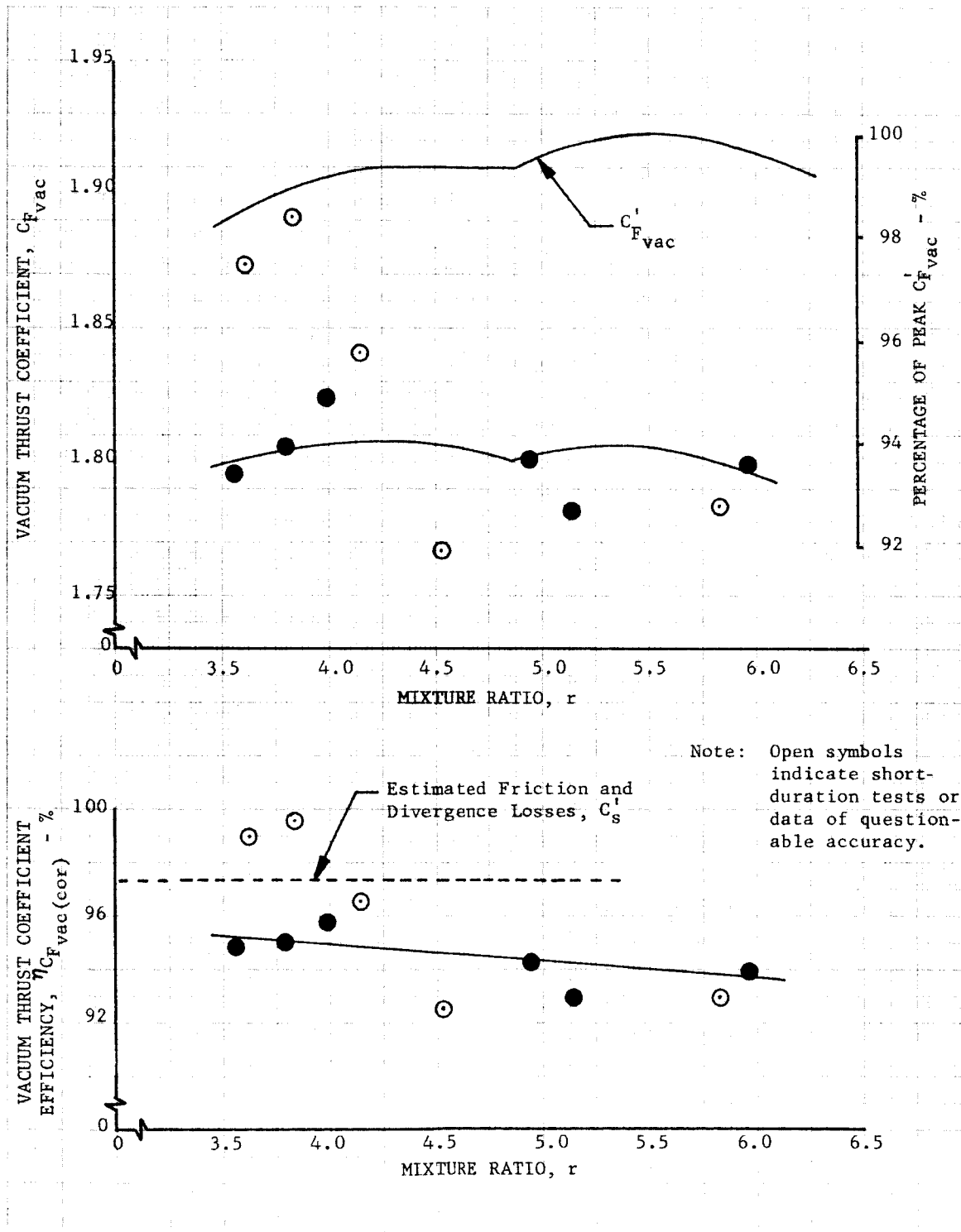


Figure VI-4. Flox/Methane Vacuum Thrust Coefficient With  
Injector R(1-C): 82.6%  $F_2$  in Flox

DF 50108

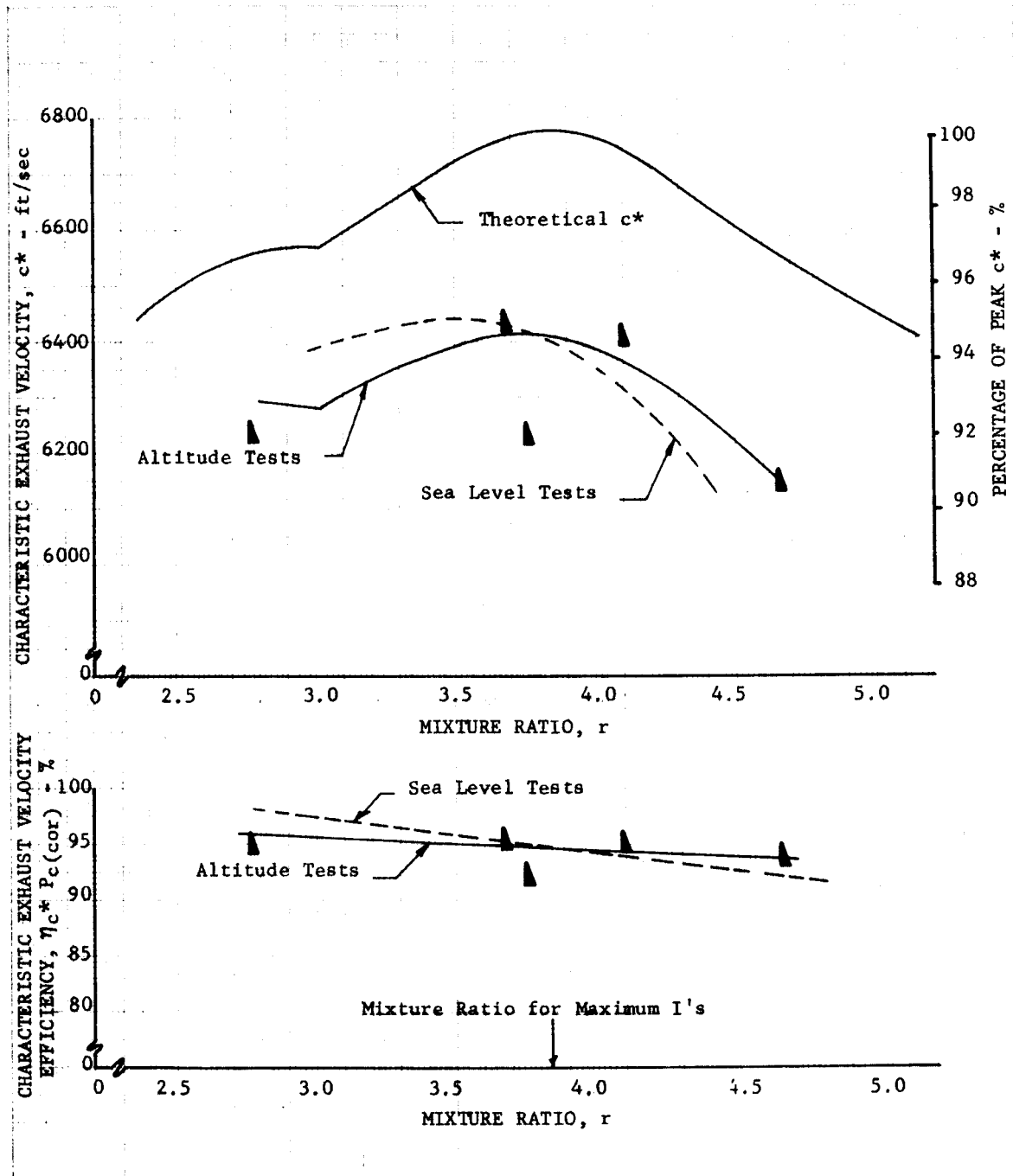


Figure VI-5. Flox/Butene-1 Characteristic Exhaust Velocity With  
Injector S(2-A): 70.4%  $F_2$  in Flox

DF 54463

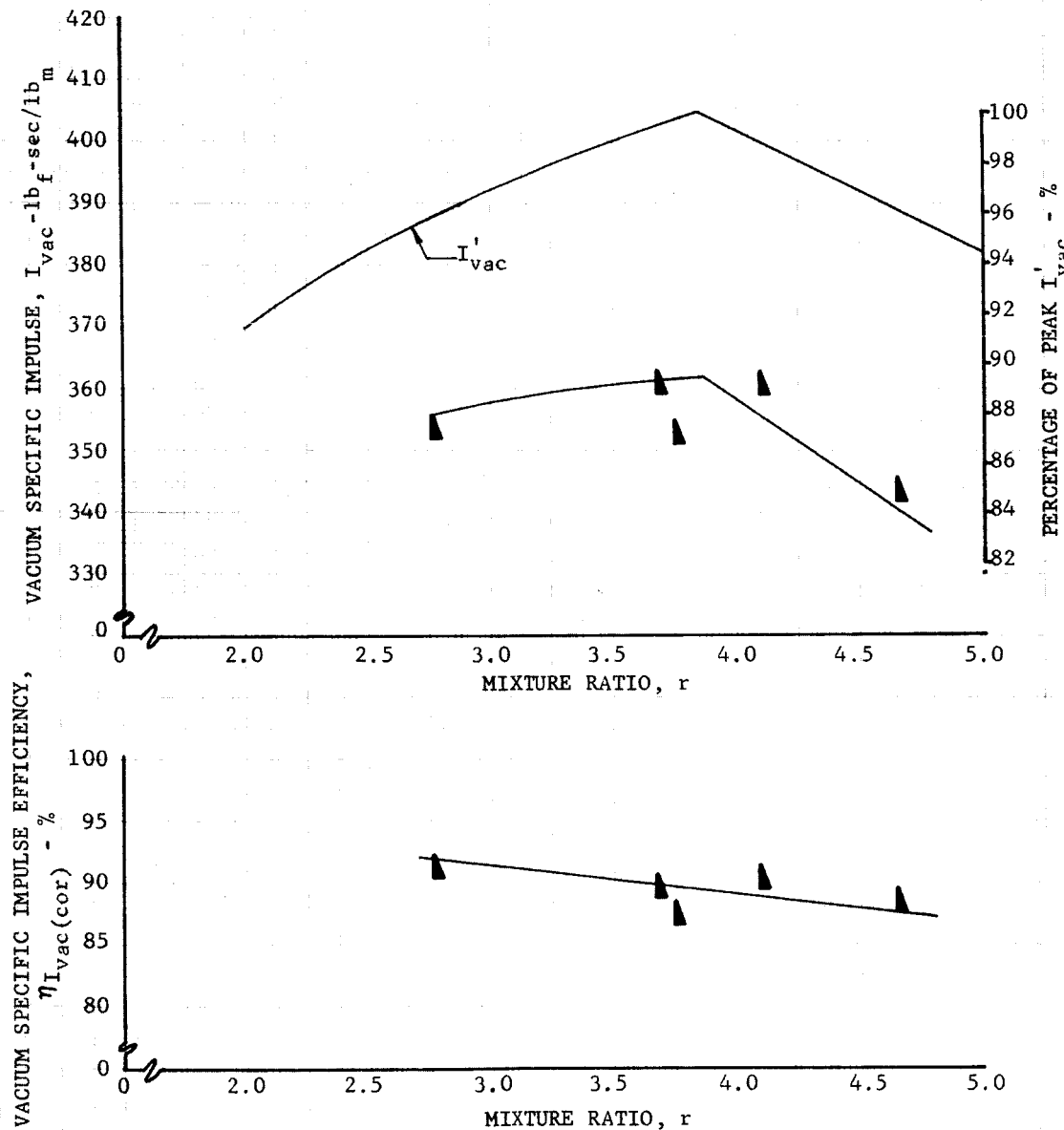


Figure VI-6. Flox/Butene-1 Vacuum Specific Impulse With  
Injector S(2-A): 70.4%  $F_2$  in Flox

DF 52707

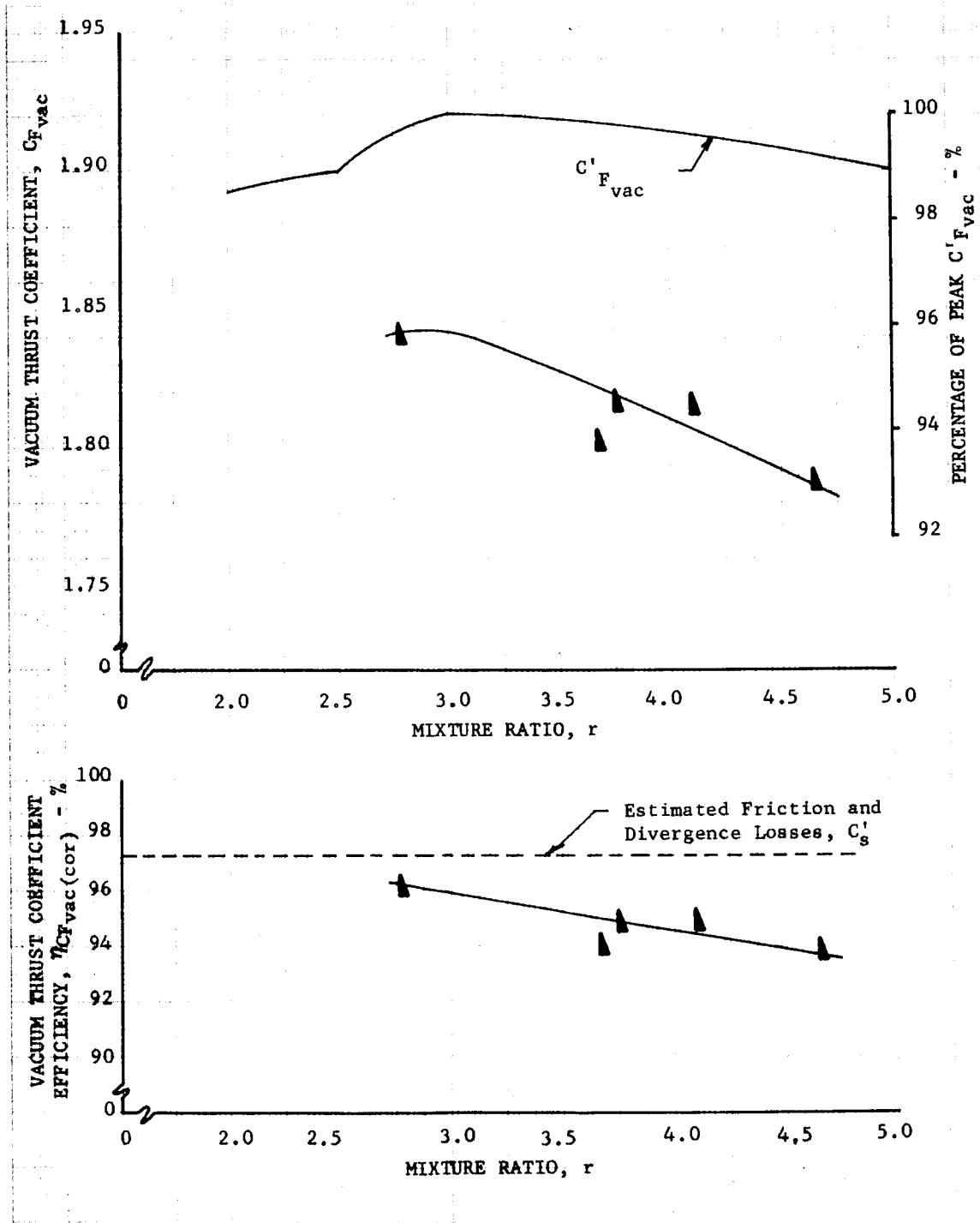


Figure VI-7. Flox/Butene-1 Vacuum Thrust Coefficient With  
Injector S(2-A): 70.4%  $F_2$  in Flox

DF 52705

In all cases the vacuum thrust coefficient losses were greater than those attributed to nozzle friction and divergence losses,  $C_{*}'$ . This difference, which increases at higher mixture ratios, is attributed primarily to non-equilibrium chemical recombination during expansion; however, incomplete mixing of combustion reaction products has been shown to be the major cause of combustion inefficiency, and incomplete mixing can also produce substantial thrust coefficient losses. The indicated losses of approximately 2 to 4% are significantly less than losses predicted by nonequilibrium kinetic calculations. Table VI-3 compares the calculated kinetic losses with those estimated from the altitude tests. The kinetic results shown in table VI-3 are based on nonequilibrium performance calculations made using the one-dimensional kinetic flow program developed by United Aircraft Corporation Research Laboratories (Reference 18). The sudden-freeze point approximation is an extension of Bray's sudden-freeze point method (Reference 19) to include one-dimensional nozzle flows with several concurrent chemical reactions (Reference 20). Table VI-4 presents the elementary reaction mechanism and reaction rate constants employed in the one-dimensional kinetic flow deck calculations. This mechanism and the rate constants are consistent with Reference 21, except that third-body effects of CO and the minor constituents have been incorporated. The sudden-freeze point calculations used only reactions 1 through 8. Kinetic losses predicted by the two methods agree within approximately 20%;

TABLE VI-3. REDUCTION IN VACUUM SPECIFIC IMPULSE  
DUE TO REACTION RATE LIMITED EXPANSION<sup>(1)</sup>

Fuel	F <sub>2</sub> In Flox, %	Mixture Ratio	$\Delta I_{vac}$ , Kinetic Method <sup>(2)</sup> sec	$\Delta I_{vac}$ , Sudden-Freeze Point Method <sup>(3)</sup> sec	$\Delta I_{vac}$ , Test Results <sup>(4)</sup> , sec
Methane	82.6	6.00	--	38	15
		5.75	42	44	14
		5.25	34	40	12
		4.75	29	36	11
		4.25	26	32	8
		3.75	--	25	6
Butene-1	70.4	4.00	--	40	10
		3.85	--	42	10
		3.50	--	37	8
		3.25	--	33	7

(1) Theoretical vacuum specific impulse based on 100-psia chamber pressure, nozzle area ratio of 40, and both propellants at their normal boiling points.

(2) One-dimensional kinetic equilibrium calculations (Reference 18).

(3) Method of References 19 and 20.

(4) Expansion vacuum impulse losses after correcting for nozzle friction and divergence losses and combustion efficiency.



however, losses based on test results are only 20 to 40% of the predicted losses. This indicates that the recombination reaction mechanisms and rates currently believed to be the best available do not adequately describe the flox/light hydrocarbon recombination process.

TABLE VI-4. ELEMENTARY REACTIONS AND REACTION RATE CONSTANTS EMPLOYED IN FLOX/METHANE REACTION MECHANISM

Number	Reaction	Rate <sup>(1)</sup>
1	$H + H + H \rightarrow H_2 + H$	$k_f = 1.156 \times 10^{13} T^{-0.5061} \text{ exp } (3690/T)$
2	$H + F + H \rightarrow HF + H$	$k_f = 1.551 \times 10^{12} T^{-0.6042} \text{ exp } (3780/T)$
3	$H + H + HF \rightarrow H_2 + HF$	$k_f = 1.222 \times 10^{12} T^{-0.5061} \text{ exp } (3690/T)$
4	$H + H + F \rightarrow H_2 + F$	$k_f = 3.000 \times 10^{12} T^{-0.5061} \text{ exp } (3690/T)$
5	$H + H + H_2 \rightarrow H_2 + H_2$	$k_f = 5.555 \times 10^{13} T^{-0.5061} \text{ exp } (3680/T)$
6	$H + F + F \rightarrow HF + F$	$k_f = 6.634 \times 10^{11} T^{-0.6042} \text{ exp } (3780/T)$
7	$H + F + H_2 \rightarrow HF + H_2$	$k_f = 6.035 \times 10^{12} T^{-0.6042} \text{ exp } (3780/T)$
8	$H + F + HF \rightarrow HF + HF$	$k_f = 1.871 \times 10^{11} T^{-0.6042} \text{ exp } (3780/T)$
9	$H + F + CO \rightarrow HF + CO$	$k_f = 3.102 \times 10^{12} T^{-0.6042} \text{ exp } (3780/T)$
10	$H + H + CO \rightarrow H_2 + CO$	$k_f = 2.312 \times 10^{13} T^{-0.5061} \text{ exp } (3690/T)$
11	$H + H + MC \rightarrow H_2 + MC^{(2)}$	$k_f = 2.312 \times 10^{13} T^{-0.5061} \text{ exp } (3690/T)$
12	$H + F + MC \rightarrow HF + MC^{(2)}$	$k_f = 3.102 \times 10^{12} T^{-0.6042} \text{ exp } (3780/T)$
13	$F + H_2 \rightarrow HF + H$	$k_f = 4.190 \times 10^8 T^{0.7470} \text{ exp } (-6950/T)$

(1) Expressed in lb-moles, ft<sup>3</sup>, sec, and °R.

(2) MC refers to minor constituents.

### C. ALTITUDE IGNITION

Smooth hypergolic ignition was achieved in all simulated altitude tests. Ignition delays for all of the simulated altitude tests are given in table VI-1. Table VI-5 compares the average ignition delay times for the sea level and vacuum starting conditions. Because this delay time includes injector filling, the comparisons are made between sea level and altitude test series with the same injector. For methane and butene-1 the average delay times at vacuum conditions were approximately 40 msec longer than at sea level ambient conditions; however, the start transient was equally smooth and no pressure spikes were encountered. The averaged data are presented to give an indicative comparison and the 40 msec increase should not be considered an absolute value.

TABLE VI-5. AVERAGE IGNITION DELAYS FOR SEA LEVEL AND ALTITUDE TESTS

Fuel	Injector	Average Sea Level Ignition Delay Time, msec	Average Vacuum Ignition Delay Time, msec
Methane	R(1-C)	58	93
Butene-1	S(2-A)	115	163

#### D. ACOUSTIC LINER OPERATION

The five flox/butene-1 simulated altitude tests were made using the pentad injector, S(2-A), and an uncooled chamber incorporating the quarter-length acoustic liner, described in Section III. This design provided a theoretical absorption coefficient above 95% over the 2800 to 3200 cps frequency range. The acoustic liner was required to suppress severe first tangential mode combustion instability encountered during the earlier sea level testing. The primary frequency of the instability occurred at approximately 3100 cps with peak-to-peak amplitudes as high as 60 psi. Strong first and second harmonics were also recorded at 6400 and 9600 cps.

The acoustic liner performed as expected in reducing the instability. In figures VI-8 and VI-9, frequency-amplitude relationships obtained with this injector in uncooled sea level tests without the liner are compared with those in the uncooled simulated-altitude tests using the liner. Each figure compares tests having approximately the same mixture ratio and flow rates. Peak-to-peak pressure variations up to 60 psi were reduced to less than 1 psi with the liner.

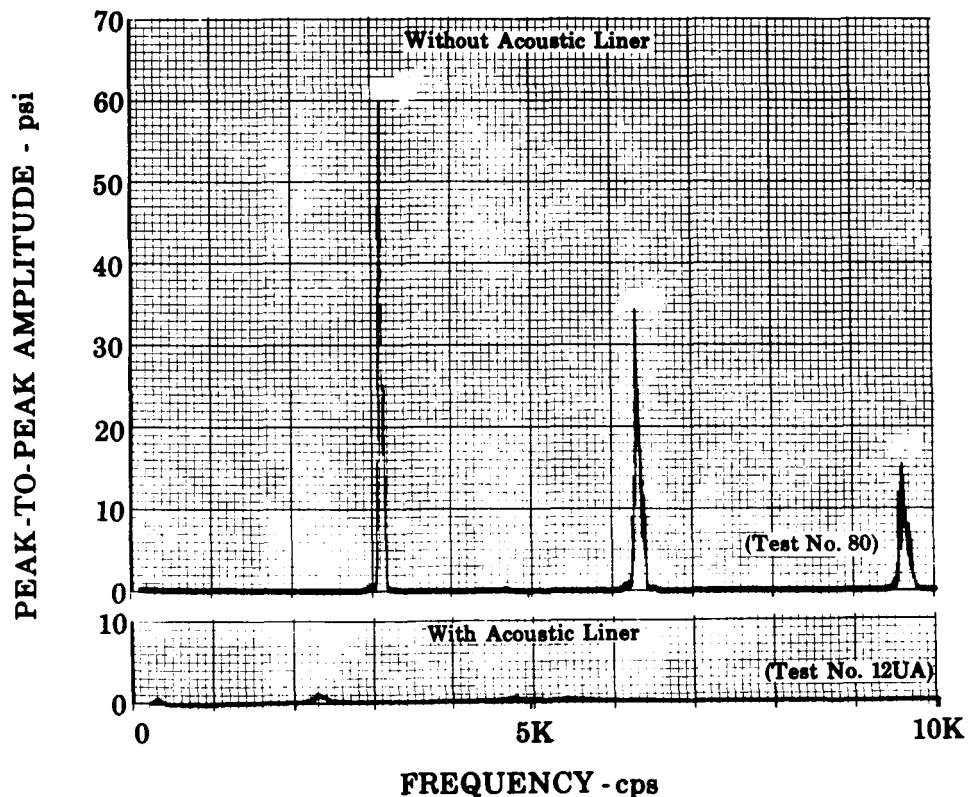


Figure VI-8. Chamber Pressure Stability With Flox/Butene-1:  $r \approx 4.1$

FD 19280

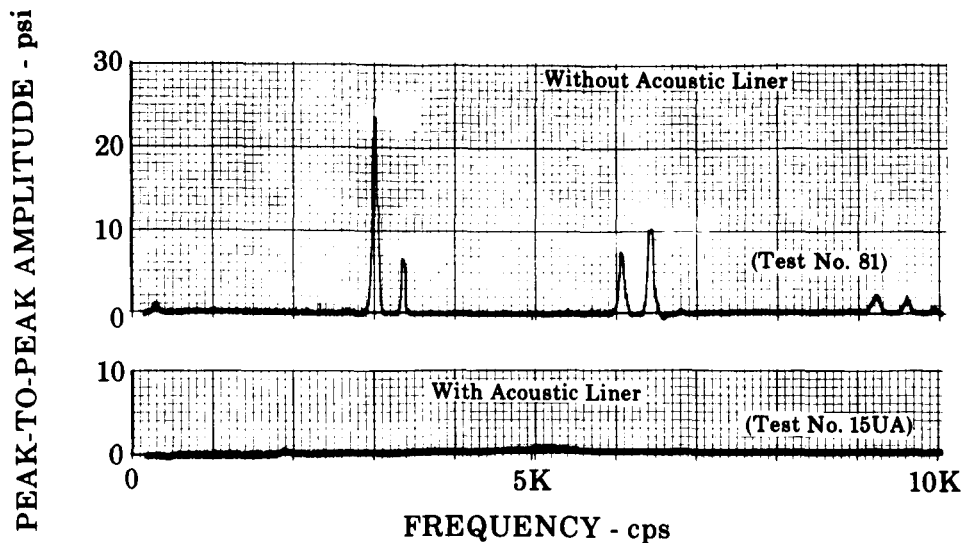


Figure VI-9. Chamber Pressure Stability with Flox/Butene-1:  $r \approx 3.65$  FD 19281

### E. NOZZLE HEAT TRANSFER

In figures VI-10 through VI-13 film coefficients from representative simulated altitude tests using methane with injector R (1-C) are compared with coefficients predicted by the Bartz equation. The chamber coefficients show the effects of injector wall impingement on film coefficient but are in all cases lower than the Bartz predictions in the throat region. The total chamber heat transfer rates for these tests were comparable to those of the sea level tests. The amount of chamber heat transfer reduction from the Bartz predictions is discussed in Section V. Film coefficients in the nozzle are very close to the Bartz predicted values. The data point 30 inches from the injector face (located close to the diffuser seal band) yields low film coefficient values due to the heat transferred to the band.

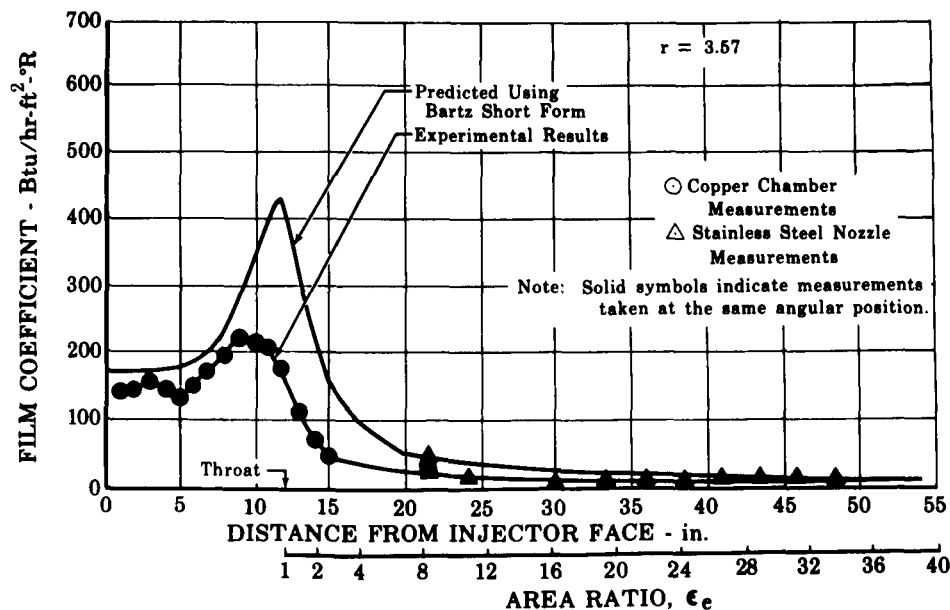


Figure VI-10. Comparison of Flox/Methane Heat Transfer Coefficients: Test No. 6UA

FD 19766

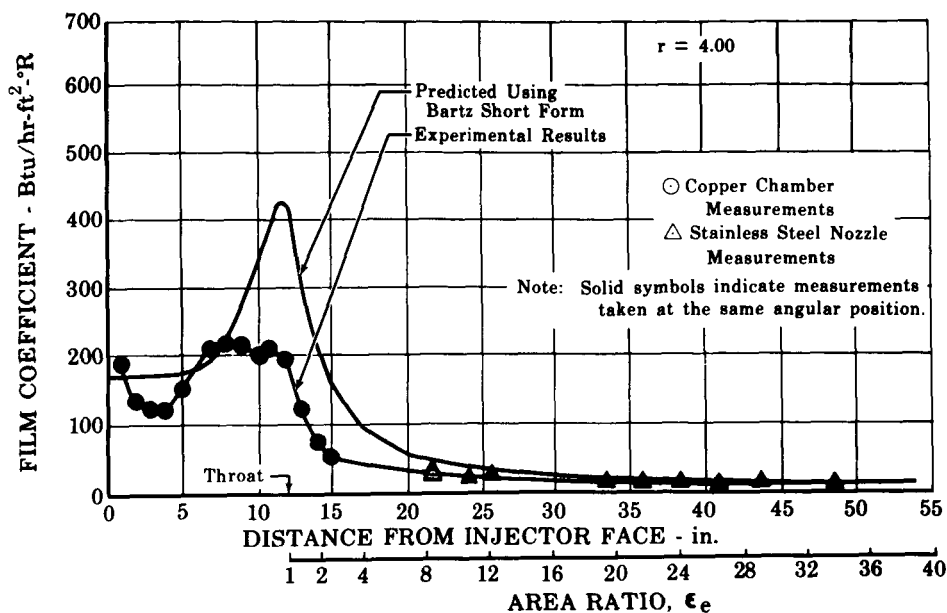


Figure VI-11. Comparison of Flox/Methane Heat Transfer Coefficients: Test No. 9UA

FD 19767

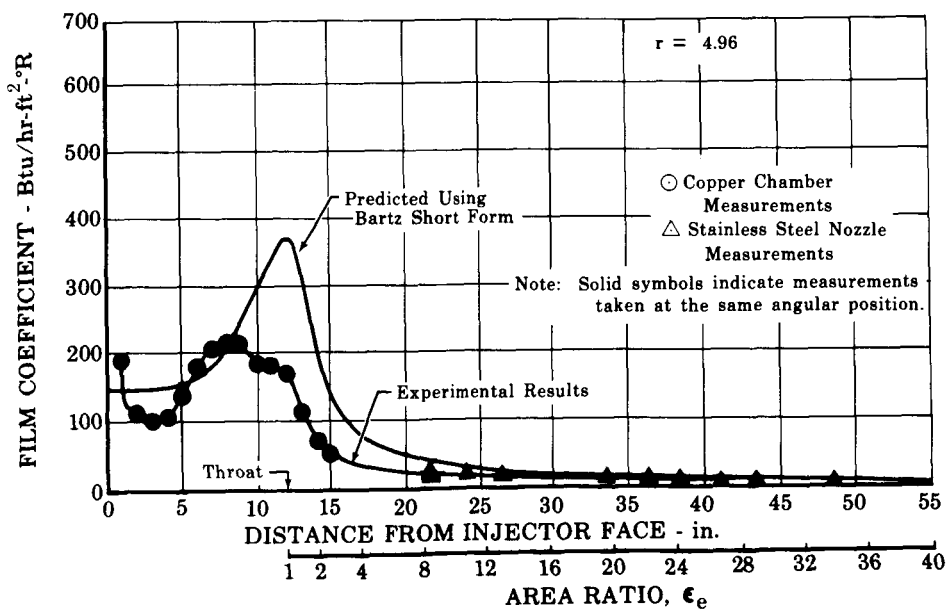


Figure VI-12. Comparison of Flox/Methane Heat Transfer Coefficients: Test No. 10UA

FD 19768

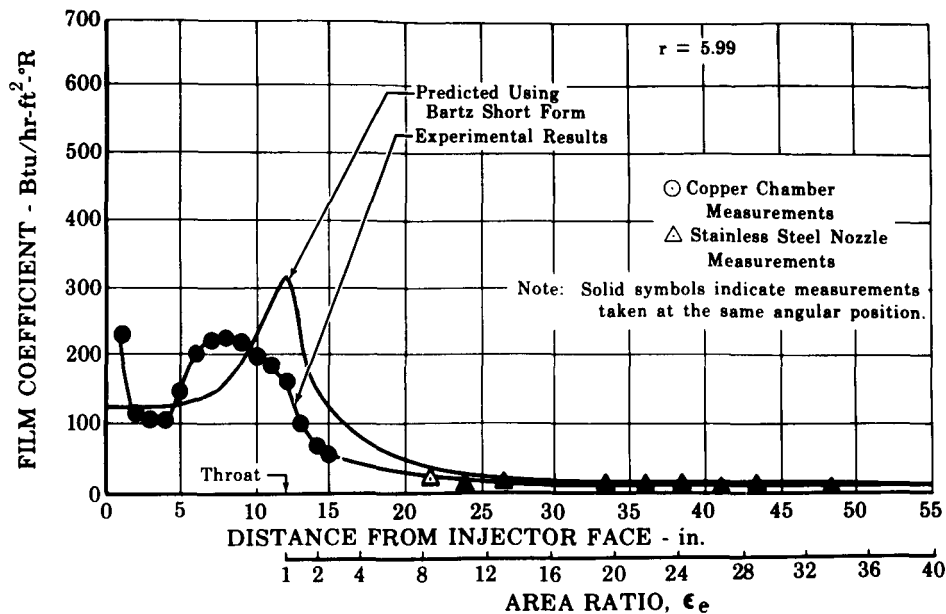


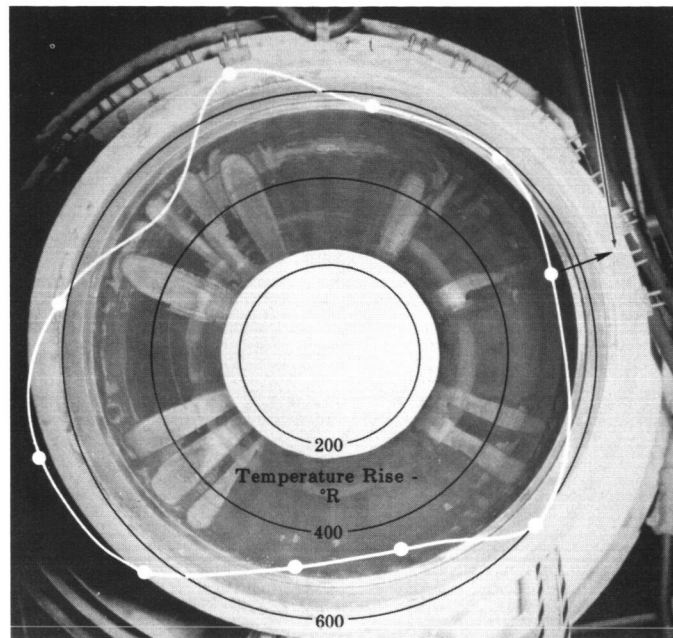
Figure VI-13. Comparison of Flox/Methane Heat Transfer Coefficients: Test No. 11UA

FD 19769

Figures VI-14 and VI-15 present circumferential throat temperature rise profiles for tests No. 6UA and 11UA, superimposed on photographs taken of the copper chamber from the injector end after each respective test. The areas of highest temperature rise show agreement with the light-colored streaks in the photograph, indicating oxidizer-rich areas. The last five flox/methane tests showed substantial improvement in temperature uniformity over that obtained with the same injector in previous tests. The improvement in the temperature pattern is attributed to the 38 fuel holes drilled near the outer circumference of the injector before test No. 7UA. The carbon deposits in the exhaust nozzle were lighter than in the chamber. Figure VI-16 shows the nozzle after test No. 6UA. The lighter streaks correspond to the high temperature rise areas.

Figures VI-17 and VI-18 present film coefficient data from butene-1 tests using the modified pentad injector. As with the sea level tests (tests 77 through 82), the experimental film coefficients were considerably above those predicted by the Bartz equation. This is surprising in light of the complete damping of the combustion instability. Previous acoustic liner testing on other programs has shown that reduction of the amplitude of the instability has produced a corresponding reduction in the chamber heat flux. The difference between the low heat fluxes (approximately 275 Btu/lb) encountered in stable flox/butene-1 tests with triplet injector R (1-C) and the higher heat fluxes in unstable tests with triplet injector R (2-B) indicates that instability was a major contributor to high heat fluxes in previous tests. Figures VI-19 and VI-20 show that very little carbon was deposited on the wall in either the chamber or exhaust nozzle, an indication of oxidizer combustion products near the wall. Apparently the propellant distribution produced by the pentad element geometry prevented carbon buildup on the chamber wall, and this distribution, rather than combustion instability, was the predominant factor in the high heat fluxes encountered.

Axial Thermocouples are  
Located at this Position

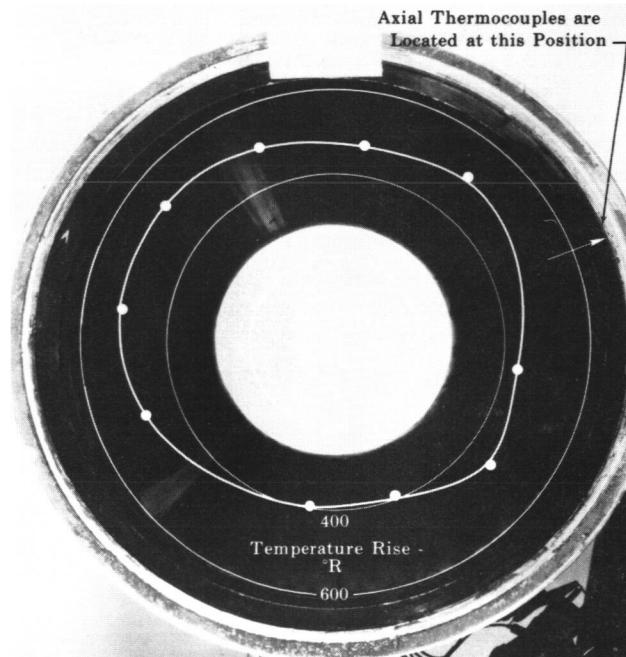


Note:  
Temperature rise taken  
6.0 sec from start of test

Figure VI-14. Circumferential Throat Temperature Rise Profile:  
Methane Test No. 6UA (Superimposed on Copper  
Chamber Photograph Taken After the Test)

FD 19770

Axial Thermocouples are  
Located at this Position



Note:  
Temperature rise taken  
6.0 sec from start of test

Figure VI-15. Circumferential Throat Temperature Rise Profile:  
Methane Test No. 11UA (Superimposed on Copper  
Chamber Photograph Taken After the Test)

FD 19771

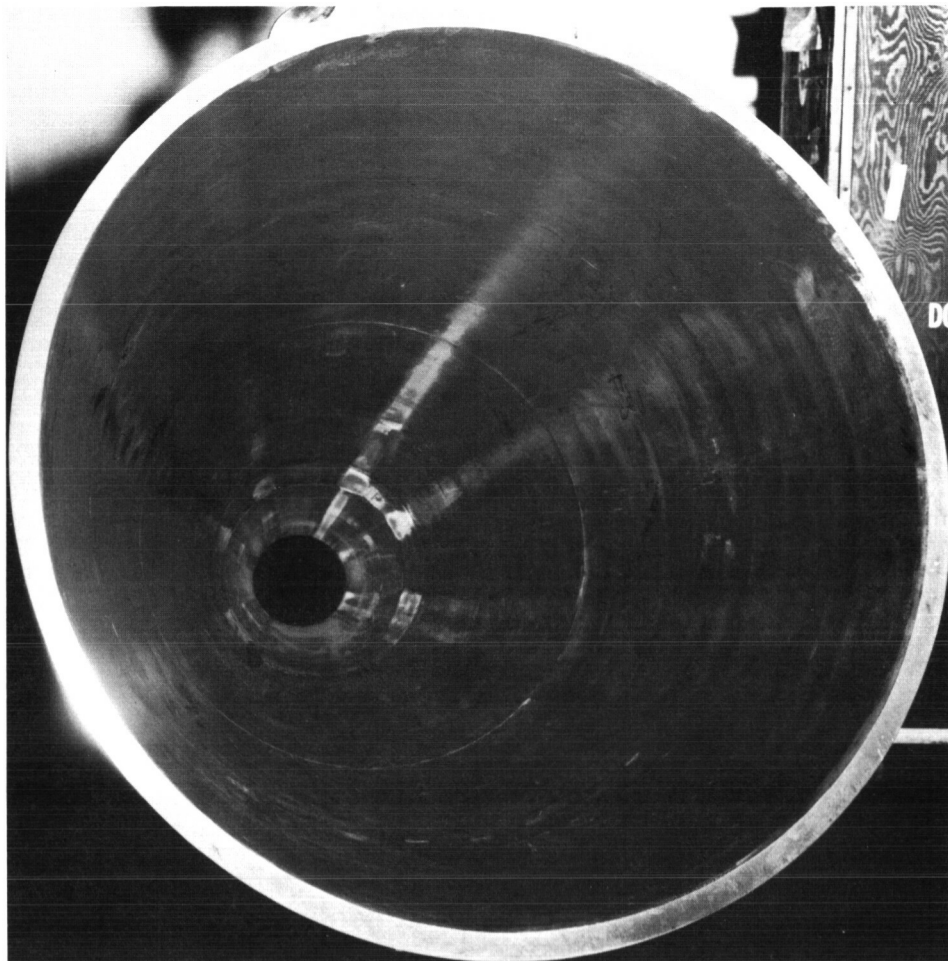


Figure VI-16. Nozzle Deposits After Test No. 6UA (Flox/Methane)

FE 60095

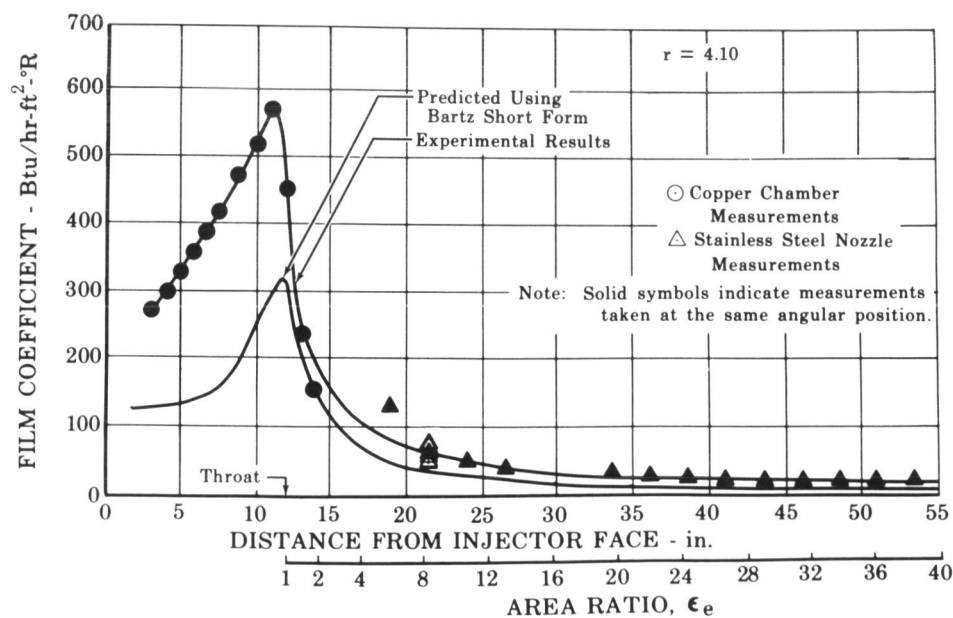


Figure VI-17. Comparison of Flox/Butene-1 Heat Transfer Coefficients: Test No. 12UA

FD 19772

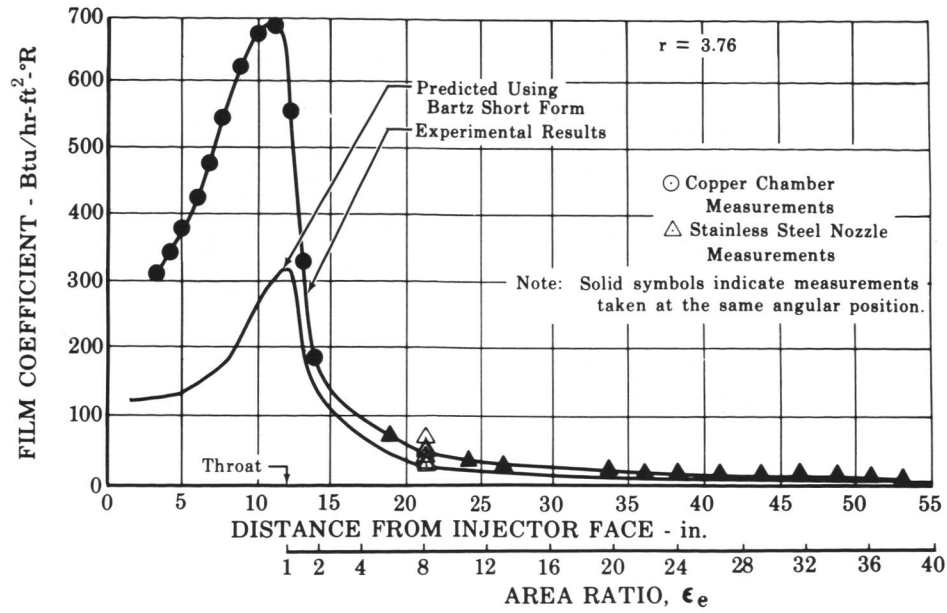


Figure VI-18. Comparison of Flox/Butene-1 Heat Transfer Coefficients: Test No. 14UA

FD 19773

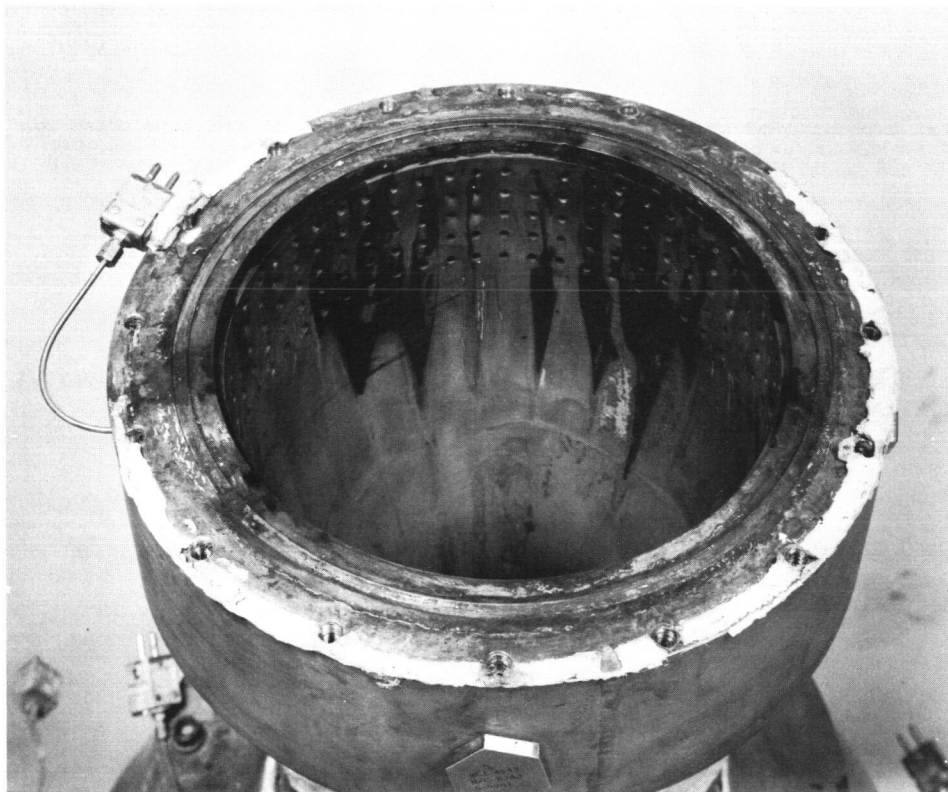


Figure VI-19. Chamber Deposits After Test No. 16UA (Flox/Butene-1)

FE 65565



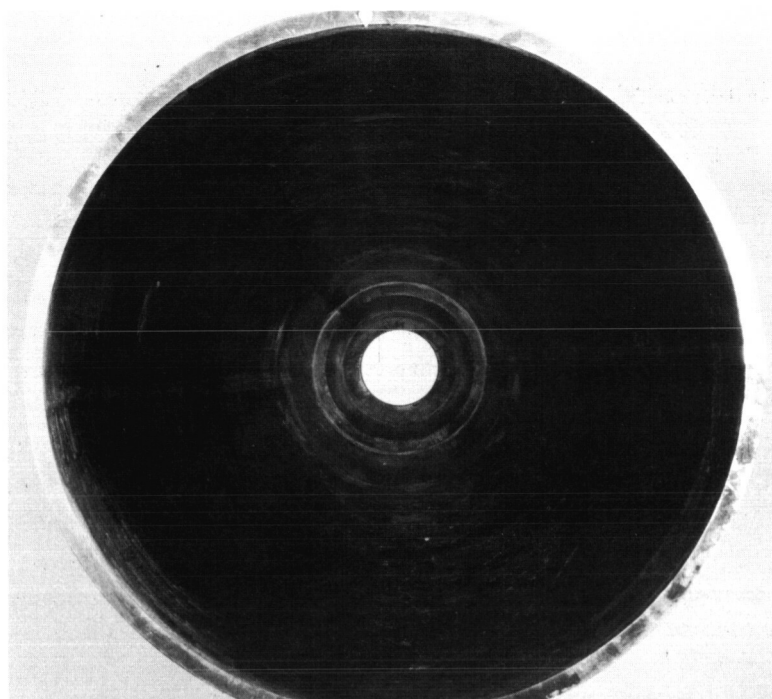


Figure VI-20. Nozzle Deposits After Test No. 16UA (Flox/Butene-1)

FE 65566

Table VI-6 shows a comparison of measured and theoretical heat losses in various sections of the engine. The average ratio of measured-to-theoretical total heat loss rates for the chamber and nozzle in the methane tests was 0.78 compared to 2.00 for the butene-1 tests. The average ratio of measured-to-theoretical heat transfer rates in the stainless steel skirt was 0.74 for methane and 1.83 for butene-1. The value of this ratio was relatively unaffected by mixture ratio whereas the chamber data presented in Section V showed a definite reduction at low mixture ratios. For both fuels approximately 55% of the total heat transferred occurred upstream of the nozzle throat.

TABLE VI-6. MEASURED AND PREDICTED HEAT TRANSFER RATES FOR ALTITUDE TESTS

Test No.	Fuel	Mixture Ratio	Total Measured Heat Loss Rate, Btu/sec	Total Theoretical Heat Loss Rate, Btu/sec	$\left(\frac{Q_{\text{measured}}}{Q_{\text{theoretical}}}\right)_{\text{total}}$ %	$\left(\frac{Q_{\text{measured}}}{Q_{\text{theoretical}}}\right)_{\text{skirt}}$ %	Percent of Total Heat Transferred to Chamber
2UA	Methane	4.54	1144	1277	89.5	79.2	62.2
3UA	Methane	5.16	1099	1209	91.0	80.8	61.2
4UA	Methane	4.17	1109	1310	84.7	80.0	60.0
5UA	Methane	3.81	981	1388	70.7	67.1	58.5
6UA	Methane	3.57	937	1471	63.7	63.0	57.3
7UA	Methane	3.85	1115	1471	75.8	84.5	49.7
8UA	Methane	3.67	1059	1455	72.8	79.1	51.4
9UA	Methane	4.00	1065	1488	71.6	73.6	54.8
10UA	Methane	4.96	957	1344	71.2	68.7	56.9
11UA	Methane	5.99	874	1016	84.5	67.8	61.6
12UA	Butene-1	4.10	2321	1181	197	200	52.6
13UA	Butene-1	2.77	2538	1301	195	231	48.9
14UA	Butene-1	3.76	2223	1099	202	150	61.5
15UA	Butene-1	3.68	2554	1320	194	166	56.4
16UA	Butene-1	4.66	2327	1104	211	168	59.9

## SECTION VII

### TRANSPIRATION-COOLED ALTITUDE TESTS — TASK IV

#### A. TEST DESCRIPTION

Ten transpiration-cooled altitude tests were conducted to evaluate transpiration-cooling flow requirements with liquid methane and the performance degradation caused by incomplete mixing of the coolant and combustion products. The test rig, shown mounted on the test stand in figure VII-1, consisted of the transpiration-cooled chamber and uncooled nozzle described in Section III. Injector R(1C) was used for all tests. Propellant inlet conditions were 82.6% flox at 160°R and liquid methane at approximately 200°R. Coolant flow rates were varied from an initial conservative value, 8% of the total flow, to the minimum predicted value of 4%. The test durations and operating conditions are shown in table VII-1. During six of the tests injector mixture ratio excursions were made to provide a wide range of data with a minimum number of tests.

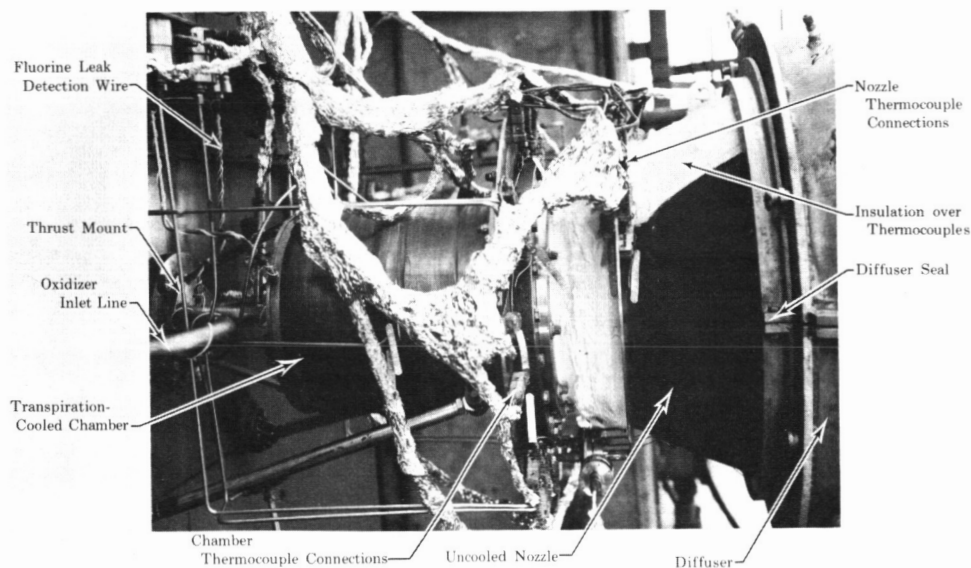


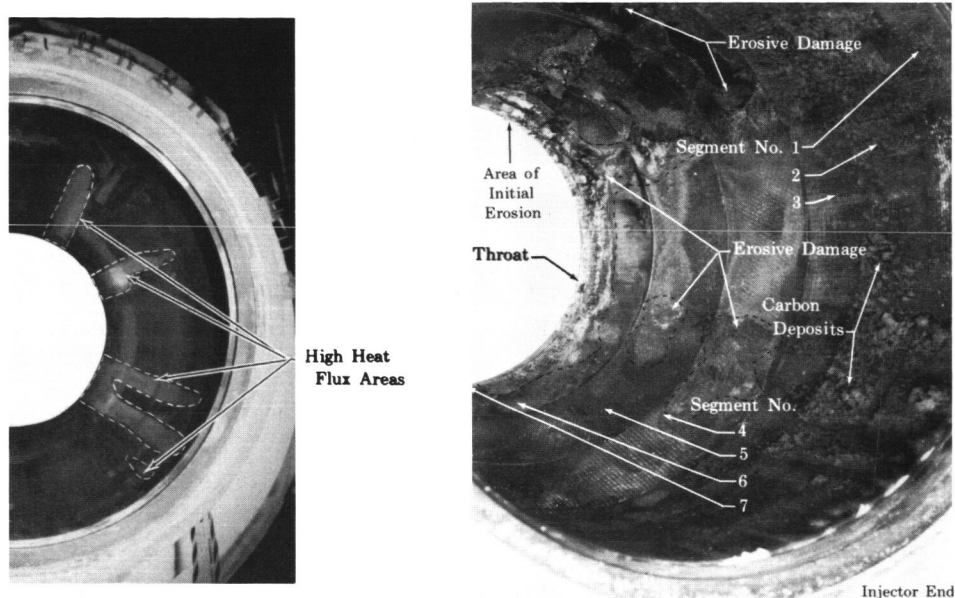
Figure VII-1. Transpiration-Cooled Chamber Mounted in Test Facility

FD 19774

TABLE VII-1. TEST CONDITIONS — TRANSPIRATION-COOLED TESTS

Test No.	Fuel	Percent F <sub>2</sub> in F <sub>1</sub> Cx	Test Duration, sec	Excursion Duration, sec	P <sub>c</sub> , psia	F <sub>1</sub> , lb	$\dot{Q}_{c1}$ , lb/sec	$\dot{Q}_{c2}$ , lb/sec	T <sub>01</sub> , °R	T <sub>02</sub> , °R	T <sub>03</sub> , °R	T <sub>04</sub> , °R	$\Delta P_{01}$ , psi	$\Delta P_{02}$ , psi	Injector	Percent of Total Propellant Used for Cooling	Ignition Delay, millise	Diffuser Pressure, psia	Comments
1T	Methane	82.6	3.0	--	110.6		11.4	2.63	1.23	152	189		6	117	R(1-C)	8.06	110	0.22	Shutdown due to false high temperature reading.
2T	Methane	82.6	6.0	--	108.5	5452	11.1	2.73	1.20	155	194	200	5	118	R(1-C)	7.98	50	0.23	Check out test.
3T-1	Methane	82.6	10.0	5.5	103.1	5192	11.3	1.95	1.26	152	194	197	19	58	R(1-C)	8.68	50	0.23	
3T-2				4.5	104.4	5301	12.2	1.62	1.20	163	192	194	24	44		7.99	50	0.20	
4T-1	Methane	82.6	10.0	5.5	100.4	4975	10.3	2.44	1.00	165	210	214	18	118	R(1-C)	7.26	50	0.28	
4T-2				4.5	99.1	4910	10.5	1.94	0.90	152	197	209	17	72		6.71	50	0.26	
5T-1	Methane	82.6	10.0	5.5	102.1	5038	11.0	2.70	0.61	152	197	210	16	107	R(1-C)	4.23	50	0.25	
5T-2				4.5	101.1	5034	10.8	2.10	0.60	153	193	210	18	78		4.42	50	0.24	
6T-1	Methane	82.6	7.9	5.5	97.1	4645	11.6	1.75	0.51	151	206	213	20	55	R(1-C)	4.37	50	0.22	Shutdown due to low coolant flow.
6T-2				2.4	96.8	4793	11.7	1.57	0.60	149	203	214	24	44		4.33	50	0.22	
7T	Methane	82.6	8.3	--	103.9	5455	11.3	2.80	1.17	153	194	196	15	91	R(1-C)	7.82	60	0.28	Chamber damage due to coolant leakage.
8T	Methane	82.6	8.6	--	100.9	5122	11.1	2.47	0.75	161	205	200	19	171	R(1-C)	5.24	50	0.20	Shutdown due to oxidizer flow oscillation.
9T-1	Methane	82.6	20.0	7.0	105.9	5393	10.8	2.75	0.57	154	195	206	17	168	R(1-C)	4.01	118	0.20	
9T-2				7.0	104.0	5244	11.0	2.62	0.37	181	186	201	18	169		4.05		0.19	
9T-3				6.0	104.6	5237	11.0	2.44	0.37	175	185	201	17	149		4.08		0.19	
10T-1	Methane	82.6	30.0	11.0	101.0	4931	11.5	1.96	0.36	154	196	225	18	76	R(1-C)	4.01	30	0.20	
10T-2				9.0	98.6	4821	11.5	1.79	0.38	177	194	222	20	72		4.17		0.19	
10T-3				10.0	99.0	4856	12.1	1.65	0.57	168	190	211	20	61		4.01		0.20	

During the first series of six transpiration-cooled tests, nonuniform erosion of the Rigimesh chamber walls was noted, and the erosion progressed with each test. After these six tests the Rigimesh chamber walls were eroded in four segments just upstream of the throat and in the first segment of the diverging section. Damage to the Rigimesh on most segments was confined to the top layers of the eight-layer Rigimesh, except for the upstream throat segment, which was completely eroded through in several places. The eroded areas were found to correspond directly to the high heat flux areas found in uncooled altitude tests conducted with this injector as shown in figure VII-2. The severe damage of the upstream throat segment resulted from the large percentage of the coolant flow diverted from the Rigimesh after the initial erosion was completely through.



Uncooled Chamber

Transpiration-Cooled Chamber

Figure VII-2. Correlation of Uncooled Chamber Heat Flux Pattern  
With Transpiration-Cooled Chamber Damage

FD 19775

Prior to test No. 7, fuel coolant holes were drilled in the injector face to provide uniform circumferential heat distribution (see Section VI). This test was aborted by a high Rigimesh temperature reading. Erosive damage occurred to both throat segments, with temperature distortion of the Rigimesh flow characteristics noted in the five upstream chamber segments. Data indicated that the chamber damage was caused by coolant leakage between the segments that resulted in reduced coolant flow through the Rigimesh walls. During chamber disassembly it was found that coolant leakage occurred between the segments because of improper sealing.

For the third series of tests, the chamber was modified to accept additional chamber assembly pins to assure adequate compression of the rubber sealing compound used between the segments. No hardware damage was noted after the first two tests (8.6 and 20 seconds duration). After the third test in this series, superficial Rigimesh erosion was found in several

segments with severe erosion of the downstream throat segment. Data revealed that the downstream throat segment eroded through at about 14 seconds into this 30-second test. The severity of the erosion in this segment was again due to coolant flow diversion from the Rigimesh, once the segment had eroded through. There was no damage to the upstream throat segment. This test was conducted using the predicted minimum permissible coolant flow rate, approximately 4% of the total flow. The failure was apparently a result of Rigimesh porosity changes that occurred at local high heat flux areas.

## B. PERFORMANCE

Table VII-2 present calculated performance data for the ten transpiration-cooled tests. Performance data reduced in accordance with the methods described in Appendix A. Figure VII-3 presents vacuum specific impulse and vacuum specific impulse efficiency as a function of engine mixture ratio and percent propellant used for cooling. As expected from the no-mixing performance predictions, the data show a peak specific impulse at a lower engine mixture ratio than the uncooled tests. The maximum performance occurs when the injector propellants, approximately 95% of the total flow, are operating near their optimum mixture ratio. The higher peak specific impulse measured in the transpiration-cooled tests is caused by performance gains realized from increased mixing in the chamber. Apparently, the effect of coolant mixing is substantial so that, not only are the transpiration-cooling losses small, but the injector performance (or, more correctly, the performance of the propellants flowing through the injector) is improved as well. The characteristic exhaust velocity efficiency, which is shown in figure VII-4, was calculated using the propellant flow introduced upstream of the throat. The data from tests No. 7T and 10T-3 were eliminated from figure VII-4 because throat erosion during these tests produced questionable characteristic velocities. The higher characteristic exhaust velocity efficiencies (based on injector mixture ratio) of the transpiration-cooled tests, as compared with the uncooled tests, were again probably the result of increased turbulence promoted by the partial mixing of the coolant and combustion gases upstream of the throat. The characteristic exhaust velocity efficiency that is shown in figure VII-5 was calculated using the total propellant flow rate. This parameter and the vacuum thrust coefficient efficiency, also shown in figure VII-5, are useful for predicting vacuum specific impulse efficiency from the following relationship:

$$\eta_{I_{vac}} = \eta_c^* \eta_{C_F_{vac(cor)}}$$

where  $\eta_c^*$  and  $\eta_{C_F_{vac(cor)}}$  are determined at equal engine mixture ratios. The thrust coefficient efficiency for the transpiration-cooled tests is somewhat higher than the uncooled tests because of the coolant addition downstream of the nozzle throat.

TABLE VII-2. CALCULATED PERFORMANCE DATA — TRANSPIRATION.  
COOLED TESTS

Test No.	Fuel	$r_{inj}$	$r_{chamber}$	$r_{eng}$	$c^*(1)$ ft/sec	$I'_{vac}$ sec	$C'_{Fvac}$ (2)	$Q_p$ Btu/sec	$c^*P_c$ ft/sec	$\eta_{c^*P_c}$ (3)	$\eta_{c^*P_c}$ (cor)	$\eta_{I_{vac}}$	$\eta_{I_{vac}}$ (cor)	$I_{vac}$ sec	$I_{vac}$ (cor)	$C_{Fvac}$	$\eta_{C_{Fvac}}$	$\eta_{C_{Fvac}}$ (cor)	$\Delta t$ Used, sec
1T	Methane	4.33	3.20	2.95	6637	386	1.869	350	6451	0.965	0.940	0.950	0.953	362	365	1.812	0.973	0.999	0.8
2T	Methane	4.08	3.09	2.83	6660	381	1.863	350	6575	0.987	0.962	0.950	0.953	362	365	1.812	0.973	0.999	1.3
3T-1	Methane	5.78	3.90	3.52	6777	395	1.890	350	6488	0.957	0.932	0.905	0.908	358	359	1.815	0.960	0.986	0.3
3T-2	Methane	7.54	4.86	4.33	6937	406	1.911	350	6348	0.915	0.892	0.871	0.873	354	356	1.830	0.958	0.984	1.2
4T-1	Methane	4.22	3.22	3.00	6681	386	1.870	350	6641	0.994	0.968	0.939	0.942	362	364	1.787	0.956	0.981	1.4
4T-2	Methane	5.44	4.05	3.72	6805	398	1.896	350	6757	0.993	0.967	0.925	0.928	368	370	1.786	0.942	0.967	4.2
5T-1	Methane	4.07	3.51	3.32	6722	393	1.883	350	6443	0.959	0.934	0.900	0.903	353	354	1.785	0.948	0.973	0.3
5T-2	Methane	5.16	4.30	4.01	6857	403	1.906	350	6764	0.986	0.961	0.925	0.928	372	374	1.795	0.942	0.967	1.8
6T-1	Methane	6.30	5.03	4.67	6947	410	1.913	350	6588	0.948	0.924	0.848	0.850	347	349	1.718	0.899	0.923	0.9
6T-2	Methane	7.46	5.86	5.40	6969	416	1.921	350	6483	0.930	0.906	0.829	0.830	345	346	1.732	0.902	0.926	0.9
7T	Methane	4.52	3.21	3.08	6682	387	1.872	350	6296	0.942	0.918	0.947	0.950	367	368	1.893	1.011	1.038	4.2
8T	Methane	4.50	3.66	3.45	6742	395	1.887	350	6500	0.964	0.939	0.909	0.912	358	360	1.798	0.953	0.978	4.7
9T-1	Methane	3.95	3.44	3.27	6715	392	1.881	350	6751	1.005	0.979	0.954	0.958	374	375	1.802	0.958	0.984	2.7
9T-2	Methane	4.19	3.63	3.44	6736	395	1.887	350	6685	0.992	0.967	0.937	0.941	370	371	1.803	0.955	0.981	3.1
9T-3	Methane	4.51	3.86	3.65	6775	398	1.895	350	6742	0.995	0.969	0.938	0.941	374	375	1.804	0.952	0.977	2.1
10T-1	Methane	5.87	4.86	4.56	6934	409	1.912	350	6499	0.937	0.913	0.860	0.862	351	353	1.759	0.920	0.945	1.9
10T-2	Methane	6.43	5.20	4.86	6964	412	1.912	350	6420	0.922	0.898	0.844	0.846	348	349	1.763	0.922	0.946	4.1
10T-3	Methane	7.32	5.84	5.43	6974	416	1.921	350	6241	0.895	0.872	0.814	0.816	339	340	1.767	0.920	0.944	9.6

(1)  $c^*$  is determined at the chamber mixture ratio.

(2)  $I'_{vac}$  and  $C'_{Fvac}$  are determined at the engine mixture ratio.

(3) Delivered  $c^*P_c$  data is based on the total of the injector flow and the coolant flow introduced upstream of the throat.

(4)  $\Delta t$  used, is the amount of time over which the performance figures are averaged.

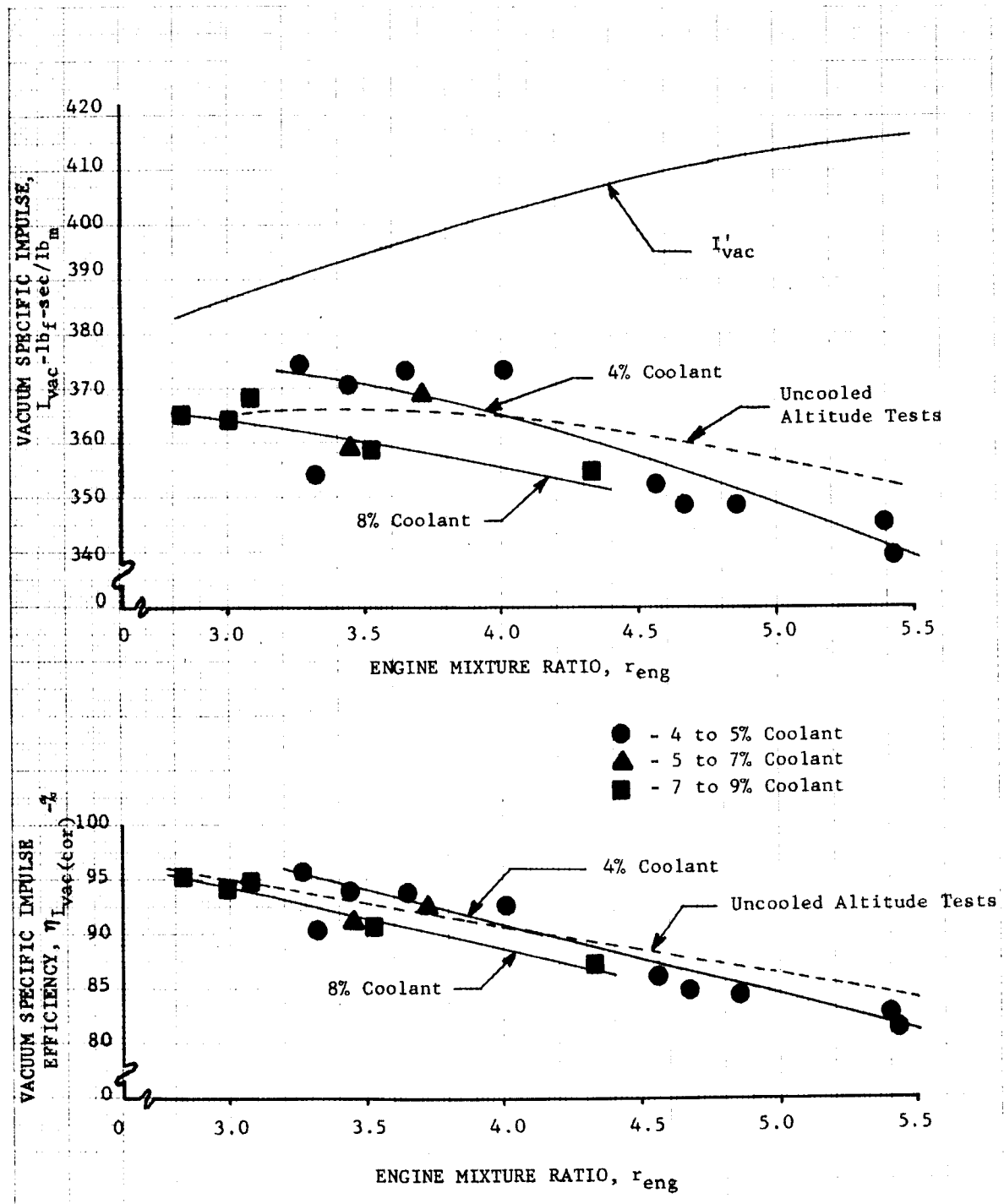


Figure VII-3. Flox/Methane Transpiration-Cooled Test Results — Vacuum Specific Impulse

DF 54406

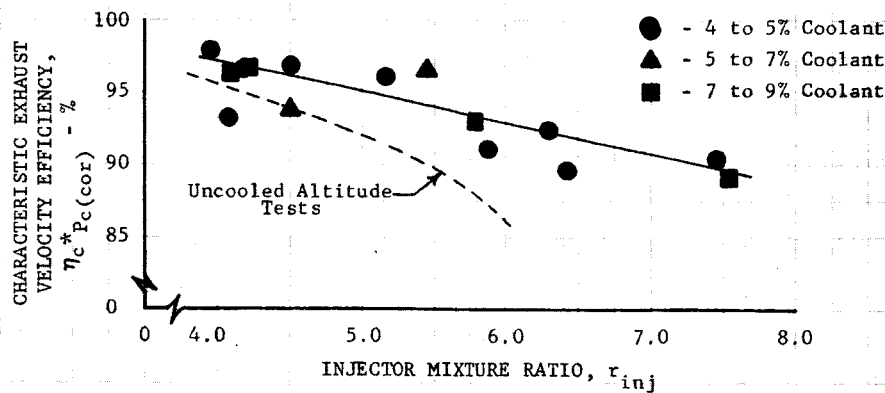


Figure VII-4. Flox/Methane Transpiration-Cooled Test Results — Characteristic Exhaust Velocity Efficiency

DF 54407

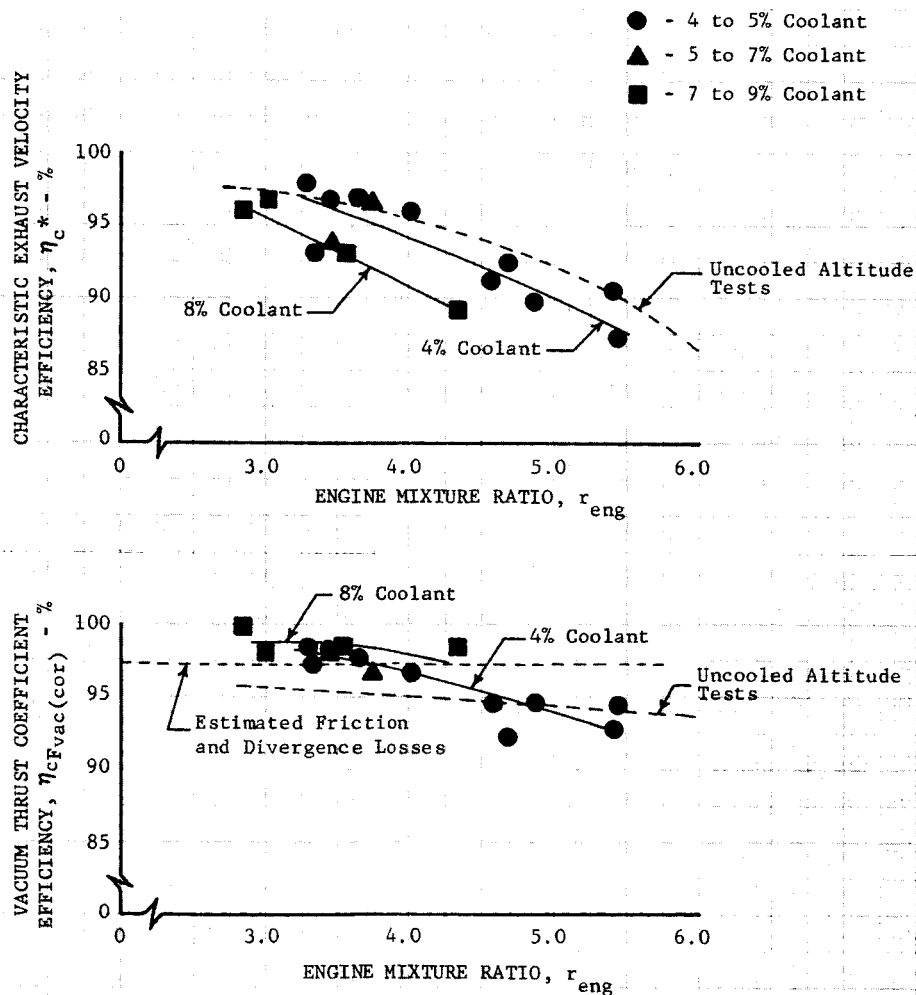


Figure VII-5. Flox/Methane Transpiration-Cooled Test Efficiencies

DF 54408



Vacuum specific impulse efficiency for the limiting case of no mixing between the injector propellant stream and coolant streams was calculated for each of the transpiration-cooled tests. The no-mixing calculations were based on the methods detailed in Appendix A (equation A-42). Characteristic exhaust velocity efficiencies, kinetic expansion efficiencies, and stream thrust coefficients used in these calculations were based on uncooled test results at the injector (main stream) mixture ratio. The contribution of the coolant was based on isentropic expansion of the individual segment flows entering at the segment Rigimesh hot-side temperature. Figure VII-6 compares the measured performance of each test with the no-mixing predictions. The no-mixing values were calculated using flow rates and inlet temperatures measured in each test. It can be seen that in all cases the measured performance was higher than the no-mixing prediction, indicating a significant amount of mixing between the streams. The amount of mixing and the performance gained will depend on a large number of variables, including: injector design, chamber configuration, amount of coolant used, and the thrust level. As shown in these tests, the increased mixing due to transpiration cooling can result in a performance increase at low mixture ratios.

### C. COOLING REQUIREMENTS

Table VII-3 presents coolant flow rates and Rigimesh combustion side temperatures for each of the eight chamber segments. Data in this table were averaged over the same time intervals as the performance data for the transpiration-cooled tests. Figure VII-7 shows the ratio of the calculated chamber heat transfer film coefficients to the film coefficients predicted from the uncooled tests. The calculated film coefficients are determined from the enthalpy rise of the coolant and the measured wall temperatures. It was assumed that the coolant exit temperature was equal to the Rigimesh hot-side temperature. Figure VII-8 gives the same ratio except that the predicted film coefficients are based on analytically determined values using the Bartz short form method. For most of the segments, figure VII-8 shows film coefficient ratios closer to the anticipated value of 1.0 than figure VII-7. The higher film coefficient ratio in the first segment is attributed to injector effects similar to those observed in the uncooled tests. The low values of film coefficient measured in the eighth segment were due to coolant carryover effects because of high coolant flow rates from the two throat segments. These data are consistent with those found under Contract NAS3-4195 (Reference 1) and indicate that the factors that reduce the film coefficients in the uncooled tests (presumably carbon deposition or free carbon in the boundary layer) are partially negated by the coolant flow, and that the analytically predicted film coefficients based on the Bartz short form are more valid for predicting transpiration-cooling-flow requirements. The data indicate that the film coefficient tends to increase with higher coolant flow rates. This contrasts with the

results of other investigators using gaseous coolants, such as hydrogen, nitrogen, and air. References 22 and 23 present correlations that show decreasing film coefficients with increasing coolant flow rates. This anomaly may be caused by the reduction in effect of carbon formation at high flow rates.

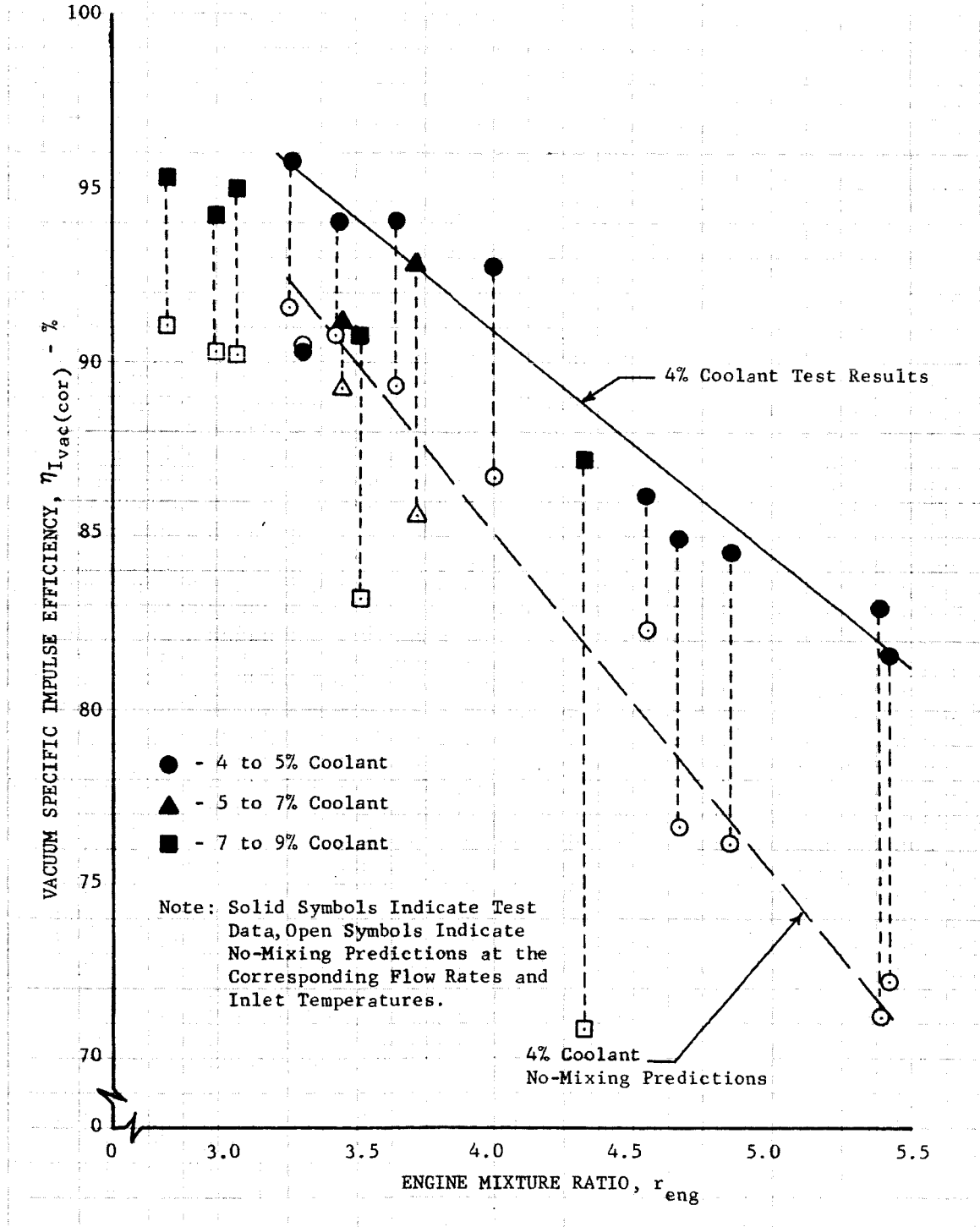


Figure VII-6. Comparison of Measured and No-Mixing Predicted Vacuum Specific Impulse for Transpiration-Cooled Tests

DF 54409

TABLE VII-3. COOLANT FLOW AND RIGIMESH TEMPERATURE DATA

Test No.	Segment 1 (1)		Segment 2		Segment 3		Segment 4		Segment 5		Segment 6		Segment 7		Segment 8	
	Wall Temperature, °R	$(\dot{Q}_c/A) \times 10^3$ , lb/sec-in <sup>2</sup>	Wall Temperature, °R	$(\dot{Q}_c/A) \times 10^3$ , lb/sec-in <sup>2</sup>	Wall Temperature, °R	$(\dot{Q}_c/A) \times 10^3$ , lb/sec-in <sup>2</sup>	Wall Temperature, °R	$(\dot{Q}_c/A) \times 10^3$ , lb/sec-in <sup>2</sup>	Wall Temperature, °R	$(\dot{Q}_c/A) \times 10^3$ , lb/sec-in <sup>2</sup>	Wall Temperature, °R	$(\dot{Q}_c/A) \times 10^3$ , lb/sec-in <sup>2</sup>	Wall Temperature, °R	$(\dot{Q}_c/A) \times 10^3$ , lb/sec-in <sup>2</sup>	Wall Temperature, °R	$(\dot{Q}_c/A) \times 10^3$ , lb/sec-in <sup>2</sup>
2T	1447	1.95	836	1.76	1310	1.91	1326	1.97	1217 (2)	2.99	1007 (2)	5.39	1483	3.83	1104	1.43
3T-1	1464	2.09	800	1.98	1253	2.08	1479	2.07	978 (2)	3.15	749 (2)	6.00	1020	3.69	510	1.35
3T-2	1400	2.01	799	1.90	1325	1.98	1435	1.96	801 (2)	2.93	599 (2)	5.59	720	3.58	646	1.30
4T-1	1245	1.71	713	1.56	970	1.66	1471 (2)	1.66	1372 (2)	2.47	1065 (2)	4.89	1380 (2)	2.76	531	1.06
4T-2	1466	1.52	987	1.42	1357	1.51	1743	1.48	1365 (2)	2.25	1300	3.99	713	2.67	999	1.01
5T-1	1525	0.95	666	0.90	1232	0.97	2130 (2)	0.88	1946 (2)	1.40	1530 (2)	2.96	1672 (2)	2.67	777	0.76
5T-2	1608	0.93	739	0.87	1406	0.95	1808	0.75	1860 (2)	1.32	1172	2.94	884	2.05	1157	0.81
6T-1	1404	0.98	1171	0.91	1176	0.97	1696 (2)	0.90	1511 (2)	1.42	1172 (2)	3.03	1325 (2)	1.94	568	0.71
6T-2	1584	0.98	1114	0.87	1310	0.95	1661 (2)	0.76	1382 (2)	1.36	1108	3.06	1170 (2)	1.98	770	0.73
8T	1548	1.27	1322	1.24	964	1.20	1292	1.23	1039	1.63	721	3.91	1412	2.12	944	0.78
9T-1	1942	0.93	1479	0.94	1502	0.90	1748	0.70	1804	1.18	1625	2.85	1354	1.89	1453	0.70
9T-2	1271	0.89	1330	0.95	825	0.89	1050	0.55	2800	1.14	1865	2.73	966	1.94	2128	0.73
9T-3	1211	0.90	1375	0.97	749	0.90	850	0.87	2643	1.18	1706	2.64	1124	1.91	2073	0.70
10T-1	2110	0.92	1654	0.96	1706 (2)	0.89	1810 (2)	0.92	1435	1.14	1027	2.66	1821	1.78	896	0.67
10T-2	2239	0.95	1483	1.00	1505 (2)	0.93	1618 (2)	0.96	1859	1.24	844	2.64	1824	1.82	1320	0.67
10T-3	2060	0.95	1646	0.99	1040 (2)	0.92	1503 (2)	0.96	2252	1.24	957	2.57	1780	1.82	1373	0.66

(1)  $\dot{Q}_c/A$  = Coolant flow (lb/sec) per area of Rigimesh (in<sup>2</sup>) for segment.

(2) Bad thermocouple reading; temperature estimated from coolant flow and heat flux predicted by Bartz short form method.

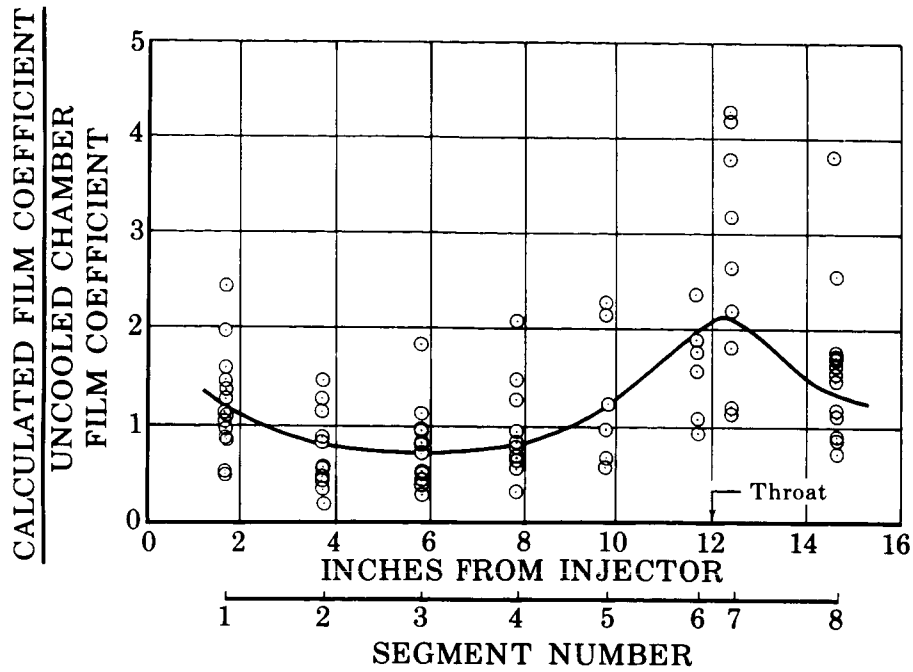


Figure VII-7. Ratio of Transpiration-Cooled Chamber Film Coefficients to Film Coefficients From Uncooled Chamber

FD 22537

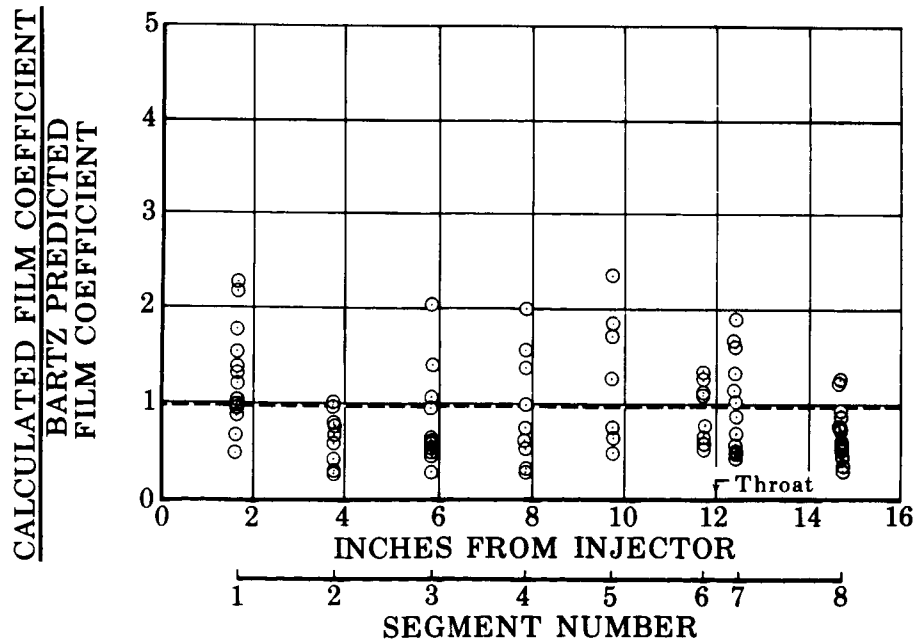


Figure VII-8. Ratio of Transpiration-Cooled Chamber Film Coefficients to Bartz Short Form Predicted Film Coefficients

FD 22536

#### D. NOZZLE HEAT TRANSFER

Figure VII-9 compares average nozzle coefficients (calculated from nozzle skin temperature data) obtained in the transpiration-cooled tests to those obtained in the uncooled altitude tests and those analytically predicted by the Bartz short form method. A significant reduction in film coefficient because of the effect of transpiration-coolant carryover is shown. This reduction exists for a considerable distance downstream from the nozzle attachment point and is dependent on the coolant flow rate. As discussed in Section III-E, this film cooling effect is sufficient to allow use of a radiation cooled nozzle extension downstream of an expansion ratio of 9.0 in a 100 psia, 5000-lb thrust engine.

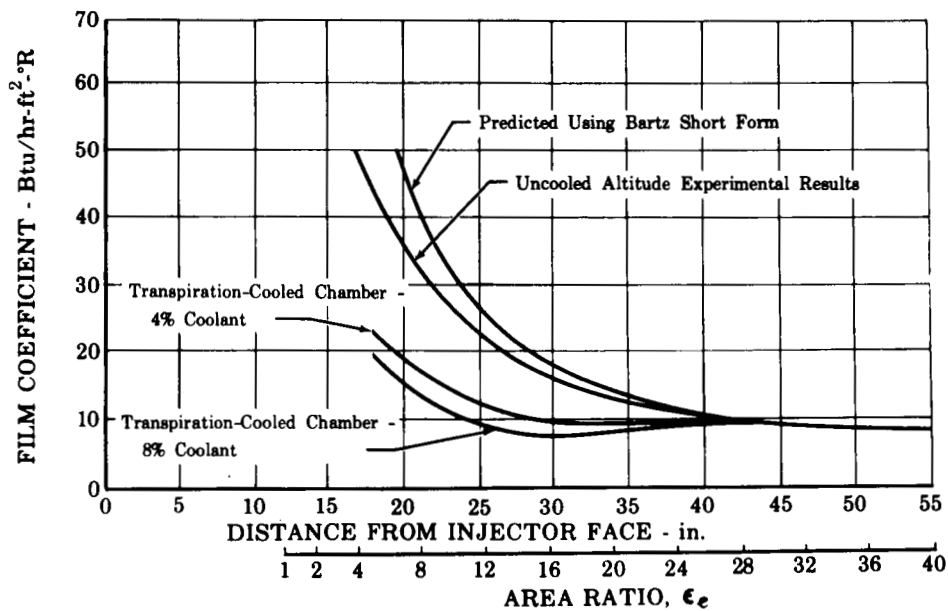


Figure VII-9. Comparison of Flox/Methane Average Nozzle Heat Transfer Film Coefficients

FD 19776

## SECTION VIII

### REGENERATIVELY COOLED ALTITUDE TESTS — TASK V

#### A. TEST DESCRIPTION

Two flox/butene-1 convectively cooled tests were made under simulated altitude conditions using the steam-driven ejector system. Injector R (1-C) was used with the modified RL10 pass-and-a-half tubular thrust chamber discussed in Section III. Liquid flox was injected at approximately 160°R and liquid butene-1 was supplied at approximately 190°R. The tests were supplementary cooled with the coolant flow controlled separately from the injector fuel flow. The cooling jacket exit pressure was maintained at 150 psia by a computer-controlled electrohydraulic valve operating in a pressure control mode.

Test No. 1R ran the programed 10.0 seconds with a constant 7.5 lb/sec coolant flow rate, approximately 1.9 times the injector fuel flow. Post-test inspection of the chamber revealed that 11 of the 180 tubes had been burned through at the tube ends nearest the injector face (approximately 1.3 inches from the injector face). The inner wall of the coolant inlet manifold was also eroded and showed definite indications of oxidizer impingement. Several additional tubes had small splits in the chamber section, probably as a result of the reduced coolant flow through the complete tubes. The erosion and splitting of the tubes can be seen in figure VIII-1.

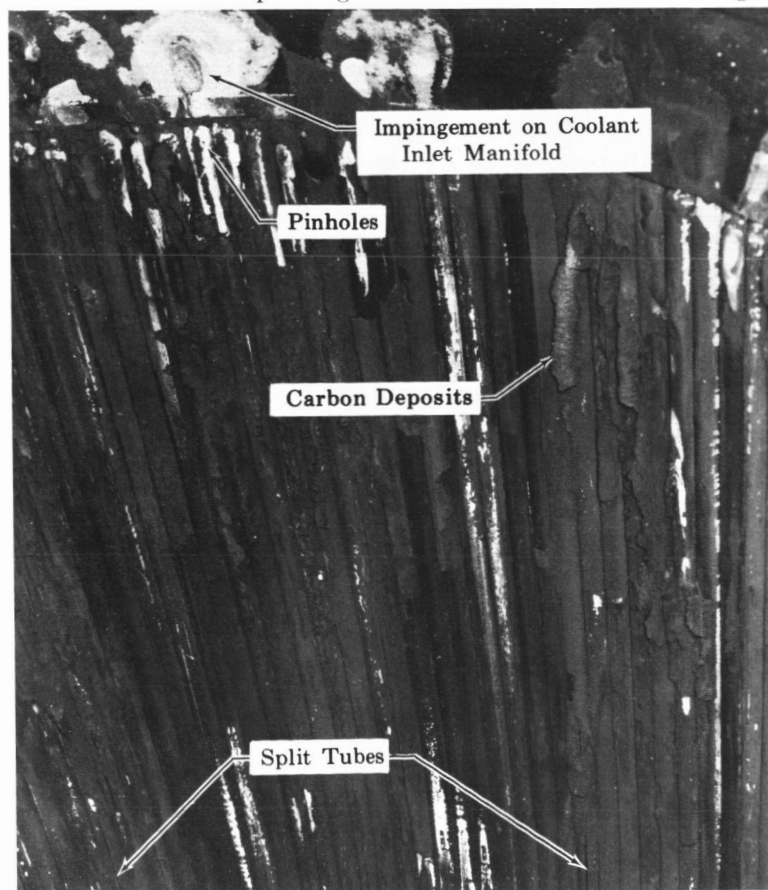


Figure VIII-1. Damage to Tubular Chamber After Test 1R

FD 19777

A gradual closing of the jacket exit pressure control valve (at constant coolant inlet flow rate) indicated that the initial burnout occurred approximately 1.3 seconds after the start of the test or approximately 0.5 second after full chamber pressure was reached. The position of this valve at the end of the test indicated that about 45% of the coolant was being diverted through the holes in the tubes and into the combustion chamber.

The chamber damage was attributed to several factors as follows:

1. An oxidizer flow-measuring transducer experienced a zero shift during the start transient. Because this transducer was used as a reference by the control system, the oxidizer flow rate was approximately 30% higher than the programed set point. This resulted in a high mixture ratio and a chamber pressure of approximately 125 psi.
2. The high chamber pressure caused a reduction in the fuel flow rate by reducing the injector differential pressure and by increasing the injector face heat flux, thereby choking off the fuel through the porous Rigimesh face. The combination of high oxidizer flow and low fuel flow resulted in a mixture ratio approximately 70% higher than the set point value.
3. Irregular carbon formation on the walls immediately downstream of the injector indicated that oxidizer impingement occurred. This was attributed to distortion of the fuel flow caused by the excessive chamber pressure and injector face heat flux.
4. The burnout occurred early in the test before an equilibrium carbon layer had time to develop. Test results from Contract NAS3-4195 (Reference 1) indicated that from 4.0 to 6.0 seconds were required to build up an equilibrium carbon layer and during this time heat fluxes are higher than equilibrium values.
5. The low coolant pressure drop, i.e., approximately 2.0 psi, through the RL10 chamber probably resulted in some nonuniform coolant distribution.

It was surmised that none of these problems was severe enough to have individually caused the damage; however, it was decided that additional chamber modifications should be made to increase the cooling margin in the chamber region. A second chamber using tube fillers and a high conductivity filler braze (see Section III-F) was fabricated for additional testing. This modified chamber was used in test No. 2R using the same flow rates originally programed for test No. 1R. A controls sequence change was made to decrease the opening rate of the oxidizer control valve. This was done to reduce the possibility of a transducer shift and also to provide a fuel-rich period to increase the rate of carbon buildup. This test ran the programed 10.0 seconds; however, chamber damage similar to that pre-

viously encountered was also sustained in this test. It is estimated that the initial burnout occurred at approximately 1.7 seconds into the test, or about 0.4 seconds after full chamber pressure was attained. Fifty-four of the 180 tubes were damaged in an area limited to the chamber for a distance of approximately 3 inches downstream of the injector. Definite indications of injector impingement were noted from the groupings of the damaged tubes and the appearance of the eroded silver filler. At the end of the test, approximately 35% of the coolant was being diverted into the chamber through the burned areas. The remainder of the chamber was satisfactorily cooled with the remaining coolant.

During test No. 2R the injector fuel pressure drop was significantly higher than predicted from measured flow areas and from water flow tests. The injector pressure drops increased with time, and for most of the run prevented full fuel flow from being achieved. Analysis of the fuel composition showed 97+% purity with no unusual contamination. The low temperature viscosity of the fuel was approximately equal to the literature value for pure butene-1 and no particulate contamination was found. It was concluded that the fuel properties did not cause the high injector pressure drops. Apparently, fusion of the Rigimesh face of the injector had occurred during the transpiration cooled methane tests to the point that satisfactory cooling of the injector face was no longer possible and local boiling occurred. The boiling produced the high injector pressure drops, and may also have distorted the fuel distribution, thereby increasing variations in the circumferential heat flux.

In both tests No. 1R and 2R a sudden rise in coolant inlet and outlet pressures was noted during the start transient as chamber pressure suddenly increased to the desired value. The rise in chamber pressure and coolant pressure occurred approximately 1.1 seconds after the test start, as shown in figure VIII-2 for test No. 2R. Because the coolant flow had been stabilized prior to the start transient and was completely separate from the injector flow, the sudden pressure rise can only be attributed to the sudden increase in chamber heat flux that occurred with the chamber pressure buildup. It is believed that this sudden increase in heat flux caused localized boiling that rapidly increased the bulk specific volume of the coolant. The rapid increase in volume caused a pressure surge to both the upstream and downstream coolant control valves, resulting in a sudden reduction in coolant flow. This type of pressure surge is commonly found with cryogenic fluids under somewhat different conditions (Reference 24). Oscillations in the measured coolant flow indicate that the pressure surge may have initiated coolant flow instability during this time. The oscillations ceased in approximately 0.5 second. The decrease in coolant pressure drop during this time (start +1.3 sec to start +1.8 sec) indicates this to be the time of burnout. The large fraction of the coolant flow which was diverted through holes in the tubes caused the coolant inlet pressure differential to decrease to approximately 25% of the pre-start value.



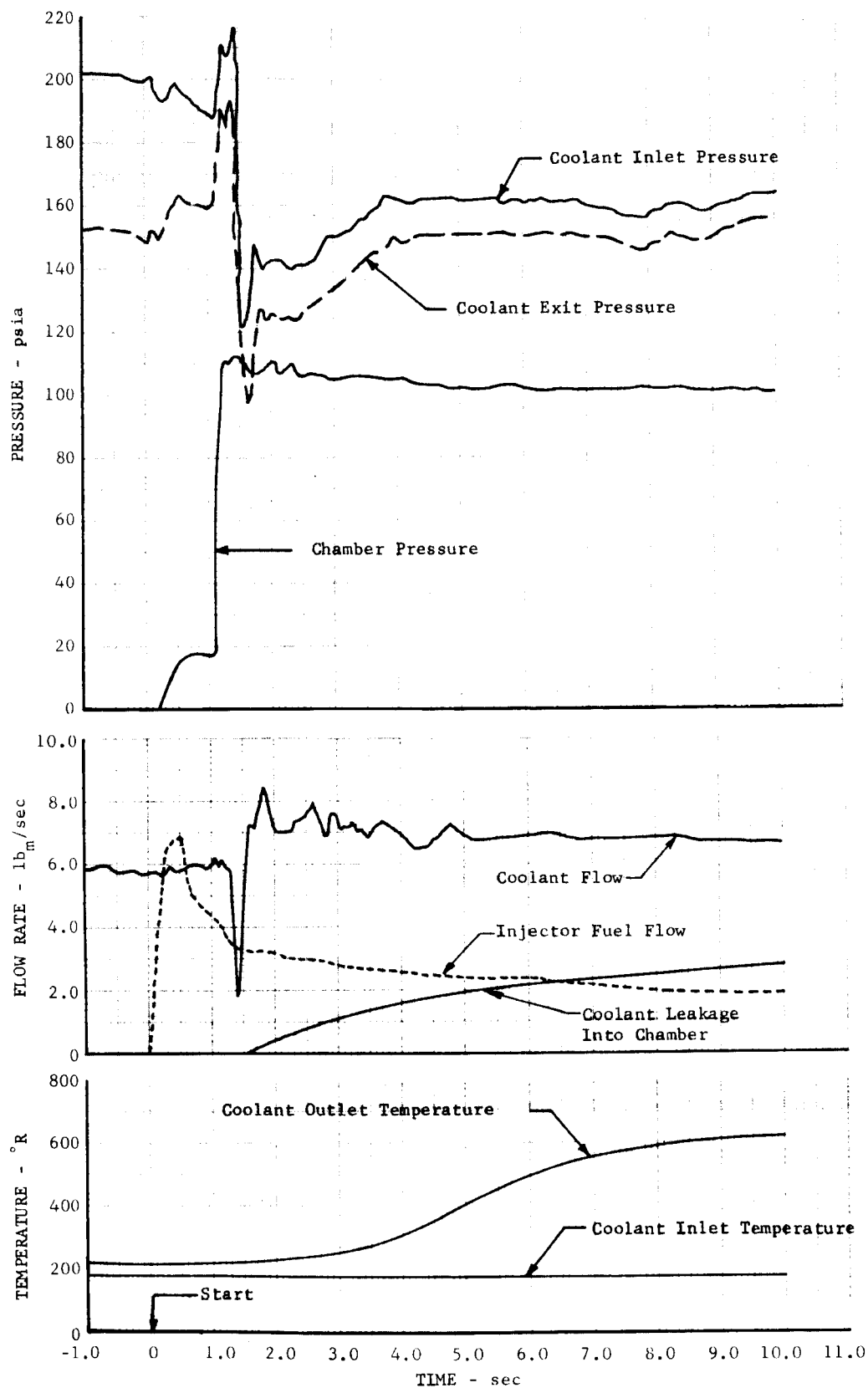


Figure VIII-2. Time History Showing Coolant Pressure Surge During Test No. 2R DF 57358

An inherent problem in regenerative cooling with butene-1, or any low hydrogen-to-carbon ratio hydrocarbon fuel, is variation in circumferential heat flux. Circumferential variations occur to some extent with any combination of propellants. This variation is caused by circumferential variations in the mixture ratio of the gases in contact with the wall and local variations in the radiation and turbulence level. These factors affect heat flux directly and for hydrocarbon fuels they can also affect the thickness of the carbon buildup on the wall. For hydrocarbon fuels with flox, particularly low hydrogen-to-carbon ratio hydrocarbon fuels, the effect of carbon deposition on the walls can have a much greater effect on the local heat transfer rate than the other factors listed. Thus, for similar injectors, flox/hydrocarbon combinations would be expected to have larger variations in circumferential heat flux than nonhydrocarbon fuels, and flox/butene-1 would be expected to produce higher variations in circumferential heat flux than flox/methane. Figure VIII-3 compares the circumferential temperature profiles for flox/butene-1 and flox/methane using the same injector at the same equivalence ratio. Propellant inlet velocities for the two tests are also nearly the same because the difference in density between the two fuels compensates for the difference in fuel mass flow rate. The relative variation in circumferential temperature rise is much larger for the butene-1 tests, even though the fuel flow through the Rigmesh, hence the amount of film cooling is greater with butene-1. At higher equivalence ratios the circumferential variations increase for both fuels but is always higher for flox/butene-1. As equivalence ratios approach 1.0, oxidizer rich streaks occur which completely eliminate the carbon layer and produce heat fluxes that in some cases exceed values predicted from the Bartz method.

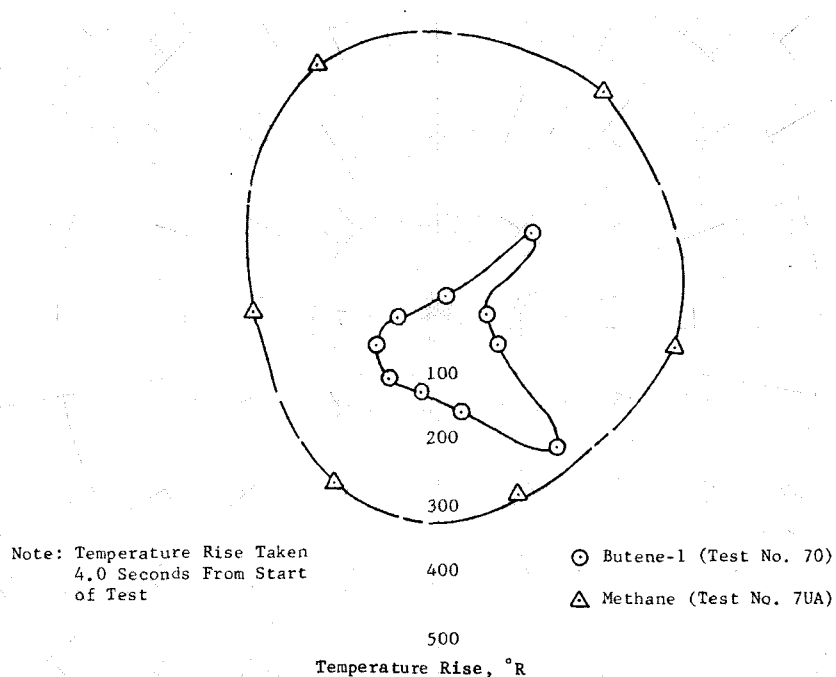


Figure VIII-3. Comparison of Methane and Butene-1 Temperature Profiles with Injector R(1C) DF 57359

It is not known how much the excessive fuel pressure drops may have adversely affected the coolant distribution and circumferential heat flux, or how much circumferential heat flux variations may have contributed to the coolant pressure surge. At this point it can only be concluded that for successful regenerative cooling circumferential heat flux variations and coolant pressure surge effects should be minimized.

In both of these tests the majority of the chamber tubes operated without damage for the full 10 seconds (8 seconds with reduced coolant flow). The satisfactory cooling of these tubes (and the damaged tubes in areas somewhat downstream of the injector) indicate that regenerative cooling with butene-1 can be accomplished with injectors designed to produce uniform circumferential heat flux.

## **B. PERFORMANCE**

Tables VIII-1 and VIII-2 present measured and calculated performance data for the regeneratively cooled tests. Performance data were reduced using the methods outlined in Appendix A. The propellant flow rates include the fuel flow that was injected through the burned areas of the coolant tubes. This leakage flow was determined by subtracting the jacket discharge flow rate from the coolant flow rate measured upstream of the jacket inlet. The discharge flow was estimated as a function of time from the recorded discharge valve position, jacket discharge temperature, jacket discharge pressure, and the known flow characteristics of the valve.

## **C. COOLING RESULTS**

Although in both of these tests almost half of the coolant flow was diverted into the combustion chamber through the burned areas, which occurred during the first two seconds of the firing, the majority of the tubes and the remainder of the burned tubes were effectively cooled for the remaining eight seconds. This indicates that regenerative cooling with butene-1 can be achieved; however, extreme care must be exercised to eliminate high heat flux areas caused by nonuniform injector patterns.

TABLE VIII-1. MEASURED PERFORMANCE DATA - REGENERATIVE-COOLING TESTS(1)

Test No.	Cooling Configuration	Test Duration, sec	$P_c$ , psia	$F$ , lb	$\dot{w}_o$ , lb/sec	$\dot{w}_f$ , lb/sec	$T_o$ , °R	$T_f$ , °R	$\Delta P_o$ , psi	$\Delta P_f$ , psi	Coolant Inlet Temperature, °R	Coolant Outlet Temperature, °R	Coolant Flow Rate, lb/sec	Coolant Inlet Pressure, psia	Coolant Outlet Pressure, psia	Ignition Delay, millise	Comments
1R	Supplementary	10.0	128.0	6523	12.4	6.72(2)	161	196	27	147	189	625	7.53(3)	158	155	65	Tube burnout at 1.3 seconds.
2R	Supplementary	10.0	103.5	5205	10.5	4.21(2)	156	204	21	155	188	620	6.50(3)	160	150	175	Burnout at 1.7 seconds.

(1) Tests were conducted with 70.4% flox/butene-1 using injector R(1-C).

(2) Includes coolant leakage.

(3) Coolant flow into jacket; approximately 45% of this was diverted through the burned tubes in test No. 1R, 35% in test No. 2R.

TABLE VIII-2. CALCULATED PERFORMANCE DATA - REGENERATIVE-COOLING TESTS

Test No.	Fuel	$r$	$\dot{w}_p$ , lb/sec	$c^*_{p_c}$ , ft/sec	$I'_{vac}$ , sec	$C^*_{p_c}$ , ft/sec	$c^*_{p_c}$ , ft/sec	$Q_c$ , Btu/sec	$Q_n$ , Btu/sec	$\eta_{c^*p_c}$	$\eta_{c^*p_c}$	$\eta_{c^*p_c}$	$I_{vac}$ , sec	$I_{vac}$ , sec	$\eta_{I_{vac}}$	$\eta_{I_{vac}}$	$\eta_{CF_{vac}}$	$\eta_{CF_{vac}}$	$\Delta t_{used}$ , sec	
1R	Butene-1	1.90(2)	19.1	6157	363	1.890	6116	5988	291	213	0.993	0.973	0.969	342	346	0.943	0.946	0.953	0.974	8.11
1R	Butene-1	2.5(2)	14.7	6463	381	1.899	6331	6152	317	233	0.979	0.952	0.958	353	357	0.927	0.931	0.946	0.971	8.10

(1)  $\Delta t_{used}$  is the time over which the performance figures are averaged.

(2) Includes coolant leakage

Table VIII-3 compares the estimated heat transfer rates for these tests with those predicted by the Bartz short form. The overall heat transfer rate and the chamber-nozzle heat transfer split measured in the uncooled tests were used to estimate the amount of heat transferred to the chamber and nozzle. By this estimation method, the chamber heat transfer rate was approximately 40% of the Bartz prediction, which compares to the reduction measured in the uncooled tests with this injector. This substantiates the calculation method and indicates that the nozzle heat transfer rate was approximately 30% of the Bartz value. Analytical calculations using these percentages of the Bartz predictions verify that regenerative cooling with nucleate boiling butene-1 can be achieved at the 5000-lb thrust level.

TABLE VIII-3. EXPERIMENTAL AND THEORETICAL HEAT TRANSFER RATES FOR REGENERATIVE TESTS

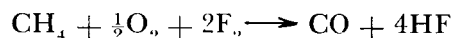
Test No.	Experimental Heat Transfer Rate, Btu/sec	Theoretical Heat Transfer Rate, Btu/sec	$\left(\frac{Q_{\text{measured}}}{Q_{\text{theoretical}}}\right)_{\text{total}}$ , %	$\left(\frac{Q_{\text{measured}}}{Q_{\text{theoretical}}}\right)_{\text{chamber}}$ , %	$\left(\frac{Q_{\text{measured}}}{Q_{\text{theoretical}}}\right)_{\text{nozzle}}$ , %
1R	504	1630	31	39	25
2R	550	1570	35	41	29

## SECTION IX

### PREDICTED PERFORMANCE OF FLOX/LIGHT HYDROCARBON PROPELLANTS

#### A. THEORETICAL PERFORMANCE

The theoretical performance of most bipropellant combinations is commonly expressed as a function of mixture ratio. When evaluating flox mixtures with hydrocarbon fuels, the percentage of fluorine in the oxidizer is an additional variable that must be optimized for maximum specific impulse. Because oxygen releases more energy than fluorine with carbon, and fluorine releases more energy with hydrogen, the optimum fluorine concentration for these fuels is sharply defined and occurs at less than 100% fluorine. The optimum flox mixture for each hydrocarbon can be determined by balancing the carbon and oxygen to form CO and the hydrogen and fluorine to form HF. Using methane for example, the stoichiometric equation is:



In this equation the relative mole ratio of fluorine to oxygen is four to one or 82.6% fluorine by weight. Theoretical shifting equilibrium calculations verify 82.6% as the fluorine concentration for maximum specific impulse. Similar stoichiometric equations can accurately predict the optimum flox concentration for any hydrocarbon fuel.

Figure IX-1 presents the theoretical vacuum specific impulse for methane, propane, and butene-1 with the optimum flox concentrations for each. Inlet conditions are liquid flox at its normal boiling point and liquid fuel at 180°R. It is assumed that the fuels would be stored at approximately this temperature to reduce heat transfer between the fuel and oxidizer and also to increase their liquid heat capacity and hence their cooling ability. Figure IX-2 shows the effect of area ratio on theoretical performance. This relationship is applicable to the range of data presented in this report and can be used to extrapolate the delivered performance shown in this section (for area ratio = 40) to other area ratios. As area ratio increases, nozzle efficiency (nonequilibrium effects and friction losses) may be reduced slightly; however, this effect is predicted to be less than 0.5% over an area ratio range of 40 to 100.

#### B. PERFORMANCE LOSSES

Several sources of performance loss must be considered when estimating deliverable vacuum specific impulse. Theoretical shifting equilibrium vacuum specific impulse must be corrected for combustion inefficiency, nozzle friction and divergence, and chemical nonequilibrium expansion. For transpiration-cooled engines an additional effect is encountered from mixing between coolant and combustion products.

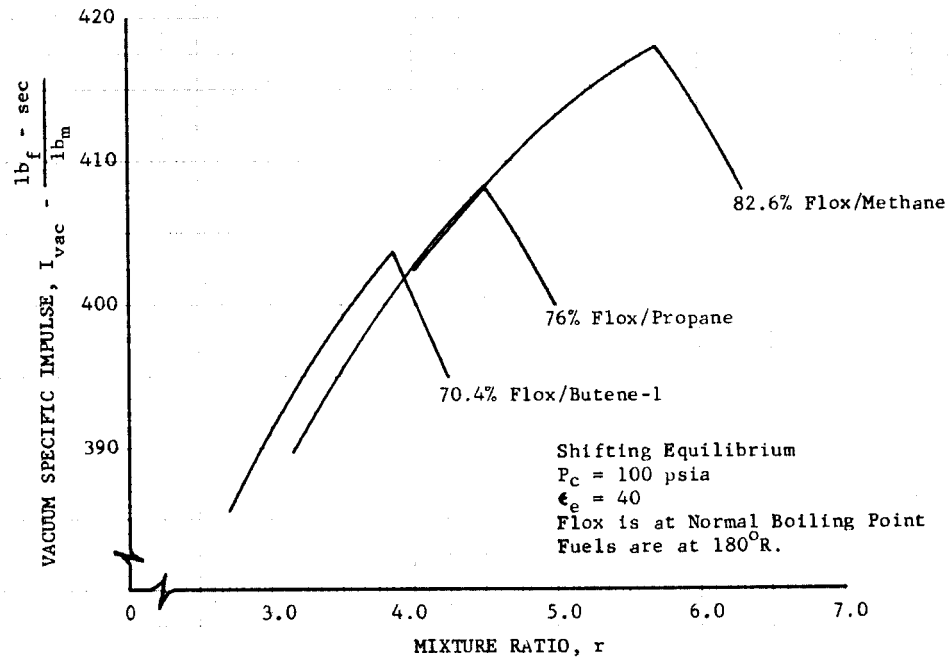


Figure IX-1. Theoretical Vacuum Specific Impulse of Flox/Light Hydrocarbon Propellants

DF 54608

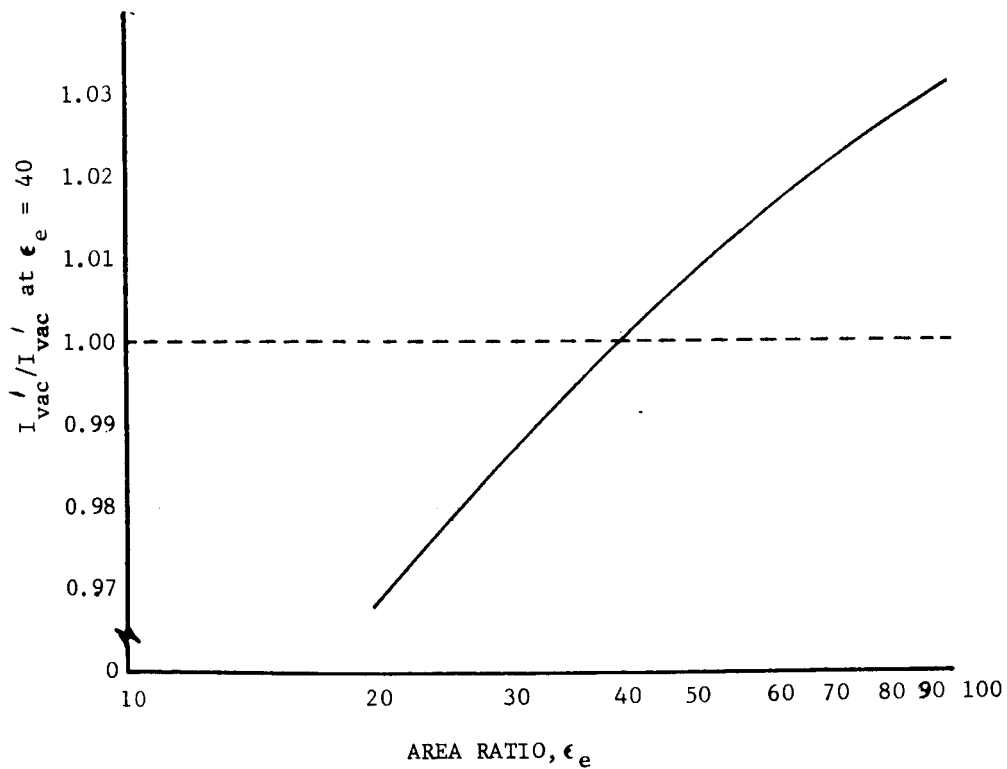


Figure IX-2. Effect of Area Ratio on Vacuum Specific Impulse

DF 54548

Figure IX-3 presents characteristic velocity efficiency determined from the highest performance injectors used in this program for flox/methane, flox/propane, and flox/butene-1. Also shown on these figures are curves showing the efficiencies that now appear readily attainable with moderate injector development. At the low mixture ratios a minimum increase of 1 to 2% should be achieved during a normal development program. Because mixing is more critical at the theoretical optimum mixture ratio than at lower values, larger improvements of 2 to 3% can be expected in this area with injectors having increased interelement mixing. The predicted efficiency curves indicate a 2.5% improvement for methane and butene-1 at their respective theoretical optimum mixture ratios. The predicted increase for propane is higher, 3.5%, because testing with this fuel was discontinued early in the test program, hence injector development was not as advanced. At the optimum mixture ratios the predicted efficiencies are: methane — 95%, propane — 96%, and butene-1 — 97%. It is expected that higher efficiencies will be easier to achieve with propane and butene-1 because (1) they optimize at lower mixture ratios where equal changes in fuel concentration do not produce such extreme variations in mixture ratio as with methane and because (2) transpiration cooling of the injector face is not a requirement.

Nozzle friction and divergence losses are accounted for by the stream thrust coefficient,  $C'_s$ . Based on a minimum surface area bell nozzle having an area ratio of 40,  $C'_s$  was calculated to be 0.973 for the three flox/light hydrocarbon combinations tested, over the range of mixture ratios of interest. The value of  $C'_s$  was calculated using the method of characteristics including the effects of wall friction as presented in Reference 25. Values of  $C'_s$  calculated by this method have proved to be quite accurate in numerous research and development programs.

Chemical nonequilibrium expansion in a rocket nozzle results in a performance loss that may be included by means of a nozzle kinetic efficiency,  $\eta_k$ . Figure IX-4 presents nozzle kinetic efficiencies for methane, propane, and butene-1 with their respective optimum flox percentages, at thrust levels from 3,000 to 20,000 pounds. Kinetic efficiencies at the 5000-pound thrust level for methane and butene-1 were determined from uncooled altitude test data. Since the flox/propane combination was not tested in a high-expansion-ratio nozzle it was assumed to have a kinetic efficiency between methane and butene-1 at equal equivalence ratios. Kinetic efficiencies at thrust levels other than 5000 pounds were obtained by correcting theoretical Bray sudden-freeze point predictions by the ratio of the measured-to-predicted loss at the 5000-pound thrust level. This is a rather crude approach to scaling of kinetic data and is justified only because the kinetic losses, and the variation of kinetic loss with thrust, are both small. Figure IX-5 shows the predicted variation in  $\eta_k$  estimated for throttled operation.



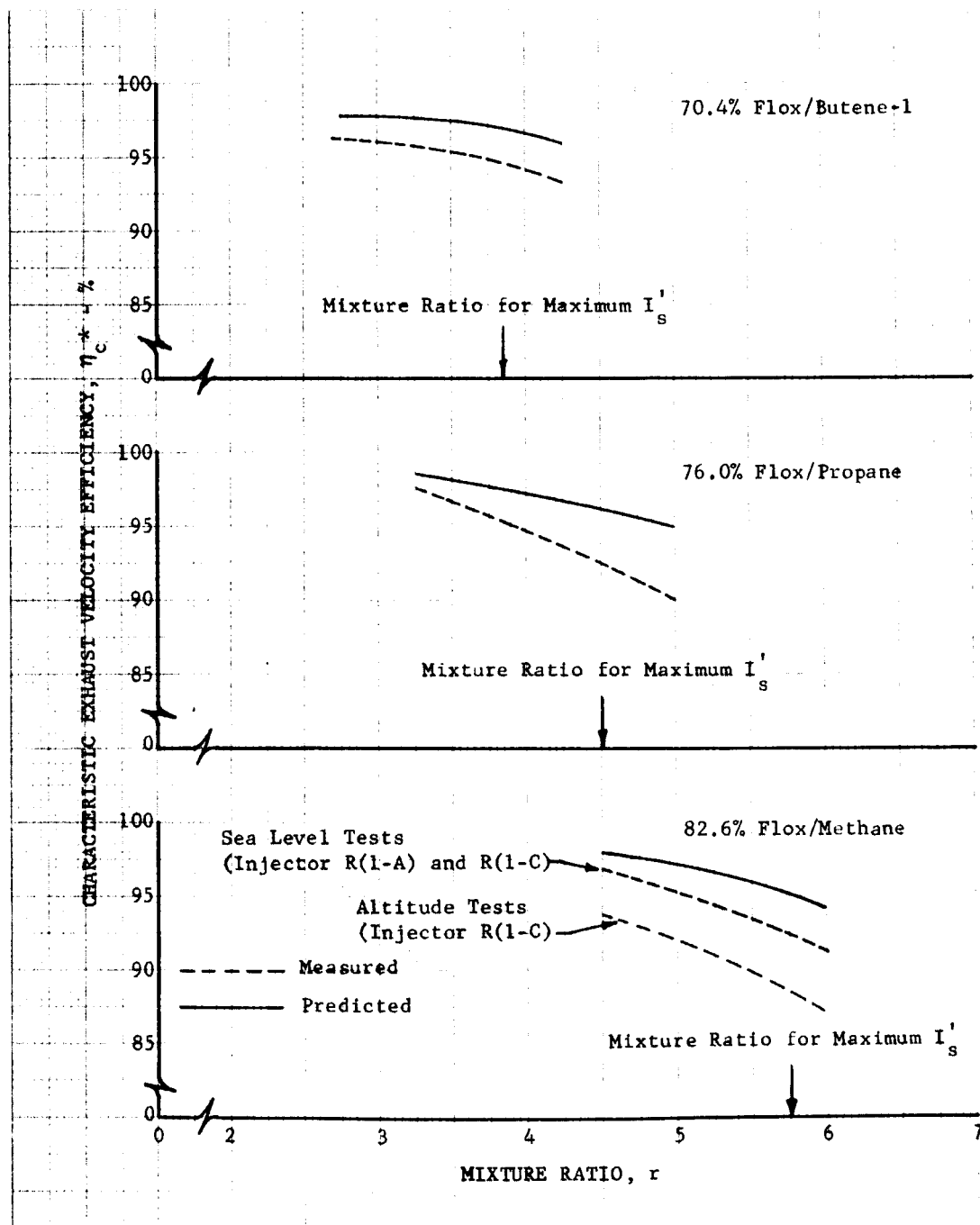


Figure IX-3. Measured and Predicted Full Thrust Characteristic Exhaust Velocity Efficiency

DF 54609

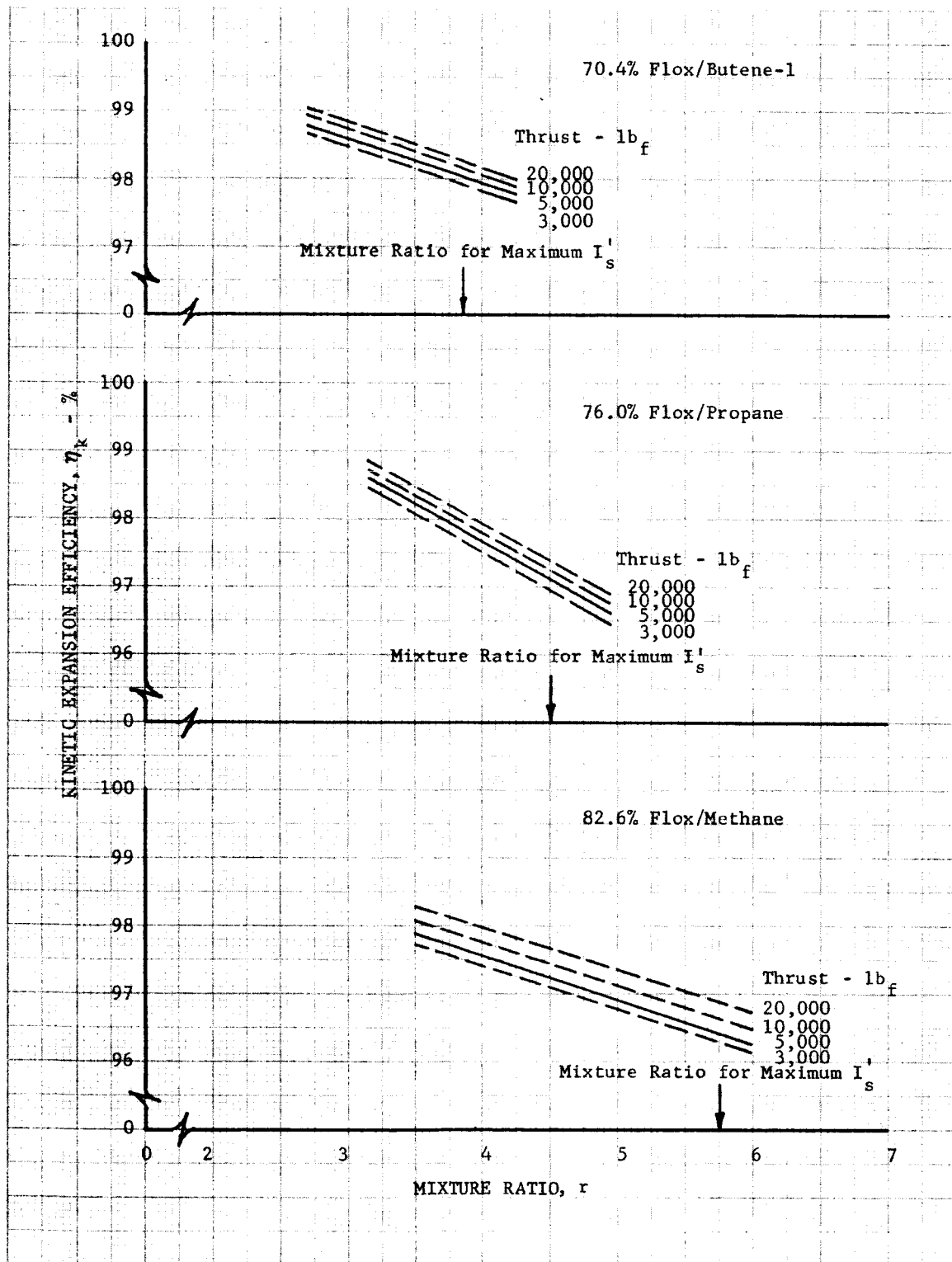


Figure IX-4. Kinetic Expansion Efficiency

DF 54613

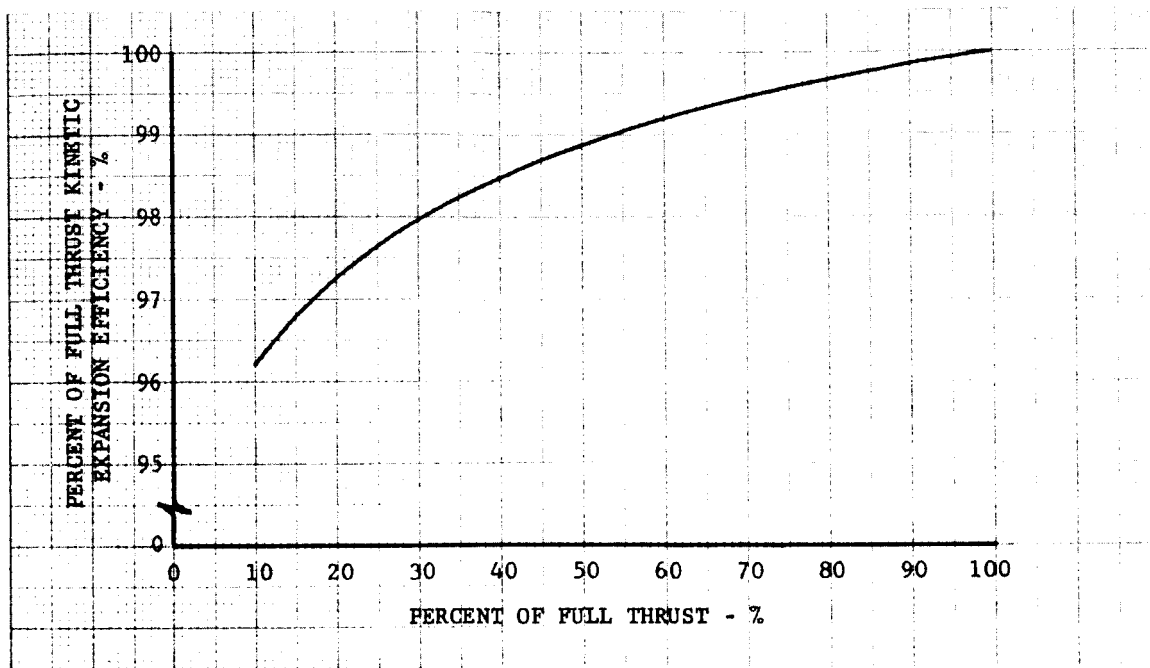


Figure IX-5. Variation of Kinetic Expansion Efficiency for Throttling Operation

DF 54611

For thrust chambers that do not use mass transfer cooling, the delivered vacuum impulse is calculated as:

$$I_{vac} = \eta_c^* \cdot C_s' \cdot \eta_k \cdot I_{vac}$$

For chambers employing mass transfer cooling, several methods have been investigated for correction of theoretical performance for incomplete coolant mixing. The maximum loss can be estimated by calculating a specific impulse assuming zero mixing between the mainstream and coolant. The predicted no-mixing specific impulse is calculated by equation A-42 (Appendix A) using corrections for combustion and kinetic efficiencies based on the injector mixture ratio. As shown in Section VII, significant mixing of the coolant and injector propellants does occur. In fact, at low engine mixture ratios, test results have shown higher performance in transpiration cooled chambers than in uncooled chambers, i.e., apparently coolant mixing is causing recovery of some injector performance losses. The amount of mixing and its effect on performance will depend on several factors, including the combustion efficiency, injector mixture ratio distribution, chamber configuration, amount of coolant and the thrust level. The effect of these factors is impossible to assess without experimental data at conditions close to those being considered. Therefore, in this report, performance estimates with transpiration cooling for flox/methane and flox/propane are limited to the 5000-pound thrust level. It is expected that for the level of injector efficiencies shown in figure IX-3, increased mixing at low thrust will compensate for the reduced percentage of coolant flow

at higher thrust, so that the performance will not vary significantly between 3,000 and 20,000 lb<sub>r</sub>. For appreciably higher injector efficiencies, the performance increase due to coolant-injector flow mixing would be reduced. Under these conditions, vacuum specific impulse would decrease slightly as thrust is reduced and the required weight fraction of coolant is increased. However, if the mixture ratio is optimized, the percent reduction in transpiration cooling should never exceed more than 50% of the percent of propellant used for cooling, as predicted in figure IX-10.

### C. PREDICTED ENGINE PERFORMANCE

Two levels of performance were calculated for each fuel: the first was based on efficiencies measured in the test program; the second was based on the efficiencies predicted with moderate additional injector development. All performance estimates are for a 100-psia chamber pressure and a nozzle expansion ratio of 40. The cooling methods and design considerations affecting each of these three flox/light hydrocarbon combinations are detailed in the following paragraphs.

#### 1. FLOX/BUTENE-1

The flox/butene-1 performance estimates were based on the use of regeneratively cooled chambers and nozzles. Figure IX-6 shows the estimated performance as a function of thrust level and mixture ratio. In estimating the thrust chamber cooling requirements, 35% of the Bartz predicted heat flux was used throughout. This is approximately equal to the percentage measured in the uncooled chamber and is slightly higher than the 25% measured in the uncooled nozzle. With this percentage of the Bartz heat flux, all engines in the 3,000 to 20,000-pound thrust range were satisfactorily cooled at the optimum mixture ratio of 3.85. With throttling it is necessary to operate at reduced mixture ratios as the thrust level was decreased, as shown in figure IX-7. This was required to increase the coolant flow rate to maintain the coolant exit temperature below the saturation point (bulk boiling) at the 150-psia jacket exit pressure. Under Contract NAS3-4195 the feasibility of film boiling was demonstrated; however, chamber cooling with bulk boiling has not been established and presents several potential problems. Flow stability with bulk boiling is a potential problem, pressure drops with bulk boiling could be excessively high, and injector problems could be encountered with two-phase flow. All points shown on these curves that are at mixture ratios below 3.85 are shown as dotted lines and the operating mixture ratio indicated on the curve. The use of a radiation-cooled nozzle would eliminate the need for any mixture ratio shifts and would provide slightly higher performance at reduced thrust levels.

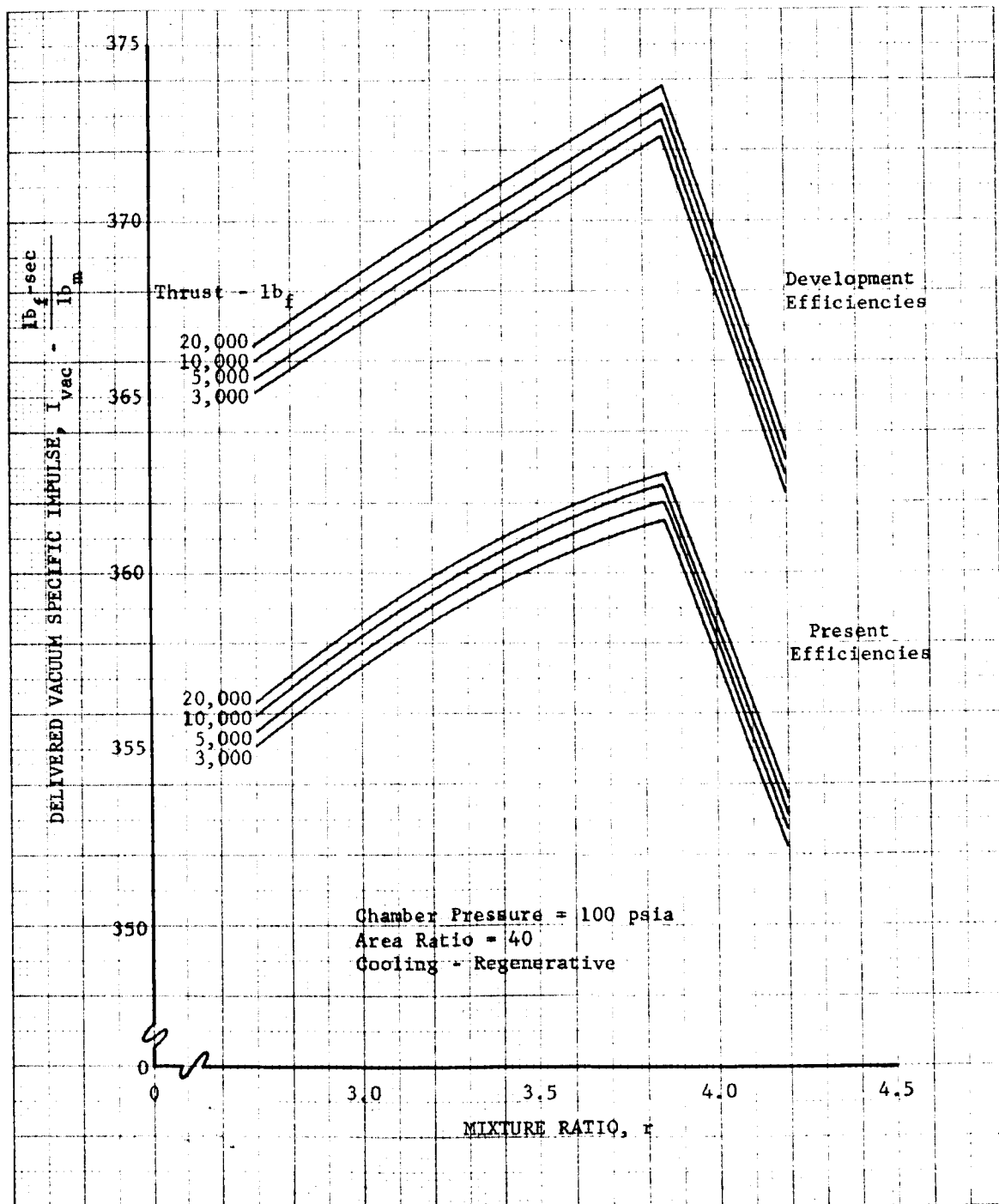


Figure IX-6. Flox/Butene-1 Performance

DF 54549

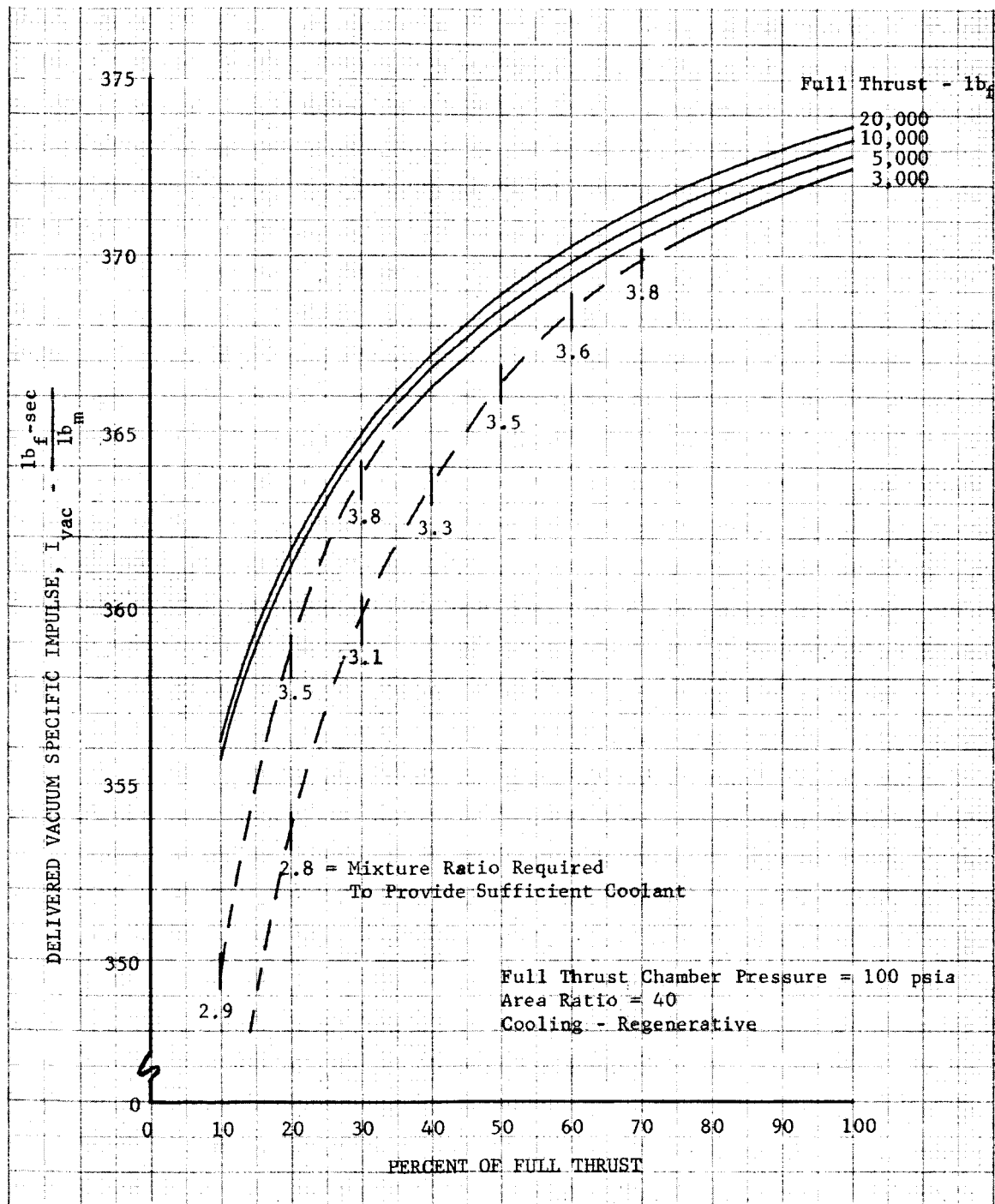


Figure IX-7. Predicted Flox/Butene-1 Performance With Throttling

DF 54550

## 2. FLOX/METHANE

Figure IX-8 shows the measured and predicted vacuum specific impulse for transpiration-cooling using flox/methane at 5000-pounds thrust. The lower curve is based on the measured vacuum specific impulse data taken from Section VII (figure VII-3). Because of the difficulty in estimating the effect of mixing on performance, the predicted performance with additional development is conservatively based on efficiencies measured in sea level tests rather than the "predicted"  $\eta_c^*$  data presented in figure IX-3. Mixing improvements are based on Task V test results as shown in figure VII-6. Figure IX-9 shows predicted engine performance over a 10-to-1 throttling range.

Figure IX-10 shows transpiration-cooling-flow requirements for flox/methane at several additional thrust levels. These flows are based on the use of a transpiration-cooled chamber with a radiation-cooled nozzle. The radiation-cooled nozzle attachment area ratios were determined using a maximum wall temperature of 2460°R based on heat fluxes corrected for transpiration-coolant carryover comparable to that measured. Radiation skirt attachment area ratios varied from 7.9 at 20,000-pound thrust to 9.5 at the 3000-pound thrust level. Transpiration-cooling requirements were calculated using 100% of the Bartz predicted heat flux and a chamber wall temperature of 2160°R. At 5000-pounds thrust, the use of a completely transpiration-cooled nozzle would reduce performance less than 1% from that shown. Because of the narrow liquid range of methane, negligible performance gains would be obtained by the use of a partially regeneratively cooled nozzle.

## 3. FLOX/PROPANE

Flox/propane performance at 5000-pounds thrust was predicted based on regenerative cooling of the nozzle and chamber up to the point at which propane reached its saturation temperature (150-psia jacket pressure). The remainder of the chamber was transpiration cooled. Using 50% of the Bartz film coefficients in the nozzle and 45% in the chamber, regenerative cooling was possible throughout the nozzle and in approximately 65% of the chamber. This reduction in the chamber Bartz coefficients compares to that measured in the sea level tests. The 50% reduction in the nozzle was interpolated from data with the other two fuels. Based on 100% of the Bartz heat flux and a 2160°R wall temperature in the transpiration-cooled section, it was determined that 2% of the propellant was required for transpiration cooling. The performance data shown in figure IX-11 are based on the estimated combustion efficiency for a developed injector, but do not include any recovery due to transpiration-coolant mixing. This is probably slightly conservative; however, characteristic velocity data with propane transpiration cooling in Contract NAS3-4195 (Reference 1) indicated that propane losses would be greater than with methane at equal percentages of coolant flow.

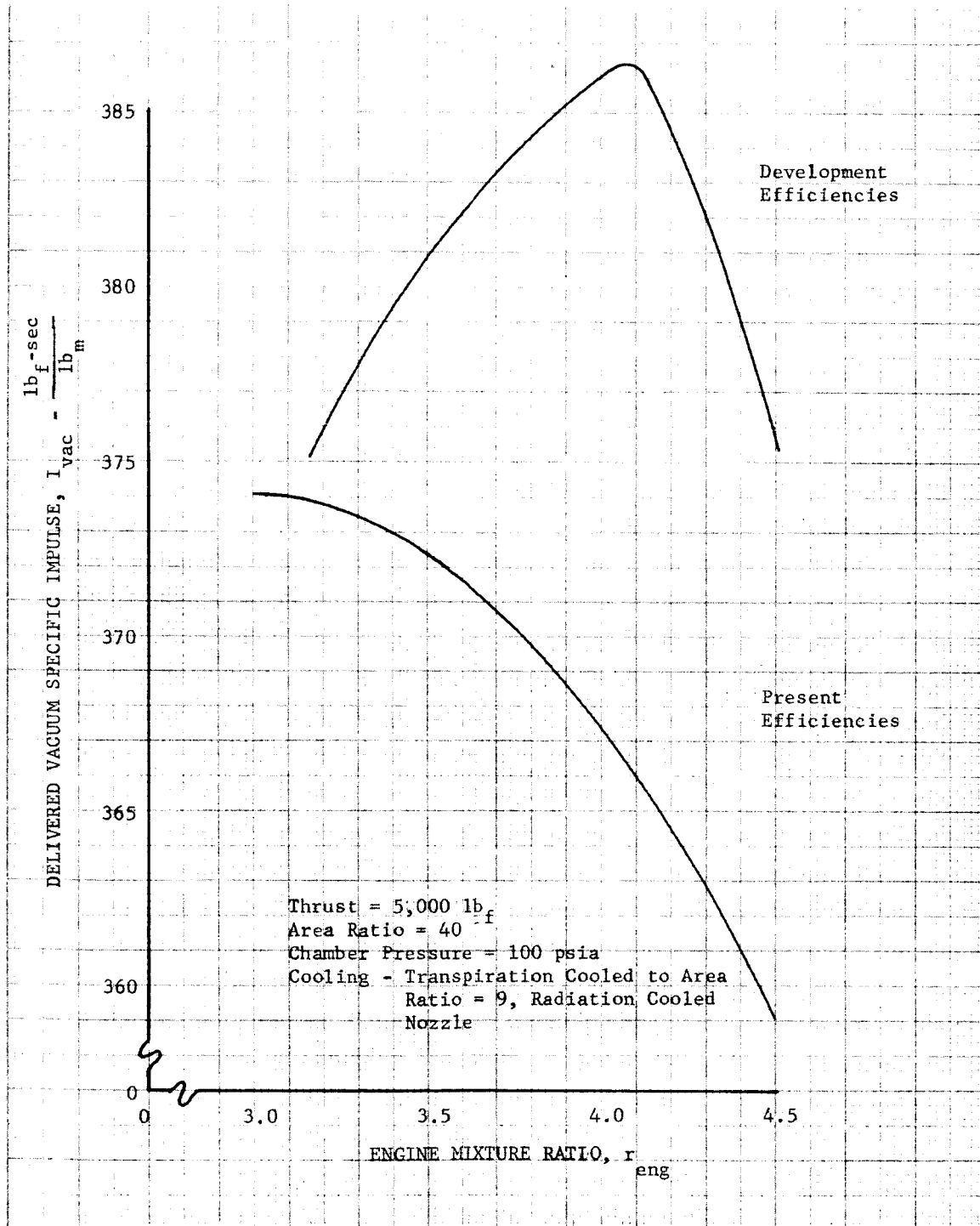


Figure IX-8. Flox/Methane Performance With Transpiration-Cooling

DF 54551



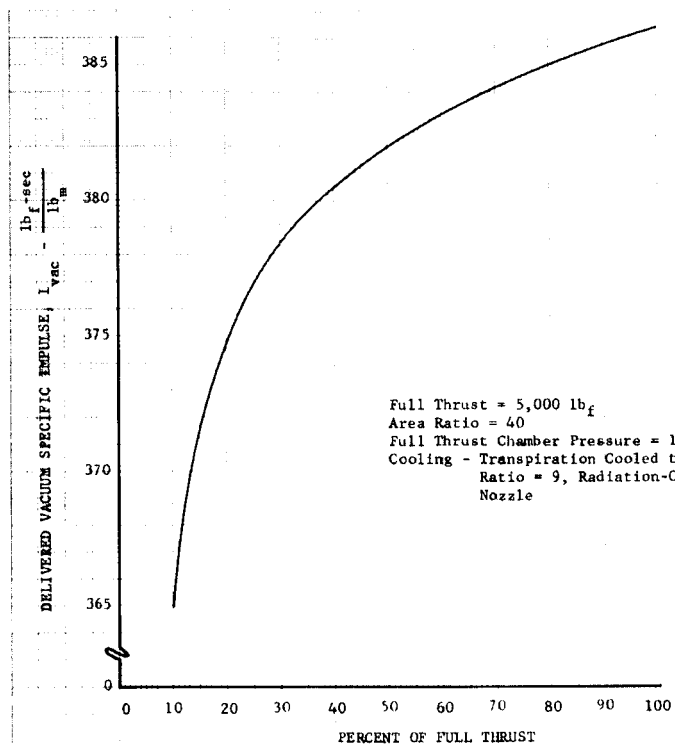


Figure IX-9. Predicted Flox/Methane Performance With Throttling

DF 54552

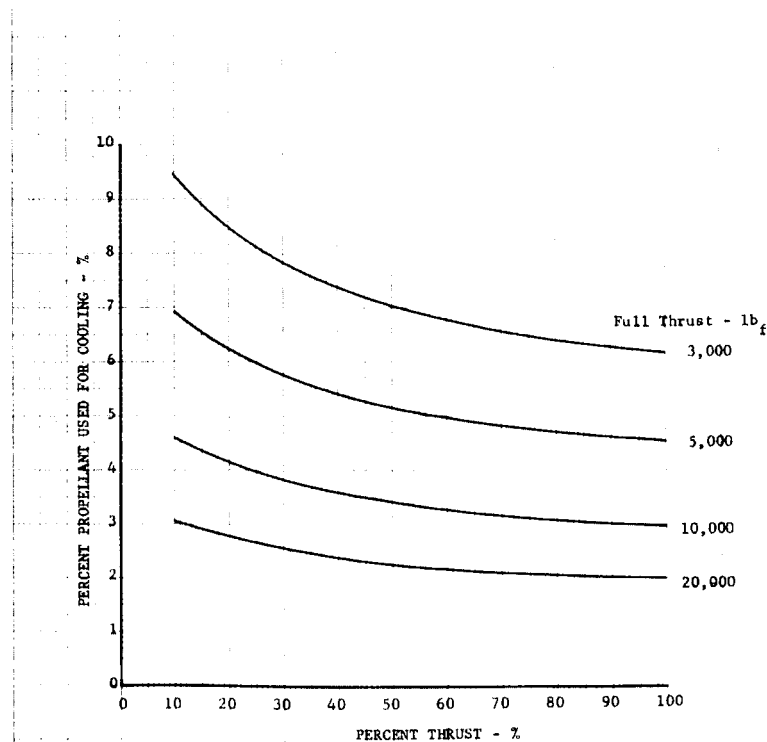


Figure IX-10. Flox/Methane Transpiration-Cooling Flow Requirements

DF 54553

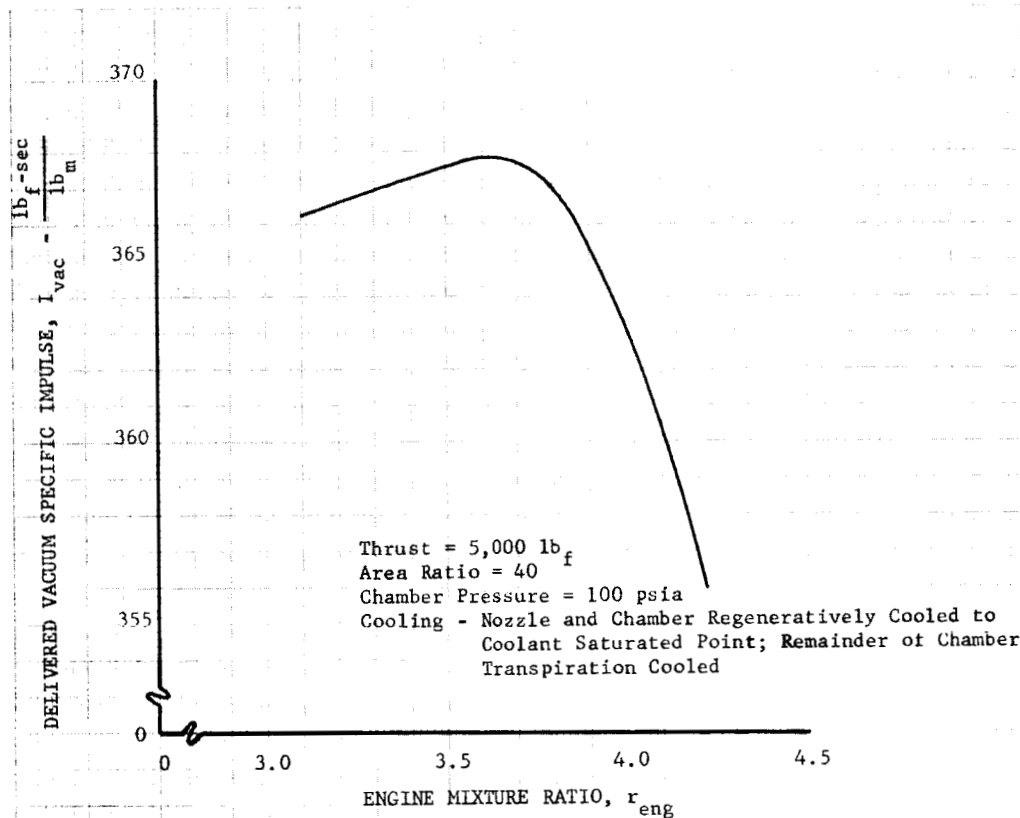


Figure IX-11. Predicted Flox/Propane Performance

DF 54554

With the reductions in heat transfer rates estimated above, the use of a radiation-cooled skirt would allow regenerative cooling of the complete chamber for engines with thrust levels above approximately 10,000 pounds. Full thrust performance would be close to that shown for butene-1; however, throttling ranges would be limited without mixture ratio reductions. In the throttled mode this would reduce the performance below that of butene-1.

#### D. RANGE OF APPLICABILITY

On the basis of these data it is concluded that: (1) methane-transpiration cooling is feasible and yields the highest performance of the flox/light hydrocarbon fuels, (2) a regeneratively cooled butene-1 engine is possible to thrust levels below 3000 pounds and offers performance close to methane, and (3) propane does not offer any performance advantages over either methane or butene-1, except in unthrottled engines above 10,000-pounds thrust.

**SECTION X**  
**REFERENCES**

1. "Investigation of Light Hydrocarbon Fuels with Flox Mixtures as Liquid Rocket Propellants — Final Report," Pratt & Whitney Aircraft, PWA FR-1443, prepared under Contract NAS3-4195, NASA CR-54445, 1 September 1965.
2. Priem, R. J., and M. F. Heidman, "Propellant Vaporization as a Design Criteria for Rocket-Engine Combustion Chambers," NASA TR R-67, 1960.
3. Lamberis, S., L. P. Combs, and R. S. Levine, "Stable Combustion Processes in Liquid Propellant Rocket Engines," Fifth AGARD Colloquium, 9 to 13 April 1962.
4. Ingebo, R. D., and H. H. Foster, "Drop-Size Distribution for Cross-current Breakup of Liquid Jets in Airstreams," NACA TN 4087, 1957.
5. "Rocket Motor Injector Performance — Initial Survey," Northern Research and Engineering Corporation, Report No. 1046-1, prepared for Pratt & Whitney Aircraft, January 1962.
6. "Rocket Motor Injector Performance — Correlation of Experimental Data," Northern Research and Engineering Corporation, Report No. 1046-2, prepared for Pratt & Whitney Aircraft, March 1962.
7. Ingebo, R. D., "Drop-Size Distribution for Impinging-Jet Breakup in Airstreams Simulating the Velocity Conditions in Rocket Combustors," NACA TN-4222, March 1958.
8. "Performance Characteristics of Compound A/Hydrazine Propellant Combinations — Volume 1 — Technical Discussion," Rocketdyne Division of North American Aviation, TR-65-107, May 1965.
9. "Chamber Technology for Space-Storable Propellants — Task II," Rocketdyne Division of North American Aviation, R-6028-2, 13 October 1965.
10. Elverum, G. W. and T. F. Morey, "Criteria for Optimum Mixture-Ratio Distribution Using Several Types of Impinging-Stream Injector Elements," Jet Propulsion Laboratory, Memorandum 30-5, 25 February 1959.
11. Johnson, B. H., "An Experimental Investigation of the Effects of Combustion on the Mixing of Highly Reactive Liquid Propellants," Jet Propulsion Laboratory, Technical Report No. 32-689, 15 July 1965.
12. "Absorbing Liners for Rocket Combustion Chambers — Theory and Design Techniques," Pratt & Whitney Aircraft, Report No. AFRPL-TR-66-234, August 1966.
13. "RL10 Rocket Engine Thrust Chamber Fabrication," Pratt & Whitney Aircraft, PWA FR-480, September 1962.

14. Bartz, D. R. "A Simple Equation For Rapid Estimation of Rocket Nozzle Convective Heat Transfer Coefficients," Jet Propulsion, January 1957.
15. "Research on a Hydrogen-Fluorine Propulsion System — Final Report," PWA FR-1585, NASA CR-72074, 21 October 1966. Confidential (Title U).
16. "Advanced Throttling Concepts — Final Report," Pratt & Whitney Aircraft, PWA FR-1077, prepared under Contract AF 04(611)-9575, March 1965.
17. Mosier, S. A., R. E. Dotson, and O. K. Moehrbach, "Hypergolic Ignition of Light Hydrocarbon Fuels with Fluorine-Oxygen (Flox) Mixtures," Pratt & Whitney Aircraft, presented at the 1965 Fall Meeting of the Western States Section of the Combustion Institute, 25 October 1965.
18. Zupnik, T. F., E. N. Nilson, and V. J. Sarli, "Investigation of Nonequilibrium Flow Effects in High Expansion Ratio Nozzles," Computer Program Manual, UAC Research Laboratories Report C910096-11, NASA CR-54042, Topical Report under Contract NAS3-2572, September 1964.
19. Bray, K. N. C., and J. P. Appleton, "Atomic Recombination in Nozzles, Methods of Analysis for Flows with Complicated Chemistry," University of Southampton, Department of Aeronautics and Astronautics, May 1961.
20. Hofland, R., Jr., and W. G. Burwell, "Development and Evaluation of Sudden Freezing Criteria for Predicting Nonequilibrium Mixture Properties in Expanding One-Dimensional Flow Fields," UAC Research Laboratories Report No. C110035-1, July 1964.
21. Sarli, V. J., "Investigation of Nonequilibrium Flow Effects in Hydrogen-Fluorine Rocket Nozzles," Quarterly Progress Report No. 3, United Aircraft Research Laboratories, E910370-9, May 1966. Confidential. (Title U.)
22. Rubesin, M. W., "The Influence of Surface Injection on Heat Transfer and Skin Friction Associated with the High-Speed Turbulent Boundary Layer," NACA RM A55L13, 20 February 1956.
23. Pappas, C. C. and A. F. Okund, "Measurement of Heat Transfer and Recovery Factor of a Compressible Turbulent Boundary Layer on a Sharp Cone with Foreign Gas Injection," NASA TN D-2230, April 1964.
24. Steward, W. G., "Transfer Line Surge," Advances in Cryogenic Engineering, p. 313, Plenum Press, New York, 1965.
25. "Digital Computer Programs for Rocket Nozzle Design and Analysis — Volume II — Bell Nozzle Design," Pratt & Whitney Aircraft, PWA FR-1021, prepared under NASA Contract NAS9-2487, 26 June 1964.

## APPENDIX A

### DATA REDUCTION AND PERFORMANCE CALCULATIONS

#### 1. DATA REDUCTION PROCEDURES

##### A. UNCOOLED SEA LEVEL TESTS

Three computer programs were used for reducing data obtained during the uncooled Task II tests. The first program operated on the digital tape recordings made during test firings and converted instrumentation signals into engineering parameters in convenient units. In addition to reducing the stand tape, this program used some of the recorded parameters to calculate propellant flow rates and approximate heat loss to the chamber wall. The approximate heat loss was estimated by comparing the predicted temperature rise with the actual temperature rise of several of the thermocouples located on the chamber. Also, within this program, the parameters to be used in the performance calculations were averaged every eight 0.0125-sec scans to provide an average value for each 0.10-sec interval. The parameters\* averaged were:

$P_{c_i}$	Chamber pressure, psia
$F_i$	Thrust, lb <sub>f</sub>
$W_{f_i}$	Fuel flow parameter, $\frac{1b}{\text{sec}\sqrt{\rho_f}}$
$W_{o_i}$	Oxidizer flow parameter, $\frac{1b}{\text{sec}\sqrt{\rho_o}}$
$T_f$	Fuel injector inlet temperature, °R
$T_o$	Oxidizer injector inlet temperature, °R
$T_{f_o}$	Fuel orifice temperature, °R
$T_{o_o}$	Oxidizer orifice temperature, °R

The second program used the above data as input for calculating the chamber performance parameters for each 0.1-sec interval. Redundant measurements were averaged to provide high measurement accuracy. If one of the values recorded for each parameter was in error it was omitted from the averages. The oxidizer flow rate was calculated by:

$$\dot{W}_o = \frac{W_{o_1}\sqrt{\rho_o} + W_{o_2}\sqrt{\rho_o}}{2} \quad (A-1)$$

---

\*A complete list of symbols used in this Appendix is given in Paragraph 3.

Where  $\rho_o$  was determined from curve fits of oxygen and fluorine density data taken from References 1 and 2\* using the known flox concentration, the assumption of an ideal solution, and the measured flox flow nozzle temperature. Fuel flow rate was calculated in the same manner using the measured fuel orifice temperature and curve fits of fuel density (References 3 and 4).

The thrust coefficient was calculated from test data as follows:

$$C_F = \frac{F}{A_t P_c} \quad (A-2)$$

For these tests,  $A_t$  was calculated from a RMS average throat diameter measured during each build of the engine. Nominal chamber throat diameter was 5.98 inches.

The experimental thrust coefficient was compared to a theoretical value calculated as follows:

$$C'_F = C'_{F_{vac}} - \frac{\epsilon_e P_a}{P_c} \quad (A-3)$$

Using  $P_a = 14.696$  psia and  $\epsilon_e = 1.98$ :

$$C'_{F_{s1}} = C'_{F_{vac}} - \frac{1.98 (14.696)}{P_c} \quad (A-4)$$

where the prime denotes a theoretical value.

The value of  $C_F$  may be corrected for nozzle frictional and divergence losses through use of a calculated stream thrust coefficient efficiency,

$$C_s = \frac{C_{F_{vac}}}{C'_{F_{vac}}} \quad (A-5)$$

For a nozzle with a 15-deg half angle and an area ratio of 1.98,  $C_s$  was calculated to be 0.9722 for all propellant combinations used in this program. These calculations were based on the method of characteristics, including effects of wall friction (Reference 5). Values of  $C_s$  calculated by this method have proved to be quite accurate in numerous research and development programs.

Thus:

$$C'_{F(C_s)} = 0.9722 C'_{F_{vac}} - \frac{1.98 (14.696)}{P_c} \quad (A-6)$$

Experimental characteristic exhaust velocity was calculated in two ways:

$$c^*_{P_c} = \frac{A_t g_o P_c}{\dot{w}_p} \quad (A-7)$$

---

\*References used in this Appendix are listed in Paragraph 4.

The subscript  $P_c$  is used to denote that  $c^*$  has been calculated from chamber pressure. For comparison,  $c^*$  may also be calculated from thrust measurements by assuming that a theoretical  $C_F$  corrected for nozzle divergence and friction losses (equation (A-6)) is an accurate estimate of the experimental  $C_F$ .

$$c_{F'}^* = \frac{I_s g_o}{C_{F'} (C_s)} = \frac{F g_o}{\dot{w}_p C_{F'} (C_s)} \quad (A-8)$$

Equation (A-6) indicates that small changes in  $P_c$  have a negligible effect on  $C_{F'}$  making  $c^*$  almost directly proportional to thrust. Hence, comparison of  $c_{F'}^*$  and  $c_{P_c}^*$  provided a check on the consistency of the thrust and chamber pressure measurements.

Theoretical vacuum specific impulse, characteristic exhaust velocity, and vacuum thrust coefficient were calculated in theoretical performance programs using thermochemical data published by the Joint Army-Navy-Air Force (JANAF) Thermochemical Panel. Theoretical shifting equilibrium performance data from the performance programs were stored in the data reduction program in tabular form. The theoretical data used for comparison with measured data were based on the propellant inlet conditions measured during each test. Theoretical data calculated using inlet conditions corresponding to liquid fuel at its normal boiling point and liquid flux at 155°R were corrected to the actual inlet conditions by determining the changes in enthalpy between the measured and reference conditions.

$$\Delta h_f = (T_f - T_{nbp}) c_{p_f} \quad (A-9)$$

$$\Delta h_o = (T_o - 155) c_{p_o} \quad (A-10)$$

$$\Delta h_p = \frac{\dot{w}_f \Delta h_f + \dot{w}_o \Delta h_o}{\dot{w}_f + \dot{w}_o} \quad (A-11)$$

where:

- $T_{nbp}$  = Temperature of the fuel at the normal boiling point, °R
- $c_{p_f}$  = Average constant pressure specific heat of fuel, Btu/lb - °R
- $c_{p_o}$  = Average constant pressure specific heat of oxidizer, Btu/lb - °R.

For calculating theoretical sea level specific impulse:

$$I_{sl}' = I_{vac}' - \frac{P_a A_e}{\dot{w}_p} \quad (A-12)$$

$$\dot{w}_p = \frac{A_t P_c g_o}{c^*} \quad (A-13)$$

$$I_{sl}' = I_{vac}' - \frac{P_a \epsilon c'^*}{g_o P_c} = I_{vac}' - 0.9044 \frac{c'^*}{P_c} \quad (A-14)$$

The following efficiencies were then calculated:

$$\eta_{c^*P_c} = \frac{c^*_{P_c}}{c^*_{P_c'}}$$

$$\eta_{c^*F} = \frac{c^*_F}{c^*_{F'}}$$

$$\eta_{I_s} = \frac{I_{s1}}{I_{s1'}}$$

$$\eta_{C_F} = \frac{C_F}{C_{F'}}$$

These values were calculated neglecting heat loss to the chamber walls and using the chamber pressure measured as a static value at the injector face. In a noncombustion situation, this would be very close to the total pressure because the velocity is low at this point. There is, however, a loss in total pressure (momentum loss) due to heat addition, i.e., combustion, at a finite velocity. Estimates of momentum loss were made over the range of mixture ratios and chamber pressures of interest. It was determined that the total pressure after burning may be found with sufficient accuracy from:

$$P_T = 0.974 P_c \quad (A-15)$$

The propellant inlet enthalpy can be adjusted for heat transferred to the chamber by determining the enthalpy change from the standard conditions:

$$\Delta h_{p(\text{cor})} = \Delta h_p - \frac{q_{ch}}{\dot{w}_p} \quad (A-16)$$

The efficiencies that follow were then calculated using theoretical and experimental values corrected for momentum loss by replacing  $P_c$  with  $P_T$  in all calculations, basing the theoretical values on corrected enthalpy, and correcting  $C_F$  for nozzle divergence and friction effects through the use of  $C_{F_s}$ . The values  $c^*_{P_c}$  and  $C_F$  are also corrected for thermal expansion of the nozzle throat as shown in figure A-1. In determining the thermal correction, wall temperature was taken at the mean time of the increment used for the averaged data.

$$\eta_{c^*P_c(\text{cor})} = \frac{c^*_{P_c(\text{cor})}}{c^*_{P_c'(\text{cor})}}$$

$$\eta_{c^*F(\text{cor})} = \frac{c^*_{F(\text{cor})}}{c^*_{F'(\text{cor})}}$$



$$\eta_{I_s(\text{cor})} = \frac{I_{s1}(\text{cor})}{I_{s1}'(\text{cor})}$$

$$\eta_{C_F(\text{cor})} = \frac{C_F(\text{cor})}{C_F'(C_s)(\text{cor})}$$

Values of  $\eta_{C_F(\text{cor})}$  near 1.0 indicate that the corrected  $C_F'$  used for calculating  $C_F^*(\text{cor})$  was valid.

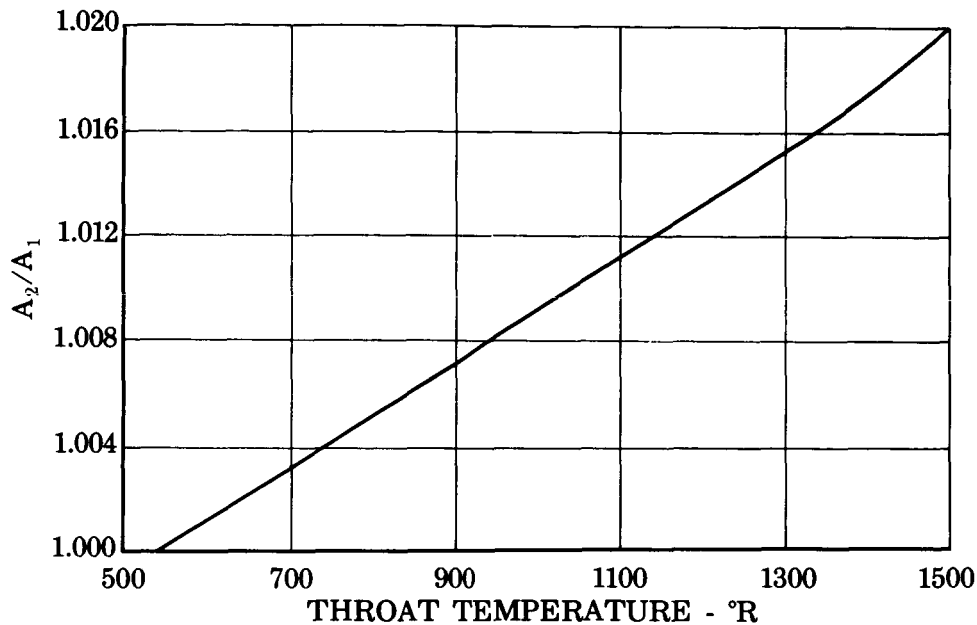


Figure A-1. Increase in Throat Area Due to Temperature Increase

FD 19783

All performance values (calculated for every 0.1-sec interval) were printed and stored on magnetic tape. The printed data were then reviewed to determine the steady-state portion of the test. A third program was then used to average the data over a requested time increment using the data previously stored on tape.

#### B. UNCOOLED ALTITUDE TESTS

The programs used in analyzing the uncooled altitude data are very similar to those used in the sea level analysis (subparagraph A). The first program uses the stand tape to calculate the same values as the sea level program with the addition of diffuser-half-shell pressure, HSP (i), and an approximate nozzle heat transfer rate,  $q_n$ . The performance calculations are the same as those used for uncooled sea level tests except for the following changes and additions. An average diffuser pressure is calculated from test data:

$$P_d = \frac{\text{HSP}(1) + \text{HSP}(2) + \text{HSP}(3) + \text{HSP}(4)}{4} \quad (\text{A-17})$$

The measured thrust in the diffuser is corrected to vacuum thrust using figure A-2.

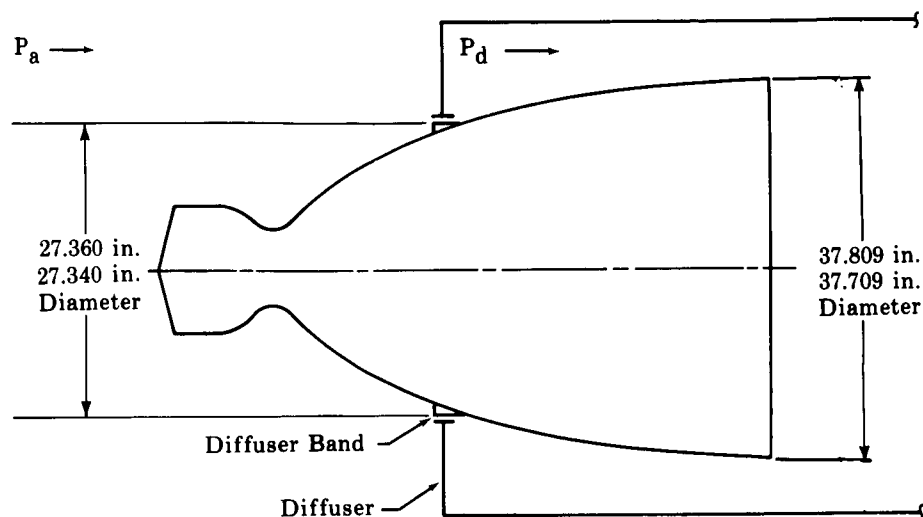


Figure A-2. Diffuser and Chamber Schematic

FD 14460A

The vacuum thrust calculation is as follows:

$$\begin{aligned}
 A_1 &= \text{Projected area of diffuser band} = 587.5 \text{ in.}^2 \\
 A_e &= \text{Projected area of exit} = 1119.8 \text{ in.}^2 \\
 F_{\text{measured}} &= \dot{m}V_e + P_e A_e - P_a A_1 - P_d (A_e - A_1) \\
 F_{\text{vac}} &= \dot{m}V_e + P_e A_e \\
 F_{\text{measured}} &= F_{\text{vac}} - P_a A_1 - P_d (A_e - A_1) \\
 F_{\text{vac}} &= F_{\text{measured}} + P_a A_1 + P_d (A_e - A_1) \\
 F_{\text{vac}} &= F_{\text{measured}} + P_a (587.5) + P_d (532.3) \quad (\text{A-18})
 \end{aligned}$$

The thrust coefficient and vacuum specific impulse are :

$$C_{F_{\text{vac}}} = \frac{F_{\text{vac}}}{A_t P_c} \quad (\text{A-19})$$

$$I_{\text{vac}} = \frac{F_{\text{vac}}}{\dot{w}_o + \dot{w}_f} \quad (\text{A-20})$$

Characteristic exhaust velocity was calculated from thrust as follows:

$$c^*_F = \frac{I_{\text{vac}} g_o}{C_{F'} (C_s)} = \frac{I_{\text{vac}} (32.174)}{C_{F'} (C_s)} \quad (\text{A-21})$$

where:

$$C_{F'} (C_s) = C_s C_{F'_{\text{vac}}}$$

The following efficiencies were then determined:

$$\eta_{c^*_{P_c}} = \frac{c^*_{P_c}}{c^*_{\prime}}$$

$$\eta_{c^*_{F}} = \frac{c^*_{F}}{c^*_{\prime}}$$

$$\eta_{I_{vac}} = \frac{I_{vac}}{I'_{vac}}$$

$$\eta_{C_{F_{vac}}} = \frac{C_{F_{vac}}}{C'_{F_{vac}}}$$

Corrections for momentum and heat losses were made using the same methods as used in the uncooled sea level data reduction program except that theoretical vacuum specific impulse and characteristic exhaust velocity were corrected using different enthalpy changes.

In calculating  $c^*_{\prime}$  the enthalpy change is given by:

$$\Delta h_{p(cor)} = \Delta h_p - \frac{q_{ch}}{\dot{w}_o + \dot{w}_f} \quad (A-22)$$

where  $q_{ch}$  is the heat transferred to the chamber.  $I'_{vac}$  was calculated using the enthalpy correction

$$\Delta h_{p(cor)} = \Delta h_p - \frac{q_n + q_{ch}}{\dot{w}_o + \dot{w}_f} \quad (A-23)$$

where  $q_n$  is the heat transferred to the nozzle.

The following efficiencies are defined:

$$\eta_{c^*_{P_c(cor)}} = \frac{c^*_{P_c(cor)}}{c^*_{\prime(cor)}}$$

$$\eta_{c^*_{F(cor)}} = \frac{c^*_{F(cor)}}{c^*_{\prime(cor)}}$$

$$\eta_{I_{vac(cor)}} = \frac{I_{vac}}{I'_{vac(cor)}}$$

$$\eta_{C_{F_{vac(cor)}}} = \frac{C_{F_{vac}}}{C'_{F(cor)}}$$

### C. REGENERATIVE COOLING ALTITUDE TESTS

Performance calculations for these tests were identical to those used in the uncooled altitude tests. Theoretical performance values were based on the measured injector inlet temperatures. Heat loss to the coolant (per pound of propellant) was used to calculate the heat loss correction to  $I'_{vac}$  and was calculated from:

$$\Delta h_c = \frac{\dot{w}_c c_{p_c} (T_{in} - T_{out})}{\dot{w}_o + \dot{w}_f} \quad (A-24)$$

where  $T_{in}$  and  $T_{out}$  are coolant jacket inlet and outlet temperatures. The fraction of heat transferred to the chamber was estimated from uncooled chamber data and used to determine the heat loss corrections to  $c^*$ .

$$q_{ch} = \frac{q_{ch}' \Delta h_c}{q_n' + q_{ch}'} \quad (A-25)$$

where the prime indicates heat transfer rates calculated using uncooled chamber and nozzle data.

### D. TRANSPIRATION COOLED ALTITUDE TESTS

Three computer programs were used to reduce data from the transpiration cooled tests. The program that operates on the stand data tape is identical to the uncooled altitude program with the following additions:

$W_{ci}$	Chamber coolant flow parameter, $\frac{1b}{sec \sqrt{\rho_c}}$
$P_{cm_i}$	Chamber coolant manifold pressure, psia
$P_{cs(i)}$	Chamber coolant segment pressure ( $i = 1$ to $8$ ), psia
$T_c$	Chamber coolant manifold temperature, °R
$T_{c_o}$	Chamber coolant orifice temperature, °R

The performance program uses the above data as input to complete the data reduction. This program is the same as that used in the uncooled altitude performance calculations except for the following changes and additions:

Chamber coolant flow was calculated by:

$$\dot{w}_c = \left( \frac{W_{c_1} \sqrt{\rho_c} + W_{c_2} \sqrt{\rho_c}}{2} \right) \quad (A-26)$$

Where  $\rho_c$  is the coolant density calculated from curve fits of coolant density and the chamber coolant orifice temperature.

Flow through the individual chamber segments was calculated as follows:

$$\dot{w}_{\text{seg}(i)} = 0.66845 A C_D \sqrt{\rho_c (P_{cm} - P_{cs(i)})} \quad (\text{A-27})$$

Where  $w_{\text{seg}(i)}$  is the flow through each segment

$A$  = area of metering orifice

$C_D$  = discharge coefficient for the metering orifice

$P_{cm}$  = the average chamber coolant manifold pressure

$P_{cs(i)}$  = pressure in each segment downstream of the metering orifice

Inaccuracies arising from the large number of pressures and discharge coefficients involved were then minimized by correcting the individual flow rates from equation (A-27) by a constant to produce the same total coolant flow as equation (A-26).

Mixture ratios are given by:

$$r_{\text{inj}} = \frac{\dot{w}_o}{\dot{w}_f} \quad (\text{A-28})$$

where  $r_{\text{inj}}$  is the mixture ratio of the injector

$$r_{\text{chamber}} = \frac{\dot{w}_o}{\dot{w}_f + \dot{w}_{\text{cup}}} \quad (\text{A-29})$$

where  $r_{\text{chamber}}$  is the mixture ratio upstream of the throat and  $\dot{w}_{\text{cup}}$  is the coolant flow through the segments upstream of the throat.

$$r_{\text{eng}} = \frac{\dot{w}_o}{\dot{w}_f + \dot{w}_c} \quad (\text{A-30})$$

where  $r_{\text{eng}}$  is mixture ratio of the engine.

The theoretical performance data used for comparison with measured data were based on a propellant enthalpy assuming liquid fuel and liquid coolant at the normal boiling point and liquid oxidizer at 155°R. To correct the theoretical values to correspond to the actual propellant inlet conditions, the changes in fuel and oxidizer enthalpy were calculated from equations A-9 and A-10 and the change in coolant enthalpy was calculated from:

$$\Delta h_c = (T_c - T_{\text{nbp}}) c_{p_c}$$

and:

$$\Delta h_p = \frac{\dot{w}_o \Delta h_o + \dot{w}_f \Delta h_f + \dot{w}_c \Delta h_c}{\dot{w}_o + \dot{w}_f + \dot{w}_c} \quad (\text{A-31})$$

$$\Delta h_{\text{pup}} = \frac{\dot{w}_o \Delta h_o + \dot{w}_f \Delta h_f + \dot{w}_{\text{cup}} \Delta h_c}{\dot{w}_o + \dot{w}_f + \dot{w}_{\text{cup}}} \quad (\text{A-32})$$

where  $\Delta h_{pup}$  is change in enthalpy of the propellants upstream of the throat. Theoretical  $I_{vac}$  is calculated at the engine mixture ratio, equation (A-30), using  $\Delta h_p$  to correct for enthalpy changes in the chamber and the nozzle. Theoretical  $c^*$  is calculated at the chamber mixture ratio, equation (A-29), using  $\Delta h_{pup}$  to correct for enthalpy changes in the chamber upstream of the throat.

The following efficiencies were then calculated:

$$\begin{aligned}\eta_{c^* P_c} &= \frac{c^* P_c}{c^{*'} } \\ \eta_{I_{vac}} &= \frac{I_{vac}}{I_{vac}'} \\ \eta_{C_F} &= \frac{C_F}{C_F'}\end{aligned}$$

To correct theoretical vacuum specific impulse for heat loss to the nozzle the enthalpy was adjusted as follows:

$$\Delta h_{p(cor)} = \Delta h_p - \frac{q_n}{\dot{w}_o + \dot{w}_f + \dot{w}_c} \quad (A-33)$$

The efficiencies shown below were then calculated using theoretical and experimental values corrected for momentum loss by replacing  $P_c$  with  $P_T$  in all calculations and correcting  $I'_{vac}$  for nozzle heat loss.

$$\begin{aligned}\eta_{c^* P_{c(cor)}} &= \frac{c^* P_{c(cor)}}{c^{*'} (cor)} \\ \eta_{I_{vac(cor)}} &= \frac{I_{vac}}{I_{vac}' (cor)} \\ \eta_{C_F(cor)} &= \frac{C_F(cor)}{C_F' (cor)}\end{aligned}$$

An additional characteristic velocity efficiency,  $\eta_{c^*}$ , was calculated using a characteristic velocity based on the total propellant flow rate ( $\dot{w}_o + \dot{w}_f + \dot{w}_c$ ) and the corrected chamber pressure ( $P_T$ ). This was ratioed to a theoretical  $c^*$  calculated at the engine mixture ratio, equation (A-30). This parameter and the vacuum thrust coefficient efficiency,  $\eta_{CFvac(cor)}$ , are useful for predicting vacuum specific impulse efficiency:

$$\eta_{I_{vac}} = \eta_{C_F vac(cor)} \eta_{c^*} \quad (A-34)$$

A predicted characteristic exhaust velocity ( $c^*$ ) was calculated for each transpiration cooled test assuming no mixing between the transpiring coolant and the injector propellant stream. It was also assumed that there

was no intermixing of the coolant streams from the different segments. A theoretical  $c^*$  was calculated for the mainstream propellants at the mainstream throat total pressure and injector mixture ratio. Next, the coolant from each of the six upstream segments was expanded adiabatically to the mainstream throat static pressure by use of the following equation.

$$\frac{P_c}{P_t} = \left( \frac{T_{w(i)}}{T_{t(i)}} \right)^{\frac{k}{k-1}} \quad (A-35)$$

where:

- $P_c$  = Chamber pressure, psia
- $P_t$  = Throat pressure, psia
- $T_{w(i)}$  = Coolant chamber wall temperature of the segment, psia
- $T_{t(i)}$  = Coolant stream throat temperature of the  $i^{\text{th}}$  segment, psia
- $k$  = Specific heat ratio (evaluated at the average of the coolant chamber wall temperature and coolant stream throat temperature)

After iterating on equation (A-35) to obtain a correct average specific heat ratio, a throat area was determined:

$$A_T = A_{m.t.} + \sum_{i=1}^6 A_{t(i)} \quad (A-36)$$

where:

$$A_{m.t.} = \frac{\dot{w}_{inj} \eta_{c^*} c_{inj}^*}{P_c g_o}$$

$$A_{t(i)} = \frac{\dot{w}_i R T_{t(i)}}{v_{t(i)} P_t}$$

$$v_{t(i)} = \sqrt{\frac{2g k R T_{w(i)}}{k-1} \left[ 1 - \left( P_t / P_{w(i)} \right)^{\frac{k-1}{k}} \right]}$$

and  $c^*$  and  $\eta_{c^*}$  are based on the injector mixture ratio. A  $c^*$  predicted is then defined:

$$c_{pred}^* = \frac{P_c A_T g_o}{\dot{w}_{inj} + \sum_{i=1}^6 \dot{w}_i} \quad (A-37)$$

A predicted vacuum specific impulse was also calculated assuming no mixing of the coolant streams with each other or with the mainstream gases. The mainstream exhaust gases were expanded adiabatically to a series of exhaust pressures, at which the specific impulse and area were calculated. The coolant flow from each segment was also adiabatically expanded from the coolant chamber wall temperature and pressure to the same series of

exhaust pressures. Using an average value of  $k$  velocity, area, and specific impulse were calculated for each coolant stream as follows:

$$V_i = \sqrt{\frac{2g k R T_{w(i)}}{k-1} \left( 1 - \left( \frac{P_e}{P_{w(i)}} \right)^{\frac{k-1}{k}} \right)} \quad (A-38)$$

$$A_i = \frac{\dot{w}_{seg(i)}}{\rho_i V_i} \quad (A-39)$$

$$I_{s(i)} = V_i / g_0 \quad (A-40)$$

For those segments upstream of the throat, coolant stream areas were calculated at the mainstream throat pressure. An area ratio was then calculated for each exhaust pressure by:

$$\epsilon_e = \frac{A_{m,e.} + \sum_{i=1}^8 A_{e(i)}}{A_{m,t.} + \sum_{i=1}^6 A_{t(i)}} \quad (A-41)$$

where:

$$A_{m,e.} = \frac{\dot{w}_{inj} \eta_c * \eta_k}{\rho_{m,e.} V_{m,e.}}$$

The predicted vacuum specific impulse is then:

$$I_{vac} = \frac{C_s \left[ \eta_c * \eta_k \dot{w}_{inj} I'_{vac(inj)} + \sum_{i=1}^8 \dot{w}_{seg(i)} I_{s(i)} + P_e \sum_{i=1}^8 A_{e(i)} \right]}{\left[ \dot{w}_{inj} + \sum_{i=1}^8 \dot{w}_{seg(i)} \right]} \quad (A-42)$$

where the subscript, inj, denotes quantities based on the injector mixture ratio and propellant flow. Plotting the results of equation (A-42) vs area ratio (A-41) for each exhaust pressure, the predicted impulse was obtained at the desired area ratio of 40.

## 2. EXPERIMENTAL DATA ERROR ANALYSIS

To validate the experimental performance data, a statistical data error analysis was made for two typical Task III — Uncooled Altitude Tests. The propellant flow path and the instrumentation configuration were similar for all Task III tests; therefore, the results of this analysis are indicative of the maximum errors involved in all uncooled altitude data. These results are also applicable to the Task V — Regenerative Cooling Altitude Tests, which used a similar test setup, and the characteristic exhaust velocity data in the Task II — Uncooled Sea Level Tests. The propellant flow path and instrumentation locations are shown in figure A-3. The measured parameters that directly affect performance and their estimated



precision are shown in table A-1. Also presented are full-scale range of the recording instruments and a nominal value used in testing. Estimated precisions for each instrument were determined by the Instrumentation Engineering Section. This group maintains a computerized history of evaluations, calibrations and maintenance history relating to all instrumentation devices (see Section IV-D).

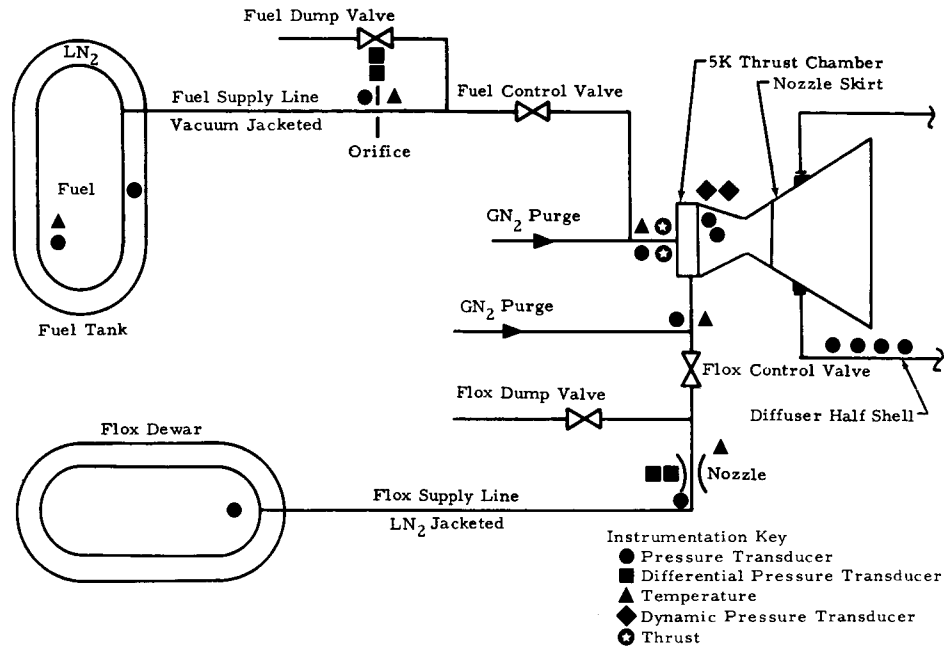


Figure A-3. Propellant Flow Diagram for Uncooled Altitude Tests

FD 12834B

Estimates of performance data accuracy were obtained by combining the precision estimates for the individual parameters using a statistical variation analysis (Reference 6). Basically, the accuracy of a function may be estimated by combining the precisions of the independent variables in that function in the following manner:

$$\sigma_{\phi}^2 = \sum_{i=1}^n \left( \frac{\partial \phi}{\partial x_i} \right)^2 (\sigma_{x_i})^2$$

where:

$\sigma_{\phi}$  = the accuracy of the parameter ( $\phi$ )

$\frac{\partial \phi}{\partial x_i}$  = the partial derivative of the function with respect to the ith variable

$\sigma_{x_i}$  = the precision value associated with the ith variable.

For example, in calculating characteristic exhaust velocity based on chamber pressure

$$c^*_{P_c} = \frac{A_{t_o} g_o P_c}{\dot{w}_p}$$

the error,  $\sigma_{c^*P_c}$ , is given by: :

$$(\sigma_{c^*P_c})^2 = \left( \frac{\partial c^*P_c}{\partial A_t} \right)^2 (\sigma_{A_t})^2 + \left( \frac{\partial c^*P_c}{\partial P_c} \right)^2 (\sigma_{P_c})^2 + \left( \frac{\partial c^*P_c}{\partial \dot{w}_p} \right)^2 (\sigma_{\dot{w}_p})^2$$

where:

$$\left( \frac{\partial c^*P_c}{\partial A_t} \right) = \frac{g_o P_c}{\dot{w}_p}$$

$$\left( \frac{\partial c^*P_c}{\partial P_c} \right) = \frac{A_t g_o}{\dot{w}_p}$$

$$\left( \frac{\partial c^*P_c}{\partial \dot{w}_p} \right) = \frac{A_t g_o P_c}{\dot{w}_p^2}$$

Tables A-2 and A-3 give error estimates for performance data based on mixture ratios of 5.7 and 4.0, respectively. Note that the estimated errors in the theoretical values of  $c^*$  and  $C_F$  are significantly smaller for a mixture ratio of 4.0 than those for a mixture ratio of 5.7. This is due to a much smaller change in the theoretical parameters for an equal change in percent of fluorine at a mixture ratio of 4.0.

The error estimates given in these tables are pessimistic because they do not reflect the increased accuracy obtained by averaging and comparing redundant measurements, and they use the maximum error in flox concentration derived from a weight analysis. Flox concentrations were verified by chemical analysis of each mix and usually were better than the values shown in these tables.

TABLE A-1. PRECISION ESTIMATES OF RECORDED PARAMETERS

Header	Full-Scale Range	Nominal Value	Precision (% of Nominal) Confidence Level	
			95 (2 $\sigma$ )	68 (1 $\sigma$ )
Flox Nozzle Differential Pressure	200 psid	43.4 psid (r = 5.7) 39.2 psid (r = 4.0)	$\pm 1.4533$ $\pm 1.6133$	$\pm 0.7266$ $\pm 0.8067$
Fuel Orifice Differential Pressure	100 psid	17.9 psid (r = 5.7) 32.9 psid (r = 4.0)	$\pm 1.7467$ $\pm 0.9533$	$\pm 0.8733$ $\pm 0.4767$
Chamber Pressure <sup>(1)</sup>	200 psia	100.0 psia	$\pm 0.3287$	$\pm 0.1643$
Fuel Orifice Downstream Temperature	40-960°R	180°R		
Oxidizer Nozzle Downstream Temperature	140-360°R	155°R		
Thrust <sup>(1)</sup>	-10,000 lb	-4035 lb	$\pm 1.0267$	$\pm 0.5133$
Tare		0.0 lb	$\pm 0.6600$	$\pm 0.3300$ (3)
A <sub>1</sub> (Projected Area of Diffuser Band)		532.3 in. <sup>2</sup>	$\pm 0.06267$	$\pm 0.0313$
A <sub>e</sub> (Projected Area of Nozzle Exit)		1119.8 in. <sup>2</sup>	$\pm 0.0567$	$\pm 0.0283$
Throat Area		28.033 in. <sup>2</sup>	$\pm 0.0107$	$\pm 0.00533$
Flox Weight System	10,000 lb		$\pm 0.1333\%$ of reading	$\pm 0.0666\%$ of reading
	50,000 lb		$\pm 0.3333\%$ (2)	$\pm 0.1666\%$ (2)

(1) Indicates redundant instrumentation.

(2) This is the uncertainty in a single measurement; three weighings are required to mix flox, one below 10K and two above 10K; (1) Dewar (Tare weight), (2) LO<sub>2</sub> weight, (3) Fluorine + LO<sub>2</sub> weight.

(3) Expressed as a percentage of nominal thrust.

TABLE A-2. ACCURACY OF FLOX-METHANE UNCOOLED ALTITUDE DATA:  
MIXTURE RATIO,  $r = 5.7$

Calculation	Nominal Value	Bias Limit (% of Nominal) Confidence Level		Accuracy (% of Nominal) Confidence Level	
		95 ( $2\sigma$ )	68 ( $1\sigma$ )	95 ( $2\sigma$ )	68 ( $1\sigma$ )
% $F_2$	82.6%			$\pm 2.3667$	$\pm 1.1833$
$\rho_o$	89.09			$\pm 0.5513$	$\pm 0.2756$
$\dot{w}_o$	11.57			$\pm 0.9000$	$\pm 0.4500$
$\dot{w}_f$	2.028			$\pm 1.9733$	$\pm 0.9867$
$r$	5.70			$\pm 2.1733$	$\pm 1.0867$
$C_F$	1.7836			$\pm 1.0467$	$\pm 0.5233$
$F_{vac}$	5000			$\pm 0.9933$	$\pm 0.4967$
$P_c$	100.0			$\pm 0.3287$	$\pm 0.1643$
$c^*P_c$	6640			$\pm 0.8867$	$\pm 0.4433$
$I_{vac}$	367.8			$\pm 1.2867$	$\pm 0.6433$
$I'_{vac}$	418.0	-0.6373	-0.3187		
$c^*'$	6990	-0.9533	-0.4767		
$C_{F_{vac}}$	1.926	-0.2420	-0.1210	$\pm 0.1727$	$\pm 0.0863$
$c^*_F$	6314	+0.2427	+0.1213	$\pm 1.2933$	$\pm 0.6467$
$\eta_{c^*P_c}$	94.99%	+0.9533	+0.4767	$\pm 0.8867$	$\pm 0.4433$
$\eta_{c^*_F}$	90.33%	+0.9533	+0.4767	$\pm 1.2933$	$\pm 0.6467$
$\eta_{I_{vac}}$	87.99%	+0.6360	+0.3180	$\pm 1.2867$	$\pm 0.6433$
$\eta_{C_{F_{vac}}}$	92.61%	+0.2447	+0.1223	$\pm 1.0600$	$\pm 0.5300$
$C_{F(cor)}$	1.831			$\pm 1.0467$	$\pm 0.5233$
$c^*P_{c(cor)}$	6467			$\pm 0.8867$	$\pm 0.4433$
$c^*'(cor)$	6937	-0.9600	-0.4800		
$I'_{vac(cor)}$	416.7	-0.640	-0.3200		
$\eta_{C_{F(cor)}}$	95.08%	+0.2453	+0.1227	$\pm 1.0600$	$\pm 0.5300$
$\eta_{c^*_F(cor)}$	91.02%	+1.2000	+0.6000	$\pm 1.2933$	$\pm 0.6467$
$\eta_{I_{vac(cor)}}$	88.26%	+0.6420	+0.3210	$\pm 1.2867$	$\pm 0.6433$
$\eta_{c^*P_{c(cor)}}$	95.72%	+0.9600	+0.4800	$\pm 0.8867$	$\pm 0.4433$

TABLE A-3. ACCURACY OF FLOX-METHANE UNCOOLED ALTITUDE DATA:  
MIXTURE RATIO,  $r = 4.0$

Calculation	Nominal Value	Bias Limit (% of Nominal) Confidence Level		Accuracy (% of Nominal) Confidence Level	
		95 ( $2\sigma$ )	68 ( $1\sigma$ )	95 ( $2\sigma$ )	68 ( $1\sigma$ )
% $F_2$	82.6%			$\pm 2.3667$	$\pm 1.1833$
$\rho_o$	89.09			$\pm 0.5513$	$\pm 0.2756$
$\dot{w}_o$	11.0			$\pm 0.9667$	$\pm 0.4833$
$\dot{w}_f$	2.75			$\pm 1.6267$	$\pm 0.8133$
$r$	4.0			$\pm 1.9000$	$\pm 0.9500$
$C_F$	1.7836			$\pm 1.0467$	$\pm 0.5233$
$F_{vac}$	5000			$\pm 0.9933$	$\pm 0.4967$
$P_c$	100			$\pm 0.3287$	$\pm 0.1643$
$c^*P_c$	6565			$\pm 0.9000$	$\pm 0.4500$
$I_{vac}$	363.6			$\pm 1.3067$	$\pm 0.6533$
$I'_{vac}$	402.7	+0.0827	+0.0413	$\pm 0.3973$	$\pm 0.1987$
$c^*$	6800	+0.1400	+0.0700	$\pm 0.2253$	$\pm 0.1127$
$C_{Fvac}$	1.905			$\pm 0.3493$	$\pm 0.1747$
$c^*_F$	6311			$\pm 0.3533$	$\pm 0.6767$
$\eta_{c^*P_c}$	96.50%	-0.1380	-0.0690	$\pm 0.9333$	$\pm 0.4667$
$\eta_{c^*F}$	92.81%	-0.1360	-0.0690	$\pm 1.3733$	$\pm 0.6867$
$\eta_{I_{vac}}$	90.31%	-0.0807	-0.0403	$\pm 1.3667$	$\pm 0.6833$
$\eta_{C_{Fvac}}$	93.63%			$\pm 1.1067$	$\pm 0.5533$
$C_{F(cor)}$	1.8312			$\pm 1.0467$	$\pm 0.5233$
$c^*P_{c(cor)}$	6394			$\pm 0.9000$	$\pm 0.4500$
$I'_{vac(cor)}$	400.5	+0.0827	+0.0413	$\pm 0.3993$	$\pm 0.1997$
$c^*_{(cor)}$	6761	+0.1380	+0.0690	$\pm 0.2267$	$\pm 0.1133$
$\eta_{C_{F(cor)}}$	96.13%			$\pm 1.1000$	$\pm 0.5500$
$\eta_{c^*F(cor)}$	93.34%	-0.1353	-0.0677	$\pm 1.3733$	$\pm 0.6867$
$\eta_{I_{vac(cor)}}$	90.79%	-0.0807	-0.0403	$\pm 1.3667$	$\pm 0.6833$
$\eta_{c^*P_{c(cor)}}$	97.10%	-0.1373	-0.0687	$\pm 0.9333$	$\pm 0.4667$

Another possible source of error in the data arises from the chemical purity of the propellants. Methane was purchased as a 95% purity gas and was further scrubbed to remove the bulk of the  $\text{CO}_2$ . Butene-1 and propane were purchased as pressurized liquids with 98% guaranteed minimum purities. The guaranteed maximum concentrations of the diluents are shown in table A-4. Fluorine was purchased with a guaranteed minimum purity of 99%. The maximum concentrations of the fluorine diluents are shown in table A-4. Increased flox concentration accuracy was obtained by including the oxygen diluents, for the fluorine batch being used, in the mixing calculations. A purity assay was received with each shipment of fluorine. Figure A-4 shows the effect of including the maximum impurities on the theoretical vacuum specific impulse. It can be seen that the maximum error incurred through neglecting the impurities was less than 0.4%. Figure A-4 also shows that most of this error is due to the methane impurities.

TABLE A-4. GUARANTEED PURITIES OF PURCHASED PROPELLANTS

Propellant	Major Specie <sup>(1)</sup>								
	HF + $\text{CF}_4$	$\text{O}_2$ + $\text{N}_2$	$\text{CO}_2$	Ethane	Propane	Butanes	Pentanes	Hexanes	Heptanes and Higher
Fluorine (99% Minimum)	0.1	0.9							
Oxygen (99.6% Minimum)		0.4							
Methane (95.14% Minimum)		0.71	0.1	3.32	0.39	0.23	0.08	0.02	0.01
Butene-1 (98.1% Minimum)						1.90			
Propane (98.3% Minimum)				1.04		0.66			

<sup>(1)</sup>Contaminants are given by weight percentages.

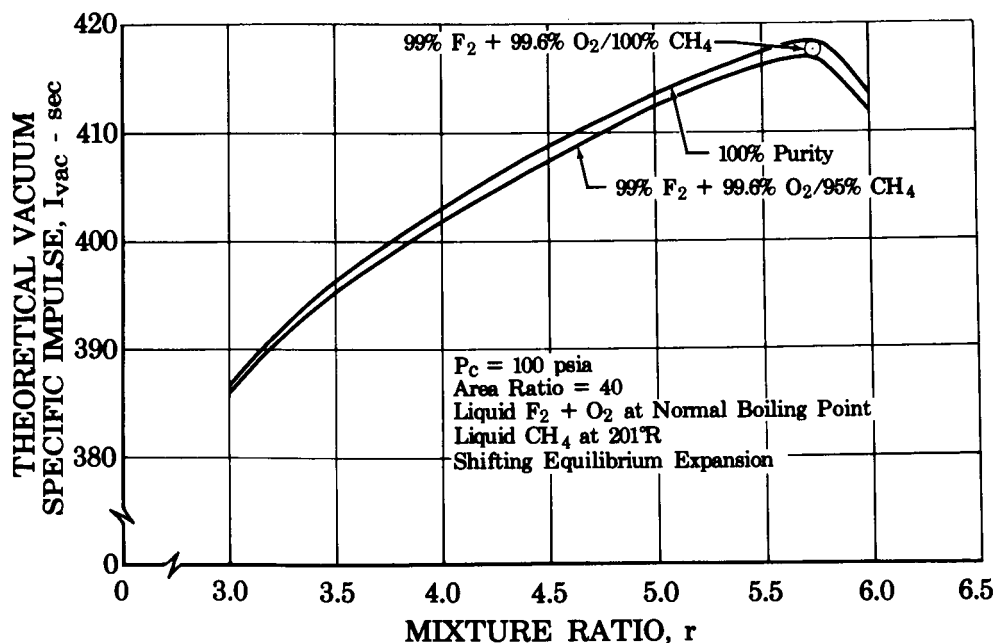


Figure A-4. Effect of Propellant Contaminants on Theoretical Performance: 82.6%  $\text{F}_2$  in Flox/Methane

FD 19784

### 3. SYMBOLS USED IN APPENDIX A

$A_e$	Nozzle exit area, in. <sup>2</sup>
$A_t$	Throat area, in. <sup>2</sup>
$C_F$	Thrust coefficient
$C_{F_{sl}}$	Sea level thrust coefficient
$c_p$	Constant pressure specific heat, Btu/lb <sub>m</sub> °R
$C_s$	Stream thrust coefficient
$c^*$	Characteristic exhaust velocity, ft/sec
$\epsilon_e$	Nozzle exit to throat area ratio, $A_e/A_t$
$F$	Thrust, lb
$g_o$	Gravitational constant - 32.174, lb <sub>m</sub> -ft/lb <sub>f</sub> -sec <sup>2</sup>
$h$	Enthalpy, Btu/lb
$I_s$	Specific impulse at $P_e = P_a$ , lb <sub>f</sub> - sec/lb <sub>m</sub>
$I_{sl}$	Sea level specific impulse, lb <sub>f</sub> -sec/lb <sub>m</sub>
$I_{vac}$	Specific impulse at $P_a = 0$ , lb <sub>f</sub> -sec/lb <sub>m</sub>
$K$	Curve fit constant
$P_a$	Ambient pressure, psia
$P_c$	Chamber pressure, psia
$P_d$	Half shell pressure, psia
$P_T$	Chamber pressure corrected for momentum loss, psia
$q$	Heat transferred to wall, Btu/sec
$T$	Propellant inlet temperature, °R
$r$	Mixture ratio, (oxidizer/fuel)
$\rho$	Density, lb/ft <sup>3</sup>
$V$	Velocity, ft/sec
$W$	Flow parameter, lb/sec- $\sqrt{\rho}$
$\dot{w}$	Flow rate, lb/sec- $\sqrt{\rho}$
$\eta$	Efficiency

Subscripts:

c	Coolant
ch	Chamber
cup	Chamber coolant upstream of throat
(C <sub>s</sub> )	Corrected for C <sub>s</sub>
(cor)	Corrected for momentum loss, heat loss, and C <sub>s</sub>
e	Exit
inj	Injector flow
n	Nozzle
nbp	Normal boiling point
o	Oxidizer (through injector)
f	Fuel (through injector)
m	Mainstream or injector flow
p	Propellant
t	Throat
vac	Value at P <sub>a</sub> = 0

4. REFERENCES

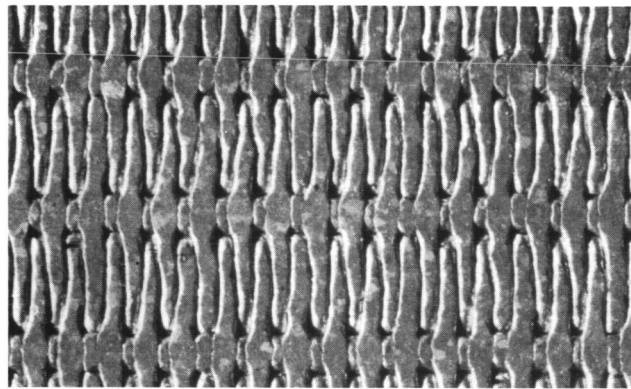
1. Stewart, R. B., J. G. Hust, and R. D. McCarty, "Interim Thermodynamic Properties for Gaseous and Liquid Oxygen at Temperatures from 55 to 300°K and Pressures to 300 atm," National Bureau of Standards, Report 7922, 1 October 1963.
2. "Liquid Propellant Manual," Johns Hopkins Applied Physics Laboratory Liquid Propellant Information Agency, March 1961.
3. Arnitt, R. L., K. S. Pitzer, and F. D. Rossini, "Selected Values of Physical and Thermodynamic Properties of Hydrocarbons and Related Derivatives," American Petroleum Institute Project 44, Carnegie Press, New York, 1953.
4. Timmermans, J., "Physico-Chemical Constants of Pure Organic Compounds," Elsevier Publishing Co., Inc., New York, 1950.
5. "Digital Computer Programs for Rocket Nozzle Design and Analysis — Volume II — Bell Nozzle Design," Pratt & Whitney Aircraft PWA FR-1021, prepared under NASA Contract NAS9-2487, 26 June 1964.
6. Colbert, D. L., "Use of Partial Derivatives in Variation Analysis," Pratt & Whitney Aircraft SMR FR-1993, 30 September 1966.



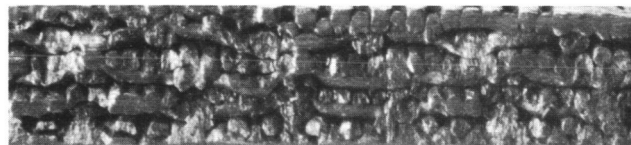
## APPENDIX B

### TRANSPIRATION COOLING FLOW ANALYSIS

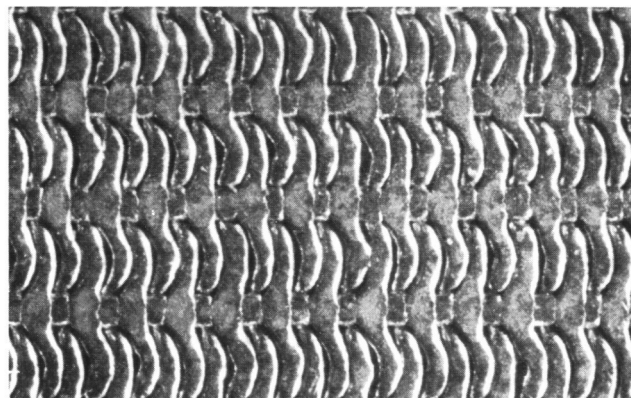
The porous chamber walls of the transpiration-cooled chamber (Section III, paragraph D) were constructed with a sintered multiple-layer woven wire sheet known under the registered trade name of Rigimesh (figure B-1). The chamber itself was divided into eight separate segments, using several different Rigimesh porosities, connected to a common manifold. Coolant flow-metering orifices within each segment provided for the distribution of the total coolant among the individual segments. To size the segment orifices to give the desired coolant distribution it was necessary to provide an accurate estimate of the coolant pressure drop across the Rigimesh in each segment. Due to the complex dependence of this coolant pressure drop on such factors as heat flux, coolant flow rate, and Rigimesh flow characteristics, a detailed analysis (a refinement of the analysis conducted under Contract NAS3-4195) was conducted.



Side A



Cross  
Section



Side B

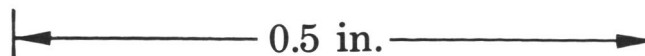


Figure B-1. Rigimesh Sections

FD 19785

## 1. PRESSURE DROP PREDICTION METHOD

The pressure drop prediction method used in this analysis involved the solution of differential equations describing the pressure and temperature profiles across the porous Rigimesh walls. The solutions of these differential equations were obtained numerically through the use of an IBM 7090 digital computer. Using measured or estimated Rigimesh properties and flow characteristics, the coolant pressure drops were calculated for given coolant flow rates, chamber heat fluxes, and chamber pressures.

The analytical model consisted of the adiabatic segment manifold and porous Rigimesh chamber wall shown in figure B-2. Heat flux to the chamber wall causes the coolant to be heated as it enters the segment manifold and passes through the Rigimesh. As the segment is assumed to be insulated or adiabatic, the increase in coolant energy is equated to the chamber heat flux at the chamber side of the Rigimesh. Heat is transferred within the Rigimesh itself by means of conduction; at the chamber side of the Rigimesh this heat conduction can also be equated with the chamber heat flux.\*

$$q_w = AG \left[ h - h_i + \frac{1}{2g_o J} \left( \frac{G}{\rho \phi} \right)^2 \right] \Bigg|_{x=L} = Ak \frac{dT}{dx} \Bigg|_{x=L}$$

where the term  $(G/\rho\phi)$  is the average coolant velocity at the chamber. Part of the heat being conducted through the Rigimesh is convectively transferred to the coolant flowing through the Rigimesh, and is equated to the rate of increase in the energy content of the coolant.

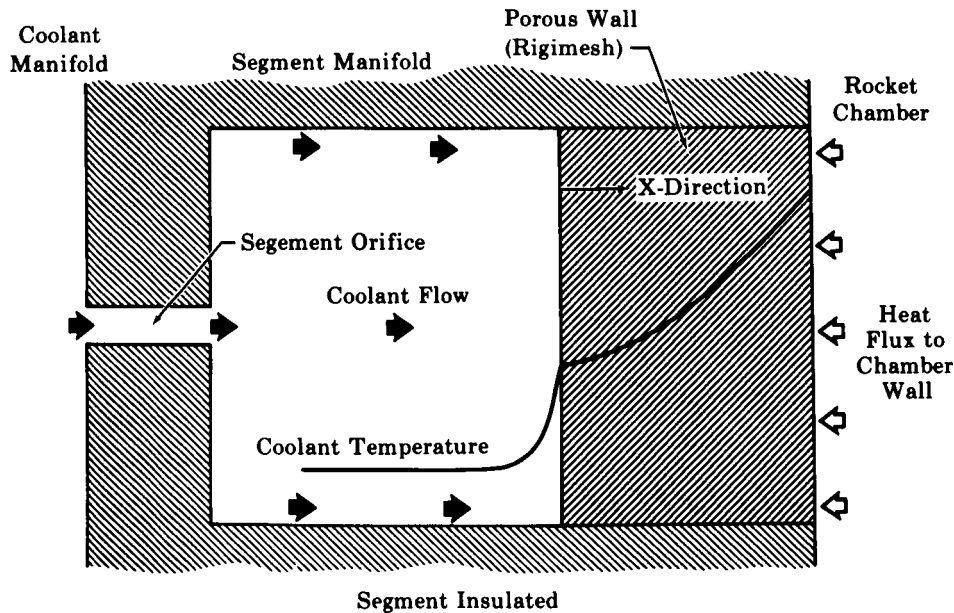


Figure B-2. Model of Transpiration-Cooled Segment

FD 14459A

\*Nomenclature in this appendix is presented in paragraph 4.

$$\frac{d}{dx} \left( k \frac{dT}{dx} \right) = G \frac{d}{dx} \left[ c_p T + \frac{1}{2g_o J} \left( \frac{G}{\rho \phi} \right)^2 \right]$$

Here the assumption that the coolant is in thermal equilibrium with the Rigimesh appears to be reasonable (Reference 1\*). Where the coolant is vaporized within the Rigimesh pores, vaporization is assumed to occur at a point rather than over a finite distance. The coolant pressure drop across the Rigimesh is essentially due to internal friction, with small contributions due to expansion effects and possible choking at the chamber side of the Rigimesh. The pressure gradient is given by:

$$\frac{d}{dx} \left[ P + \frac{\rho}{2g_o} \left( \frac{G}{\rho \phi} \right)^2 \right] = - \frac{f \beta G^2}{2g_o \rho}$$

The coolant pressure at the chamber side of the Rigimesh is equal to the static chamber pressure if flow is not choked, or equal to the choking pressure if flow is choked.

$$P \Big|_{x=L} = P_c \text{ (if not choked)}$$

$$\left( \frac{G}{\rho \phi} \right) \Big|_{x=L} = \sqrt{\frac{g_o \gamma R T}{M}} \Big|_{x=L} \text{ (if choked)}$$

Where  $P$  is implicitly expressed as a function of  $\rho$  in the last equation, if two-phase flow occurs at the chamber side of the Rigimesh.

The system of differential equations just described, consisting of the two differential equations and three boundary conditions, was solved by integrating across the Rigimesh from the chamber side to the segment manifold. The integration was performed numerically using the 4th-order Runge-Kutta numerical integration technique. All coolant properties (such as density, heat capacity, viscosity, heat of vaporization, and boiling point) were treated as functions of temperature and/or pressure.

Rigimesh properties required for solution of the differential equation system included the thickness, porosity, thermal conductivity, choked flow area and friction factor. Measured Rigimesh thicknesses varied from 0.104 to 0.135 inch depending on the Rigimesh type. Rigimesh porosities, determined through the measurement of the apparent and actual densities, were found to range from 10 to 13%. Although no measurement was made of thermal conductivity, sufficiently accurate values were estimated from the thermal conductivity of the pure metal (N-155 Multimet) and the Rigimesh porosities, based on comparisons with the thermal conductivities of other porous metal matrixes. The thermal conductivity was assumed to vary with temperature in the same manner as that of the pure metal.

---

\*References in this appendix are presented in paragraph 5.

The choked flow areas and friction factors were determined from flow measurements made on Rigimesh samples using both water and gaseous nitrogen as the flow media. Figure B-3 presents typical gaseous nitrogen flow data obtained from two of the samples. The slope transitions in each curve are indicative of the choking point (i.e., the flow rate at which the gas reaches the acoustic velocity at the downstream side of the Rigimesh). Note that the upstream choking pressure is considerably greater than the upstream choking pressure for an isentropic expansion, because most of the pressure drop is due to friction and not expansion effects. The choked flow areas calculated from the gas density, acoustic velocity and flow rate at the choking point were found to range from 0.6 to 0.9% of the area of side A (see figure B-1). Flow measurements made in the opposite direction indicated that while the choked flow area of side B was considerably larger than that of side A, the pressure drop was essentially independent of the flow direction. This is because the choking effects are insignificant compared with the frictional effects in most cases.

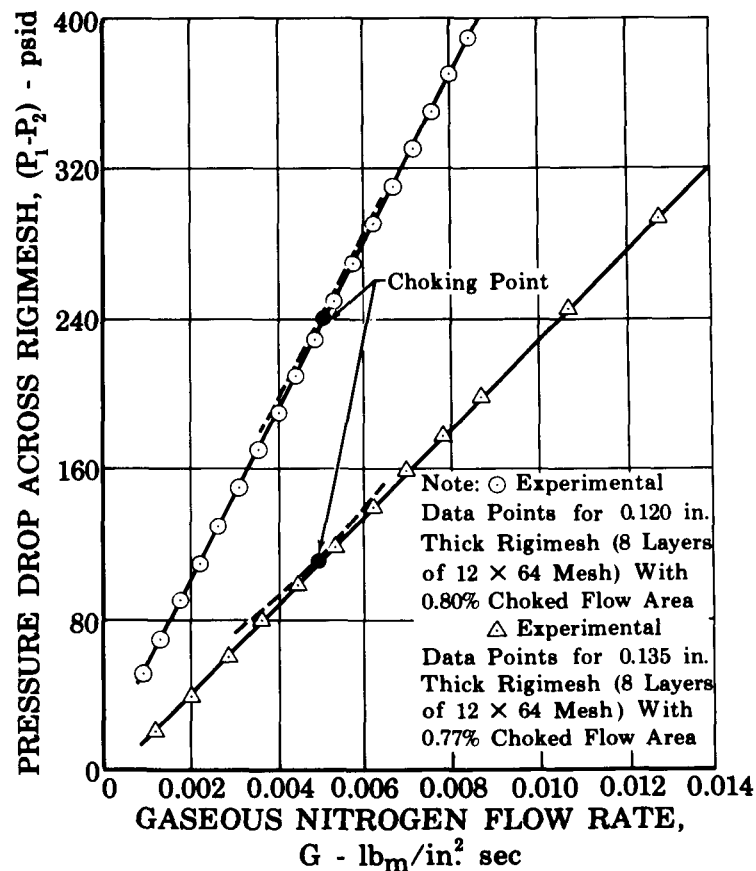


Figure B-3. Rigimesh - Gaseous Nitrogen Flow Data

FD 19786

The Rigimesh friction factor was obtained from flow data by means of a friction factor correlation method presented in Reference 2. This method uses two friction factor coefficients obtained from flow data to give a generalized friction factor curve, much the same as that obtained for pipe flow data. The pressure gradient for flow through Rigimesh is given by:

$$\frac{dP}{dx} = - \frac{f\beta G^2}{2g_o\rho} - \frac{d}{dx} \left[ \frac{\rho}{2g_o} \left( \frac{G}{\rho\phi} \right)^2 \right]$$

where the friction term contains the sum of viscous and inertial contributions.

$$\frac{f\beta G^2}{2g_o\rho} = \frac{\alpha\mu G}{g_o\rho} + \frac{\beta G^2}{g_o\rho}$$

Here  $\alpha$  and  $\beta$  are the viscous and inertial coefficients of the friction factor. These two coefficients are obtained from integrated forms of the pressure gradient equation by plotting  $[(P_1 - P_2)g_o\rho/GL\mu]$  versus  $(G/\mu)$  for a liquid, or

$$\left[ \frac{(P_1^2 - P_2^2)g_o M}{2GLRT\mu} - \frac{G}{L\phi_c^2\mu} \ln\left(\frac{P_1}{P_2}\right) \right] \text{ versus } (G/\mu)$$

for isothermal gas flow. Figures B-4 and B-5 present these plots for water flow data and the gaseous nitrogen flow data given in figure B-3. The viscous coefficient,  $\alpha$ , is the intercept on these plots and the inertial coefficient,  $\beta$ , is the slope. The water flow data on these plots probably

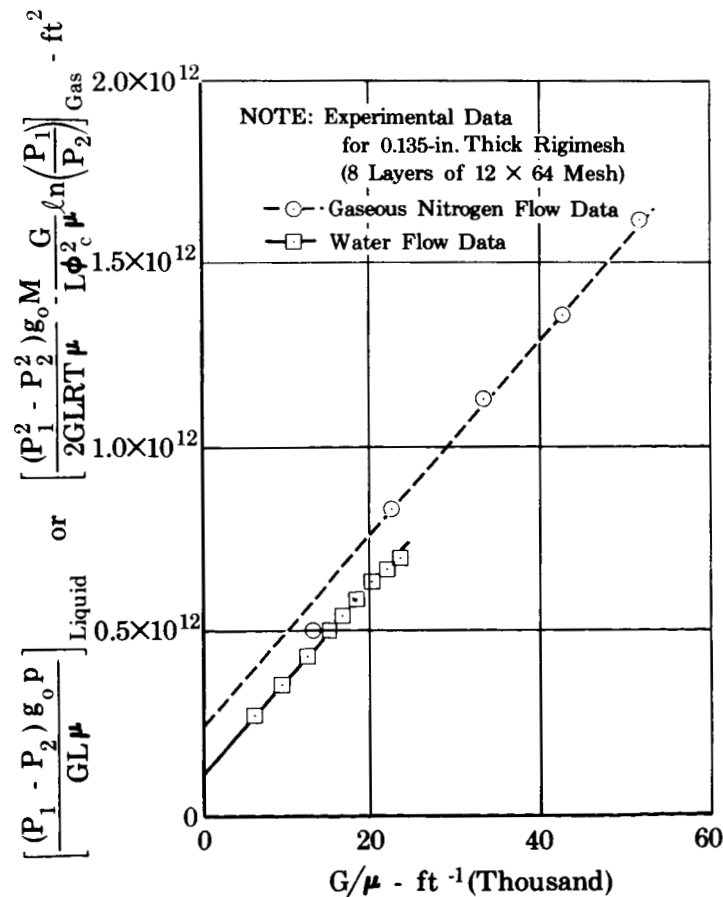


Figure B-4. Friction Factor Reduction Plot

FD 19787

give the most accurate values of the two coefficients because the incompressible nature of the water enables more accurate measurements. Using  $\alpha$  and  $\beta$ , a special Reynolds number is defined as  $N_{Re} = \beta G / \alpha \mu$ . Figure B-6 presents the above flow data reduced in the form of the friction factor versus Reynolds number. Hence, after the viscous and inertial coefficients have been determined for a given piece of Rigimesh, the friction factor can be calculated for any coolant, at any temperature and any flow rate by the theoretical relationship  $f = 2/N_{Re} + 2$ .

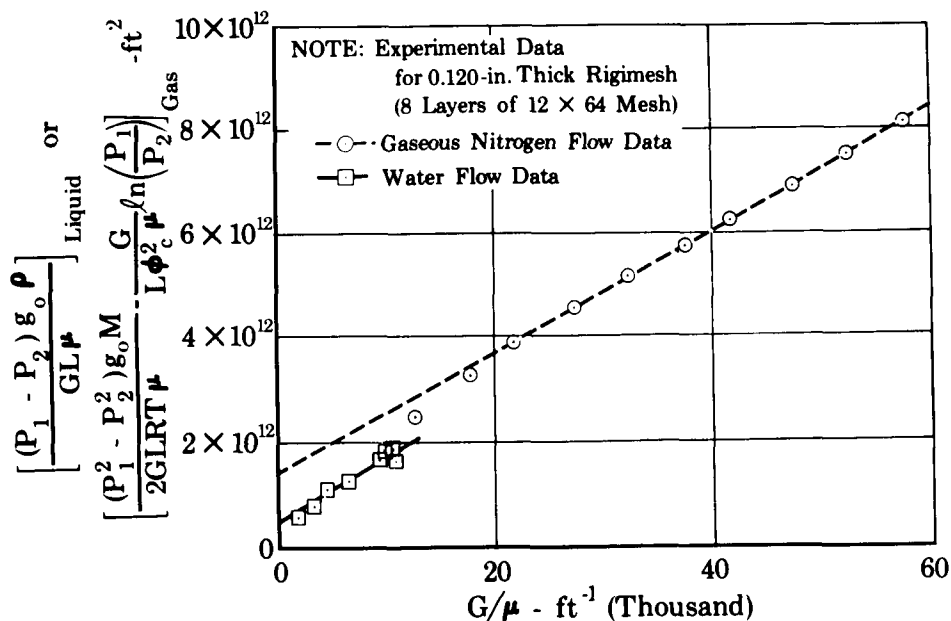


Figure B-5. Friction Factor Reduction Plot

FD 19788

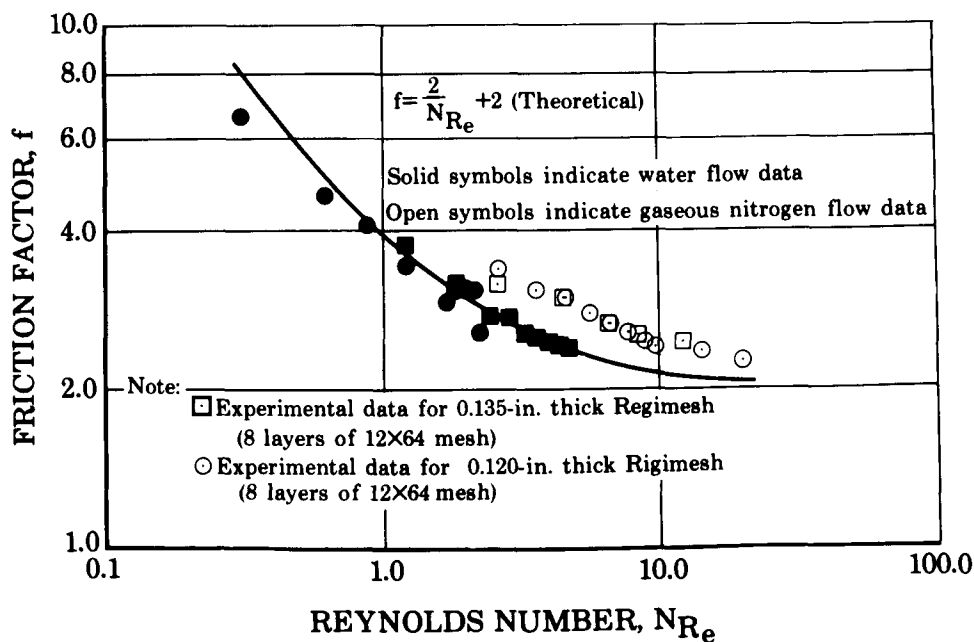


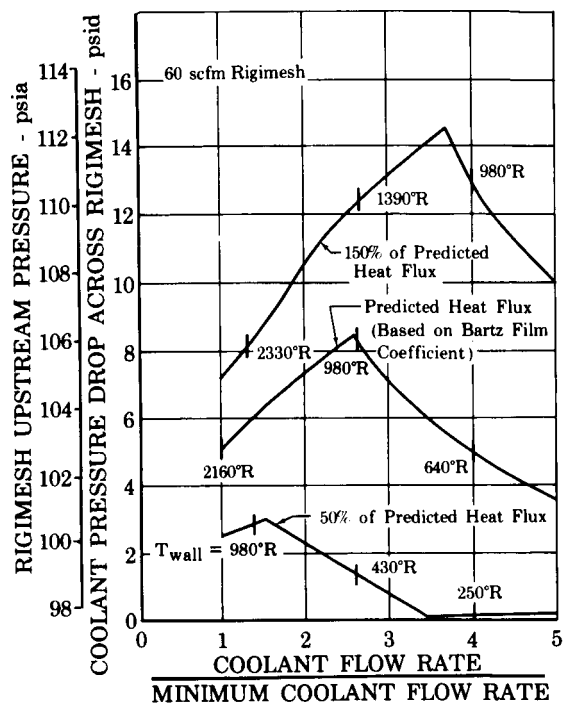
Figure B-6. Rigimesh Friction Factor Plot

FD 19789

Typical solutions are presented in figure B-7, which gives the predicted pressure drop versus coolant (liquid methane) flow rate for each chamber segment. The minimum coolant flow rate corresponds to a wall temperature of  $2160^{\circ}\text{R}$ . The left portions of the curves (i.e., positive slopes at low coolant flow rates) represent a region where the coolant is gaseous through the Rigimesh pores. The portions of the curves with negative slopes at somewhat higher coolant flow rates indicate a region where the coolant is liquid through the initial part of the Rigimesh pore and gaseous through the remainder of the pore. At sufficiently large flow rates, the coolant is liquid throughout the pore, and the pressure drop increases with increasing flow rate, as illustrated by the right portions of the 50% heat flux curve.

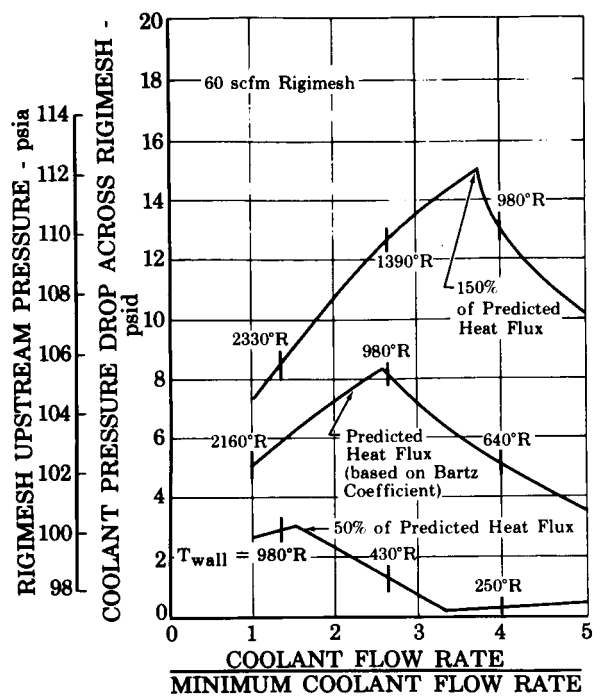
## 2. PARAMETRIC STUDY

A parametric study was conducted to examine the sensitivity of the predicted pressure drops to the various influencing parameters. The local heat flux was found to be the most sensitive parameter, as illustrated by figure B-7. Localized variations of this parameter, and the inherent uncertainty in using the Rigimesh temperature to determine heat flux, make the prediction of the pressure drop and the comparison with experimental results most difficult. The effects of other influencing parameters were investigated using the conditions corresponding to segment No. 2. The pressure drop is also sensitive to the friction factor (composed of the viscous and inertial contributions), as can be seen in figure B-8. Although the viscous and inertial coefficients of the friction factor were measured for Rigimesh test specimens, large local variations and high-temperature hysteresis compound the sensitivity of these two parameters. Other parameters such as chamber pressure, coolant inlet temperature and Rigimesh thermal conductivity have less significant sensitivity effects; these are also shown in figure B-8. The pressure drop in most cases was found to be insensitive to parameters such as porosity and choked flow area.



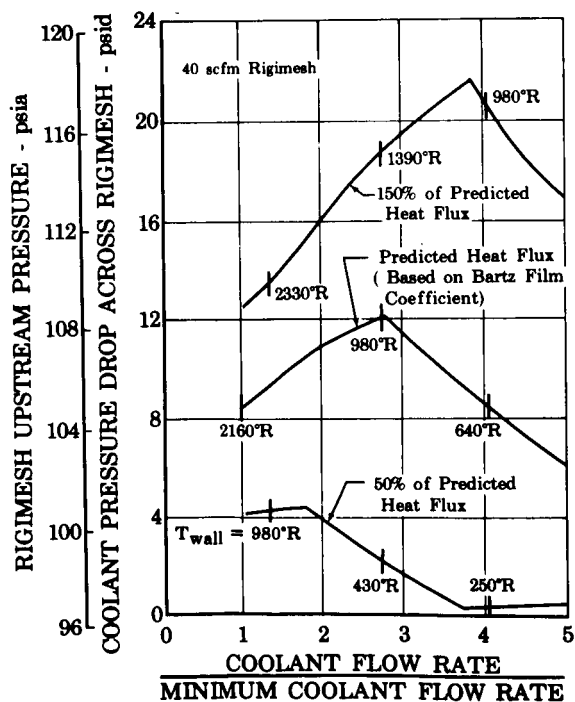
Segment No. 1

FD 19790



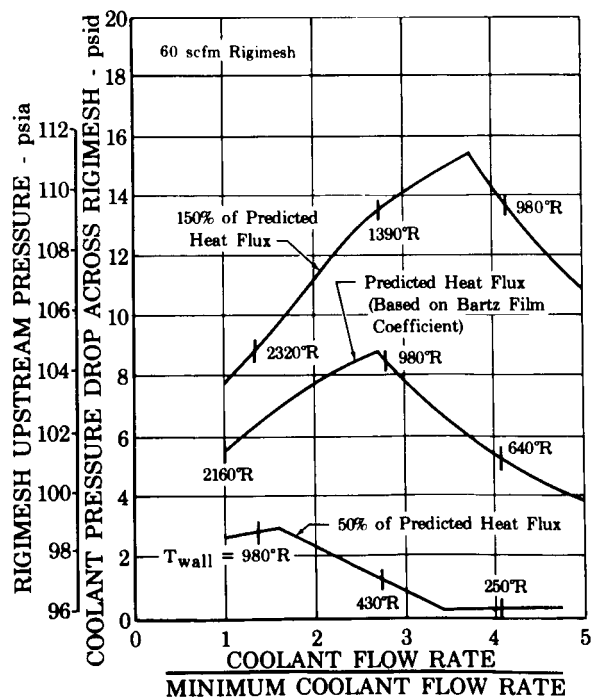
Segment No. 2

FD 19791



Segment No. 3

FD 19792

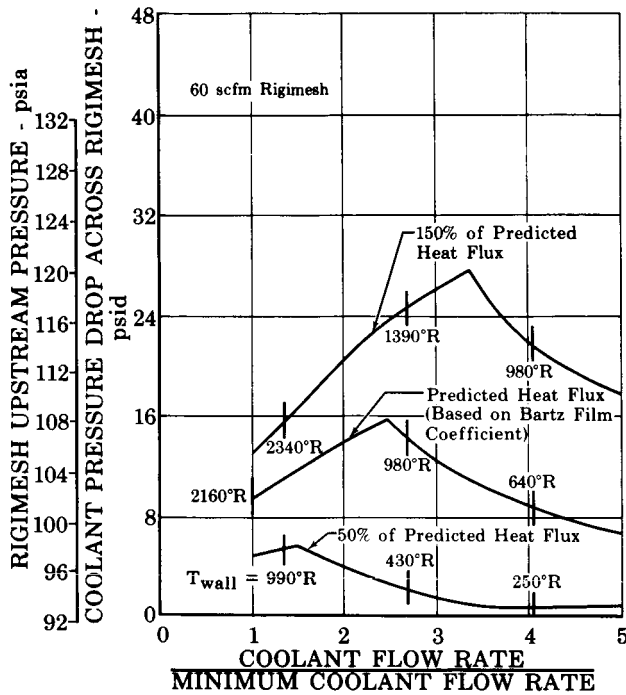


Segment No. 4

FD 19793

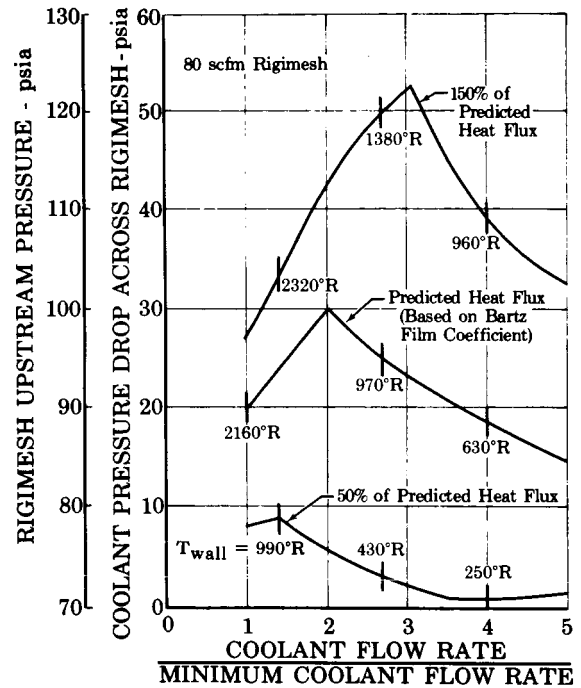
Figure B-7. Effect of Heat Flux on Coolant Pressure Drop Across Rigimesh





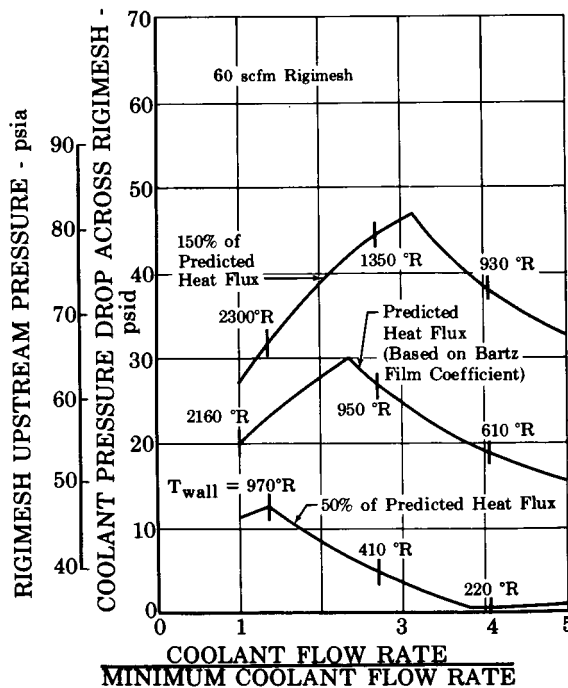
Segment No. 5

FD 19794



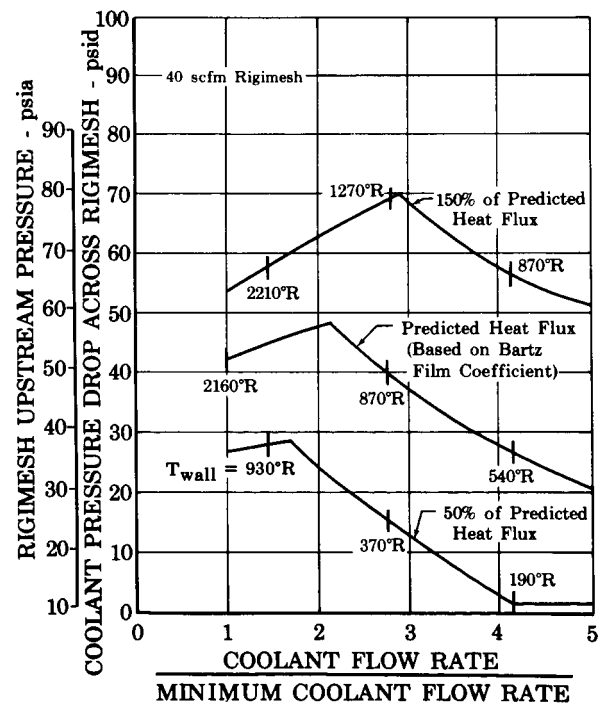
Segment No. 6

FD 19795



Segment No. 7

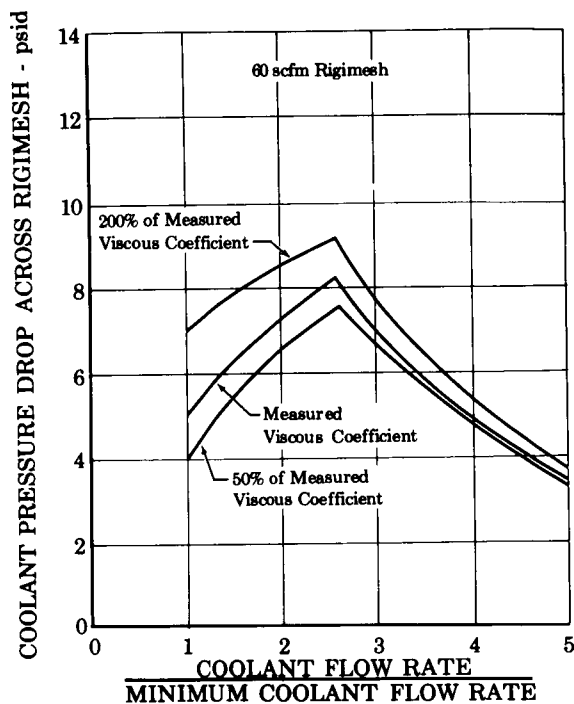
FD 19796



Segment No. 8

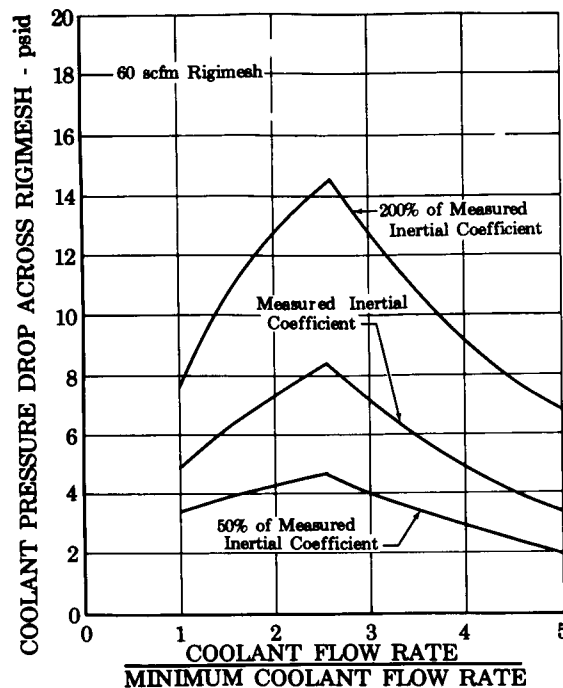
FD 19797

Figure B-7. Effect of Heat Flux on Coolant Pressure Drop Across Rigimesh (Continued)



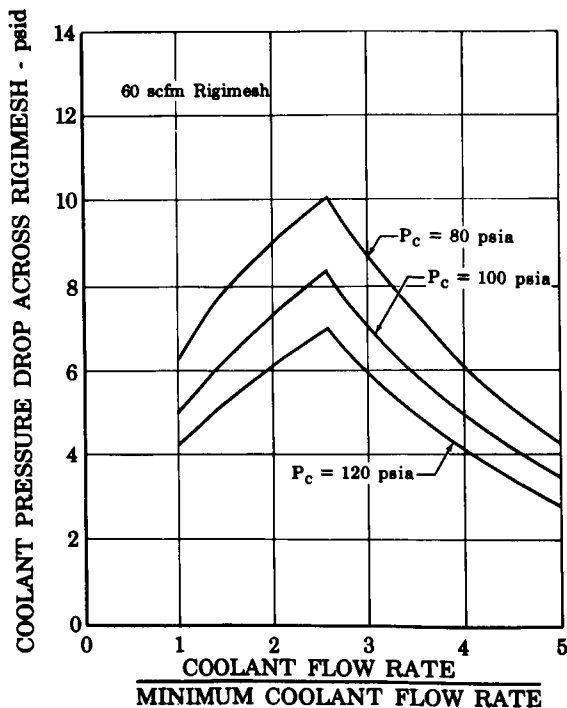
Viscous Coefficient

FD 19798



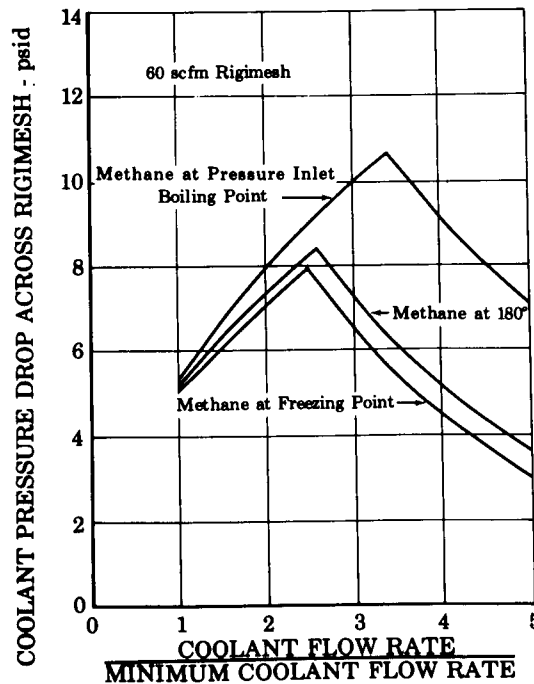
Inertial Coefficient

FD 19799



Chamber Pressure

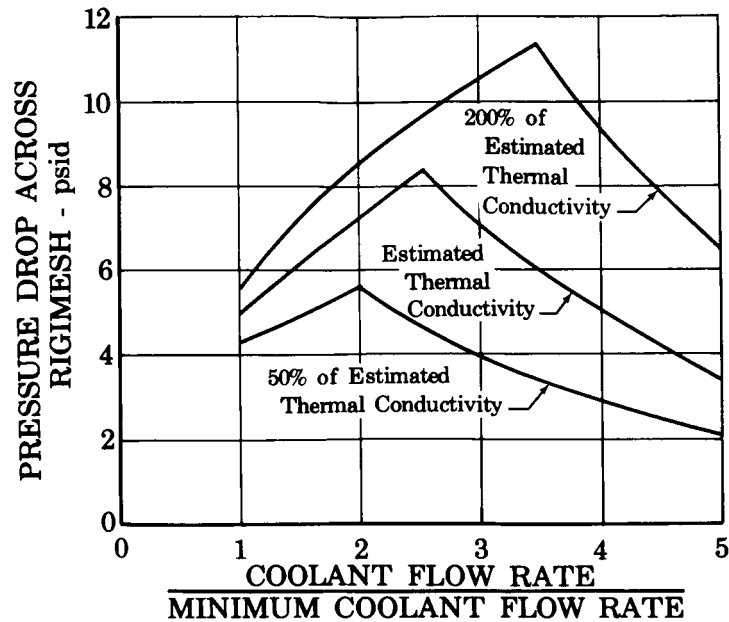
FD 19800



Coolant Inlet Temperature

FD 19801

Figure B-8. Effect of Parametric Variations on Coolant Pressure Drop Across Rigimesh;  
Segment No. 2



Rigimesh Thermal Conductivity

FD 19802

Figure B-8. Effect of Parametric Variations on Coolant Pressure Drop Across Rigimesh; Segment No. 2 (Continued)

### 3. CORRELATION OF TEST RESULTS

The predicted methane pressure drops for the eight transpiration-cooled chamber segments as presented in figure B-7 show three levels of heat flux in an attempt to estimate maximum, minimum, and expected values of predicted pressure drop. Table B-1 presents a comparison of the experimental pressure drops from the Task IV tests with the analytical predictions to verify the validity of the analytical model. Satisfactory agreement of actual and predicted pressure drops was obtained for most of the points studied, although large discrepancies were found in many of the remaining points. This deviation was not unexpected because a large number of parameters that influence the flow cannot be accounted for in an analytical solution of what is already a complex flow system. Rigimesh properties often deviate grossly from the nominal values, especially in material with a high-temperature history as shown during injector testing. Also, where boiling occurred within the Rigimesh pores, the pressure drops were higher than those predicted. This was expected because boiling occurs over a finite flow distance, rather than at a particular point as assumed. The sensitivity of pressure drop to heat flux, in addition to the inherent uncertainty in measuring heat flux from a localized Rigimesh temperature reading and a total segment coolant flow rate, compounded the difficulty of obtaining good agreement between the experimental and predicted results. This analytical model is still considered to be a valuable tool for providing initial estimates of coolant pressure drop and wall temperatures. In all cases the predicted pressure drops were sufficiently

accurate; the actual coolant distribution did not deviate more than a maximum of 15% from the desired distribution, and generally did not deviate more than 5%.

**TABLE B-1. COMPARATIVE SUMMARY OF EXPERIMENTAL AND MEASURED RIGIMESH PRESSURE DROPS**

Test No.		Segment No. 1	Segment No. 2	Segment No. 3	Segment No. 4	Segment No. 5	Segment No. 6	Segment No. 7	Segment No. 8
2T	Coolant Flow Rate, $\text{lb}_m/\text{sec-in}^2$	0.00195	0.00176	0.00191	0.00197	0.00299	0.00539	0.00383	0.00143
	Heat Flux, $\text{Btu/sec-in}^2$	2.06	1.00	1.78	1.87	2.55*	3.69*	4.18	1.09
	Measured Pressure Drop, psid	10.8	23.4	14.1	8.5	5.3	27.9	21.7	9.7
	Predicted Pressure Drop, psid	11.9	4.6	15.6	10.8	15.2	29.6	50.9	31.6
3T-2	Coolant Flow Rate, $\text{lb}_m/\text{sec-in}^2$	0.00201	0.00190	0.00198	0.00196	0.00293	0.00559	0.00358	0.00130
	Heat Flux, $\text{Btu/sec-in}^2$	2.05	1.03	1.88	2.05	1.60*	2.36*	1.77	0.59
	Measured Pressure Drop, psid	11.6	24.6	14.3	16.3	10.8	25.5	15.8	8.1
	Predicted Pressure Drop, psid	12.1	4.6	17.0	12.3	8.0	15.0	25.4	15.5
4T-2	Coolant Flow Rate, $\text{lb}_m/\text{sec-in}^2$	0.00152	0.00142	0.00151	0.00148	0.00225	0.00399	0.00267	0.00101
	Heat Flux, $\text{Btu/sec-in}^2$	1.63	0.95	1.46	2.00	2.10*	3.65	1.28	0.68
	Measured Pressure Drop, psid	13.4	24.3	17.6	18.1	11.0	38.3	28.3	
	Predicted Pressure Drop, psid	9.5	5.3	13.0	11.4	13.8	31.5	19.4	21.9
5T-2	Coolant Flow Rate, $\text{lb}_m/\text{sec-in}^2$	0.00093	0.00087	0.00095	0.00075	0.00132	0.00294	0.00205	0.00081
	Heat Flux, $\text{Btu/sec-in}^2$	1.13	0.43	0.96	1.07	1.95*	2.37	1.21	0.65
	Measured Pressure Drop, psid	8.8	14.2	8.9	23.0	15.4	14.7	29.4	
	Predicted Pressure Drop, psid	5.3	1.8	7.2	4.6	10.7	19.4	19.7	20.5
6T-2	Coolant Flow Rate, $\text{lb}_m/\text{sec-in}^2$	0.00098	0.00087	0.00095	0.00076	0.00136	0.00306	0.00198	0.00073
	Heat Flux, $\text{Btu/sec-in}^2$	1.16	0.67	0.88	0.96*	1.34*	2.30	1.59*	0.38
	Measured Pressure Drop, psid	10.2	22.0	12.5	31.9	18.2	9.3	19.2	
	Predicted Pressure Drop, psid	5.6	3.1	6.7	4.2	7.9	19.1	27.7	13.1

\*Bad thermocouple data, heat flux estimated from film coefficients predicted by Bartz short-form method.

#### 4. NOMENCLATURE

$A$	Chamber wall surface area
$\alpha$	Viscous coefficient
$\beta$	Inertial coefficient
$c_p$	Coolant heat capacity
$\gamma$	Specific heat ratio
$d$	Differential operator
$f$	Friction factor
$G$	Coolant flow rate per unit area
$g_o$	Gravitational constant
$h$	Coolant enthalpy
$h_i$	Coolant enthalpy at inlet
$k$	Rigimesh thermal conductivity
$L$	Rigimesh thickness
$M$	Molecular weight of coolant
$\mu$	Coolant viscosity
$N_{Re}$	Reynolds number
$P$	Coolant pressure
$P_c$	Chamber pressure
$\phi$	Porosity
$\phi_c$	Choked flow area per unit cross-sectional area
$q_w$	Chamber heat flux
$R$	Universal gas constant
$\rho$	Coolant density
$T$	Coolant temperature
$x$	Rigimesh linear dimensions in coolant flow direction

#### Subscripts:

1	Upstream side of Rigimesh
2	Downstream side of Rigimesh

#### 5. REFERENCES

1. "Applied Research for Transpiration Cooling of Spacecraft Engine Thrust Chambers," PWA FR-854, 17 December 1963.
2. Weger, E. and D. B. Greenberg, "An Investigation of the Viscous and Inertial Coefficients for the Flow of Gases through Porous Sintered Metals With High Pressure Gradients — Interim Technical Report No. 1," Johns Hopkins University, March 1959.

## APPENDIX C

### DISTRIBUTION LIST

National Aeronautics and Space Administration Lewis Research Center 21000 Brookpark Road Cleveland, Ohio 44135 Attn: Contracting Officer, MS 500-210	1	National Aeronautics and Space Administration Langley Research Center Langley Station Hampton, Virginia 23365 Attn: Library	1
Liquid Rocket Technology Branch, MS 500-209	8	National Aeronautics and Space Administration Manned Spacecraft Center Houston, Texas 77001 Attn: Library	1
Technical Report Control Office, MS 5-5	1	H. J. Brasseaux, PESD-Propulsion	1
Technology Utilization Office, MS 3-16	1	W. Hammock	1
AFSC Liaison Office, MS 4-1	2	National Aeronautics and Space Administration George C. Marshall Space Flight Center Huntsville, Alabama 35812 Attn: Library	1
D. L. Nored, MS 500-209	1	Keith Chandler, R-P&VE-PA	1
Library	2	National Aeronautics and Space Administration Western Operations Office 150 Pico Boulevard Santa Monica, California 90406 Attn: Library	1
W. E. Roberts, MS 3-17	1	Jet Propulsion Laboratory 4800 Oak Grove Drive Pasadena, California 91103 Attn: Library	1
Office of Reliability & Quality Assurance, MS 500-203	1	W. B. Powell	1
Harold Valentine, MS 501-2	1	Office of the Director of Defense Research & Engineering Washington, D. C. 20301 Attn: Dr. H. W. Schulz, Office of Asst. Dir. (Chem. Technology)	1
E. W. Conrad, MS 100-1	1	Defense Documentation Center Cameron Station Alexandria, Virginia 22314	1
Carl Aukerman, MS 86-1	1	RTD (RTNP) Bolling Air Force Base Washington, D. C. 20332	1
National Aeronautics and Space Administration Washington, D. C. 20546 Attn: Code MAT, Charles H. King	1	Arnold Engineering Development Center Air Force Systems Command Tullahoma, Tennessee 37389 Attn: AEOIM	1
RPX	2	Advanced Research Projects Agency Washington, D. C. 20525 Attn: D. E. Mock	1
RPL	2	Aeronautical Systems Division Air Force Systems Command Wright-Patterson Air Force Base Dayton, Ohio Attn: D. L. Schmidt, Code ASRCNC-2	1
SV, Robert F. Schmidt	1	Air Force Missile Test Center Patrick Air Force Base, Florida Attn: L. J. Ullian	1
RPX, Frank W. Stephenson, Jr.	1		
Scientific and Technical Information Facility P. O. Box 33 College Park, Maryland 20740 Attn: NASA Representative Code CRT	6		
National Aeronautics and Space Administration Ames Research Center Moffett Field, California 94035 Attn: Library	1		
C. A. Syvertson	1		
National Aeronautics and Space Administration Flight Research Center P. O. Box 273 Edwards, California 93523 Attn: Library	1		
National Aeronautics and Space Administration Goddard Space Flight Center Greenbelt, Maryland 20771 Attn: Library	1		
C. R. Gunn, Delta Propulsion Office	1		
National Aeronautics and Space Administration John F. Kennedy Space Center Cocoa Beach, Florida 32931 Attn: Library	1		
R. A. Raffaelli	1		

**Pratt & Whitney Aircraft**  
**PWA FR-2227**

Air Force Systems Command (SCLT/Capt. S. W. Bowen) Andrews Air Force Base Washington, D. C. 20332	1	Picatinny Arsenal Dover, New Jersey Attn: I. Forsten, Chief Liquid Propulsion Laboratory	1
Air Force Rocket Propulsion Laboratory (RPR) Edwards, California 93523	1	U. S. Atomic Energy Commission Technical Information Services Box 62 Oak Ridge, Tennessee Attn: A. P. Huber, Code ORGDP	1
Air Force Rocket Propulsion Laboratory (RPM) Edwards, California 93523	1	Box P	
Air Force FTC (FTAT-2) Edwards Air Force Base, California 93523 Attn: Col. J. M. Silk	1	Air Force Aero Propulsion Laboratory Research & Technology Division Air Force Systems Command United States Air Force Wright-Patterson AFB, Ohio 45433 Attn: APRP (C. M. Donaldson)	1
Air Force Office of Scientific Research Washington, D. C. 20333 Attn: SREP, Dr. J. F. Masi	1		
Office of Research Analyses (OAR) Holloman Air Force Base, New Mexico 88330 Attn: RRRT	1	Aerojet-General Corporation P. O. Box 296 Azusa, California 91703 Attn: Librarian	1
Maj. R. E. Brocken, Code MDGRT	1		
U. S. Air Force Washington 25, D. C. Attn: Col. C. K. Stambaugh, Code AFRST	1	Aerojet-General Corporation 11711 South Woodruff Avenue Downey, California 90241 Attn: F. M. West, Chief Librarian	1
Commanding Officer U. S. Army Research Office (Durham) Box CM, Duke Station Durham, North Carolina 27706	1	Aerojet-General Corporation P. O. Box 1947 Sacramento, California 95809 Attn: Technical Library 2484-2015A	1
U. S. Army Missile Command Redstone Scientific Information Center Redstone Arsenal, Alabama 35808 Attn: Chief, Document Section	1	Dr. C. M. Beighley	1
Dr. W. Wharton	1	D. T. Bedsole	1
Bureau of Naval Weapons Department of the Navy Washington, D. C. Attn: J. Kay, Code RTMS-41	1	Aeronutronic Division of Philco Corporation Ford Road Newport Beach, California 92600 Attn: Dr. L. H. Linder, Manager Technical Information Department	1
Commander U. S. Naval Missile Center Point Mugu, California 93041 Attn: Technical Library	1	Aeroprojects, Incorporated 310 East Rosedale Avenue West Chester, Pennsylvania 19380 Attn: C. D. McKinney	1
Commander U. S. Naval Ordnance Test Station China Lake, California 93557 Attn: Code 45	1	Aerospace Corporation P. O. Box 95085 Los Angeles, California 90045 Attn: J. G. Wilder, MS-2293	1
Code 753	1	Library-Documents	1
W. F. Thorm, Code 4562	1	Arthur D. Little, Inc. Acorn Park Cambridge 40, Massachusetts Attn: A. C. Tobey	1
Commanding Officer Office of Naval Research 1030 E. Green Street Pasadena, California 91101	1	Astropower, Incorporated Subs. of Douglas Aircraft Company 2968 Randolph Avenue Costa Mesa, California Attn: Dr. George Moc, Director, Research	1
Director (Code 6180) U. S. Naval Research Laboratory Washington, D. C. 20390 Attn: H. W. Carhart	1		

Astrosystems, Incorporated 1275 Bloomfield Avenue Caldwell Township, New Jersey Attn: A. Mendenhall	1	University of Denver Denver Research Institute P. O. Box 10127 Denver, Colorado 80210 Attn: Security Office	1
ARO, Incorporated Arnold Engineering Development Center Arnold AF Station, Tennessee 37389 Attn: Dr. B. H. Goethert, Chief Scientist	1	Douglas Aircraft Company, Inc. Santa Monica Division 3000 Ocean Park Blvd. Santa Monica, California 90405 Attn: J. L. Waisman	1
Atlantic Research Corporation Shirley Highway & Edsall Road Alexandria, Virginia 22314 Attn: A. Scurlock	1	R. W. Hallet	1
Security Office for Library	1	G. W. Burge	1
Battelle Memorial Institute 505 King Avenue Columbus, Ohio 43201 Attn: Report Library, Room 6A	1	Fairchild Stratos Corporation Aircraft Missiles Division Hagerstown, Maryland Attn: J. S. Kerr	1
Beech Aircraft Corporation Boulder Facility Box 631 Boulder, Colorado Attn: J. H. Rodgers	1	General Dynamics/Astronautics P. O. Box 1128 San Diego, California 92112 Attn: F. Dore	1
Bell Aerosystems, Inc. Box 1 Buffalo, New York 14205 Attn: T. Reinhardt	1	Library & Information Services (128-00)	1
W. M. Smith	1	Convair Division General Dynamics Corporation P. O. Box 1128 San Diego, California 92112 Attn: Mr. W. Fenning	1
Bendix Systems Division Bendix Corporation Ann Arbor, Michigan Attn: John M. Bureger	1	Centaur Resident Project Office	
The Boeing Company Aero Space Division P. O. Box 3707 Seattle, Washington 98124 Attn: Ruth E. Peerenboom (1190)	1	General Electric Company Re-Entry Systems Department P. O. Box 8555 Philadelphia, Pennsylvania 19101 Attn: F. E. Schultz	1
J. D. Alexander	1	General Electric Company Flight Propulsion Lab. Department Cincinnati 15, Ohio Attn: D. Suichu	1
Chemical Propulsion Information Agency Applied Physics Laboratory 8621 Georgia Avenue Silver Spring, Maryland 20910	1	Grumman Aircraft Engineering Corporation Bethpage, Long Island, New York Attn: Joseph Gavin	1
Chrysler Corporation Missile Division Warren, Michigan Attn: John Gates	1	Hercules Powder Company Allegheny Ballistics Laboratory P. O. Box 210 Cumberland, Maryland 21501 Attn: Library	1
Chrysler Corporation Space Division New Orleans, Louisiana Attn: Librarian	1	IIT Research Institute Technology Center Chicago, Illinois 60616 Attn: C. K. Hersh, Chemistry Division	1
Curtiss-Wright Corporation Wright Aeronautical Division Woodridge, New Jersey Attn: G. Kelley	1	Kidde Aero-Space Division Walter Kidde & Company, Inc. 675 Main Street Belleville 9, New Jersey Attn: R. J. Hanville, Director of Research Engineering	1



**Pratt & Whitney Aircraft**  
**PWA FR-2227**

Lockheed Missiles & Space Company P. O. Box 504 Sunnyvale, California Attn: Y. C. Lee, Power Systems R&D Technical Information Center	1 1 1	Republic Aviation Corporation Farmingdale, Long Island, New York Attn: Dr. William O'Donnell	1
Lockheed-California Company 10445 Glen Oaks Blvd. Pacoima, California Attn: G. D. Brewer	1	Rocket Research Corporation 520 South Portland Street Seattle, Washington 98108	1
Lockheed Propulsion Company P. O. Box 111 Redlands, California 92374 Attn: Miss Belle Berlad, Librarian H. L. Thackwell	1 1 1	Rocketdyne Division of North American Aviation, Inc. 6633 Canoga Avenue Canoga Park, California 91304 Attn: Library, Department 596-306 R. P. Pauckert E. V. Zettle	1 1 1
Lockheed Missiles & Space Company Propulsion Engineering Division (D.55-11) 1111 Lockheed Way Sunnyvale, California 94087	1	Rohm and Haas Company Redstone Arsenal Research Division Huntsville, Alabama 35808 Attn: Librarian	1
Marquardt Corporation 16555 Saticoy Street Box 2013 — South Annex Van Nuys, California 91404 Attn: Librarian W. D. Boardman, Jr.	1 1 1	Space-General Corporation 777 Flower Street Glendale, California Attn: C. E. Roth	1
Martin-Marietta Corporation Martin Division Baltimore 3, Maryland Attn: John Calathes (3214)	1	Stanford Research Institute 333 Ravenswood Avenue Menlo Park, California 94025 Attn: Thor Smith	1
McDonnell Aircraft Corporation P. O. Box 6101 Lambert Field, Missouri Attn: R. A. Herzmark	1	Texaco Experiment, Incorporated P. O. Box I-T Richmond, Virginia 23202 Attn: E. B. Monteath Librarian	1 1
North American Aviation, Inc. Space & Information Systems Division 12214 Lakewood Boulevard Downey, California 90242 Attn: Technical Information Center, D/096-722 (AJ01) H. Storms	1 1 1	Thiokol Chemical Corporation Alpha Division, Huntsville Plant Huntsville, Alabama 35800 Attn: Technical Director	1
Northrop Space Laboratories 1001 East Broadway Hawthorne, California Attn: Dr. William Howard	1	Thiokol Chemical Corporation Reaction Motors Division Denville, New Jersey 07834 Attn: A. Sherman Librarian	1 1
Purdue University Lafayette, Indiana 47907 Attn: Technical Librarian	1	Thiokol Chemical Corporation Redstone Division Huntsville, Alabama Attn: John Goodloe	1
Radio Corporation of America Astro-Electronics Division Defense Electronic Products Princeton, New Jersey Attn: S. Fairweather	1	TRW Systems, Incorporated 1 Space Park Redondo Beach, California 90200 Attn: G. W. Elverum STL Tech. Lib. Doc. Acquisitions H. Burge	1 1 1

TRW, Incorporated 1  
TAPCO Division  
23555 Euclid Avenue  
Cleveland, Ohio 44117  
Attn: P. T. Angell

United Aircraft Corporation  
Corporation Library  
400 Main Street  
East Hartford, Connecticut 06118  
Attn: Dr. David Rix 1  
Erle Martin 1

United Aircraft Corporation  
Pratt & Whitney Division  
Florida Research & Development Center  
P. O. Box 2691  
West Palm Beach, Florida 33402  
Attn: R. J. Coar 1  
Library 1

United Aircraft Corporation 1  
United Technology Center  
P. O. Box 358  
Sunnyvale, California 94088  
Attn: Librarian

Vought Astronautics 1  
Box 5907  
Dallas 22, Texas  
Attn: Warren C. Trent